

8502360

Babaie, Hassan Ali

STRUCTURAL AND TECTONIC HISTORY OF THE GOLCONDA  
ALLOCHTHON, SOUTHERN TOiyABE RANGE, NEVADA

*Northwestern University*

PH.D. 1984

University  
Microfilms  
International 300 N. Zeeb Road, Ann Arbor, MI 48106

UNIVERSITY OF UTAH LIBRARIES

## INFORMATION TO USERS

This reproduction was made from a copy of a document sent to us for microfilming. While the most advanced technology has been used to photograph and reproduce this document, the quality of the reproduction is heavily dependent upon the quality of the material submitted.

The following explanation of techniques is provided to help clarify markings or notations which may appear on this reproduction.

1. The sign or "target" for pages apparently lacking from the document photographed is "Missing Page(s)". If it was possible to obtain the missing page(s) or section, they are spliced into the film along with adjacent pages. This may have necessitated cutting through an image and duplicating adjacent pages to assure complete continuity.
2. When an image on the film is obliterated with a round black mark, it is an indication of either blurred copy because of movement during exposure, duplicate copy, or copyrighted materials that should not have been filmed. For blurred pages, a good image of the page can be found in the adjacent frame. If copyrighted materials were deleted, a target note will appear listing the pages in the adjacent frame.
3. When a map, drawing or chart, etc., is part of the material being photographed, a definite method of "sectioning" the material has been followed. It is customary to begin filming at the upper left hand corner of a large sheet and to continue from left to right in equal sections with small overlaps. If necessary, sectioning is continued again—beginning below the first row and continuing on until complete.
4. For illustrations that cannot be satisfactorily reproduced by xerographic means, photographic prints can be purchased at additional cost and inserted into your xerographic copy. These prints are available upon request from the Dissertations Customer Services Department.
5. Some pages in any document may have indistinct print. In all cases the best available copy has been filmed.

University  
Microfilms  
International  
300 N. Zeeb Road  
Ann Arbor, MI 48106

NORTHWESTERN UNIVERSITY

Structural and Tectonic History of the Golconda Allochthon, Southern  
Toiyabe Range, Nevada

A DISSERTATION

SUBMITTED TO THE GRADUATE SCHOOL  
IN PARTIAL FULFILLMENT OF THE REQUIREMENTS

for the degree

DOCTOR OF PHILOSOPHY

Field of Geological Sciences

By

Hassan Ali Babaie, H.A.

Ph.D.

EVANSTON, ILLINOIS

August 1984

## ABSTRACT

The Golconda allochthon and the subjacent autochthonous Permian Diablo Formation in the southern Toiyabe Range record Paleozoic and Triassic depositional and tectonic events that permit partial reconstruction of the architecture of the local North American continental margin in that period. The allochthon consists of moderately- to steeply-dipping NNW-striking fault-bounded packets that mainly include upper Paleozoic rocks. In general, the lowest packets contain terrigenous rocks, and hemipelagic, volcanogenic-basaltic, and pelagic rocks occur in progressively higher packets. Subordinate packets of lower Paleozoic and Lower Triassic rocks occur at the base of the allochthon. Serpentinite occurs near the base of the allochthon as clasts in terrigenous packets and as lenses in packet-bounding faults.

Five phases of deformation are recognized in the upper Paleozoic packets: 1) isoclinal F1 folding and formation of axial plane cleavage, 2) thrust imbrication, 3) F2a folding in packet-bounding thrusts and local F2b folding along the thrusts, 4) F3 kink folding, and 5) local F4 folding and faulting at the Golconda thrust zone. Deformation of lower Paleozoic rocks in the Golconda allochthon occurred partly before attachment to the allochthon. The Lower Triassic rocks are less deformed than the other rocks in the allochthon. The autochthonous Diablo Formation is homoclinal with sporadic mesoscopic folds. An east-west component of contraction that persisted through most phases of deformation is indicated by the tectonic fabric in upper Paleozoic

rocks.

The Golconda allochthon may represent an accretionary prism of a west-dipping subduction zone related to an intraoceanic island arc that existed between the Mississippian and Early Triassic. Upper Paleozoic rocks were deposited in the continental shelf and slope, and abyssal plain of an oceanic basin that existed east of the arc. The Triassic rocks may be interpreted as foreland basin deposits of the Golconda accretionary prism. These were overthrust by the prism and were partly incorporated with lower Paleozoic rocks into it as the prism prograded east, relative to North America, by accretion. The serpentinites may represent oceanic crustal or mantle rocks that were incorporated into the allochthon by upward plastic motion along packet-bounding thrusts or extensional faults, sedimentary processes, or a combination of these.

#### ACKNOWLEDGEMENTS

I am particularly grateful to R. C. Speed for introducing me to the problem, his continuous support and guidance throughout the work, and critical review of the manuscript. I would like to thank A. A. Babaie and my wife S. Babaie for their field assistance.

I wish to thank B. M. Murchey and D. L. Jones and A. G. Harris for the identification of radiolaria and conodonts, respectively. This research was funded by grants from Gulf Oil Co. and NSF # EAR-7911150 (R. C. Speed, principal investigator) and by the Geological Society of America and Northwestern University's Special Dissertation Fund.

ABSTRACT

ACKNOWLEDGEMENTS

TABLE OF CONTENTS

LIST OF FIGURES

LIST OF TABLES

LIST OF REFERENCES

CHAPTER I

Background

Statement of the Problem

Methodology

CHAPTER II

Introduction

Algorithms

Unconformities

Autocorrelation

TABLE OF CONTENTS

	<u>page</u>
ABSTRACT .....	ii
ACKNOWLEDGEMENTS .....	iv
TABLE OF CONTENTS .....	v
LIST OF TABLES .....	viii
LIST OF PLATES .....	viii
LIST OF FIGURES .....	x
CHAPTER 1: INTRODUCTION .	1
Background .....	1
Statement of the problem .....	11
Method of study .....	13
CHAPTER 2: TECTONOSTRATIGRAPHY OF THE GOLCONDA ALLOCHTHON IN STUDY AREA .....	14
Introduction .....	14
Allochthonous rocks .....	23
I- Upper Paleozoic rocks .....	23
1) Terrigenous rocks .....	25
Depositional environment .....	30
2) hemipelagic rocks .....	32
Depositional environment .....	32
3) Volcanogenic rocks .....	33
Depositional environment .....	35
4) Pelagic rocks .....	40
Depositional environment .....	41
Facies analysis .....	42
II- Lower Paleozoic rocks .....	44
III- Triassic and Triassic (?) rocks .....	45
Depositional environment .....	46
Unit 6 .....	47
Autochthonous rocks .....	49
Lower Paleozoic rocks .....	49
Diablo Formation (Pd) .....	50
Depositional environment .....	51
Toiyabe Quartz Latite (Tql) .....	52
Ophir pluton (Tgr) .....	52

CHAPTER 3: STRUCTURAL GEOLOGY OF THE GOLCONDA ALLOCHTHON ..... 53

Introduction ..... 53  
 Pre-thrust deformation ..... 56  
 Syn-thrust deformation ..... 57  
 Post-thrust deformation ..... 57  
 Method and terminology ..... 57  
 F1 folds ..... 60  
     Domain 12 ..... 60  
     Domain 7 ..... 66  
     Other domains ..... 66  
 F2a folds ..... 81  
 F2b folds ..... 86  
 F3 folds ..... 90  
     Domain 7h5 ..... 92  
     Domain 8 ..... 97  
     Domain 12 ..... 102  
     Discussion ..... 102  
     Geometric analysis of kinks ..... 107  
         Migration model ..... 107  
         Rotation model ..... 110  
         Results ..... 110  
 Tectonic fabric at the Golconda thrust zone ..... 116  
 Tectonic fabric in domain 9 ..... 123  
 Tectonic fabric of the Diablo Formation ..... 131  
 Tectonic fabric of autochthonous lower Paleozoic rocks... 137

Strain analysis ..... 140  
 Introduction ..... 140  
 Theory of strain of elliptical grains ..... 140  
     Initial grain shape ..... 143  
     Initial grain orientation ..... 143  
     Ductility contrast between grain and matrix.... 144  
     Volume change during strain ..... 145  
     Orientation, amount, and strain axial ratio.... 147  
     Incremental rotations ..... 147  
     Errors ..... 148  
 Strain measurement in the study area ..... 148  
     Two-dimensional strain analysis ..... 153  
         Results ..... 154  
         Correlation between different methods..... 158  
         Implications ..... 165  
     Three-dimensional strain analysis..... 169  
         Results ..... 171  
         Packet 7 ..... 171  
         Packet 12 ..... 176  
         Discussion ..... 176

CHAPTER 4

Age  
 Kine  
 Pale  
 Serp  
 Corr

REFERENCE

APPENDIX

Group

Group

APPENDIX

VITA ...



.... 53  
.... 53  
.... 56  
.... 57  
.... 57  
.... 60  
.... 60  
.... 66  
.... 66  
.... 81  
.... 86  
.... 90  
.... 92  
.... 97  
.... 102  
.... 102  
.... 107  
.... 107  
.... 110  
.... 110  
.... 116  
.... 123  
.... 131  
.... 137  
.... 140  
.... 140  
.... 140  
.... 143  
.... 143  
.... 144  
.... 145  
.... 147  
.... 147  
.... 148  
.... 148  
.... 153  
.... 154  
.... 158  
.... 165  
.... 169  
.... 171  
.... 171  
.... 176  
.... 176

CHAPTER 4- KINEMATICS OF SEQUENTIAL PROCESSES AND RECONSTRUCTION  
OF THE PALEOGEOGRAPHY ..... 182

Age of emplacement of the Golconda allochthon in the area.. 182  
Kinematics of sequential events ..... 183  
Paleogeography and plate tectonics reconstruction..... 192  
Serpentinization..... 199  
Correlation with other parts of the Golconda allochthon... 202  
    Jett to Wall Canyons ..... 202  
    New Pass Range ..... 203  
    Northern Nevada ..... 205

REFERENCES ..... 207

APPENDIX I- METHODS OF TWO DIMENSIONAL STRAIN ANALYSIS ..... 219

    Group I methods ..... 219  
        Slope method ..... 219  
        Arithmetic, geometric, and harmonic mean methods ..... 220

    Group II methods ..... 222  
        Shimamoto-Ikeda method ..... 222  
        Polar graph method ..... 223  
        Tobisch and others method ..... 224  
        Holst method ..... 225  
        Robin method ..... 225  
        Rf/φ method ..... 226

APPENDIX II- METHOD OF THREE-DIMENSIONAL STRAIN ANALYSIS..... 229

VITA ..... 236

LIST OF TABLES

<u>Table</u>	<u>Page</u>
Chapter 1	
1-1 Lithology, age, and contacts of four tectonostratigraphic complexes that make up the Golconda allochthon in different parts of Nevada	3
Chapter 2	
2-1 Lithology and age of autochthonous units in the Golconda allochthon and their relationship to fault-bounded packets and lithic types	16
2-2 Description and age of the radiolaria and conodonts dated in this study	24
2-3 Lithology and age of terrigenous lithic units	27
2-4 Facies and depositional environment of the four major upper Paleozoic lithic types in the Golconda allochthon	43
Chapter 3	
3-1 Deformational events in the upper paleozoic section of the Golconda allochthon	54
3-2 Deformational events in the lower Paleozoic (?) packet 9	124
3-3 Results of two-dimensional strain for 34 thin sections	155
3-4 Results of three-dimensional strain analysis for the 9 specimens in packet 7 and 12	172

LIST OF PLATES

1 Geologic map of the Golconda allochthon in the southern Toiyabe Range, Nevada	237
---	-----

Page  
rati- 3  
uthon  
  
Gol- 16  
ult-  
onts 24  
27  
ajor 43  
thon  
  
of 54  
cket 124  
ons 155  
e 9 172  
  
ern 237

2 Orientation of cleavage and bedding in the Golconda allochthon 238  
3 Geologic map of the Golconda allochthon in Ophir Canyon 239

LIST OF FIGURES

<u>Figure</u>	<u>Page</u>
Chapter 1	
1-1 Locality map and geography of the study area	2
1-2 Map showing the extent of the Golconda allochthon and the location in the study area	5
1-3 Two major tectonic models for the formation and emplacement of the Golconda allochthon	10
Chapter 2	
2-1 Geological map of the study area showing the distribution of lithic units, packets, and cross section transects	15
2-2 Tectonostratigraphy of all the rocks in the study area	18
2-3 Cross sections in the Golconda allochthon of the study area	20
2-4 Location and number of dated specimens in the Golconda allochthon	22
2-5 Location of clastic and fault zone serpentinites	29
Chapter 3	
3-1 Map showing structural domains in the Golconda allochthon	58
3-2 Three-dimensional diagram of a fold showing the parameters measured for fabric analysis	59
3-3 Distribution of the amplitude and halfwavelength of F1 folds	61
3-4 Orientation data of F1 structures in domain 12	63
3-5 Orientation of F1 structures in three subdomains of domain 12b	64
3-6 Orientation data of F1 structures in domain 7h5	67
3-7 Orientation data of F1 structures in domain 1	69
3-8 Orientation data of F1 structures in domain 3	70
3-9 Orientation data of F1 structures in domain 4	71
3-10 Orientation data of F1 structures in domain 5	72

3-11 Ori  
 3-12 Ori  
 3-13 Ori  
 3-14 Ori  
 3-15 Ori  
 3-16 Ori  
 3-17 Ori  
 all  
 3-18 Con  
 Oph  
 3-19 Ori  
 Can  
 3-20 Ori  
 mac  
 def  
 3-21 Ori  
 hal  
 3-22 Ori  
 3-23 Ge  
 ure  
 3-24 Ori  
 3-25 Sun  
 the  
 fol  
 3-26 Ori  
 kin  
 3-27 Ori  
 3-28 Sun  
 sh  
 fo  
 3-29 Ori  
 dor  
 3-30 Ori  
 3-31 Ori  
 3-32 Sun  
 3-33 Ori  
 3-34 Mi  
 of  
 3-35 A  
 di  
 3-36 Di  
 the  
 3-37 Re  
 3-38 Pi  
 tu  
 3-39 Or  
 th

3-11	Orientation data of F1 structures in domain 7t3	73
3-12	Orientation data of F1 structures in domain 8	75
3-13	Orientation data of F1 structures in domain 11	76
3-14	Orientation of bedding and cleavage in domain 13	77
3-15	Orientation data of F1 structures in domain 14	78
3-16	Orientation of bedding and cleavage in domain 15	80
3-17	Orientation of bedding and cleavage in the Golconda allochthon and autochthon	82
3-18	Constructed profile of the F2a macroscopic fold in Ophir Canyon	83
3-19	Orientation data of the macroscopic F2a fold in Ophir Canyon	84
3-20	Orientation data of F1 structures in both limbs of the macroscopic fold and a flexural slip model for their deformation by the F2a fold	85
3-21	Orientation of the apical angle, amplitude, and halfwavelength of the F2b folds	87
3-22	Orientation data of F2a folds in domain 7h5a	89
3-23	Geometry of a kink fold, showing lines and angles measured in the field	91
3-24	Orientation data of F3 folds in domain 7h5a	93
3-25	Summary orientation data of F3 folds in domain 7h5a and the range of allowable shortening directions for F3 folding	94
3-26	Orientation data and picture of intersecting S and Z kinks in domain 7h5a	96
3-27	Orientation data of F3 folds in domain 7h5b	98
3-28	Summary orientation data of F3 folds in domain 7h5b, showing the range of allowable shortening directions for kink folding	99
3-29	Orientation data of kinks in the southern part of domain 7h5a	100
3-30	Orientation data of F3 folds in domain 8	101
3-31	Orientation data of F3 folds in domain 12b	103
3-32	Summary orientation data of F3 folds in domain 12b	104
3-33	Orientation data of F3 folds in domain 12a	105
3-34	Migration and rotation models for formation and growth of kinks	108
3-35	A flexural slip model showing the effect of rotation on dilation and angular parameters of kinks	109
3-36	Distribution of linear and angular features of kinks in the study area	111
3-37	Relationship between geometric features of kinks	112
3-38	Pictures of kinks showing axial plane cracks and fractures	115
3-39	Orientation data of F4 folds and associated faults in the Golconda thrust zone	117

3-40	A method to determine slip direction using axial plane of a fold and associated fault	119
3-41	Orientation data of F4 folds, slip directions, associated faults, and striations in the Golconda thrust zone	120
3-42	Orientation data of kinks in the Golconda thrust zone, north of Ophir Canyon	121
3-43	Orientation data of kinks south of Ophir Canyon in the Golconda thrust zone	122
3-44	Orientation of tabular clasts and bedding in domain 9b	125
3-45	Orientation of homoclinal bedding and two cleavages in domain 9a	126
3-46	Distribution of the apical angle, amplitude, and halfwavelength of folds in domain 9a	127
3-47	Orientation data of folds in station 146 of domain 9a	128
3-48	Orientation data of folds in station 147 of domain 9a	130
3-49	Schematic diagram showing the relationship between different structural elements in domain 9a	132
3-50	Orientation of bedding and cleavage in autochthonous Diablo Formation	133
3-51	Orientation data of a fold and an associated fault in autochthonous Diablo Formation	135
3-52	Orientation of disharmonic folds in Diablo Formation	136
3-53	Orientation of bedding and cleavage in the autochthonous lower Paleozoic rocks	138
3-54	Map showing the location and number of oriented specimens for strain analysis	149
3-55	Orientation of thin sections and calculated principal directions in the oriented specimens of packet 7	151
3-56	Orientation of thin sections and calculated principal directions in the oriented specimens of packet 12	152
3-57	Typical grain long versus short axes plot in a slate specimen	156
3-58	Relationship between the coefficient of linear correlation (r) and initial grain axial ratio and strain ratio	157
3-59	Polar graph showing heart-shaped distribution	159
3-60	Typical $R_f/\phi$ , $R_i/\theta$ , and Chi-Square graphs	160
3-61	Relationship between the estimates of strain calculated by the two methods of two-dimensional strain analysis	162
3-62	Relationship between % error of each method of group I and strain ratio of all group II two-dimensional methods	163
3-63	Relationship between % error of each method of group I and average initial axial ratio	164
3-64	Relationship between % error of each method of group I and average initial axial orientation	166
3-65	Correlation between strain ratio calculated by different methods of group II	167

3-66	Rela rati
3-67	Prin in p
3-68	Rams from Unit
3-69	Rela and cond
3-70	Prin mens

4-1	An a fold
4-2	Synt tion
4-3	A fo
4-4	A fl
4-5	An a depo sect
4-6	A mo and
4-7	Thre mode allo

APP-1	Tria stra
APP-2	Mohr anal

ne	119	3-66 Relationship between the harmonic mean and strain axial ratio	168
i-	120	3-67 Principal directions and deformation plot for specimens in packet 7	173
ne	121	3-68 Ramsay and Wood's (1973) deformation plot for slates from the Caledonites of NW Europe and the Eastern United states and the results of this study	174
e,	122	3-69 Relationship between principal extensions and ratios and structural position of the specimen above the Golconda thrust in packet 7 and 12	177
he	125	3-70 Principal directions and deformation plot for specimens in packet 12	178
b	126		
in	127		
nd	128		
	130		
f-	132		

Chapter 4

us	133	4-1 An accretionary model for the formation of F1 and F2a folds in the Golconda allochthon	186
in	135	4-2 Synthetic fabric for the accretionary model of deformation of the upper Paleozoic section	187
	136	4-3 A forward flexural slip model for F2b folding	189
o-	138	4-4 A flexural slip model for F4 folding	191
i-	149	4-5 An accretionary model for late Paleozoic tectonic and depositional processes that evolved the upper Paleozoic section of the Golconda allochthon	195
al	151	4-6 A model for the Triassic paleogeography and tectonic and depositional processes	197
al	152	4-7 Three alternative tectonic models for the origin and mode of emplacement of serpentinites in the Golconda allochthon	198
ce	156		
-	157		

Appendix II

o	159		
	160		
d	162	APP-1 Triangle construction of three-dimensional method of strain analysis for specimen # 16.	234
I	163	APP-2 Mohr Circle construction of three-dimensional strain analysis for specimen # 16.	235
l	164		
I	166		
-	167		

## CHAPTER 1 - INTRODUCTION

### Background

The study area lies in the southern Toiyabe Range, Nevada, between Ophir and Marysville canyons (Figure 1-1). The range exposes extensively pre-Tertiary rocks that include 1) autochthonous and allochthonous (relative to the Golconda thrust) lower Paleozoic rocks that can be correlated with those of the Roberts Mountains allochthon and autochthon, 2) late Paleozoic and possibly Triassic cover strata (Diablo Formation of Speed and others, 1977) that lie unconformably over the autochthonous lower Paleozoic rocks, and 3) the Golconda allochthon, which includes different packets of sedimentary and volcanic rocks of early and late Paleozoic and Early Triassic ages. The pre-Tertiary rocks are intruded by a pluton of early Tertiary K-Ar age (Speed and McKee, 1976) and covered by volcanic rocks (Ferguson and Cathcart, 1954; Kleinhampl and Ziony, 1967).

This dissertation focuses mainly on 1) the Golconda allochthon and its fault-bounded packets that include varied upper Paleozoic oceanic facies (Pablo Formation of Speed, 1977a; Table 1-1), lower Paleozoic hemipelagic rocks, and terrigenous Triassic rocks, 2) the upper Paleozoic Diablo Formation (Speed and others, 1977; Chapter 2), and to a lesser degree 3) the autochthonous lower Paleozoic rocks immediately below the Golconda thrust.

The Sonoma orogeny (Silberling and Roberts, 1962) or Sonoma event (Speed, 1982) was defined in central Nevada as the cause of folding and



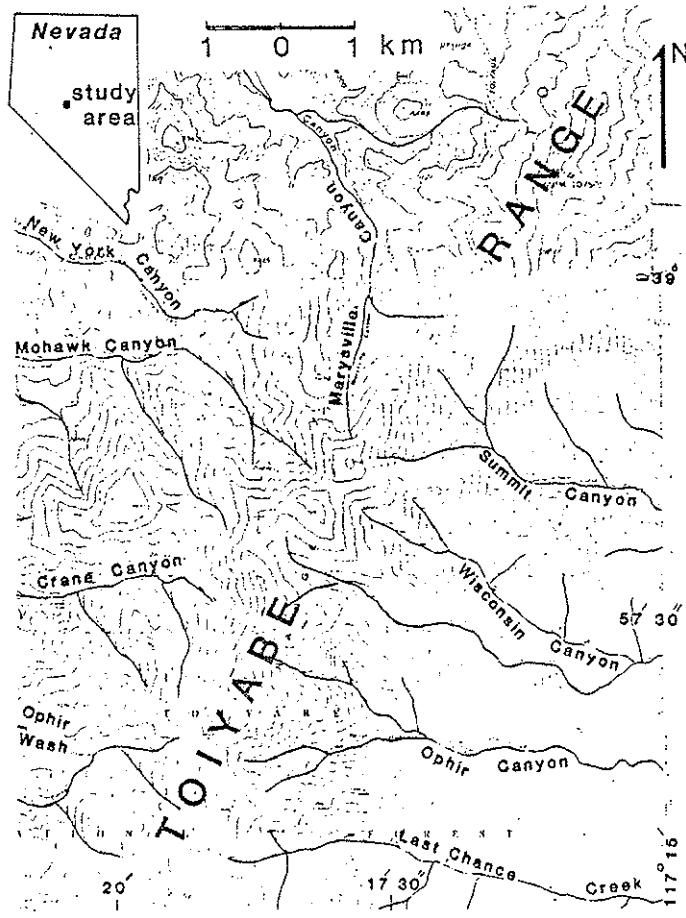


Figure 1-1. Locality map of the study area.

ia, between  
ses exten-  
allochtho-  
s that can  
and auto-  
ta (Diablo  
over the  
llochthon,  
rocks of  
e-Tertiary  
Speed and  
Gathcart,

chthon and  
ic oceanic  
Paleozoic  
per Paleo-  
and to a  
mediately

oma event  
olding and

TECTONOSTRATIGRAPHIC COMPLEX	DESCRIPTION	REFERENCES
Havallah sequence	<p>Lithology: bedded chert, pelite, quartzose sandstone, sandy limestone, pebbly sandstone, volcanogenic turbidite, tholeiitic basalt, massive sulfide, and Fe and Mn deposits.</p> <p>Fossils: middle Wolfcampian and early Leonardian fusulinids and Pennsylvanian to Early Permian conodonts (Stewart and others, 1977), detrital Middle Pennsylvanian fusulinids (Silberling and Roberts, 1962).</p> <p>Contacts: bounded at the bottom by the Golconda thrust. Upper Paleozoic overlap sequence and the Roberts Mountains allochthon make up the lower plate. Contact with overlying Triassic rocks is depositional.</p>	<p>Muller and others, 1951          Silberling and Roberts, 1962          Silberling, 1973          Stewart and others, 1977          Snyder and Brueckner, 1983</p>
Pablo Formation	<p>Lithology: clayey and silty mudstone, slate, hornfels, bedded chert, pillowed, massive, and porphyritic basalt, microgabbro, basaltic fine to coarse sandstone and green and red mudstone, and coarse grained volcanogenic sedimentary rocks.</p> <p>Fossils: Mississippian to Permian radiolaria and conodonts.</p> <p>Contacts: bounded at the base by the Golconda thrust. The lower plate of the thrust is Permian Diablo Formation and lower Paleozoic rocks. Tertiary volcanic rocks and possibly Mesozoic clastic rocks overlie these at the top. Paleogene granitic rocks intrude all rocks.</p>	<p>Ferguson and Cathcart, 1956          R. C. Speed, unpub. data, 1971-7          Speed, 1977          this study</p>
Schoonover Complex	<p>Lithology: greenstone, bedded chert, siliceous pelite, chert-pebble conglomerate, quartzose arenite, pebbly mudstone, silty limestone, and volcanogenic rocks.</p> <p>Fossils: radiolaria in chert of the lower half of the sequence of possibly latest to earliest Mississippian at the base and as young as Early Pennsylvanian in the structurally higher parts of the sequence (Miller and others, 1982).</p> <p>Contacts: the Golconda thrust separates the rocks of the sequence from the Late Mississippian to Permian shallow water rocks.</p>	<p>Fagan, 1962          Churkin and Kay, 1967          Miller and others, 1982</p>
Willow Canyon Formation	<p>Lithology: bedded chert, shale, siliceous siltstone, pillow basalt, jasperoid, bedded jasper, and minor sandstone and greenstone.</p> <p>Fossils: Leonard and possibly Guedalupian radiolaria in chert.</p> <p>Contacts: a major thrust, equivalent to the Golconda thrust, separates the formation from the autochthonous Permian Wildcat Peak Formation that is part of the overlap sequence.</p>	<p>Laule and others, 1981</p>

Table 1-1. Lithology, age, and contacts of four tectonostratigraphic complexes that make up the Golconda allochthon in different parts of Nevada.

thrusting of the oceanic upper Paleozoic rocks of the Golconda allochthon and its emplacement over the partly coeval shallow marine rocks of the continental shelf and older Roberts Mountain allochthon (Silberling and Roberts, 1962). The event is characterized by the lack of associated magmatism, metamorphism, and severe deformation of the lower plate of the Golconda thrust (Speed, 1979).

The Golconda allochthon, the upper plate of the Golconda thrust (Speed, 1971b) crops out over 380 km from the southern Toiyabe Range to northern Nevada (Figure 1-2). The tectonostratigraphic units attributed to the allochthon in different parts of Nevada include the Havallah sequence (Silberling and Roberts, 1962; Stewart and others, 1977; Snyder and Brueckner, 1983), the Pablo Formation (Ferguson and Cathcart, 1954; Speed, 1977), the Schoonover complex (Miller and others, 1982), and the Willow Canyon Formation (Laule and others, 1981). The lithology, age, and contacts of these assemblages are described briefly in Table 1-1.

The upper Paleozoic rocks of the allochthon are interpreted as deep ocean floor deposits (Speed, 1971; Silberling, 1973; MacMillan, 1972; Speed, 1977a,b; Stewart and others, 1977; Snyder and Brueckner, 1983) because of bedded radiolarian chert, red mudstone, pillowed basalt, and distal turbidite. The deep water, trace fossil, Lophoc-  
tenium (Stewart and others, 1977), occurs at places. Other upper Paleozoic rocks of the allochthon include volcanogenic turbidites and serpentinite bearing siliciclastic sedimentary breccia.

The Golconda thrust was defined in the Sonoma Range Quadrangle in

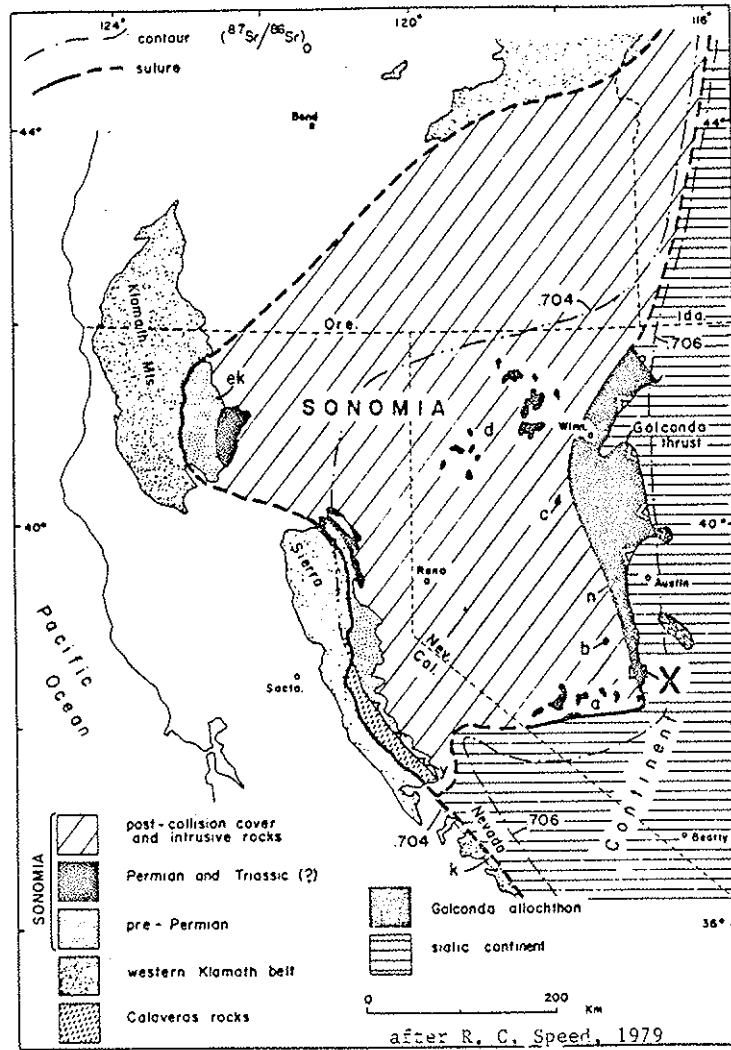


Figure 1-2. Map showing the extent of the Golconda allochthon and the location of the study area (shown by X).

north  
tain  
Range  
Forma  
Silbe  
1971b  
place  
Based  
simil  
the G  
exten  
local  
excep  
litho  
  
tonic  
and,  
partl  
Robert  
face  
chara  
ciate  
blo  
cond  
allo



allochthon (marked by X).

northern Nevada (Muller and others, 1951), extending from Battle Mountain northwest through Edna Mountain to the west side of the Sonoma Range. There, it superposes the so-called Pumpnickel and Havallah Formations (Ferguson and others, 1951, 1952; Muller and others, 1951; Silberling and Roberts, 1962), now called Golconda allochthon (Speed, 1971b), over upper Paleozoic carbonates and siliciclastic rocks and, in places, lower Paleozoic rocks of the Roberts Mountains allochthon. Based on the apparent continuity, thrust relationships, and lithic similarity of the Pablo Formation (Table 1-1) in the Toiyabe Range to the Golconda allochthon (Table 1-1) in northern Nevada, Speed (1971b) extended the Golconda thrust south of 39°, 270 miles south of its type locality. He redefined it as a single, laterally continuous fault except for Tertiary disruptions that juxtaposes rocks of different lithology and deformation.

The Golconda thrust is recognized in the study area by the tectonic juxtaposition of folded and faulted upper Paleozoic oceanic rocks and, locally, lower Paleozoic and Triassic rocks over the homoclinal, partly coeval shallow marine Diablo Formation and the rocks of the Roberts Mountains allochthon. The thrust is a regionally mappable surface across which is an abrupt facies and deformation change, and is characterized in places by the existence of many local faults and associated folds. The Pablo Formation (Table 1-1) in the upper and the Diablo Formation (Speed and others, 1977) in the lower plates of the Golconda thrust in the southern Toiyabe Range are correlated with the allochthonous upper Paleozoic rocks of the Havallah sequence and Antler

sequence in northern Nevada, respectively (Speed, 1977a; Speed and others, 1977).<sup>7</sup>

Silberling and Roberts (1962), Speed (1971b), and Silberling (1973, 1975) proposed on the basis of the unconformable superposition of rhyolitic and clastic rocks of the Permian (?) and Early Triassic Koipato Group on the Golconda allochthon that the Golconda thrust predates the Koipato. The thrusting was after the deposition of the youngest part of the Antler Sequence (Silberling and Roberts, 1962; Table 1-1), the Edna Mountain Formation of mid-Permian age. The alkalic and siliceous ash flow tuffs of the Koipato Group are interpreted as deposited on block faulted terrain (Burke, 1973). Using detailed structural and sedimentological relations, MacMillan (1972) demonstrated that the emplacement of the allochthon occurred in Early Triassic time in the New Pass Range, where the allochthon lies with angular unconformity under upper Lower Triassic conglomerate. Speed (1971b) constrained the emplacement of the allochthon between early Early Triassic and late Early Triassic using the ages of the youngest rocks overrun by the thrust and the oldest cover strata that may be correlated across the Golconda thrust, respectively.

Despite the apparently well established Late Permian-Early Triassic age of the Golconda thrust (Speed, 1971a; Silberling, 1973, 1975), the contemporaneity of the thrust with the Sonoma event has been questioned by K.B. Ketner (Pers. comm., 1982), and a Jurassic-Cretaceous age for the thrust is proposed. According to him, the Sonoma and the Golconda thrust are tectonically unrelated events of different ages. He

nd Silberling  
superposition  
arly Triassic  
olconda thrust  
ition of the  
Roberts, 1962;  
an age. The  
oup are inter-  
973). Using  
Millan (1972)  
ed in Early  
hon lies with  
erate. Speed  
between early  
the youngest  
a that may be

Early Trias-  
1973, 1975),  
s been ques-  
ic-Cretaceous  
oma and the  
rent ages. He

8

believes that the rocks of the Golconda allochthon (Havallah sequence) were deformed at an unknown and distant location during latest Permian or earliest Triassic and were then overlain unconformably by shallow water Triassic sediments. Both the Paleozoic rocks and their Triassic cover strata were then emplaced in their present location via the Golconda thrust during late Jurassic or Early Cretaceous. Ketner's reasons for the above propositions are as follows (K. B. Ketner, Pers. comm., 1982; Ketner, 1982): 1) assignment of a deep water turbidite origin for Triassic rocks in the Adobe Range of northeastern Nevada, and a shallow water origin for Triassic rocks overlying the Havallah sequence west of this range, suggest that the entire stack of the Havallah and shallow water Triassic rocks to the west are out of place and displaced to their present position after the end of the Triassic; 2) paucity of orogenic Triassic sediments in the vicinity of the Golconda allochthon; and 3) absence of convincing examples of a Triassic formation lying with sedimentary contact across the Golconda thrust. His supporting evidences for the age of the Golconda thrust are as follows: 1) a thrust of intensely deformed siliceous Permian rocks, apparently part of the Golconda allochthon, was emplaced over folds of Jurassic or younger age in the Peko Hills of northeastern Nevada; 2) the presence of widespread, thick, and coarse orogenic sediments of Cretaceous to Eocene age in Nevada.

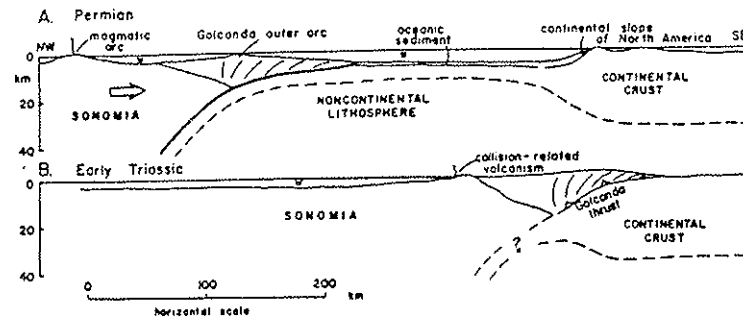
A considerable literature entertaining origins of the Golconda allochthon by plate interactions has appeared in recent years (Moore, 1970; Burchfiel and Davis, 1972; MacMillan, 1972; Speed, 1971a,b, 1974,

1977b, 1978, 1979, 1983; Silberling, 1973, 1975; Dickinson, 1977; Poole and Sandberg, 1977; Snyder and Brueckner, 1983). Although an arc-continent collision has been applied as a basis to model and interpret the late Paleozoic-Early Triassic events, timing, paleogeography, and subduction zone polarity have been matters of dispute. Almost all workers agree on the idea that in Permo-Triassic time, the rocks of the Golconda allochthon were thrust onto the continental margin of the western United States. There are basically two major competing models for the evolution and emplacement of the allochthon (Figure 1-3) as described below:

Forearc model - This model assumes that the rocks of the allochthon were deposited in oceanic basins that fronted western North America and were accreted to a forearc or accretionary prism (Karig and Sharman, 1975; Scholl and others, 1980) of a migrating island arc above a west dipping subduction zone (Speed, 1977b, 1978, 1979; Snyder and Brueckner, 1983). In this model, the Golconda thrust is the basal detachment surface under the prograding accretionary pile that brought the tectonically stacked rocks over the undersliding passive margin of the North American continental plate (Figure 1-3a).

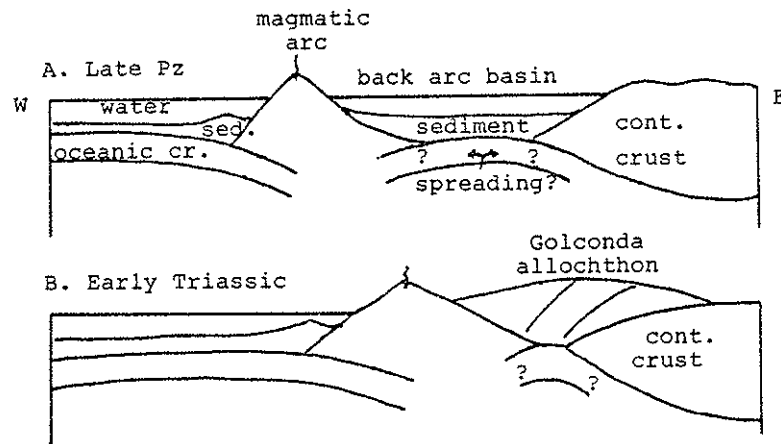
Back arc model - This model assumes that the rocks of the allochthon were deposited in a local back arc basin of a subduction zone that dipped east below Nevada and were thrust (obducted) onto the North American continental margin when the basin was closed (Burchfiel and Davis, 1972; Silberling, 1973; Churkin, 1974; Miller and others, 1982)





Sections depicting collision of Sonomia at about 40°N; w = water

a - Forearc model after R. C. Speed, 1979



b - Back arc model

Figure 1-3. Two major models for the formation and emplacement of the Golconda allochthon.

Statement of the problem

The study area is one of two locations with extensive exposures of the Golconda allochthon in southern Toiyabe Range, the other being between Jett and Peavine Canyons (R. C. Speed unpub. data 1971-3). Only meager exposures of the allochthon exist farther south in Candelaria (R. C. Speed, pers. comm., 1983). Despite its geographically significant location, the thesis area has had only few detailed investigations (Speed, 1977a; Speed and others, 1977; Speed and McKee, 1976; R. C. Speed and J.R. MacMillan unpub. data, 1971-7).

Many unresolved problems remain related to the Golconda allochthon that are critical in understanding the tectonic history and paleogeography of the western United States during late Paleozoic and Early Triassic times. In the study area, these problems include the following:

1. Late Paleozoic paleogeography of western margin of North American continent in what is now Nevada: the study area lies near to the buried edge of sialic Precambrian North America, as is indicated by strontium isotopic ratios and gravity gradients (Kistler and Peterman, 1978; Cogbill, 1979; Speed, 1982b; Figure 1-2). The edge may represent a preserved segment of the Precambrian-Cambrian passive margin of the western North America (Stewart, 1972). The isotopic 0.706 contour coincides approximately with the westernmost outcrops of autochthonous Paleozoic rocks of outer-shelf facies (Speed and Sleep, 1982). After the Precambrian rifting, rocks of the Roberts Mountains allochthon were

deposi  
1958;  
1977;  
alloch  
Missis  
A  
new ba  
receiv  
nown  
the up  
tion  
existe  
2  
archit  
kinema  
thrust  
direct  
Mesozo  
3  
the G  
tion,  
deforma  
differ  
upper  
Golcon

extensive exposures of  
 the other being  
 (data 1971-3). Only  
 south in Candelaria  
 tectonically signifi-  
 cant investigations  
 (see, 1976; R. C.

Golconda allochthon  
 history and paleogeog-  
 raphy of Early  
 Paleozoic and Early  
 Paleozoic include the follow-

of North Ameri-  
 can lies near to the  
 is indicated by  
 (Roberts and Peterman,  
 1976) may represent  
 the active margin of the  
 c. 0.706 contour  
 of autochthonous  
 (see, 1982). After  
 the allochthon were

deposited in an oceanic basin west of the suture (Roberts and others, 1958; Kay and Crawford, 1964, Stewart and Poole, 1974; Matti and McKee, 1977; Speed and Sleep, 1982) which were deformed and emplaced into the allochthon during the Antler event (Roberts, 1951) between Devonian and Mississippian.

After the eastward displacement of the Roberts Mountains thrust, a new basin was formed west of the then extended continental margin which received sediments between Mississippian and Permian or Triassic. Unknown are the location, age, extent, and nature of the basin in which the upper Paleozoic rocks of the allochthon were deposited; the location and configuration of the continental shelf and slope; and the existence and nature of an island arc associated with this basin.

2. Structure and tectonics of the Golconda allochthon: general architecture ; geometry of fault-bounded packets in the allochthon; kinematics and mechanism of tectonic processes responsible for folding, thrusting, and stacking of packets in different deformation phases; direction and magnitude of tectonic transport and strain; effects of Mesozoic and Cenozoic deformations on the Golconda allochthon.

3. History of the allochthon: time of deposition of the rocks in the Golconda allochthon and autochthon; times of deformation, accretion, and emplacement of the the allochthon; relative age of different deformation phases; relative timing of deformation and deposition in different packets; relative timing of attachment of lower Paleozoic, upper Paleozoic, and Triassic packets to the allochthon; age of the Golconda thrust.

4. Serpentinite: origin of the serpentinites that occur in fault slices in the allochthon; the source of sedimentary fragments of serpentinite in coarse grained clastic rocks; and their tectonic significance.

5. Triassic rocks in the allochthon: the site and extent of their deposition; where, when, and how they got involved with the allochthon; what is their tectonic and paleogeographic significance; what was the source of their clastics; and what constraint do they put on the age of the Golconda thrust.

6. Lower Paleozoic rocks in the allochthon: mechanism of their attachment to the base of the allochthon; their relation to the encroachment of the allochthon and nature of the continental margin; and where they were derived from.

#### Methods of study

To achieve an improved understanding and solutions to the aforementioned problems related to the Golconda allochthon, the study included detailed field mapping and description of rock types and their boundaries, sampling for protolith age, petrography, strain analysis, and measurement of tectonic fabrics. The structural data were reduced, modeled, interpreted, and combined with the sedimentologic, petrographic, and paleontologic data to evaluate the sequential processes during the development and emplacement of the allochthon.

Introd

T

of de

plate,

T

fault-

packet

2-1,

within

Althou

such t

on th

charac

that

t2, t3

1, Fi

all th

T

gic,

fault

faults

the pr

CHAPTER 2- TECTONOSTRATIGRAPHY OF THE GOLCONDA ALLOCHTHON  
IN THE STUDY AREA

Introduction

This Chapter describes the architecture, lithology, age, mechanism of deposition, and depositional environment of the rocks in the upper plate, and to a lesser extent, lower plate of the Golconda thrust.

The Golconda allochthon, in the study area, is composed of 16 fault-bounded packets with a general north-northwest trend. Each packet, indexed by a number, includes one or more lithic units (Table 2-1, Figure 2-1). The term, unit, applies to individual rock bodies within the allochthon with distinct lithology, age, and boundaries. Although unit contacts may be depositional, they are commonly faulted, such that unit and packet boundaries coincide. Lithic units are indexed on the map by a letter that identifies their interpreted depositional character (e.g., h, for hemipelagic, Table 2-1), followed by a number that indicates their structural position in the allochthon (e.g. t1, t2, t3); smaller numbers indicate lower structural positions (Table 2-1, Figure 2-1 & 2-2). Figure 2-2 illustrates tectonostratigraphy of all the rocks in the study area.

The faults that separate packets are identified by abrupt lithologic, structural, and in places, age discordance, by the occurrence of fault slices of carbonated serpentinite, by the presence of local faults and associated folds, and in the case of the Golconda thrust, by the presence of tectonized rocks. The faults that bound the packets

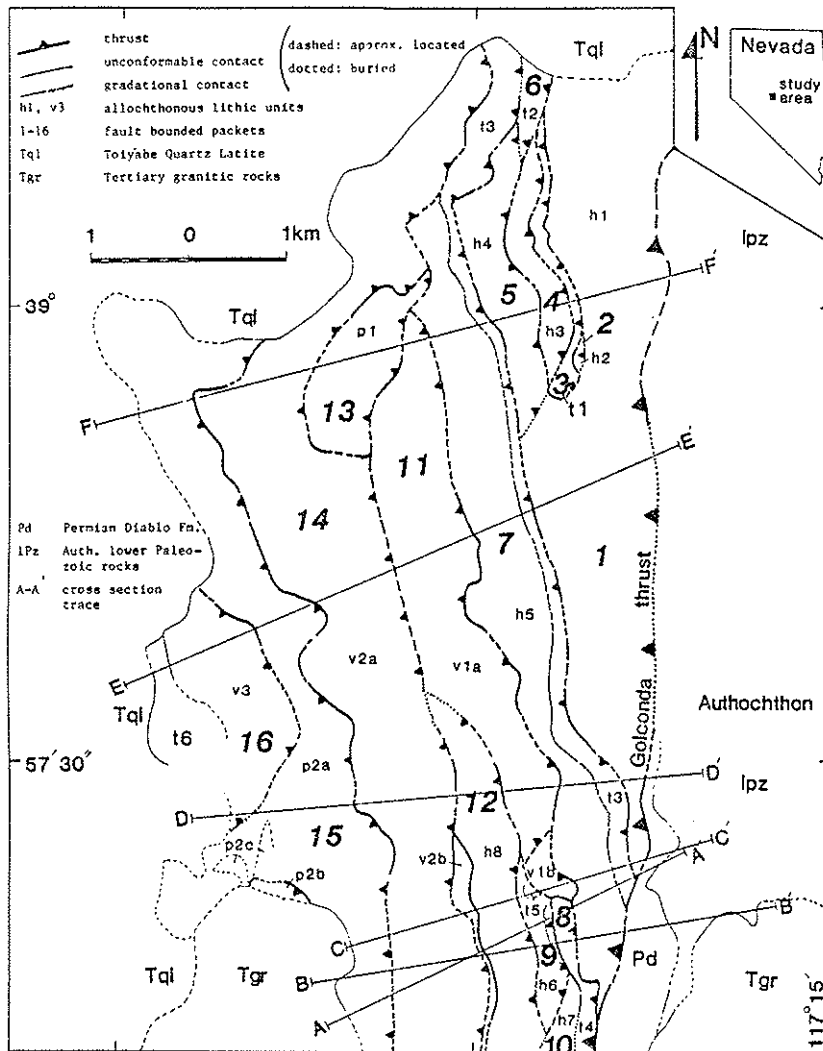


Figure 2-1. Geologic map of the study area. For description of lithic units see Table 2-1.

PACKET	INTERPRETED ROCK TYPE	MAP SYMBOL		LITHOLOGY	AGE
		UNIT	SUBUNIT		
16	volcanogenic	v <sub>3</sub>	-	volcanogenic sandstone and sedimentary breccia, pelite, and chert.	unknown
15	pelagic	p2	P <sub>2a</sub>	bedded radiolarian chert, pelite, red jasper, massive and bedded volcanogenic sandstone and siltstone.	specimen # 38 v. latest Miss. or v. earliest pennsylv.
			P <sub>2b</sub>	massive crystalline basalt.	unknown
			P <sub>2c</sub>	chert-quartzite-serpentinite sedimentary breccia.	unknown, but correlates with units v <sub>1</sub> and v <sub>2</sub>
14	volcanogenic	v <sub>2</sub>	v <sub>2a</sub>	volcanogenic sandstone and sedimentary breccia, pelite, chert, pillowed, massive, and porphyritic basalt, and pillow breccia.	specimen # 61 Permian (Guadalupian)
			v <sub>2b</sub>	massive and porphyritic basalt.	unknown
13	pelagic	p <sub>1</sub>	-	bedded chert and minor pelite interbeds.	Specimen # 72 prob. Mississippian specimen # 73 v. latest Miss. or v. earliest Pennsylv. specimen # 74 prob. Miss. or Pennsylv.
12	hemipelagic	h <sub>8</sub>	-	pelite, chert, and minor chert-quartzite sandstone.	unknown, but correlates with unit h <sub>5</sub>
11	volcanogenic	v <sub>1</sub>	v <sub>1a</sub>	as v <sub>2a</sub> .	specimen # 70 Pennsylv. to E. Permian
			v <sub>1b</sub>	mainly pillowed and other types of basalt.	unknown

Table 2-1. Lithology and age of allochthonous units in the Golconda allochthon, and their relationship to fault bounded packets and lithic associations.



10	hemipelagic	$h_7$	-	bedded pelite and chert	unknown
9	terrigenous	$t_5$	-	poorly sorted chert-quartzite-limestone sed. breccia.	unknown, but correlates with unit $t_3$
	hemipelagic	$h_6$	-	chert, slate, phyllite, and limestone.	unknown, but correlates with $h_1$ and $h_2$
8	terrigenous	$t_4$	-	pelite, chert-quartzite-limestone and breccia and sandstone.	specimen # 221 Early Ordovician
7	terrigenous	$t_3$	-	chert-quartzite-quartz-limestone-serpentinite- and pelite-bearing conglomerate, sed. breccia, and sandstone.	specimen # 266 Early-Middle Pennsylv. (Hartman to Atcham)
	hemipelagic	$h_5$	-	pelite, chert, and minor thin beds of quartz-chert-quartzite-bearing sandstone.	unknown, but same as $t_3$ , as they have gradational contact
6	terrigenous	$t_2$	-	thick quartz-chert-volcanic clast bearing sed. breccia, sandstone, and conglomerate, and clay mudstone, sandstone, chert, and quartzite.	specimen # 489a probably Triassic
5	hemipelagic	$h_4$	-	pelite, limestone, and chert.	specimen # 482 latest late Cambrian or earliest E. Ordovician
4	hemipelagic	$h_3$	-	pelite and thin bedded chert	specimen # 494 Prob. Ordovician
3	terrigenous	$t_1$	-	pelite, and serpoentinite-chert-quartzite-bearing sed. breccia and sandstone.	unknown, but correlates with unit $h_2$ and $h_8$
2	hemipelagic	$h_2$	-	fine-grained quartz sandstone.	unknown, but correlates with unit $t_3$
1	hemipelagic	$h_1$	-	dark chert, pelite, limestone, and chert-quartzite-sandstone.	unknown, but correlates with unit $h_4$

Table 2-1 cont'd



10 hemipelagic  
 9 terrigenous  
 hemipelagic  
 h<sub>7</sub>  
 h<sub>6</sub>  
 poorly sorted chert-quartzite-limestone sds. breccia.  
 chert, slate, phyllite, and limestone.  
 bedded pelite and chert

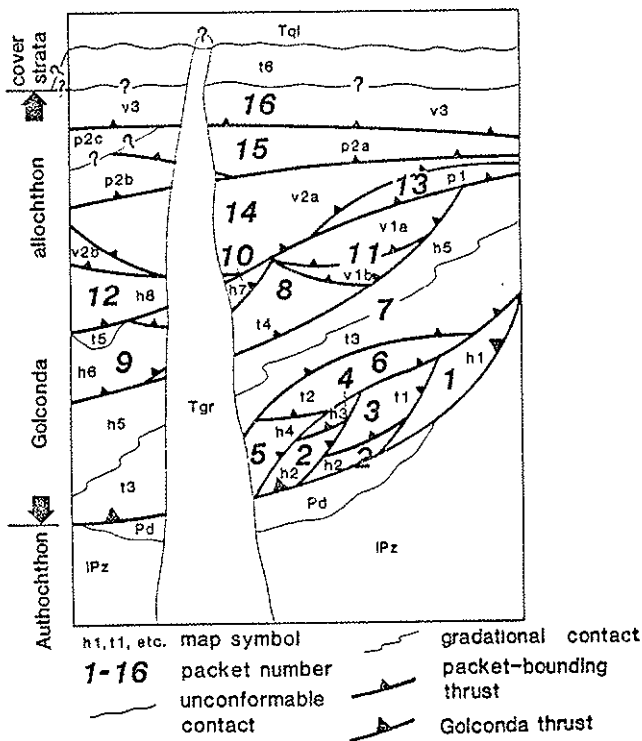


Figure 2-2. Tectonostratigraphy of all the rocks in the study area. See Table 2-1 for description of the lithic units.

unknown, but correlates with unit 13  
 unknown, but correlates with h<sub>7</sub> and h<sub>6</sub>  
 unknown

are in general moderately to steeply dipping (Figure 2-3) and except lower in the allochthon are not measurable.

The exposed width of packets varies between 0.1 and 2.2 km (Figure 2-1). In general, the structurally higher packets are wider and longer than the lower ones, and continue with almost the same lithology, though not necessarily the same age, for distances of at least 9 km. Among upper Paleozoic rocks, packets with volcanogenic and pelagic rocks make up the bulk of the Golconda allochthon in that order. Upper Paleozoic hemipelagic rocks, although more extensive than terrigenous rocks, occur in narrower and less continuous packets relative to pelagic and volcanogenic rocks.

Figure 2-3 shows cross sections of the Golconda allochthon. Two sections are shown for each transect; they provide alternative structural interpretations based on whether or not lithic units are correlated among packets. In the upper section for each transect, packets are assumed to contain unrelated rocks; in the lower section, however, similar rocks are correlated and assumed to be part of a single packet folded during syn-thrust F2a event (Chapter 3). Packets contain lithic units of varied facies that are distributed in the following order: In an east to west traverse, moving structurally upsection, rock types change from mainly terrigenous to hemipelagic, volcanogenic, pelagic, and finally to volcanogenic.

11 specimens from different parts of the allochthon have yielded radiolaria and conodonts which were identified by B. M. Murchey and D. L. Jones, and A. G. Harris, respectively. Figure 2-4 shows the number

8000  
8000  
7000  
6000  
ft  
8000  
8000  
7000  
6000  
ft  
10000  
9000  
8000  
7000  
ft  
C  
9000  
8000  
7000  
C  
9000  
8000  
7000

2-3) and except

2.2 km (Figure

ider and longer

ame lithology,

at least 9 km.

c and pelagic

at order. Upper

an terrigenous

ets relative to

allochthon. Two

ernative struc-

ts are corre-

ansect, packets

tion, however,

a single packet

contain lithic

owing order: In

, rock types

maic, pelagic,

have yielded

Murchey and D.

s the number

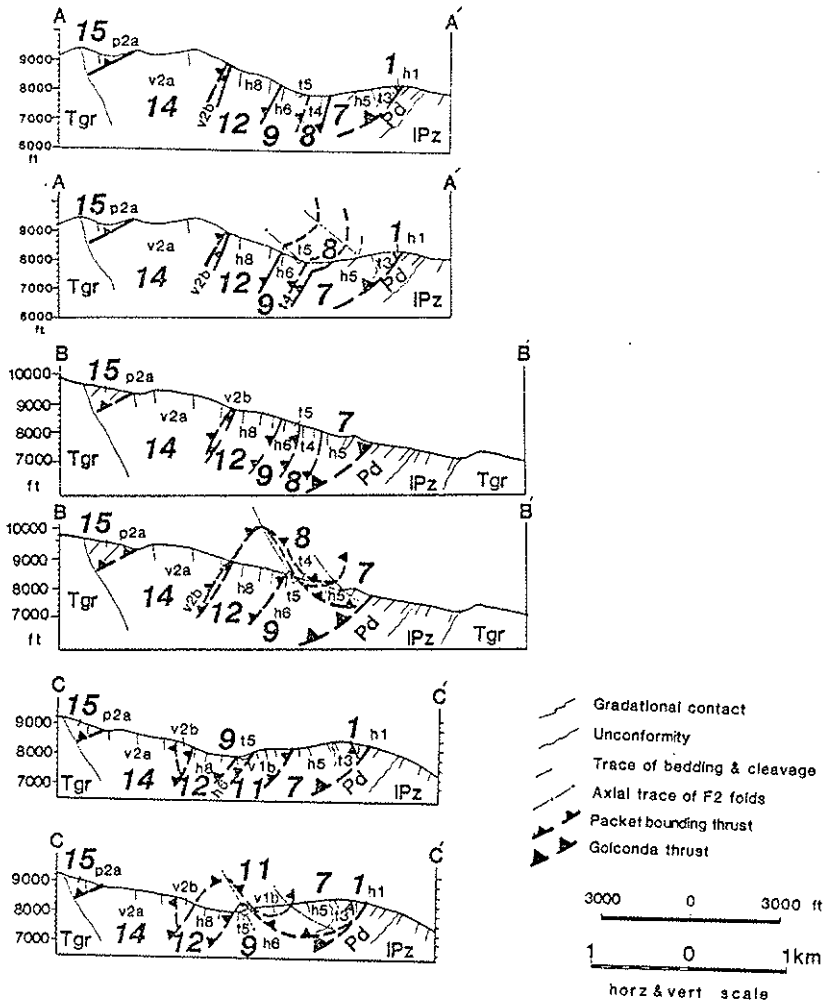


Figure 2-3. Cross sections in the Colconada allochthon. Two sections are provided for each transect; see the text for explanation.

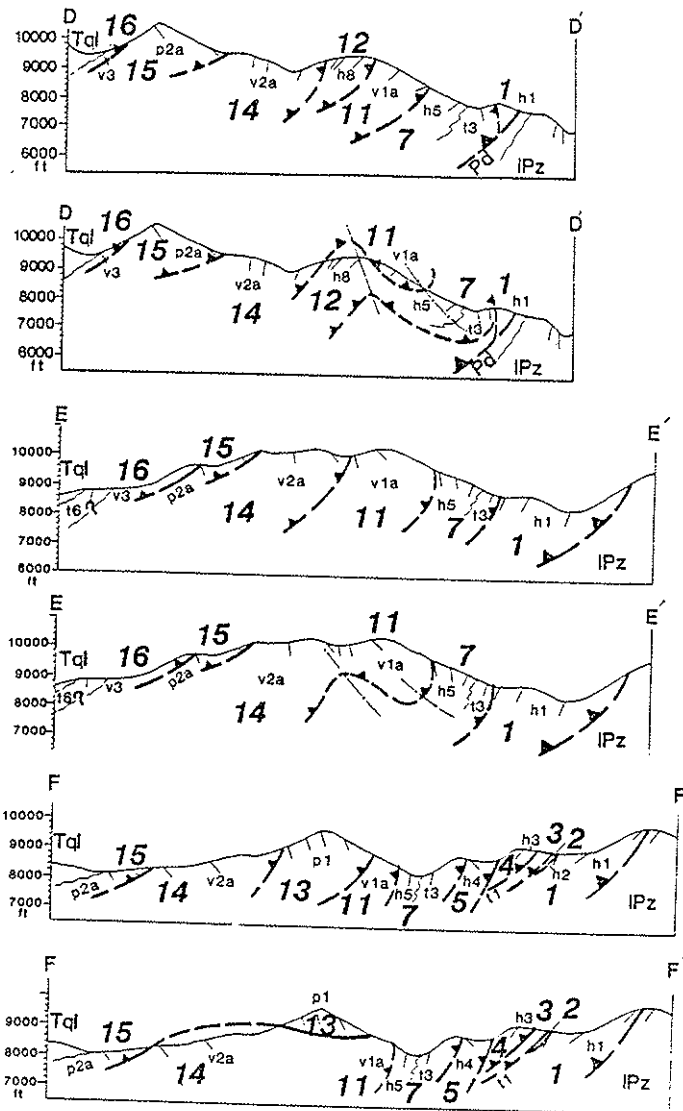
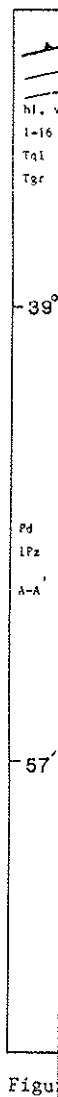


Figure 2-3 cont'd



Figure



and location of these specimens. Table 2-2 defines the identified fossils in all the packets of the allochthon during this study. Depositional ages of lithic units fall into three groups; I) upper Paleozoic, II) lower Paleozoic, and III) Triassic. The 11 ages, although not enough to define an age gradient in the allochthon if it exists, indicate nevertheless, that all the four different major lithic associations, despite their different structural positions, have overlapping ages that span a period between Mississippian and Permian.

The autochthonous rocks under the Golconda thrust include the Permian Diablo Formation (Speed and others, 1977) and lower Paleozoic rocks that belong to the Palmetto and Gold Hill Formations (Kleinhampl and Ziony, 1967). The rocks unconformably overlying the allochthon include the Toiyabe Quartz Latite (Speed and McKee, 1976; Laine, 1977) and possibly unit t6, which contains undated sedimentary rocks of probable Mesozoic or Tertiary age. The rocks of the upper and lower plates of the Golconda allochthon in the study area are described in the following sections.

#### Allochthonous rocks

##### I) Upper Paleozoic rocks

These are equivalent to the Pablo Formation of Speed (1977a) and include four major lithic types: 1) terrigenous, 2) hemipelagic, 3) volcanogenic, and 4) pelagic. The relationship between packets, lithic units, and their interpreted lithic type is given in Table 2-1 and Figures 2-1, 2-2, and 2-3. The ordered succession of lithic types

identified fos-  
dy. Deposi-  
er Paleozoic,  
although not  
exists, indi-  
hic associa-  
e overlapping

clude the Per-  
wer Paleozoic  
(Kleinhampl  
the allochthon  
Laine, 1977)  
ocks of prob-  
lower plates  
d in the fol-

(1977a) and  
ipelagic, 3)  
kets, lithic  
2-1 and Fig-  
lithic types

PACKET	MAP SYMBOL	UNIT	SUBUNIT	Fossil/AGE
16	v3	-	--	
15	p2	p2a	Specimen # 38, v. latest Miss. or v. early Penn. radiolaria	
		p2b	--	
		p2c	--	
14	v2	v2a	Specimen # 61, Permian (Guadalupian) radiolaria	
		v2b	--	
13	p1	-	Specimen # 72, prob. Mississippian radiolaria Specimen # 73, v. latest Miss. or v. earliest Penn. radiolaria Specimen # 74, prob. Miss. or Penn. radiolaria	
12	h8	-	--	
11	v1	v1a	Specimen # 70, Penn. to E. Permian radiolaria	
		v1b	--	
10	h7	-	--	
9	e5	-	--	
	h6	-	--	
8	e4	-	Specimen # 221 (limestone clast), conodonts : 1 ONFOTIDUS cf. O. SIMPLEX (Furnish) 2 PALTOIDUS BASSLERI (Furnish) 1 PARVISTODUS ? sp. oistodontiform element 1 SCALFELLOIDUS ? sp. 1 TERTRONTUS sp. 4 indet. drepanodontiform elements 2 indet. paltoodontiform elements Age : Early Ordovician	
7	e3	-	Specimen # 246 (limestone clast), conodonts: 4 p elements of HELMINOTHIRIDUS MODULIFERUS (Ellison & Graves) 1 p element of IDIOGNATHOIDES sp. aff. I. CONVEXUS of Dunn (1970) 13 p elements of IDIOGNATHOIDES ? sp. indet. (most specimens are incomplete and deformed) 33 indet. bar, blade, and platform fragments Age : Early-Middle Pennsylvanian (Nocrowan to Atokan)	
	h5	-	--	
6	e2	-	Specimen # 490a, conodonts : 10 MEGACONDOLELLA Sp. elements of probable Triassic morphotype (all elements are incomplete) 24 indet. bar, blade, and platform fragments Age : probably Triassic Ammonites and peletons collected by G. A. Poole, B. R. Wardlaw, and F. G. Poole have yielded a Triassic age (identified by N. J. Silberling) at this station.	
5	h4	-	Specimen # 482, conodonts: 1 CORNYLODUS PROAVUS Muller rounded element +1 indet. phosphatic ? problematicum Age : latest Late Cambrian or earliest Early Ordovician	
4	e3	-	--	
3	e1	-	--	
2	h2	-	--	
1	h1	-	--	

Table 2-2. Description and age of the radiolaria and conodonts dated in this study. See text for the sources.

mentioned before, reflect different depositional processes and settings which when combined can provide information on the depositional environment. In the following paragraphs, a comparison of these by lithology, age, structural position, and depositional mechanism and environment is given. An interpretation for the regional environment of deposition is given in Chapter 4.

#### 1) Terrigenous rocks

The terrigenous rocks occur in units t1, t3, thrust zone unit (tzu), t4, and t5, all of which are structurally in low levels in the Golconda allochthon (Figure 2-1, 2-2, and 2-3, Table 2-1). The major rock in these units is a polymict sedimentary breccia that contains angular clasts as coarse as boulder and, in places, megaclasts as large as 40 meters. Other rocks are pebbly pelite, calcareous sandstone, and quartz arenite. The lithology and age of these units are given in Table 2-3. The clasts in the breccia are mainly variegated chert, quartzite, quartz, pelite, limestone, carbonated serpentinite, and, to a lesser degree, quartz arenite and calcarenite. The size of clasts in unit t3 and t4 is smaller than that in units t1, tzu, and t5.

Among the clasts, limestone, serpentinite, and quartzite are the largest, and chert, sandstone, and pelite, the smallest. The quartzite clasts are lithologically similar to those in the thick Cambrian Gold Hill Formation (Kleinhampl and Ziony, 1967) that occur below the Golconda thrust north of Summit Canyon (Fig. 1-1) in the study area. Moreover, clasts of limestone and pelite are similar to lower Paleozoic rocks of the Palmetto Formation (Kleinhampl and Ziony, 1967) in the

autochth

limeston

In

better

printed

tion o

massive

anastom

calcare

where

the sed

catacl

intense

and fl

and fol

the thr

Ex

and tzu

the fin

recogni

of t5 a

Units

tact wi

those

t3 and



autochthon. Ordovician and Pennsylvanian ages, determined from the limestone clasts (Table 2-1 & 2-2), support this correlation.

In the finer grained rocks such as sandstone, bedding, although better defined, is not continuous more than few meters, and is overprinted by a tectonic foliation which is defined by a planar orientation of flattened chert and quartzite grains. The polymict breccia is massive and, locally, where clasts are of smaller size, contains an anastomosing foliation which wraps around the grains. Matrix is non-calcareous sandy and pelitic. Except in the foliated fine-grained rocks where grains are flat and elliptical, clasts, in the coarser parts of the sedimentary breccia, are angular, and in places such as unit tzu, cataclased at their rims. Both fine and coarse-grained rocks are intensely deformed as evidenced by the penetrative tectonic foliation and flattened clasts in finer grained parts, and by boudinaged clasts and folded contacts of the large tectonized blocks with their matrix in the thrust zone unit (Table 2-3).

Except for unit t5, the lithic units with coarse clasts such as t1 and tzu occur in lower structural positions (to the east) relative to the finer grained rocks of unit t3 and t4 and are in fault contact with recognized or inferred lower Paleozoic rocks (Figure 2-1). The contact of t5 and lower Paleozoic (?) rocks (h6) is probably unconformable. Units t3 and t4, on the other hand, are in depositional or fault contact with hemipelagic and volcanogenic upper Paleozoic rocks such as those in units h5 and v1. There is a gradational contact between unit t3 and h5. This contact is characterized by gradual change of medium

UNIT	LITHOLOGY	AGE
	poorly sorted polymict sedimentary breccia, conglomerate, and pebbly mudstone. clasts : sand to blocks as large as 6 m of carbonated serpentinite, subangular to angular pebble to blocks as large as 35 m of light to dark gray and light purple quartzite, subangular to subrounded sand to blocks as large as 10 m of light to dark gray, brown, red, and light green chert, fine pebbles to cobbles of chert-quartzite conglomerate, tan fine to coarse chert-quartzite sandstone, and angular greenish gray and dark pelite. These clasts occur in all the rocks. matrix : pelitic, sandy to pebbly. Other rocks include chert-quartzite sandstone, siltstone, and Mn-oxide nodules and talc. contacts : probably thrust with $h_1$ , $h_2$ , and $h_3$ , as defined by lithological discordance and the occurrence of serpentinite slices along the contacts.	unknown
$t_1$		
$t_2$	poorly sorted polymict sedimentary breccia. clasts : sand to boulder or blocks (about 5 m) of carbonated serpentinite, light gray well sorted quartz arenite, laminated calcarenite, medium gray crystalline limestone, tan crinoid bearing limestone, medium gray chert, gray pelite, and moderately sorted chert-quartzite sandstone. matrix : fine to medium sandy. contacts : upper contact is depositional (gradational) with unit $h_2$ . Lower contact with lower Paleozoic rocks of $h_1$ is fault.	maximum age of Early-Middle Pennsylvanian (Korowan to Atokan) from the limestone clasts. (Table 2-2)
$t_3$		
$t_4$	poorly sorted sedimentary breccia. clasts : pebble to fine cobble, light to dark gray chert, pelite, light gray to light brown quartzite, gray crystalline limestone, fine chert-quartzite sandstone and siltstone, and boulder and larger size carbonated serpentinite. matrix : sandy. Other rocks include interbeds of sandy to cobbly pelite with sand size grains of quartz, 1-10 cm long chert and moderately sorted, light to medium gray chert breccia. contacts : fault with unit $h_2$ , $h_3$ , $h_7$ , and $v_1b$ .	maximum age of Early Ordovician from the limestone clasts. (Table 2-2)
$t_5$	poorly sorted polymict sedimentary breccia. clasts : light gray and brown medium to coarse sand size quartz, very coarse sand to very coarse pebble gray pelite and crystalline limestone, and medium sand to huge blocks as large as 40 m of light gray quartzite. Clasts are angular to subrounded, equidimensional to tabular and have a weak preferred orientation. matrix : non-calcareous sandy. Other rocks include interbeds of quartz arenite. contacts : probably unconformable on $h_2$ . Fault with all other units.	unknown
thrust zone unit (tzu)	poorly sorted polymict sedimentary breccia or melange. clasts : fine pebble to 5 m long blocks of light gray quartzite, carbonated serpentinite, dark gray phyllite and crystalline gray limestone. matrix : pelitic, sandy and pebbly. Other rocks include gray pebbly pelite with light gray quartz arenite and light to dark well sorted chert-quartzite sandstone. Rims of large quartzite blocks are cataclastized at their folded contacts with the pelitic matrix as characterized by the occurrence of coarser grains in a fine matrix at the rim compared to the center of the blocks where grains are touching and no matrix is evident. contacts : lower contact with lower Paleozoic rocks is the Golconda Thrust. Upper contact with unit $t_3$ is probably faulted depositional.	unknown

Table 2-3. Lithology and age of terrigenous lithic units.

to coarse-grained chert-quartzite sandstone of unit t3 to interbedded sandstone and pelite and to pebbly and cobbly pelite at the base of unit h5 that farther west grades into unit h5. Unit h5, mainly chert and pelite, contains minor thin interbeds of sandstones which disappear higher in the section.

In addition to the serpentinite clasts in the terrigenous rocks that range in size between sand and blocks as large as 6 meters, or even beyond these extremes, tectonic lenses of serpentinite occur along packet bounding faults; serpentinite lenses will be referred to as fault-zone serpentinite from here on. Both types of serpentinites are carbonated, but the fault-zone serpentinites also contain fresh serpentine. The fault-zone serpentinites occur mainly at boundaries of packets at low structural positions in the Golconda allochthon as shown on Figure 2-5. These make up outcrops which are tens of meters wide and continue on strike in places (e.g. Marysville Canyon) for hundreds of meters. The highest level that fault-zone serpentinites occur in the allochthon is at the contact of packets 12 and 14 (Figure 2-5). A large serpentinite slice occurs also in the autochthonous lower Paleozoic rocks at Wisconsin Canyon. There are three possibilities for the relationship between the clastic and fault-zone serpentinites: 1) both were supplied from the same source through sedimentary or tectonic means, respectively; 2) the two serpentinite types have different sources; and 3) all serpentinites were originally clastic; the ones at packet boundaries became tectonized later. Because petrological data do not exist for these serpentinites, the three cases can not be examined against

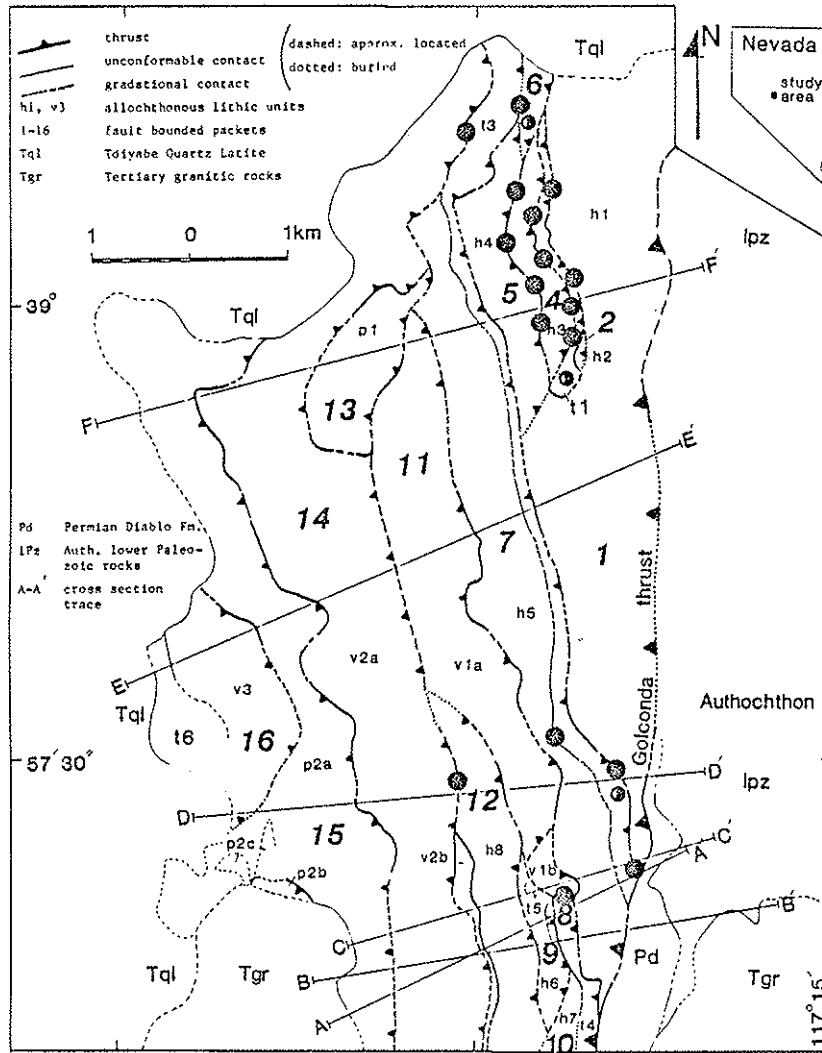


Figure 2-5. Location of fault-zone (●) and sedimentary (⊙) serpentinites.

one a  
 serpe  
 Depos  
 clast  
 the e  
 was o  
 sive  
 clast  
 (Stan  
 is fu  
 conten  
 menta  
 and pe  
 (Stan  
 tively  
 deeper  
 steep  
 plied  
 T  
 ferent  
 1973;  
 the b  
 lowest  
 packet  
 are c



one another. Possible origins and modes of emplacement of both of the serpentinites are discussed in Chapter 4.

Depositional environment - The protolith early Paleozoic age of the clasts and their lithological correlation with autochthonous rocks to the east, under the Golconda thrust, suggest a depositional basin which was open to the influx of very coarse lower Paleozoic debris. The massive sedimentary breccia and sandstone, pebbly mudstones, and megaclasts, suggest transportation by mass flows probably near a slope-base (Stanley and Unrug, 1972; Walker and Mutti, 1973). This interpretation is further supported by their chaotic texture, poor sorting, and high content of poorly sorted matrix which characterize slope-base sediments. The angularity and large size of the clasts, and the limestone and pelite clasts suggest slope instability and downslope movement (Stanley and Unrug, 1972) and short distance of transportation, respectively, probably from the shelf break or steep walls of the slope into deeper and less steep areas. The depositional site should have been steeply sided to the east by uplands of lower Paleozoic rocks that supplied the clasts of all sizes and lithologies.

The coarse and fine-grained terrigenous units may represent different facies of a sub-sea fan (Normark, 1970, 1974; Nelson and Kulm, 1973; Walker and Mutti, 1973; Nelson and Nilson, 1974) that existed at the base of the continental slope. Units t1 and tzu, structurally the lowest, and geographically the easternmost units of the terrigenous packets, contain the coarsest grained and most massive sediments. These are characteristically in fault contact with allochthonous lower

31

Paleozoic packets. Units t3 and t4, on the other hand, are bedded, graded, better sorted, and finer grained, and lie at higher structural positions, west of unit t1 and tzu. The coarse-grained units t1 and tzu are discontinuous and laterally grade, in short distances, into finer grained rocks. The following is an interpretation for depositional setting of the terrigenous rocks based on models of Normark (1970, 1974) and Nelson and Nilson (1974) of sub-sea fans. Units t1, tzu, and t5, are interpreted as inner fan sediments, which were probably derived from the walls of canyons that cut the slope, exposing lower Paleozoic rocks. Rocks that probably represent middle fan facies occur in t3 at Ophir and Wisconsin Canyons. At these places, t3 is dominantly massive fine to coarse-grained breccia, bedded, medium to coarse grained sandstone, and pelite. In places, sandstone makes lenticular bodies in the pelite. The breccia in t3 is finer grained than that in tzu and with the sandstones can be interpreted as turbidite deposited in channels. Evidences for this interpretation are Bouma ab divisions, and high sandstone/shale ratio. Stratigraphically upsection in t3, the dominant rock type is pelite. Here, sandstone is finer grained, graded, and constitute thin lenticular bodies in the pelites. These may represent interchannel deposits of a middle fan, evidenced by their low sandstone/shale ratio, finer sand grain size, and smaller sand bodies relative to pelite. These rocks grade further upsection to hemipelagic rocks of unit h5 with sporadic medium to coarse-grained, graded, and lenticular sandstones.

## 2) Hemipelagic

These higher level units include lenticular beds with minor sandstones ranging between 10 and 20 m. These units are interbedded with sand and siltstone.

### Bedding

bedded with pelite. Graded bedding is common in the basal chert, quartzite, and during formation of the upper Paleozoic rocks. Paleozoic rocks are juxtaposed against the basement of the

### Depositional

(Berger, 1974) minor and thick sandstones

nd, are bedded,  
her structural  
units t1 and t2  
s, into finer  
or depositional  
Normark (1970,  
ts t1, t2, and  
robably derived  
lower Paleozoic  
occur in t3 at  
inantly massive  
grained sand-  
r bodies in the  
t2 and with  
ed in channels.  
ons, and high  
3, the dominant  
graded, and con-  
e may represent  
by their low  
ler sand bodies  
to hemipelagic  
ed, graded, and

## 2) Hemipelagic rocks

These include units h4, h5, h7, and h8 that occur at structurally higher levels than the terrigenous rocks in the allochthon. They include light gray, green, brown, and reddish slate, which is interbedded with milky, light gray, brown, and green chert with bed thicknesses ranging between 0.2 and 30 cm, and a mode between 10 and 20 cm. Pelites are more abundant than chert. Chert beds with thin pelite interbeds, however, are locally dominant. Slates contain very fine sand and silt quartz, and minor chert and quartzite grains.

Bedding is well defined and is continuous where pelite is interbedded with chert. A penetrative slaty cleavage overprints bedding in pelite. Graded chert-quartz sandstones, laterally continuous only for distances of less than 10 meters, occur sporadically in unit h8 as thin (less than 10 cm) interbeds with pelite. Sandstones are more common at the basal gradational contact of unit h5 with t3. Sandstones contain chert, quartz, and minor quartzite grains which were highly flattened during formation of the cleavage (Chapter 3). The upper contact of the upper Paleozoic hemipelagic rocks is with volcanogenic rocks. Lower Paleozoic rocks of packet 5 and 9 were thrust into the allochthon and juxtaposed against pelagic packets during final stages of the emplacement of the allochthon (Chapter 4).

Depositional environment - These rocks are interpreted as hemipelagic (Berger, 1974) because of their mainly bedded chert and pelite and minor and thin terrigenous chert-quartz sandstone interbeds. The fine sandstones are interpreted as distal turbidite (Bouma and Hollister,

1973) because of graded bedding and their considerable content of matrix, and because they are thin-bedded, laterally discontinuous, and interfinger with bedded chert and pelite. The chert and quartzite grains in these turbidites are correlated with the ones in the subjacent coarser grained terrigenous rocks.

The hemipelagic rocks were probably deposited in the abyssal plain (Bouma and Hollister, 1973) of an ocean basin because of 1) continuity of bedding in chert, 2) uniformity in size of quartz sand and silt grains in pelite, and 3) their dominant red and green pelite and chert. Sedimentation in the basin was dominated by the deposition of the suspended or eolian mud, biogenic ooze, and terrigenous debris which were probably transported by distal turbidity currents. The eastern part of the ocean basin was fed with a subsea fan which through its channels supplied sediments for the deposition of the terrigenous rocks at the slope-base and distal turbidites in the abyssal plains of the ocean basin.

### 3) volcanogenic rocks

Units v1, v2, and v3 mainly constitute volcanogenic sedimentary breccia and sandstone, chert, pelite, and volcanic rocks. These rocks occur in packets structurally higher than the terrigenous and hemipelagic rocks of the allochthon (Figure 2-1).

The breccia is massive, poorly sorted, and contains various types of clasts that float in a sandy volcanogenic matrix. Clasts include: 1-15 cm long, angular to subrounded, green, red, milky, and gray chert; 1-20 cm long, subangular and tabular pelite; 1-20 cm long, subangular



ole content of  
 continuous, and  
 and quartzite  
 s in the subja-

e abyssal plain  
 f 1) continuity  
 sand and silt  
 lite and chert.  
 sition of the  
 us debris which  
 . The eastern  
 ich through its  
 rigenous rocks  
 l plains of the

c sedimentary  
 . These rocks  
 us and hemi-

various types  
 lasts include:  
 nd gray chert;  
 ng, subangular

to subrounded, light brown, green, and greenish gray, fine to medium grained volcanogenic sandstone; sparse, large (20-100 cm), subrounded to rounded blocks of light brown crystalline limestone; red jasper; and igneous rocks. The igneous clasts in the breccia are of two different types: volcanic and coarser grained granitic rocks. The volcanic rocks are porphyritic and contain lath-shaped sericitized plagioclase crystals with common polysynthetic and Carlsbad twinning, and chloritized and serpentized clinopyroxene and hornblende phenocrysts in a fine matrix. Plagioclase crystals are mainly bytownite, oligoclase, and andesine, as determined by the Michelle Levy method. Granitic clasts are large (1-100 cm) and contain a considerable percentage of quartz crystals, alkali feldspars with gridiron twinning, and chloritized muscovite.

Volcanogenic sandstones are poorly sorted, very fine to coarse-grained, light to medium gray, and green. These are massive, and less frequently, where finer grained, laminated, graded, loaded, and convoluted. Other rock types include light green and red chert, red, light gray, greenish gray, and green mudstone, sandstone, and pebbly sandstone with volcanogenic sandstone and chert pebbles and sporadic convolute and slump structures. Bedded red cherts contain radiolaria and yield late Paleozoic ages (Table 2-2).

Bedding is continuous and well defined in the interbedded pelite and chert in contrast to that in the mainly massive sandstone and breccia. Lateral and vertical lithological and textural variations in short distances are characteristic of the coarse volcanogenic rocks.

Facing, indicated by graded bedding and load structures, is variable, indicating folded beds.

Volcanic rocks make up the bulk of the volcanogenic-basaltic packets and include pillowed, massive, and porphyritic basalts. Pillows range in size between few centimeters and a meter. Units v1b, v2b, and p2b are the largest exposures of volcanic rocks in the volcanogenic packets (Figure 2-1). However, volcanic rocks occur in many other parts of these packets. The contact of the basalts with volcanogenic sedimentary rocks is probably faulted depositional. Two chemical analyses of the pillow basalts in Pablo and Jett Canyons, about 20 km south of the study area, by Speed (1977a) relates them to oceanic basalts except for their unusual high soda content.

In general, all structurally high packets of the Golconda allochthon are either dominantly volcanogenic or at least have volcanogenic lenses. Unit v1 is in fault contact with pelites and cherts of the structurally lower hemipelagic unit h5. No volcanogenic rock exists east of unit v1 in the allochthon. Unit v2 is structurally overlain by pelagic rocks which include minor volcanogenic sandstone. Higher in the allochthon are volcanogenic sedimentary rocks of unit v3.

Depositional environment - Chert and pelite were apparently deposited with breccia and sandstone and locally resedimented in them as indicated by their presence both as interbeds and clasts in these rocks. Clasts of chert and igneous rocks also occur in pebbly pelites that interfinger with the sedimentary breccia, indicating local resedimentation of mud and breccia. Green rims around red chert clasts in the

breccia  
The  
a shor  
derived  
graniti  
breccia  
igneous  
bedded  
chert  
volcano  
and res  
Dep  
current  
ton and  
of bedd  
sorted s  
tion fr  
structur  
breccia  
sandston  
from ch  
graded b  
1962; W  
ites are  
The

ltic pack-  
s. Pillows  
v2b, and  
lcanogenic  
ther parts  
c sedimen-  
analyses of  
uth of the  
except for

nda allo-  
lcanogenic  
s of the  
ock exists  
erlain by  
her in the

deposited  
m as indi-  
se rocks.  
lites that  
sedimenta-  
sts in the

breccia suggest that red color is primary.

The large size of chert and pelite clasts in the breccia suggests a short transportation path and that they were probably intraclasts derived from walls of local channels. Moreover, where in contact, granitic igneous clasts penetrate the adjacent chert clasts in the breccia, indicating that the chert clasts were relatively soft when igneous debris arrived at the depositional site. In addition to the bedded chert and pelite with clasts of volcanogenic sandstone, large chert clasts in the breccia contain lenses of fine to medium grained volcanogenic sandstone, indicating that pelite and chert were deposited and reseedimented with the volcanogenic debris.

Deposition in submarine canyons or channels, probably by turbidity currents (Walker and Mutti, 1973; Mutti and Ricci-Lucchi, 1978, Middleton and Hampton, 1976) is suggested by 1) the great thickness, 2) lack of bedding in the breccia and sandstone, 3) high content of poorly sorted sandy matrix, 4) rapid lateral and vertical lithological variation from breccia to sandstone to pelite, 5) graded bedding and load structures at the base of the poorly sorted massive sandstones and breccia representing Bouma a division, 6) convolute structures in finer sandstones, and 7) reseedimentation of chert and pelite clasts plucked from channel walls. The Bouma division is indicated by the massive graded breccia and sandstone with load marks, and d and (or) e (Bouma, 1962; Walker, 1965; Middleton and Hampton, 1976), represented by pelites are the most common in the volcanogenic rocks.

The occurrence of radiolarian chert and red pelite suggests that

37

the volcanogenic sediments were deposited on ocean floor. This is supported by the common slices of pillow basalts that correlate with other basalts attributed to the oceanic tholeiites. These basalts and the jasper clasts in the breccia suggest active volcanism in the basin. However, because of the unknown age and contact nature of these basalts, this interpretation is uncertain. The lithology and large size of the clasts of angular granitic igneous rocks indicate a magmatic source, most probably not far from the depositional site, that had access to the basin, probably through channels or submarine canyons possibly feeding a subsea fan. The presence of conduits is suggested by the occurrence of resedimented coeval intraformational chert and pelite clasts in the breccia and lateral variation of coarse breccia to finer grained sandstone. The breccia is therefore interpreted as submarine channel fill deposit. Radiolarian cherts and red pelites are probably background pelagic sediments on the ocean floor. The fine-grained volcanogenic laminated sandstones are interpreted as finer grained tails of the turbidites or overflows of the channel. The sparse large limestone clasts in the breccia indicate the presence of carbonates in the magmatic source area, and probably support the idea that the debris did not travel far. The carbonates may have been shallow marine deposits surrounding emergent volcanoes which supplied the volcanic debris.

The breccia in the volcanogenic packets contain two ingredients that may ascribe to an island arc source: 1) quartz bearing volcanic clasts, 2) Na-plagioclase rich volcanic clasts. An extensive arc ter-

rane, west  
(1977b). The  
strata the  
Range, and  
(Speed 197  
and arc-der  
late Middle  
provided by  
zoic grani  
1973; Kistl  
rocks in t  
island arc  
magma was  
0.706 and 0.  
west, respe  
the easternm  
erated from  
subparallel  
deflected t  
interpreted  
(Speed, 198  
1979) indicat  
tinenta cr  
(Speed, 1982  
The near

This is sup-  
 e with other  
 ults and the  
 the basin.  
 re of these  
 and large  
 cate a mag-  
 site, that  
 ine canyons  
 suggested  
 l chert and  
 breccia to  
 ted as sub-  
 elites are  
 . The fine-  
 as finer  
 annel. The  
 resence of  
 rt the idea  
 been shal-  
 upplied the  
 ingredients  
 ng volcanic  
 arc ter-

rane, west of the Golconda allochthon, has been recognized by Speed (1977b). The arc terrane is mainly covered by Mesozoic and Cenozoic strata that permit few exposures at Mina, Black rock Desert, Humbolt Range, and Union District among other regions in northwestern Nevada (Speed 1977b). The rocks of the arc terrane are mainly mafic volcanic and arc-derived sedimentary rocks chiefly of late Paleozoic and pre-late Middle Triassic age. Evidence of the arc terrane in other areas is provided by the initial strontium isotopic ratio ( $^{87}\text{Sr}/^{86}\text{Sr}$ )<sub>0</sub> for Mesozoic granitic and upper Cenozoic volcanic rocks (Kistler and Peterman, 1973; Kistler, 1974; Speed, 1977b). The Sr isotopic ratio for these rocks in the arc terrane ranges between 0.704 and 0.706, typical of island arc lithospheres, reflecting the composition of the mantle where magma was generated (Kistler and Peterman, 1978; Speed, 1977b). The 0.706 and 0.704 contours delineate the arc terrane to the east and west, respectively (Speed, 1977b); Figure 1-2). The 0.706 contour is the easternmost boundary of igneous rocks which formed from magmas generated from a subcontinental lithosphere (Speed, 1977b). This line runs subparallel to the regional N-S trend of the Golconda allochthon and is deflected to the west in the Mina region (Figure 1-2). The line is interpreted to define the westernmost Paleozoic shelf rocks in Nevada (Speed, 1982b). Gravity and seismic data (Cogbill, 1979; Prohdehl, 1979) indicate thickening and (or) a decrease in density of the continental crust of North America east and south of the 0.706 line (Speed, 1982b).

The nearest outcrop of the arc terrane to the study area is in the

Union District about 30 km to the northwest in the Shoshone Range. Here, chemical analysis of volcanic rocks indicates andesitic composition (Speed, 1977a). Silberling (1959) and Speed (1977b) report the presence of granodiorite and quartz monzonite clasts in the rocks of the arc terrane in this area. No granitic rocks older than 202 my (Middle Triassic), which is apparently younger than the andesitic unit, exists within 100 km radius of the Union district (Speed and Armstrong, 1971; McKee and Silberling, 1971; Speed, 1977b). Based on this and the paucity of granitic clasts in Triassic conglomerates above the andesitic rocks, Speed (1977b) proposed an island arc origin for these granitic rocks.

Granitic clasts are common in coarse-grained upper Paleozoic volcanogenic breccia of the Golconda allochthon in the study area, and occur with mafic volcanic clasts of probably andesitic composition. Although chemistry of these rocks is unknown, both types of the clasts in the volcanogenic rocks of the Golconda allochthon may have an island arc provenance as suggested by their petrography as described before, and indirectly from their age and geologic setting. The two types of the igneous clasts may have come from a single source as suggested by the existence of the two types in individual beds of turbidites. The age of the resedimented volcanogenic rocks is the youngest among other rocks of the allochthon (Table 2-2) and ranges between Pennsylvanian and Permian (Guadalupian), indicating a minimum age of Late Permian for the arc terrane. Its maximum age is at least Pennsylvanian.

4) Pel  
 tural  
 mainly  
 in th  
 thinn  
 to da  
 (0.1-1  
 Unit  
 thick)  
 and s  
 interb  
 pl com  
 Unit p  
 chthon  
 U  
 thrust  
 fine t  
 chert,  
 serpen  
 and c  
 tacts  
 may be  
 cherts  
 ture,

oshone Range.  
 tic composi-  
 b) report the  
 he rocks of  
 202 my (Mid-  
 esitic unit,  
 nd Armstrong,  
 this and the  
 e the andesi-  
 these grani-  
 eozoic vol-  
 dy area, and  
 composition.  
 f the clasts  
 ve an island  
 ibed before,  
 o types of  
 suggested by  
 idites. The  
 among other  
 ennsylvanian  
 Permian for

#### 4) Pelagic rocks

These rocks include units p1 and p2 that lie at the highest structural positions except relative to unit v3 (Figure 2-1). They are mainly chert that are in average thicker bedded (1-30 cm) than cherts in the hemipelagic rocks. Pelites on the other hand, are relatively thinner and less frequent. The rocks of units p1 and p2a include light to dark gray, green, and milky chert. Chert is interbedded with thin (0.1-1 cm), red and, less commonly, light gray pelite and red jasper. Unit p2a includes lenses (0.2- 6 m thick) and interbeds (0.1-15 cm thick) of fine grained, massive, or laminated volcanogenic sandstone and siltstone. The volcanogenic beds have erosional bottoms in the interbedded chert and pelite. The bedded cherts in both units p2a and p1 contain radiolaria which yield four late Paleozoic ages (Table 2-2). Unit p2a is among the most extensive packets of the Golconda allochthon.

Unit p2b is exclusively dark massive basalt and is probably a thrust sheet. Unit p2c includes interbedded pebbly polymict breccia and fine to medium grained sandstone. Clasts in these rocks are variegated chert, fine sand to gravel, angular to subangular, gray quartzite, and serpentinite. Matrix is green and silty to sandy, probably amphibole and chlorite rich. Rocks of packet 15 are metamorphosed at their contacts with a granitic pluton in upper Ophir Canyon (Figure 2-1) which may be of the same age as the Tertiary Ophir pluton. At these contacts, cherts and pelites are converted into meta-chert with quartzitic texture, and silicified meta-pelite. The effect of metamorphism diminishes

Depositional environment - The mainly homogeneous and continuously bedded radiolarian cherts, thinner red and green pelite, and the lack of terrigenous rocks suggest that these rocks are pelagic (Berger, 1974). The existence of red jasper and basalt of unit p2b may suggest active volcanism and fumaroles in the depositional site. Such interpretation can be false given the faulted nature of the basalts. The presence of sporadic channelized volcanogenic sediments in pelagic rocks indicates that the depositional basin was open to the influx of fine-grained volcanic debris, probably from the same source that fed the lithic units of the volcanogenic rocks as suggested by their similar lithology and age.

Despite their overlapping ages with the volcanogenic rocks, the pelagic rocks should have been deposited in part of the oceanic basin which was dominated by pelagic deposition and sporadically open to the influx of fine volcanogenic debris. Despite few overlaps, the ages of the radiolarian cherts in the pelagic rocks are in general older than the radiolarian cherts in the volcanogenic sequence (Table 2-1). This probably means that during the Mississippian or Pennsylvanian, the depositional basin of the pelagic rocks was remote from turbidite sources.

The massive basalt of unit p2b is interpreted as a slice of oceanic crust which was detached from the depositional site. The relationship of the coarse-grained detrital rocks of unit p2c with the pelagic rocks of p2a is unknown.

major  
This  
tion  
the a  
that  
Clast  
lower  
west  
equiv  
higher  
repres  
genous  
from  
as dis  
B  
struct  
overlapp  
region  
Since p  
its tr  
Mountai  
nown.  
genous



uously bed-  
the lack of  
er, 1974).  
gest active  
erpretation  
presence of  
indicates  
ained vol-  
chic units  
chology and  
rocks, the  
eanic basin  
pen to the  
the ages of  
older than  
2-1). This  
nian, the  
a turbidite  
of oce-  
The rela-  
with the

Facies analysis among upper Paleozoic rocks

Table 2-4 summarizes facies and depositional setting of the four major lithic types in the upper Paleozoic packets of the allochthon. This Table indicates a systematic geographic and structural distribution of facies. The structurally lowest packets in the eastern parts of the allochthon, include the coarsest grained terrigenous clastic rocks that may represent slope-base, inner, and middle fan accumulations. Clasts in these rocks can be correlated by their lithology and age with lower Paleozoic rocks below the Golconda thrust. Higher and farther west are the hemipelagic rocks which could be ocean plain or outer fan equivalent to the terrigenous rocks. Farther west and structurally higher in the allochthon are volcanogenic and pelagic rocks that represent ocean floor deposits and distal equivalents of the terrigenous deposits. The volcanogenic debris were most probably supplied from an arc terrane which was located to the west of the oceanic basin as discussed before.

Because the four upper Paleozoic lithic suites have an ordered structural position in the Golconda allochthon, and because their ages overlap, the depositional setting for each suite can be part of a regional depositional environment that prevailed during late Paleozoic. Since paleomagnetic data is not available for the Golconda allochthon, its translation and rotation with respect to the underlying Roberts Mountains allochthon and the North American continental crust is unknown. However, unique ties exist between clasts in the lower terrigenous packets of the Golconda allochthon and underlying lower Paleo-

zoic rocks  
 porting evi  
 America an  
 the Diablo  
 clast lith  
 presence of  
 allochthon,  
 the trend o  
 between the  
 graphic rec  
 upper Paleo  
 II) Lower P  
 These  
 lowest stru  
 dark phylli  
 chert and m  
 Unit hl incl  
 chert sand  
 are similar  
 h3, h5, and  
 them to be c  
 below the  
 interbeds su  
 defined and  
 generations

LITHIC ASSOCIATION	LITHOLOGY / AGE	FACIES / DEPOSITIONAL ENVIRONMENT		POSITION STRATIGRAPHIC	
		ENVIRONMENT	ENVIRONMENT	ENVIRONMENT	ENVIRONMENT
Volcanogenic	massive fine to coarse-grained volcanogenic tuffite with granitic and andesitic ? volcanic clasts, intercalated with minor radiolarian chert and pelite. These were accumulated on pillow basalt of ocean floor.	ocean floor; transportation of volcanogenic material by turbidity current from an inferred subaerially active source through submarine canyon, and accumulation in (obscure) platform with pelagic sedimentation and possibly active volcanism.	highest part of the allochthon above and terrigenous rocks	as above	as above
Pelagic	thin to thick bedded radiolarian chert, minor laminated pelite, sporadic lenses of fine grained volcanogenic tuffite, and fault slices of basalt. Depositional ages of very recent Miocene to very earliest Pliocene from radiolarian chert in different packets.	ocean floor; pelagic sedimentation of radiolarian chert and pelite, interrupted by infrequent deposition of volcanogenic tuffite, inferred association of active volcanism and fumaroles suggested by red Jasper or possibly the basalt slice.	as above	as above	as above
limpelagic	interbedded chert and pelite with minor thin-bedded fine grained tuffite derived probably from the same source as the terrigenous rocks. Their age is equivalent to the terrigenous rocks.	abyssal plain and outer fan; homopelagic deposition under the CCD with intermittent deposition of distal turbidites. Inferred seaward flow of turbidity currents.	higher part of terrigenous rocks	as above	as above
Terrigenous	poorly sorted, massive deposits with mud-sized particles and olistoliths derived from the Roberts Mountain allochthon, which had previously been accreted to the continental margin. Maximum depositional ages from fossiliferous limestone clasts, in different packets, are Miocene and Pliocene.	slope and inner fan and middle fan accumulation under the CCD. Inferred westward transport of lower basin rocks exposed at the continental slope.	lowest part of the allochthon	as above	as above

Table 2-4. Facies and depositional environment of the four major upper Paleozoic lithic associations in the Colorado allochthon.

zoic rocks belonging to the Roberts Mountains allochthon. Other supporting evidence relating the depositional environment to the North America and Nevada are: 1) existence of continental shelf deposits of the Diablo Formation under the Golconda thrust that have partly similar clast lithology and age as the terrigenous rocks in the allochthon, 2) presence of slope and slope-base terrigenous rocks at the base of the allochthon, and 3) parallelism of the 0.706 isotopic ratio contour and the trend of the allochthon, and its alignment parallel to the boundary between the shelf and slope sediments (Speed, 1977b). A paleogeographic reconstruction based on the observed facies variation in the upper Paleozoic rocks is given in Chapter 4.

#### II) Lower Paleozoic rocks

These include lower Paleozoic units h1, h6, and h7, mainly at the lowest structural positions in the Golconda allochthon. All include dark phyllite and slate, light to dark gray and light green bedded chert and meta-chert, and thin-bedded dark gray crystalline limestone. Unit h1 includes fine-grained, light brown, non-calcareous, quartz-chert sandstone. Although interbedded chert and pelite of these units are similar to those of the upper Paleozoic hemipelagic rocks (e.g., h3, h5, and h8), their thin-bedded limestone and organic pelite allows them to be distinguished and allied with the lower Paleozoic rocks below the Golconda thrust. Ordovician conodonts in two limestone interbeds support this interpretation (Table 2-1). Bedding is well defined and is continuous in these rocks. Pelites of unit h6 show two generations of cleavage; a slaty cleavage and a younger spaced cleavage

(Chapter 3) which is absent in the upper Paleozoic rocks.

45

Packet 9 contains subunit t5 which resembles allochthonous upper Paleozoic terrigenous rocks of units t1, t3, and thrust-zone unit (tzu) (Table 2-3). The contact of t5 and h6 is covered. Unit t5 includes megaclasts (up to 40 m) of quartzite and gravel-sized quartzite, chert, and limestone clasts which are embedded in a sandy matrix. Unit t5, having similar lithology as units t1, t3, t4, and tzu, belongs to the terrigenous upper Paleozoic rocks which was either deposited unconformably and (or) thrust over lower Paleozoic rocks of unit h6 or a combination of these.

Unit h1, h4, and h6 can be interpreted as hemipelagic because of their content of chert, limestone, and terrigenous sandstone interbeds. Unit h1 is allochthonous because of its tectonic position above the Golconda thrust, emplacement above upper Paleozoic autochthonous Diablo Formation, and its highly tectonized contact with unit t3. Unit h4 and h6 are clearly allochthonous because they lie between packets of upper Paleozoic rocks in the allochthon. These rocks and probably their overlying upper Paleozoic rocks of unit t5 were incorporated into the allochthon in the final stages of its emplacement as is suggested by their low structural positions (Chapter 3).

### III) Triassic and Triassic (?) rocks

These include clastic rocks that occur at low structural positions in the Golconda allochthon at Marysville Canyon (Fig. 1-1). They occur in the fault bounded unit t2 which lies between packets of upper and lower Paleozoic rocks. The Triassic rocks are calcareous fine to pebbly

sandstone  
chert,  
and sub  
calcare  
The  
traces.  
and san  
careous  
with al  
h5, and  
long pl  
chert,  
medium  
Le  
and lat  
Triassi  
typical  
(Figure  
clasts  
origin  
Deposit  
they o  
and bec  
serpent  
zoic ro

chthonous upper  
unit (tzu)  
t5 includes  
tzite, chert,  
Unit t5, hav-  
s to the ter-  
unconformably  
or a combina-

because of  
the interbeds.  
above the  
chthonous Diablo  
Unit h4 and  
ets of upper  
their over-  
to the allo-  
ed by their

al positions  
. They occur  
upper and  
me to pebbly

sandstone, pebbly conglomerate, and breccia with quartz, red and gray chert, chert-sandstone, feldspar crystals, and plagioclase-rich angular and subangular volcanic clasts. Other rocks include massive chert and calcareous mudstone.

The limy and sandy mudstone are bioturbated with horizontal traces. The sandstones are limy, thin-bedded and rippled. The pelitic and sandy rocks contain shell impressions and are at least partly calcareous. There is no cleavage in these rocks in contrast to sandstones with almost the same lithology in other units of the allochthon (e.g., h5, and h8). Sandstones include angular volcanic pebbles with thin and long plagioclase needles and angular to subangular quartz, plagioclase, chert, and opaque mineral grains which are dispersed in a fine to medium volcanogenic sandy matrix.

Lenses of carbonated serpentinite, between 5 and 10 meters thick, and laterally continuous for at least 15 m, occur at the contact of the Triassic rocks and unit t3 (Figure 2-5). These serpentinite bodies are typical of thrust contacts of many packets at low structural positions (Figure 2-5, Plate 1). However, they occur also as large sedimentary clasts in many terrigenous rocks such as t1, t3, and perhaps t2. Their origin is discussed in Chapter 4.

Depositional environment - The Triassic rocks are allochthonous because they occur between allochthonous packets of upper and lower Paleozoic, and because their boundaries with these two packets include tectonized serpentinite. The major differences between Triassic and upper Paleozoic rocks in the allochthon are in the carbonate content and lack of

cleavage in the Triassic rocks.

47

The Triassic rocks were deposited in a basin which received volcanogenic, chert, carbonate, and serpentinite debris. The angularity of the clasts suggest proximity of the depositional site to the source. A shallow marine depositional setting is inferred for these rocks based on the presence of bioturbation and bivalve shells. Best candidates for the source of all the clasts in these rocks are the Golconda allochthon and its relative autochthon. An interpretation for the environment of deposition is discussed in Chapter 4.

#### Unit t6

The westernmost outcrops of rocks unconformably below Tertiary volcanic rocks are pelitic and fine to coarse detrital rocks of unit t6. These include fine to medium grained, light purple and brown, well-sorted, and thin- to thick-bedded (1-70 cm, and a mode of 20 cm) quartzite, light brown and red silty pelite, and a poorly sorted sedimentary breccia. Clasts in the breccia are subangular glassy quartz, light to dark gray, red, and milky chert, and angular to subangular quartzite. Quartzites are graded and have curved cross laminations. Their contact with red pelite is load marked. These rocks are metamorphosed as evidenced by the presence of silicified sedimentary breccia and conversion of sandstone into quartzite, probably due to the effect of the adjacent granitic pluton.

The contact of unit t6 with v3 is not exposed and its age is unknown. The rocks of this unit are much coarser grained than those of the adjacent and structurally high units of the allochthon. Three

alternative origins of unit t6 are as follows:

1- Unit t6 is a young autochthonous deposit which was laid down after the emplacement of the allochthon in the Mesozoic or Tertiary and before the intrusion of the granitic plutons and cover by Tertiary volcanic rocks.

2- Unit t6 is part of the Golconda allochthon but unconformable on subjacent packets. A likely site of deposition for these rocks in this model is a forearc basin if they prove to have overlapping ages with lower packets of the allochthon.

3- Unit t6 is part of the Golconda allochthon and an accreted packet which was emplaced in early stages of development of the allochthon exposed in the Toiyabe Range suggested by its high structural position.

Because of their unknown age and paucity of data on their age and lithology, all these origins are tentative and remain to be examined.

The lower plate of the Golconda thrust includes lower Paleozoic rocks (lPz) and the Permian Diablo Formation (Pd) (Figure 2-1). The allochthon is overlain to the west by Tertiary volcanics (Tq1) and possibly by clastics of unit t6. Except possibly for unit t6 which was described in the previous section, other cover strata and autochthonous rocks are described in the following paragraphs.

Autochthonous lower Paleozoic rocks (lPz)

These are rocks below the Diablo Formation in Ophir and Wisconsin Canyons, and below the Golconda thrust elsewhere. At Ophir and Wisconsin Canyons, they include metamorphosed calcareous pelite, calcarenite, thick-bedded medium gray pelite and chert, gray crystalline limestone, fine-grained quartzite, and conglomerate with meta-chert, limestone, and calcarenite clasts. Clasts in the breccia are touching and, in places, floating in a metamorphosed biotite-bearing matrix. Other rocks include dark pelite and greenish gray massive and porphyritic basalt with plagioclase phenocrysts. A large serpentinite body, similar to the fault-zone serpentinites in the Golconda allochthon, occurs in this unit in Wisconsin Canyon. In Summit Canyon, the autochthonous lower Paleozoic rocks are mainly gray, fine-grained, massive or thick-bedded quartzite. They have been mapped as Cambrian Gold Hill Formation and Cambrian-Ordovician Palmetto Formation by Kleinhampl and Ziony (1967).



r Paleozoic  
re 2-1). The  
(1) and pos-  
t6 which was  
autochthonous

d Wisconsin  
and Wiscon-  
calcarenite,  
e limestone,  
limestone,  
ing and, in  
ix. Other  
porphyritic  
ody, similar  
, occurs in  
autochthonous  
e or thick-  
l Formation  
l and Ziony

Autochthonous Diablo Formation (Pd)

This unit lies immediately under the Golconda thrust in Ophir and Wisconsin Canyons. It was first assigned to the Diablo Formation by Ferguson and Cathcart (1954) in the Toiyabe Range, because of its mainly coarse chert-clast lithology and fossils that correlate with the Diablo Formation in the Candelaria Hills (Speed and others, 1977). The Diablo Formation of Ferguson and Cathcart (1954) is divided into eight structurally and spatially discrete units in the Toiyabe Range by Speed and others (1977). According to Speed and others (1977), all except two of these units are allochthonous relative to the Golconda thrust. The other two (their units d1 and d3) rest with erosional contact over lower Paleozoic rocks. Rocks assigned to the Diablo Formation in the study area are equivalent to unit d1 of Speed and others (1977) which lies under the Golconda thrust.

No fossil has been found in the study area in these rocks. However, partially correlative autochthonous Diablo rocks in Pablo and Jett Canyons, 20 km to the south, have yielded fairly late Permian (possibly Wolfcampian to Guadalupian) fossils (Speed and others, 1977).

These rocks are characteristically homoclinal and lie between highly deformed rocks of the Golconda allochthon above and lower Paleozoic autochthonous rocks below. The contact of the Diablo Formation and lower Paleozoic rocks is unconformable (Speed and others, 1977). Lithology of the rocks in the Diablo Formation is as follows: gray, plane-laminated, medium- to coarse-grained quartz- and quartz-chert-arenite, interbedded with clayey and silty sandstone; graded

conglomerate with chert and quartzite clasts; light gray and white, plane-laminated pebbly and well-sorted calcarenite; and marble. The breccia and sandstone have erosional contact, and both are tectonically foliated (Chapter 3) by the preferred planar orientation of the clasts that is parallel to an anastomosing foliation in the matrix. The foliation is homoclinal and parallel to bedding. These rocks are silicified probably due to the thermal effect of the neighboring Ophir pluton. A description of these rocks is given in Speed and others (1977).

Depositional environment - Disharmonic syndepositional folds (Chapter 3) occur in the calcarenites south of the Ophir Canyon, suggesting slumping in an unstable depositional site. Lamination in clasts of quartz arenite is folded in places, suggesting that they were soft or previously deformed when deposited in the breccia. The chert, quartzite, and other clasts in these rocks are correlated with autochthonous lower Paleozoic rocks to the east. The main difference between autochthonous Diablo Formation and allochthonous rocks of unit t3 is in the presence of calcarenite and limestone interbeds in the former and large serpentinite and other clasts in the latter, reflecting their different depositional environment.

Speed and others (1977) assign a shallow stable marine (outer shelf) environment for this unit mainly on the basis of its correlation with their unit d3 in Pablo and Jett Canyons, where broken bivalves are common, and because of the presence of well-bedded carbonates and sandstones.

gray and white, marble. The tectonically of the clasts x. The folia- e silicified Ophir pluton. A (1977).

olds (Chapter n, suggesting n clasts of were soft or chert, quartz- autochthonous between auto- t3 is in the mer and large their different

marine (outer s correlation bivalves are tes and sand-

### Toiyabe Quartz latite (Tq1)

Rocks of this unit (Ferguson and Cathcart, 1954; Speed and McKee, 1976; Laine 1977) overlie unconformably most of the Golconda allochthon on the western flank of the Toiyabe Range (Figure 2-1). It includes partly welded crystal- and crystal-pumice-ash flow tuff that give a 21.5 my K-Ar age (Kleinhampl and Ziony, 1967; Speed and McKee, 1976). The crystals consist of quartz, feldspar, biotite, and hornblende, and constitute 35% to 60% of the rock, whereas pumice varies between 0% and 15% and is devitrified (Laine, 1977). It is believed that rocks of Toiyabe quartz latites were deposited after a period of Early Miocene caldera formation, intrusion, and volcanism (Speed and McKee, 1976; Laine, 1977).

### Ophir pluton

Granitic rocks of the Ophir pluton intrude both the autochthonous and allochthonous rocks in lower and upper Ophir Canyon (Figure 2-1, Plate 1). In both areas, rocks of the autochthonous Diablo Formation (Pd), lower Paleozoic (lpz), and allochthonous units are metamorphosed at their contacts with granitic rocks of the Ophir pluton, with the development of meta-chert, meta-pelite, silicified rocks, and marble.

Ophir pluton has previously provided a 54 my K-Ar date from biotite (Speed and McKee, 1976). A 42 my K-Ar date has been obtained in the present study in the lower (eastern) part of the pluton.

The relationship between Ophir pluton and Toiyabe quartz latites is not clear. However, the rocks of the Toiyabe quartz latites lie over an undated granitic pluton in upper Ophir Canyon.

CHAPTER 3 - STRUCTURAL GEOLOGY OF THE GOLCONDA ALLOCHTHON  
IN THE STUDY AREA

Introduction

In this Chapter, structural data from all rocks of the Golconda allochthon, Diablo Formation, and to a lesser extent, autochthonous lower Paleozoic rocks are discussed. Interpretation of the kinematics of deformation is given in Chapter 4.

At least 5 phases of deformation are detected in upper Paleozoic packets (Chapter 2) of the Golconda allochthon in the study area (Table 3-1). The first (D1) consists of close to isoclinal folds (F1) of bedding mainly recorded by isolated hinges and boudins of chert in slate and by axial plane slaty cleavage (S1). The second (D2) involves thrusting and stacking of the folded rocks and is evidenced by the existence of packet-bounding faults (Chapter 2) that cut across D1 structures. The third phase (D3) includes F2a folds deforming cleavage, bedding, and packet-bounding thrusts with half-wavelengths of at least 200 meters. Such folds are detected by the regional variability of bedding and cleavage and by a macroscopic fold in packet 7 in Ophir and Wisconsin Canyons. D3 also includes local F2b folds that occur at a thrust zone between packet 7 and 8. D4 involves F3 folds including kinks in pelite and related folds with round profile in interbedded thin chert and pelite. Undeformed kinks occur together with refolded and faulted F2b folds at the contact of packet 7 and 8, indicating that kinks and associated sinusoidal folds are younger than the F2b folds.

DEFORMATION READING DEFORMATION FOLD AXIAL AXIS FOLIATION LINEA FAULT COMPLEXES  
EVENT THWAVE PLANE

DEFORMATION EVENT	READING THWAVE	FOLD PLANE	AXIAL PLANE	AXIS FOLIATION	LINEA TION	FAULT	COMPLEXES
PRE-THRUST	D <sub>1</sub>	F <sub>1</sub>	AP <sub>1</sub>	AP <sub>1</sub> x S <sub>0</sub>	S <sub>1</sub>	hounding	deposition of the four major upper Paleozoic facies of the Golconda allochthon.
							tight and (or) steeply folding (F <sub>1</sub> ) in bedding with axial plane history cleavage (S <sub>1</sub> ).
							hounding of the chert interbeds
SYN-THRUST	D <sub>2</sub>	F <sub>2a</sub>	AP <sub>2a</sub>	AP <sub>2a</sub> x S <sub>0</sub>			
							large scale open folds of bedding, cleavage, and thrusts affecting one or more packets.
							packet-locally folded rocks hounding become imbricated in packets.
POST-THRUST	D <sub>3</sub>	F <sub>2b</sub>	AP <sub>2b</sub>	AP <sub>2b</sub> x S <sub>0</sub>			
							rectilinear formation of meso-anticlinal folds in bedding and cleavage and tightly homaxial refolding (F <sub>2b</sub> ).
							microscopic kink and more rounded and larger scale folds in cleavage and bedding, respectively (F <sub>2b</sub> ), and associated axial plane features (S <sub>2</sub> ).
POST-THRUST	D <sub>4</sub>	F <sub>3</sub>	AP <sub>3</sub>	AP <sub>3</sub> x S <sub>0</sub>			
							enplacement of the allochthon over the thrust. Deformation of kinks and formation of folds (F <sub>3</sub> ) and associated local faults at the Golconda thrust.
							local faulting

Table 3-1. Deformational events in the upper Paleozoic section of the Golconda allochthon.

ALLOCHTHON

of the Golconda  
ent, autochthonous  
of the kinematics

upper Paleozoic  
study area (Table  
folds (F1) of bed-  
of chert in slate  
and (D2) involves  
evidenced by the  
cut across D1  
forming cleavage,  
gths of at least  
riability of bed-  
7 in Ophir and  
s that occur at a  
folds including  
le in interbedded  
r with refolded  
, indicating that  
the F2b folds.

At the Golconda thrust zone, mesoscopic folds (F4) cut by local faults, are related to the latest deformation (D5) along the thrust. Except for the local F2b and F4 folds, a similar sequence of deformation is evident in all packets of upper Paleozoic rocks of the allochthon.

The lower Paleozoic and Triassic rocks within the allochthon differ in lithology (Chapter 2) and structure compared to the upper Paleozoic rocks. Isoclinal folding is indicated in the lower Paleozoic rocks by the parallelism of a well developed slaty cleavage and bedding in interbedded pelite and chert. A younger spaced cleavage, absent in upper Paleozoic rocks, exists in packet 9 which is dominated by rocks of probable early Paleozoic age. Mesoscopic and variably oriented folds younger than cleavage, are among the other structures of packet 9 which are absent in upper Paleozoic packets. The tectonic fabric in the lower Paleozoic rocks may at least partly be of pre-Golconda age. Triassic rocks differ from both lower and upper Paleozoic rocks in that they are very little deformed. No cleavage or folding is evident in these rocks despite their partly similar lithology to some upper Paleozoic rocks (Chapter 2).

Any kinematic model, to explain development of the Golconda allochthon, should account for ordered accretion of varied facies of upper Paleozoic (Chapter 2), lower Paleozoic, and Triassic packets to the allochthon, and the ordered sequential deformation in these rocks. There are two alternatives to explain the above: 1) upper Paleozoic rocks were part of an originally continuous mass which were sequentially thrust into a prism and emplaced over lower Paleozoic rocks of

the co  
and Tri  
constru  
Golcond  
ferent  
occurre  
the all  
tonic e  
scheme.  
Th  
Paleozo  
be used  
Accordi  
divided  
section  
Pre-thru  
liest  
thrust  
well d  
tion in  
which  
deposi  
Permian  
formati  
taneous

local faults,  
t. Except for  
ation is evi-  
thton.

e allochthon  
to the upper  
er Paleozoic  
e and bedding  
e, absent in  
ated by rocks  
ly oriented  
s of packet 9  
e fabric in  
Golconda age.  
rocks in that  
s evident in  
upper Paleo-

conda allo-  
ies of upper  
ets to the  
these rocks.  
r Paleozoic  
were sequen-  
ic rocks of

the continental margin that later imbricated with the lower Paleozoic and Triassic rocks to form the allochthon; 2) rocks of different ages constructed smaller allochthon, which were later amalgamated into the Golconda allochthon. The geographic and structural distribution of different upper Paleozoic facies discussed in Chapter 2, the limited occurrence of lower Paleozoic and Triassic rocks at the basal part of the allochthon, and the observed evidences of the same sequence of tectonic events in all the upper Paleozoic packets supports the first scheme.

The fundamental structural feature of all packets of the upper Paleozoic section of the allochthon is their boundary faults that can be used as a reference for the formation of all other tectonic fabrics. Accordingly, the deformation in the upper Paleozoic packets can be divided in a sequence relative to thrusting of the packets into the section as pre-, syn-, and post-thrust.

Pre-thrust deformation - The isoclinal folds of beds (F1) are the earliest structures in each packet and are cut by packet boundaries. Pre-thrust deformation (D1) is manifested in the Golconda allochthon as a well developed axial plane slaty cleavage in pelite and spaced foliation in sandstone. D1 structures exist in upper Paleozoic packets, which despite their different lithology, represent varied facies of a depositional environment that persisted from late Mississippian through Permian (Chapter 2). Alternative schemes for assembling the packets and formation of these structures are as follows: 1) D1, represents simultaneous deformation of rocks of wide age span before thrust

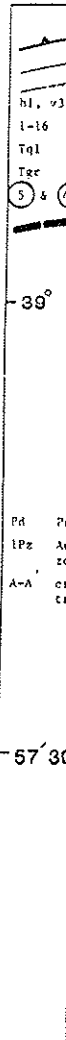
imbrication, 2) D1 is diachronous; younger in structurally lower and later-emplaced packets than in upper ones. The second scheme appears more probable because of the ordered distribution of upper Paleozoic rocks in the allochthon (Chapter 2). The order would otherwise be disturbed by isoclinal folding had they been deformed according to the first scheme. The implication of the second alternative is that D1 deformation was progressive with consistently oriented shortening.

Syn-thrust deformation - This deformation (D2) is marked by faulting of the isoclinally folded rocks and by open folding (F2a), rotation, and translation of the packets and formation of associated F2b folds. If the second scheme discussed above is correct, syn-thrust deformation was also diachronous and spanned different increments of time in different packets, and overlapped in time the pre-thrust deformation in younger packets.

Post-thrust deformation - After all or some of the packets were accreted to the allochthon, D1 structures such as slaty cleavage and first folds were folded by sporadic kink and other open and gentle folds (F3). Other post-thrust structures include local F4 folds and associated faults at the Golconda thrust that represent the latest motion along the thrust.

#### Method and terminology

The allochthonous rocks are divided into domains based on the orientation of slaty cleavage and bedding in packets (Figure 3-1). Except in packet 7, domains are indexed by the number of the packet



Figure



ly lower and  
 scheme appears  
 per Paleozoic  
 otherwise be dis-  
 rding to the  
 utive is that D1  
 ortening.

by faulting of  
 rotation, and  
 b folds. If  
 st deformation  
 time in dif-  
 deformation in

packets were  
 ty cleavage and  
 en and gentle  
 al F4 folds and  
 at the latest

based on the  
 s (Figure 3-1).  
 of the packet

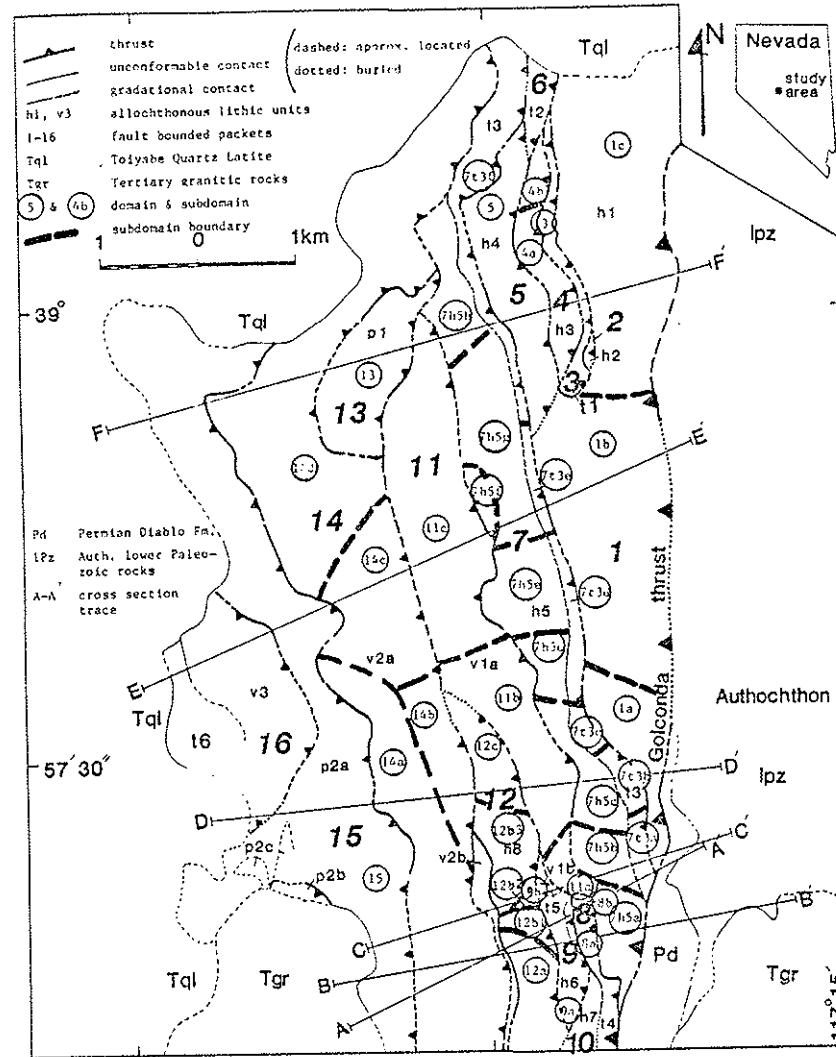
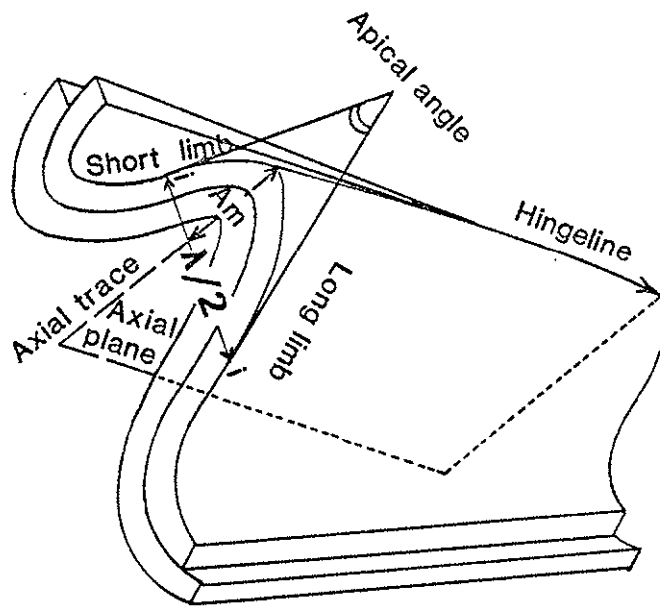


Figure 3-1. Map showing structural domains in the Golconda allochthon.



$i$  = inflection point

$\lambda/2$  = half-wavelength

$A_m$  = amplitude

Figure 3-2. Three-dimensional diagram of a fold showing the parameters measured for fabric analysis.

that  
ing t  
turn  
and c  
guish  
length  
measur  
of dia  
domain  
equal  
First  
H  
respec  
detail  
tures  
Domain  
R  
the ar  
with a  
tion  
sures  
folds  
Fl fold  
cm. M



wing the

that they include. Packet 7 is divided into domains 7h5 and 7t3 according to the corresponding lithic units (Figure 3-1). Each domain is in turn divided into subdomains that resolve local variations of bedding and cleavage within domains (e.g. 1a, 7h5c, etc.). In order to distinguish folds of different size, shape, and probably, generation, the lengths and orientation of the parameters shown on Figure 3-2 were measured. The rest of this chapter is devoted to description of folds of different generations, faults, and analysis of strain in different domains. All the fabric diagrams in this study are lower hemisphere equal area projections.

#### First folds (F1)

Hemipelagic units h5 and h8 which occur in domain 7 and 12, respectively, provide the best exposures of first structures. A detailed analysis of the two domains will be given first. D1 structures in other domains will be covered at the end of this section.

#### Domain 12

Rocks of this domain (unit h8) provide a unique opportunity for the analysis of F1 folds which are detected here as closures of beds with associated axial plane slaty cleavage, bedding-cleavage intersection (bxc lineation), and chert boudins (Table 3-1). The bedding closures of the first folds occur mostly in subdomain 12b3. Sizes of these folds are shown on Figure 3-3. Half-wavelength of the majority of the F1 folds ranges between 40 and 80 cm, but 10% are as wide as 140 to 160 cm. Most of the folds have amplitudes less than 150 cm, and the major-

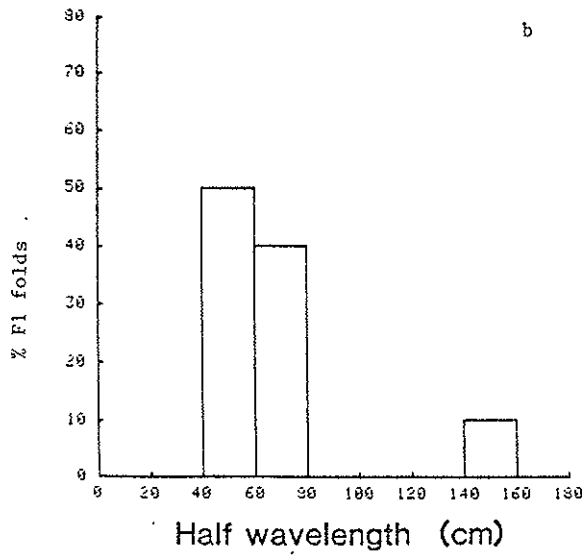
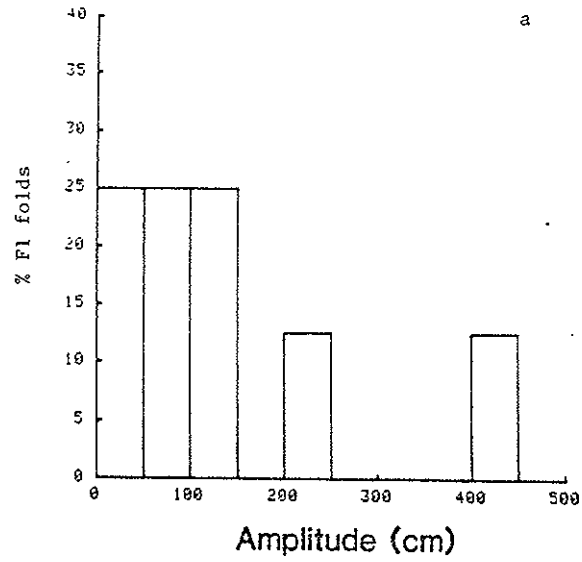


Figure 3-3. Size of F1 folds in domain 12.

ity of  
 (Figure  
 Fi  
 Slaty  
 another  
 the cl  
 and 75°  
 the mo  
 bxc line  
 obtained  
 The  
 profile  
 as their  
 continuo  
 axis att  
 lar to  
 folds (F  
 a great  
 domains  
 tions. V  
 to the Y  
 plane of  
 distribut  
 1) I  
 orientati

ity of them are individual halfwaves with uncertain inflection points (Figure 3-2). 62

Figure 3-4 shows the orientation of these folds in domain 12. Slaty cleavage and the axial planes of these folds are parallel to one another and to cherts in their limbs. Their hingelines and axes lie in the cleavage and trend between  $N1^{\circ}W$  and  $N45^{\circ}W$  and plunge between  $24^{\circ}$  and  $75^{\circ}$ . The bxc lineations distribute on a great circle parallel to the modal cleavage, axial planes, and homoclinal bedding. Most of the bxc lineations plunge N, parallel to the hingelines and fold axes obtained by bedding intersections (bxb).

The chert beds are boudinaged where interbedded with pelite. The profile length of boudins is commonly less than 10 cm, almost the same as their length on cleavage except in rare exposures where boudins are continuous for few meters on cleavage. The distribution of the long axis attitudes of boudins in both cases, measured on cleavage, is similar to that of the bxc lineations, hingelines, and fold axes of the F1 folds (Figure 3-4). Although lineations in domain 12b generally occupy a great circle, they distribute as partial girdles in different subdomains (Figure 3-5), indicating a geographic distribution of orientations. Where strain has been measured, most lineations are subparallel to the Y axis (Figure 3-70). In summary, all lineations lie in the plane of modal cleavage, axial planes, and bedding in parallel limbs, a distribution that could have been formed in the following ways:

- 1) Inhomogeneous coaxial strain: cleavage of different initial orientations formed, for example due to anisotropy, resulting in

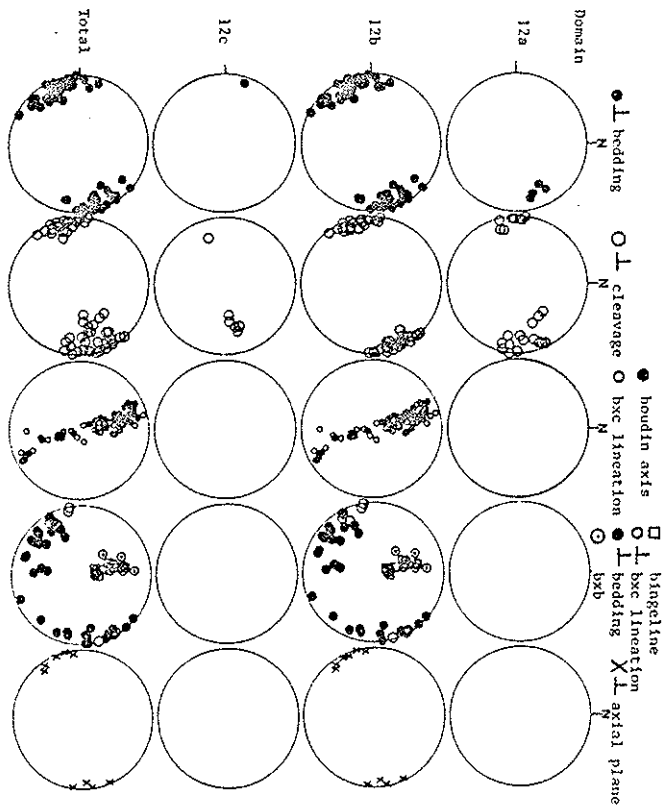


Figure 3-4. Orientation of F1 folds in domain 12.

Fig



variably oriented intersections with a bedding of constant or variable initial orientation; progressive or later flattening caused the cleavage to become subparallel and the lineations to become coplanar.

2) Inhomogeneous noncoaxial strain: orientation of the Z principal strain axis is constant but X and Y rotate, leading to the formation of differently oriented boudins on a constantly oriented cleavage.

3) Superposed folding: unidentified pre-D1 deformation caused varied orientations of intersection with D1 cleavage. Small change in the orientation of bedding and (or) cleavage can result in great variation in bxc orientation.

4) Rotation of D1 lineations on the cleavage plane: Progressive pure or simple shear could have caused migration of D1 lineations toward the X deformation direction within the flattening (cleavage) plane (Ramsay, 1967; Sanderson, 1973; Escher and Watterson, 1974; Ramsay, 1978; Bell, 1978; Rhodes and Gayer, 1979).

The geographic distribution of the lineations in the southern and northern parts of subdomain 12b (Figure 3-5), pitching at different angles and directions in the constantly oriented cleavage supports hypotheses 1 and 3. Clustering of the bxb and hingelines is most probably the result of a geographic distribution, supported by the fact that these were only measured in subdomain 12b3 (Figure 3-5) where boudins are also clustered. No lineation attributed to shear, to satisfy the fourth hypothesis, is evidenced in these rocks.



nt or variable

ng caused the  
ome coplanar.

the Z principal  
ne formation of  
eavage.

mation caused  
Small change in  
in great varia-

e: Progressive  
F1 lineations  
ing (cleavage)  
son, 1974; Ram-

e southern and  
ng at different  
eavage supports  
s is most prob-  
by the fact  
gure 3-5) where  
to shear, to  
ks.

Only few isoclinal folds were discovered in this domain. Structures of the D1 phase such as the axial plane slaty cleavage, bxc lineation, and chert boudins, however, are common. Such structures are reoriented in places because of a younger (F2a) fold.

Figure 3-6 shows the orientation of F1 lineations in domain 7h5. The boudin axes and hingelines of isoclinal folds at each subdomain cluster at low angles to the corresponding modal cleavage. The bxc lineations lie on the cleavage with a larger spread than chert boudins. Such a distribution can be explained by the same hypotheses as mentioned in domain 12. Girdles of F1 cleavage and lineations in subdomains 7h5a and 7h5b are due to F2a folds for the reasons to be discussed later.

#### Other domains

Except for domain 9, which will be treated separately, the distribution of bedding and cleavage in other domains are shown on Figures 3-7 through 3-16. Bedding is parallel to cleavage in all these domains, and both are deformed by F2a macroscopic folds. In general, the orientation range of bedding and cleavage is approximately similar in each domain and indicates deformation of the F1 folds. The partial girdle distribution of cleavage and bedding in most domains and few unusual orientations, for example in 8b and 11a, may be original; due to F2a folds, or a result of inhomogeneous strain.

Boudin axes plunge shallowly to moderately N or NW except in domains 7t3e and 13, where the steep and moderate SE plunge of boudins

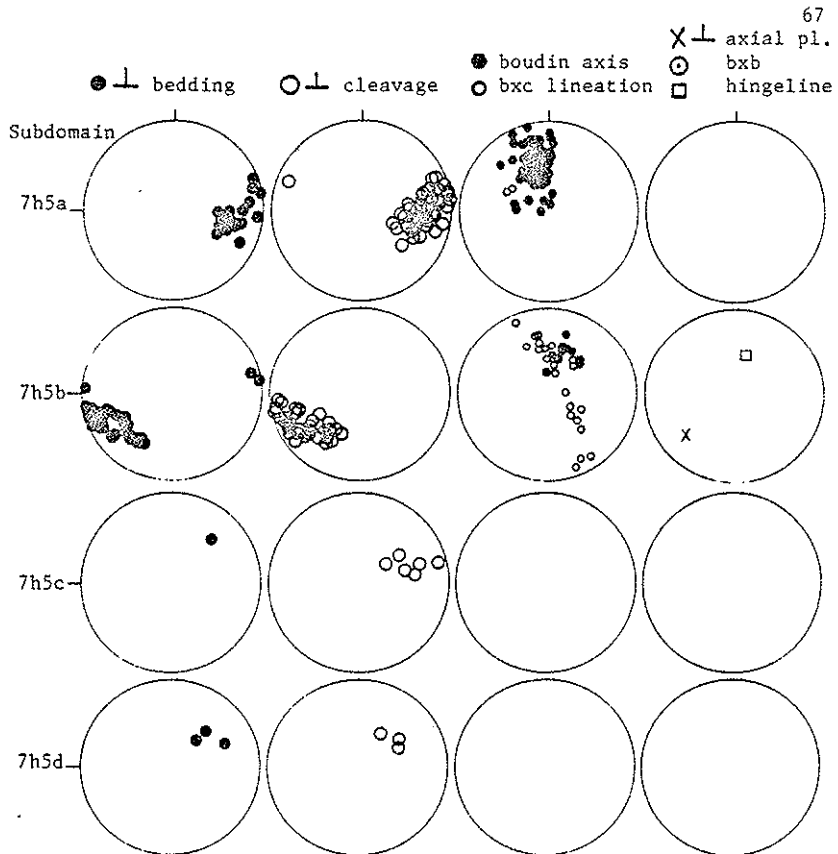


Figure 3-6. Orientation of F1 structures in domain 7h5.

7h5e

7h5f

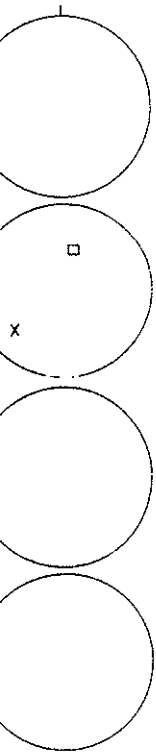
7h5g

7h5h

Total

Figure

67  
⊥ axial pl.  
⊙ bxb  
□ hingeline



7h5.

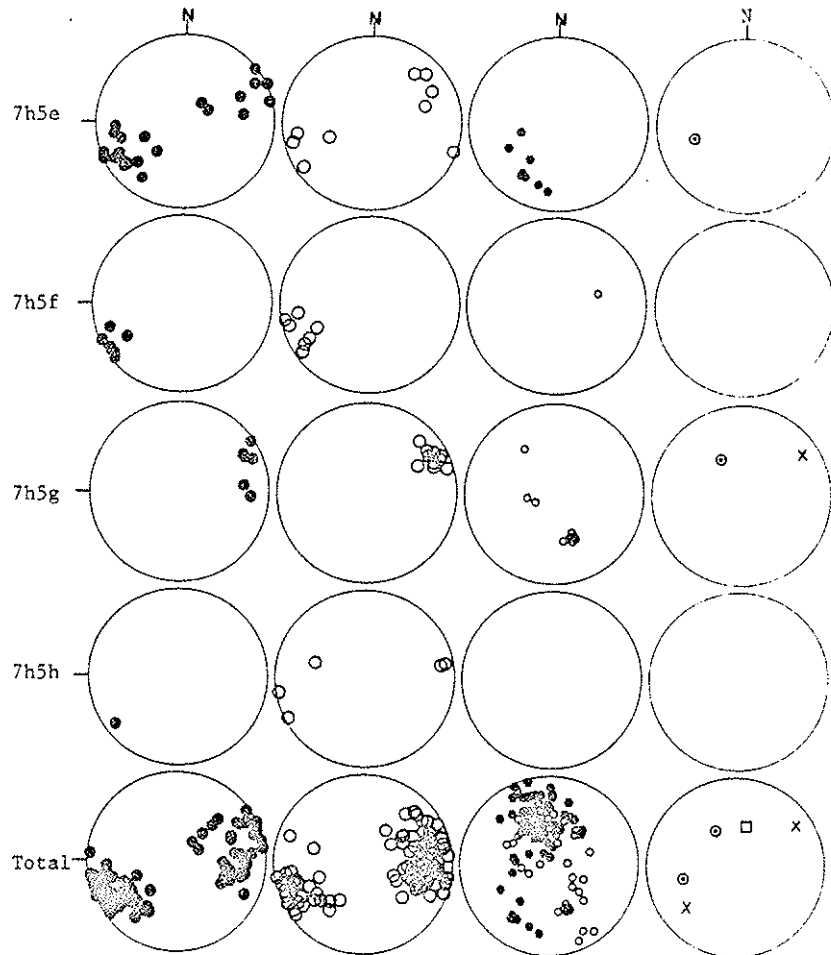


Figure 3-6 cont'd

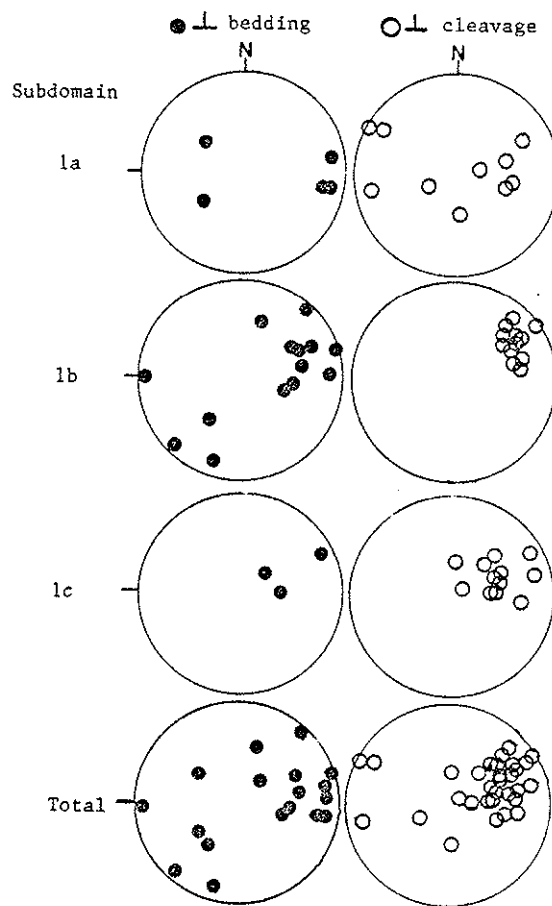


Figure 3-7. Orientation of bedding and cleavage in domain 1.

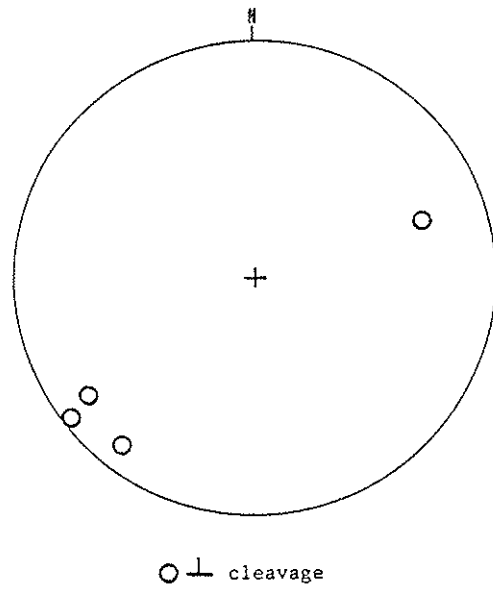


Figure 3-8. Orientation of cleavage in domain 3.

in domain 1.

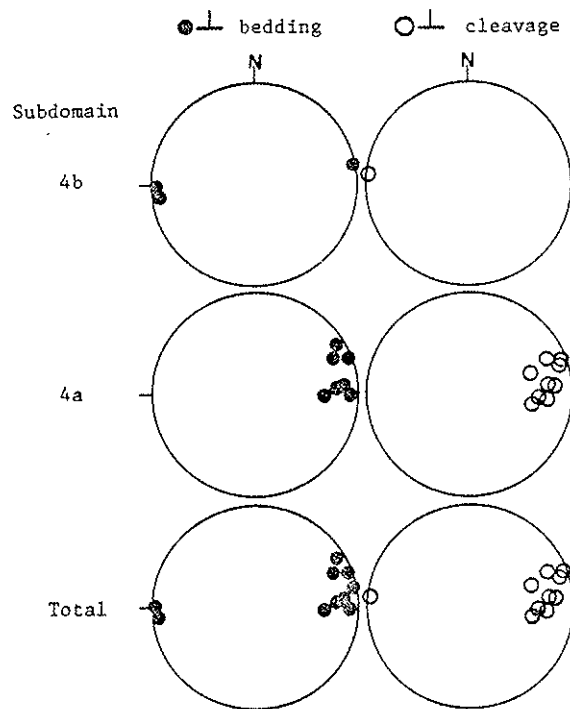


Figure 3-9. Orientation of bedding and cleavage in domain 4.

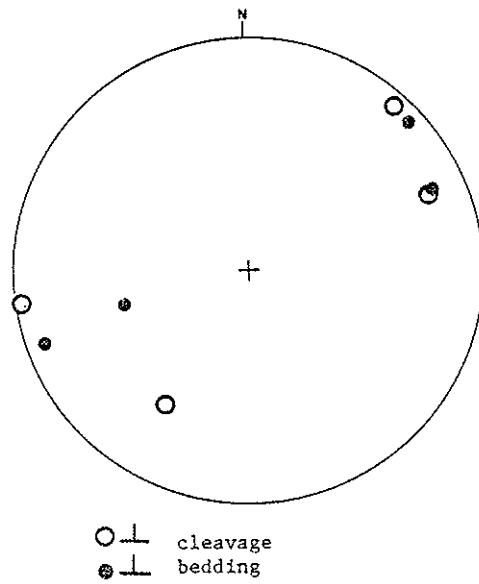


Figure 3-10. Orientation of bedding and cleavage in domain 5.

vage

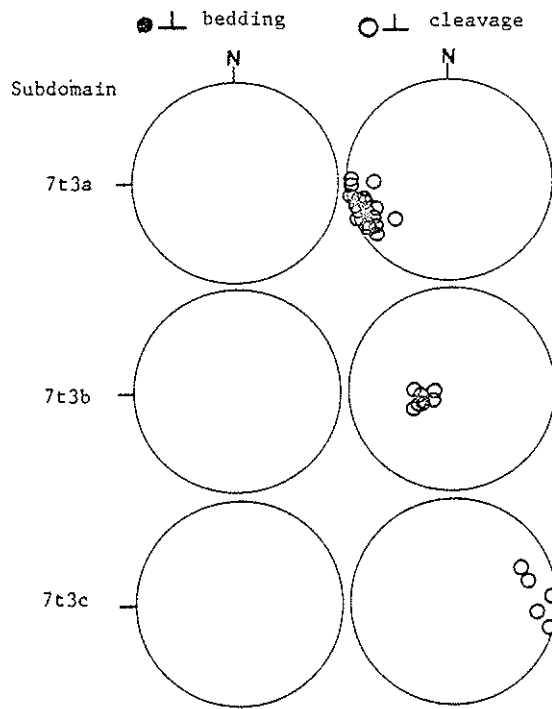


Figure 3-11. Orientation of  $F_1$  structures in domain 7t3.



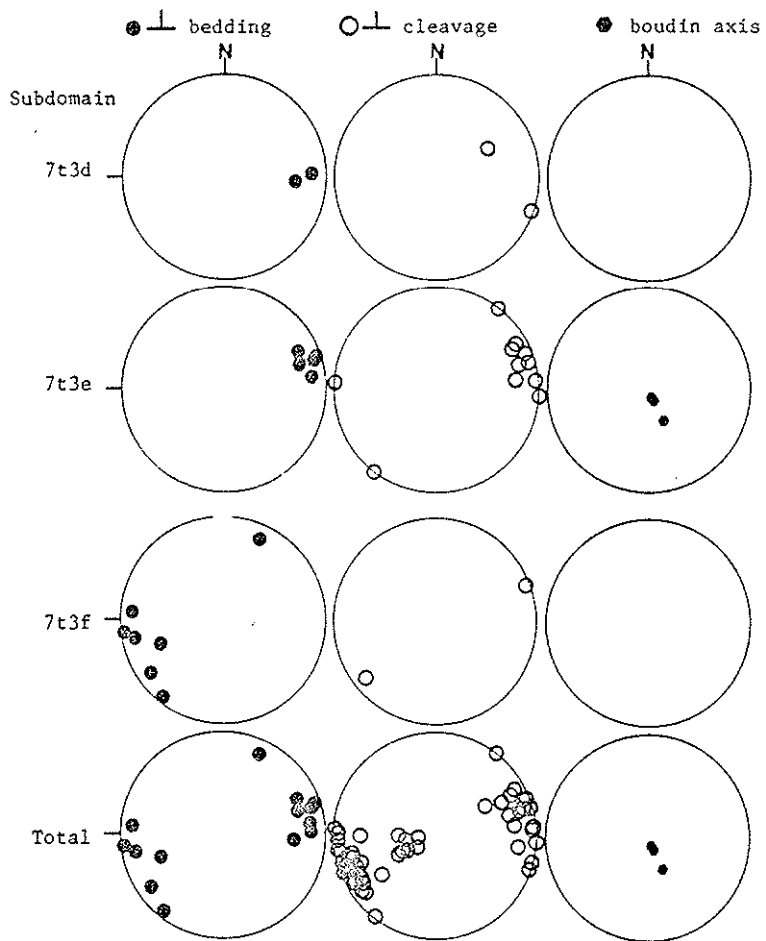


Figure 3-11 cont'd

omain 7t3.

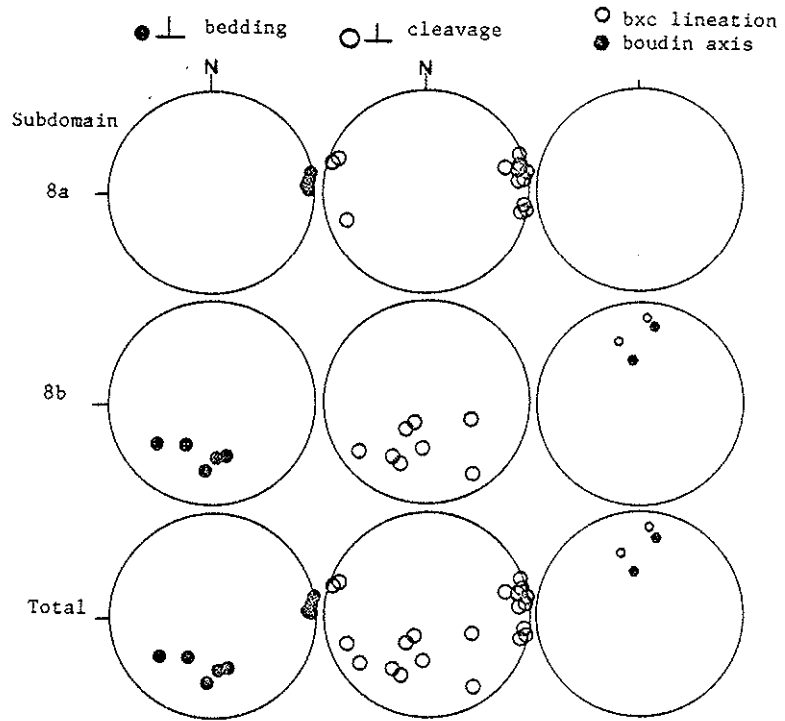


Figure 3-12. Orientation of F1 structures in domain 8.

ineation  
n axis



in 8.

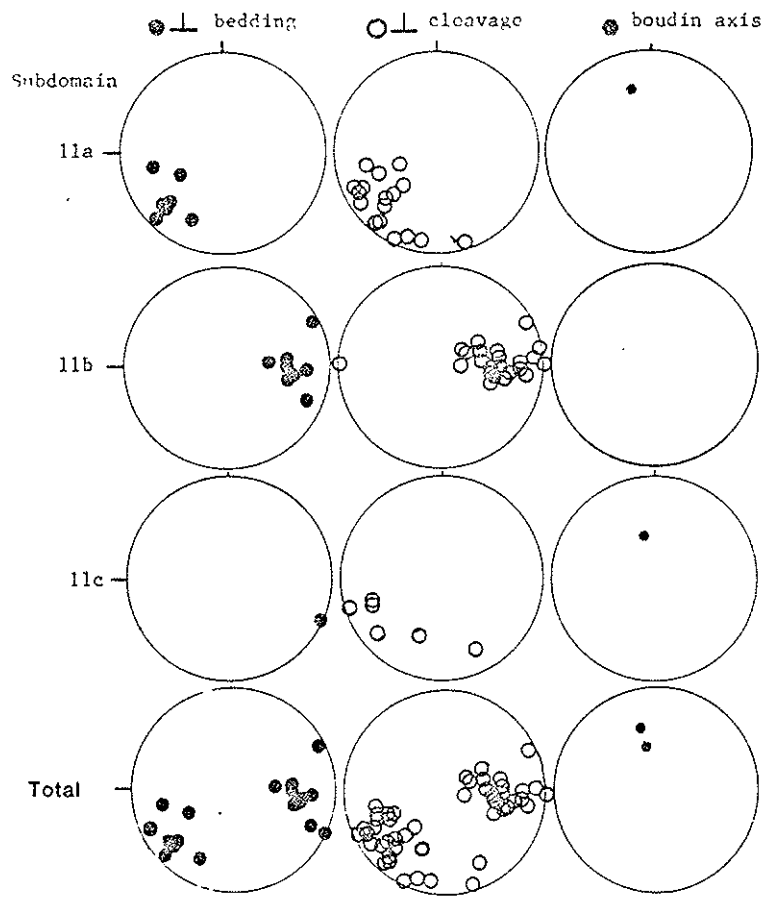


Figure 3-13. Orientation of  $F_1$  structures in domain 11.

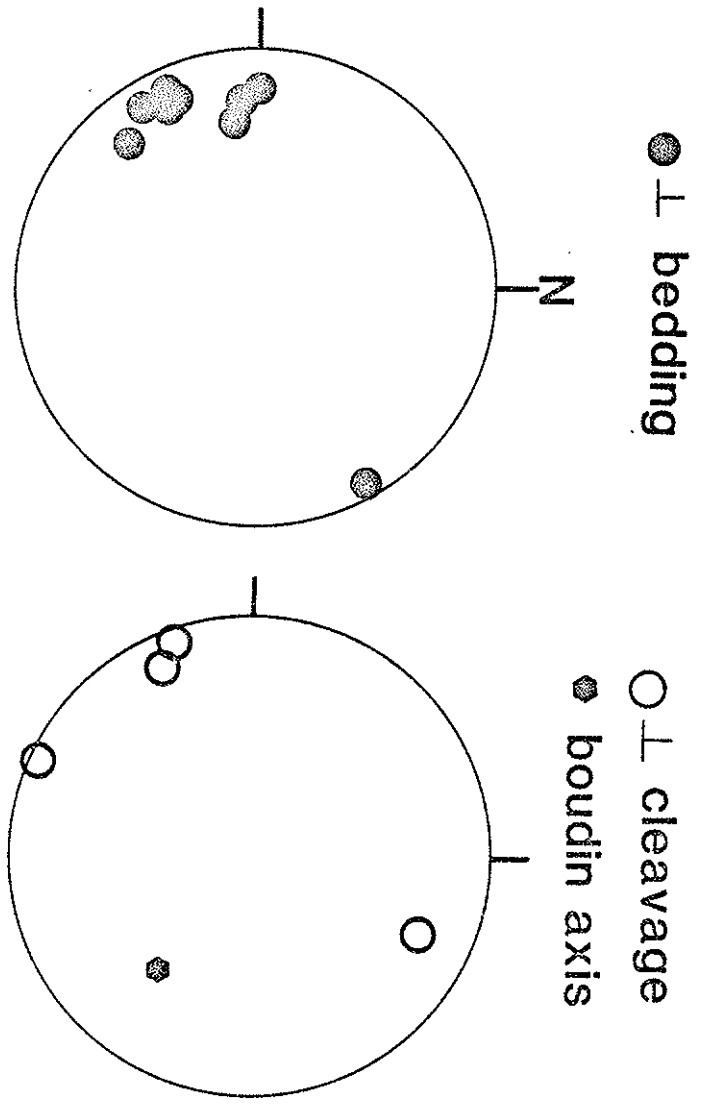


Figure 3-14. Orientation of bedding and cleavage in domain 13.

● ⊥ bedding

○ ⊥ cleavage

● boudin axis

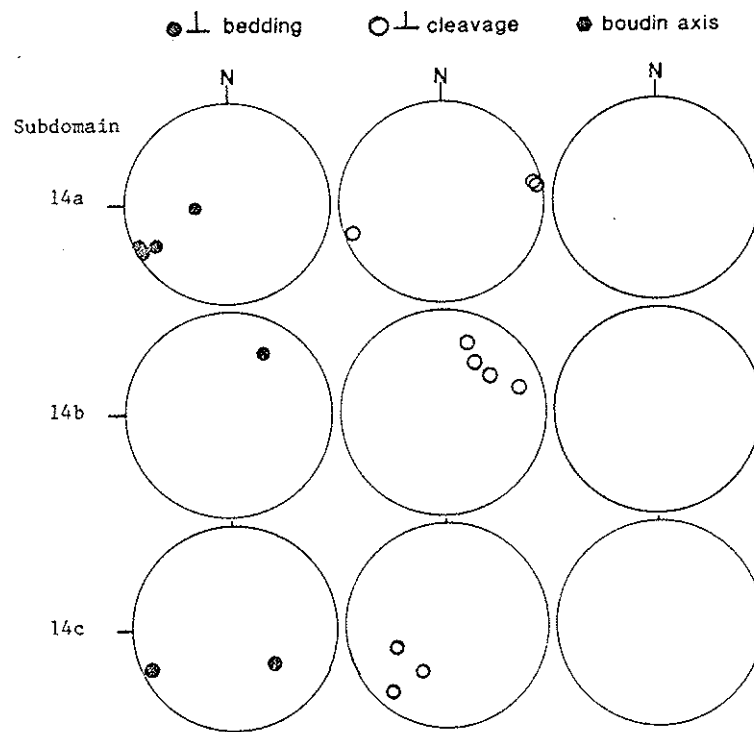


Figure 3-15. Orientation of F1 structures in domain 14.

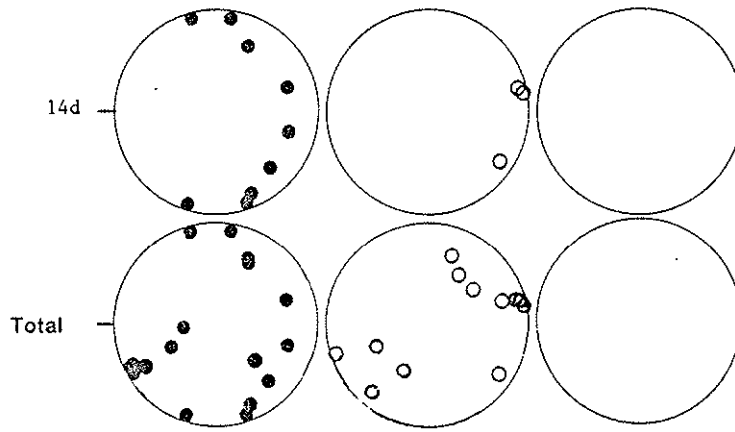


Figure 15 cont'd

● ⊥ bedding  
○ ⊥ cleavage

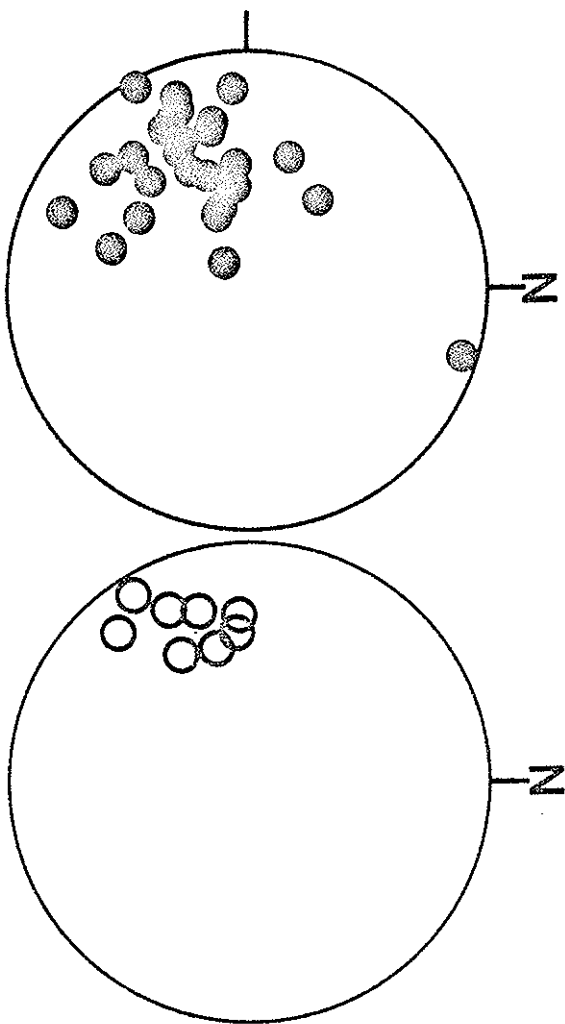


Figure 3-16. Orientation of bedding and cleavage in domain 15.



may be because of F1 and (or) F2a folding.

#### F2a folds

These are large, gentle to open folds of bedding and cleavage and packet bounding thrusts that are responsible for the variability in cleavage and bedding orientation in all the domains (Figure 3-7 through 3-16, 3-17). The statistical axes of F2a folds plunge shallowly to moderately NNW.

The best example of the F2a folds is a macroscopic fold in Ophir and Wisconsin Canyons in packet 7 (Figure 3-18). The fold is an isolated single halfwave with halfwavelength of at least 200 meters. Its axis plunges  $30^{\circ}$  N16 $^{\circ}$ W, and its axial plane, constructed from axial traces and axis, strikes N55 $^{\circ}$ W dipping  $42^{\circ}$  NE (Figure 3-19). Cross sections of this fold are shown on Plate 3 and Figure 2-3.

F2a folds, homoaxial with average lineation of F1 folds (Figure 3-17), are second phase because large range of F1 cleavage (Figure 3-19) cannot be accounted for by fanning and rather is explained by folding as discussed below, and because packet bounding thrusts are folded.

Figure 3-18 depicts a constructed profile of the macroscopic F2a fold in packet 7. Shown on the diagram are also three subdomains in this part of the packet which are defined by the fold. Summary diagrams of F1 structures in subdomain 7h5a and 7h5b are shown on Figures 3-20a,b, respectively. When combined, the two diagrams define a girdle of cleavage and bedding, which contains the pole to the axial plane of the only F1 fold measured in domain 7h5a (Figure 3-20c). The zonal axis of the girdle plunges NNW subparallel to the statistical axis of the



and cleavage and the variability in Figure 3-7 through Figure 3-19 through range shallowly to

c fold in Ophir the fold is an iso- 200 meters. Its ructed from axial 3-19). Cross sec-

l folds (Figure eavage (Figure 3- explained by fold- rustrs are folded. macroscopic F2a ree subdomains in

Summary diagrams own on Figures 3- define a girdle he axial plane of ). The zonal axis tical axis of the

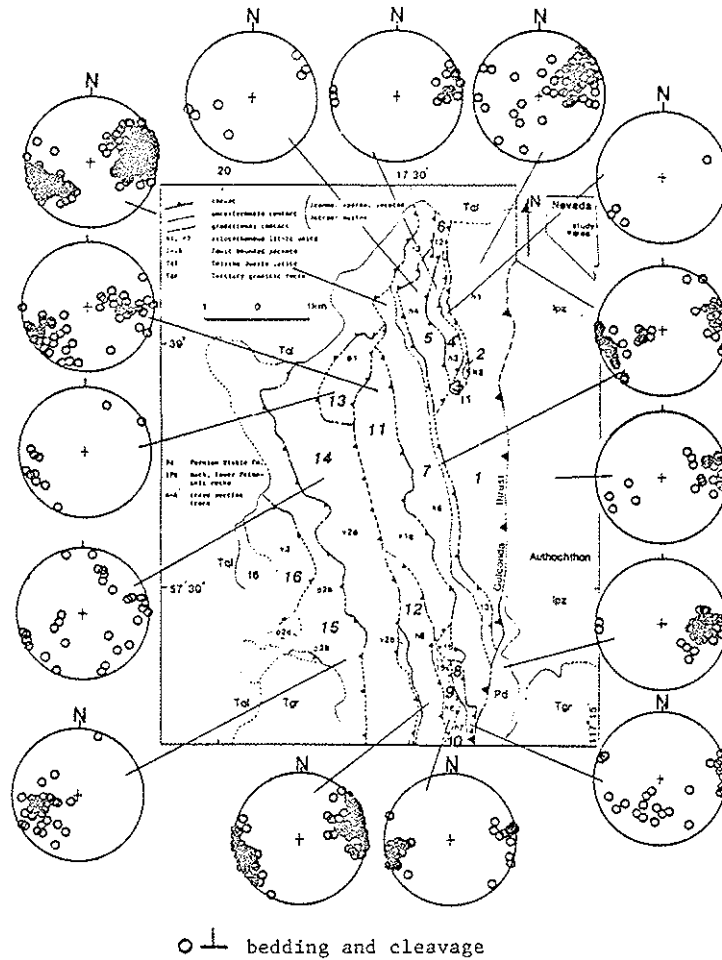


Figure 3-17. Orientation of bedding and cleavage in the Golconda allochthon and its autochthon.

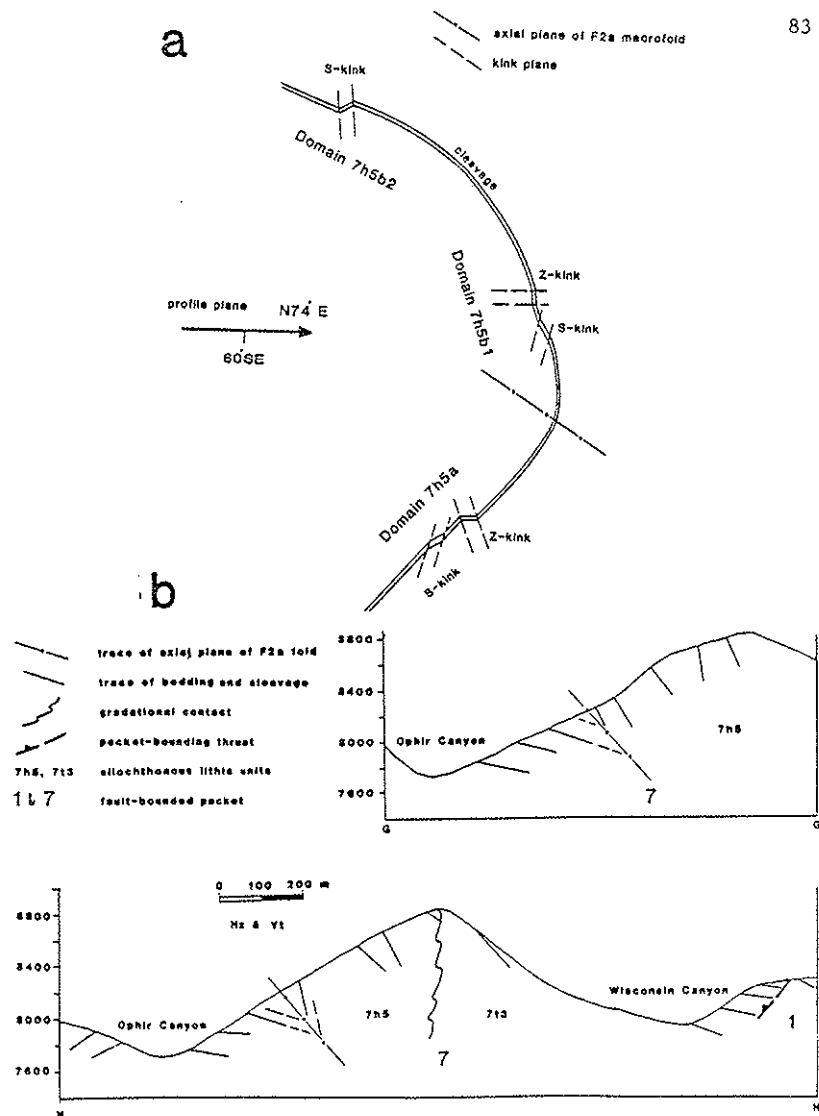
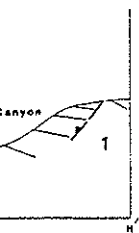
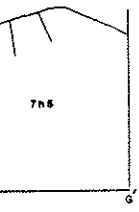
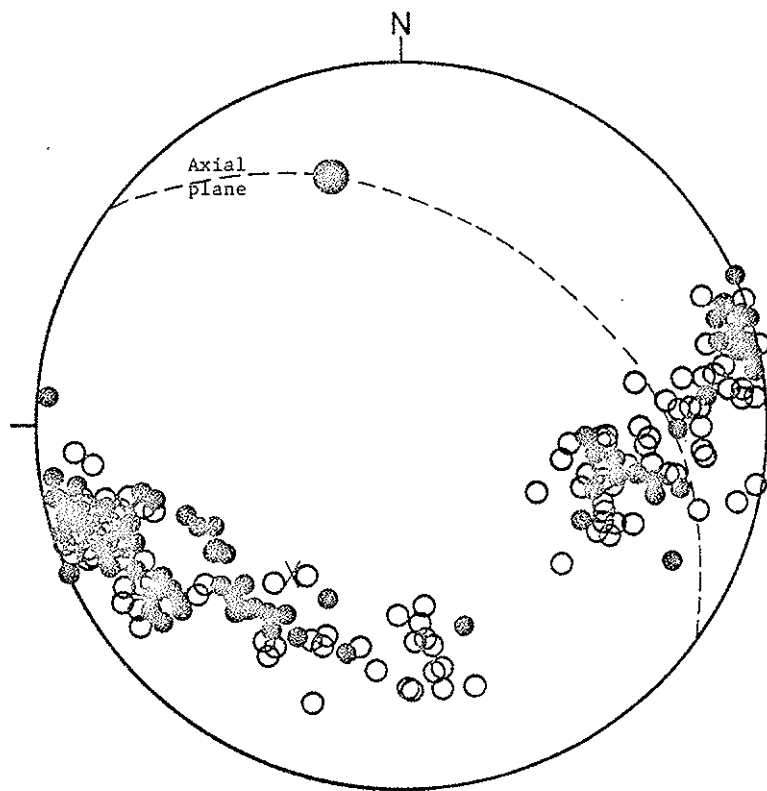


Figure 3-13. a) Constructed profile and b) cross sections of the F2a macrofold in Ophir-Wisconsin Canyons (see Plate 3)



of the F2a  
ate 3)




-  Axis of the F2a macrofold
-  Cleavage
-  Axial plane of the F2a macrofold
-  Bedding

Figure 3-19. Orientation data for macroscopic F2a fold in Ophir Canyon.

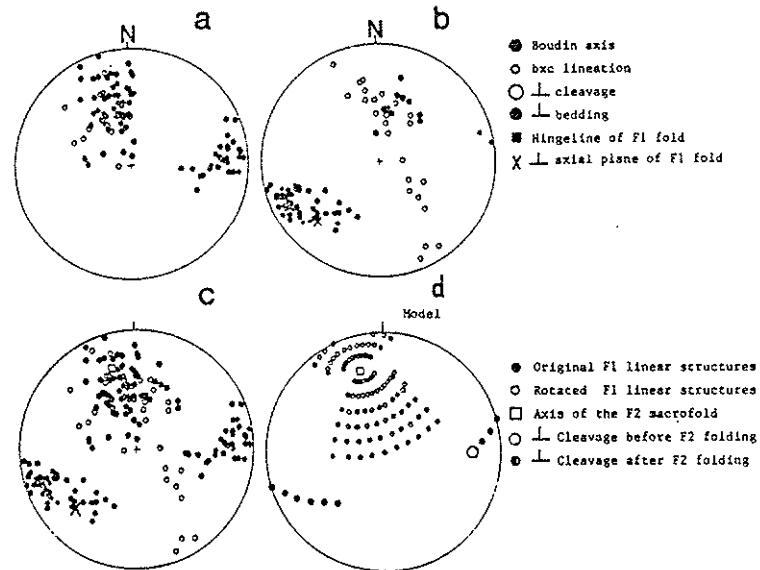


Figure 3-20. Orientation data of F1 structures in a) domain 7h5a, b) domain 7h5b, and c) domains 7h5a+7h5b. Figure 3-20d is a synthetic fabric diagram showing the effect of the F2a macrofold on F1 structures by flexural slip.

F2a fo  
 diagra  
 ural s  
 tions  
 F2a fo  
 linear  
 becaus  
 in oth  
 To ach  
 subdom  
 would b  
 actual  
 indicat  
 A model  
 F2b fol  
 Th  
 the co  
 3-1). T  
 of seve  
 serpent  
 cleavage  
 local fa  
 tion ind  
 majority  
 (Figure

86

F2a fold (Figure 3-19). Figure 3-20d illustrates a synthetic fabric diagram showing the effect of the F2a folds on F1 structures by flexural slip in domain 7h5a and 7h5b. According to this model, the lineations and poles to bedding and cleavage rotate about the axis of the F2a fold in small and great circles, respectively. The initial F1 linear and planar structures are assumed to be those in domain 7h5a because here, cleavage and bedding are homoclinal and parallel to those in other parts of packet 7 where there is no rotation by the F2a fold. To achieve the observed fabric, the cleavage of the homoclinal part of subdomain 7h5a is rotated about the zonal axis by  $100^\circ$ . No such fit would be observed if both limbs are rotated  $50^\circ$ . The good fit of the actual orientation data (Figure 3-20c) with the model (Figure 3-20d) indicates that there was flexural slip kinematics during F2a folding. A model for the F2a folding is provided in Chapter 4.

#### F2b folds

These are local structures that occur only in subdomain 7h5a at the contact with subdomains 8b and 11a in Ophir Canyon (Figure 1-1 and 3-1). This location is a thrust zone, characterized by the occurrence of several local faults, brecciation, mineralization (quartz vein), serpentinite, and lithic and structural discordance. Here, bedding and cleavage are deformed by sinusoidal folds and are cut in many places by local faults. The apical angles of these folds have a bimodal distribution indicating open and close folds (Ramsay, 1967) (Figure 3-21a). The majority of the folds have amplitude and half-wavelength less than 6 cm (Figure 3-21b,c).

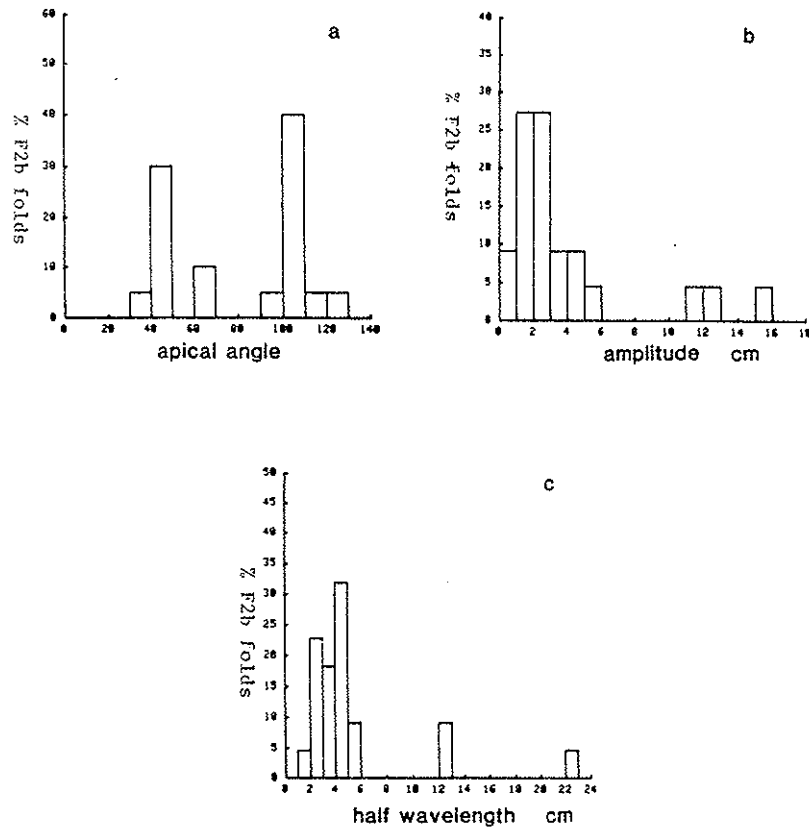


Figure 3-21. Apical angle and size of F2b folds.

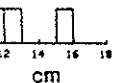


Figure 3-22a sets out the orientation of bedding and coplanar F1 cleavage in F2b folds in subdomain 7h5a. Poles to both planar elements distribute approximately on a great circle with large spread, indicating a folding event younger than isoclinal F1 folding. The poles to homoclinal bedding and cleavage, where F2b folds are absent, do not lie on the F2b phase bedding girdle. Figure 3-22b shows the orientation of the axial planes of the F2a folds. The distribution is approximately a great circle subparallel to that of the poles to cleavage and bedding, indicating homoaxial rotation of the folds. Figure 3-22c depicts the orientation of fold axes (bxb) and hingelines of the F2a folds.

The presence of local faults cutting across these folds, the occurrence of these folds at the packet boundaries and in faulted blocks that are rotated relative to homoclinal bedding and cleavage where F2b folds are absent, and their deformed attitudes, suggest that F2b folds are syn-thrust structures. At this thrust zone, smaller scale kink folds occur in unrotated orientations, indicating that F2b folds are older than the kinks. These constrain the relative age of F2b folds between F1 and kink folding. Their relationship to F2a folds is not clear; they were probably formed either synchronously or in different increments of the same syn-thrust deformation (D2).

There are two alternative ways to explain why homoclinal F1 cleavage and bedding do not lie on F2b girdle (Figure 3-22a): 1) blocks of F1 structures were first rotated, for example due to faulting, from their initial homoclinal orientation, and then deformed into F2b folds, 2) F1 cleavage and bedding were first deformed by F2b folds and then

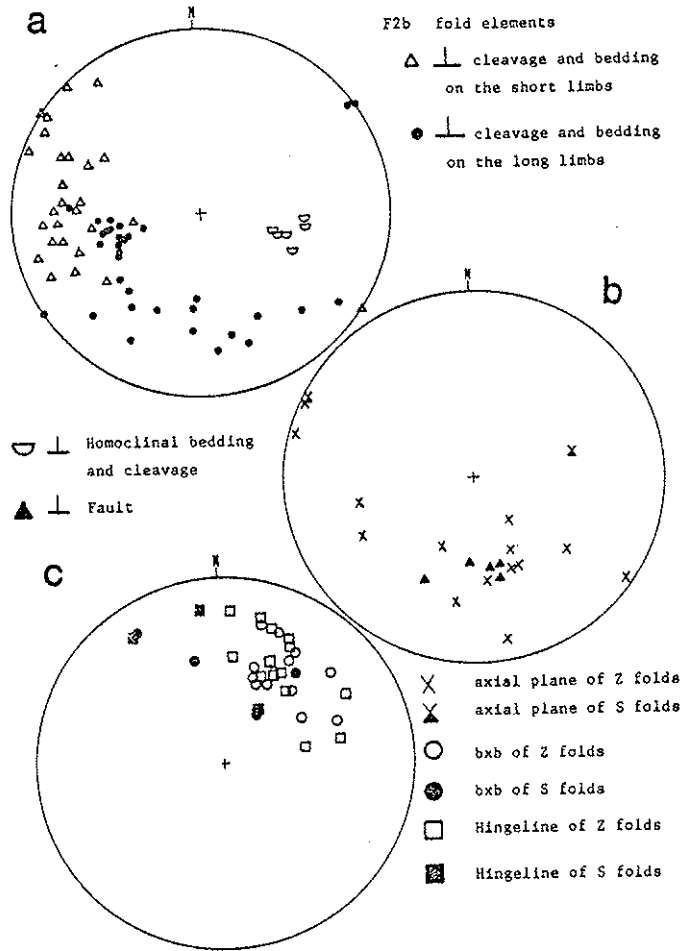


Figure 3-22. Orientation data of F2b folds in domain 7h5a.

ri  
F2  
fo  
ar  
pla  
fo  
the  
tha  
ass  
the  
F3  
inte  
clea  
F2b  
betw  
Verb  
layer  
in se  
ments  
Weiss  
1974  
1968,



rigidly rotated so as to remove the homoclinal F1 orientation from the F2b girdle.

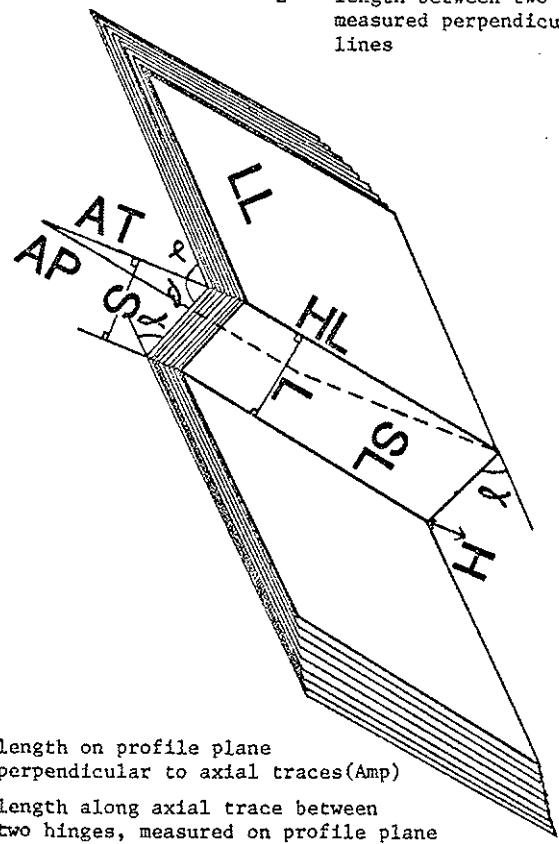
The structures depicted on Figure 3-22 are both for S and Z F2b folds; Z folds are the dominant type. Hingelines of the Z and S folds are non-parallel as a result of their differently oriented axial planes. The distribution of short and long limbs of the S and Z F2b folds shown on Figure 3-22a can be explained by homoaxial rotation of the folds, as suggested by the orientation of their axial planes, such that initially differently oriented short limbs of S and Z folds would assume subparallel attitudes after refolding. A model of formation of these folds is given in Chapter 4.

### F3 folds

F3 folds include kinks and sinusoidal folds in slates and chert interbeds, respectively. These occur in domains dominated by D1 slaty cleavage such as 7h5 and 12 (Figure 3-1) and are younger than F2a and F2b folds in Ophir Canyon for the reasons to be discussed.

Kinks are straight limbed monoclines with angular hinge zone between paired subparallel axial planes or kink planes (Ramsay, 1967; Verbeek, 1978; Rousell, 1980) (Figure 3-23). They occur in very thinly layered rocks with well developed planar anisotropy such as slates and in sets with either individual or intersecting orientations. Experiments on cards and foliated rocks (Borg and Handin, 1966; Patterson and Weiss, 1966; Donath, 1968; Weiss, 1968; Anderson, 1974; Gay and Weiss, 1974), theoretical work (Ramsay, 1962, 1967; Dewey, 1965, 1969; Weiss, 1968, 1980), and field studies (Anderson, 1964, 1968; Clifford, 1969;

- LL = long limb
- SL = short limb
- AP = axial plane
- AT = axial trace
- L = length between two hinge lines measured perpendicular to hinge lines



- S = length on profile plane perpendicular to axial traces(Amp)
- H = length along axial trace between two hinges, measured on profile plane

Figure 3-23. Geometry of a kink fold, showing lines and angles measured in the field.

Fyso  
Tobi  
unde  
nucl  
on F  
  
folds  
mine  
matio  
cusse  
  
Domai  
  
3-24)  
sinus  
wavele  
a fact  
limbs.  
fold t  
18).  
kinks  
domain  
0  
folds  
Figure  
modera

Fyson, 1968; Roberts, 1971; Hobson, 1973; Naha and Halyburton, 1974; Tobisch and Fiska, 1976; Verbeek 1978; Rousell, 1980) contributed to an understanding of the kinematics of kink folding and developed models of nucleation and growth of kinks. Geometric measures of kinks are shown on Figure 3-23.

The orientation and geometry of F3 kinks and related sinusoidal folds (see below) were analyzed in domains 7h5, 9, and 12, to determine the kinematics of this phase of folding and mechanism of kink formation and growth according to two simple models. The results are discussed in the following sections.

#### Domain 7h5

Slates of this domain (Chapter 2) are abundantly kinked (Figure 3-24). The kinks are continuous in places along their axial planes with sinusoidal folds in chert interbeds. The F3 sinusoidal have half-wavelengths of 0.5 to 2.0 meter. These larger folds contain smaller (by a factor of 10) coaxial kinks and(or) sinusoidal folds on their short limbs. The other main structure in this domain is a macroscopic F2a fold that divides domain 7h5 into subdomain 7h5a and 7h5b (Figure 3-18). Individual and intersecting S- and Z-shaped (down-plunge view) kinks are distributed geographically in different parts of these subdomains as shown on Figure 3-18.

Orientation data of S and Z kinks and related larger sinusoidal folds in subdomain 7h5a are plotted on Figure 3-24 and summarized on Figure 3-25. The hingelines of the Z-shaped kinks define a NW trending, moderately plunging maximum spread in a partial girdle that ranges

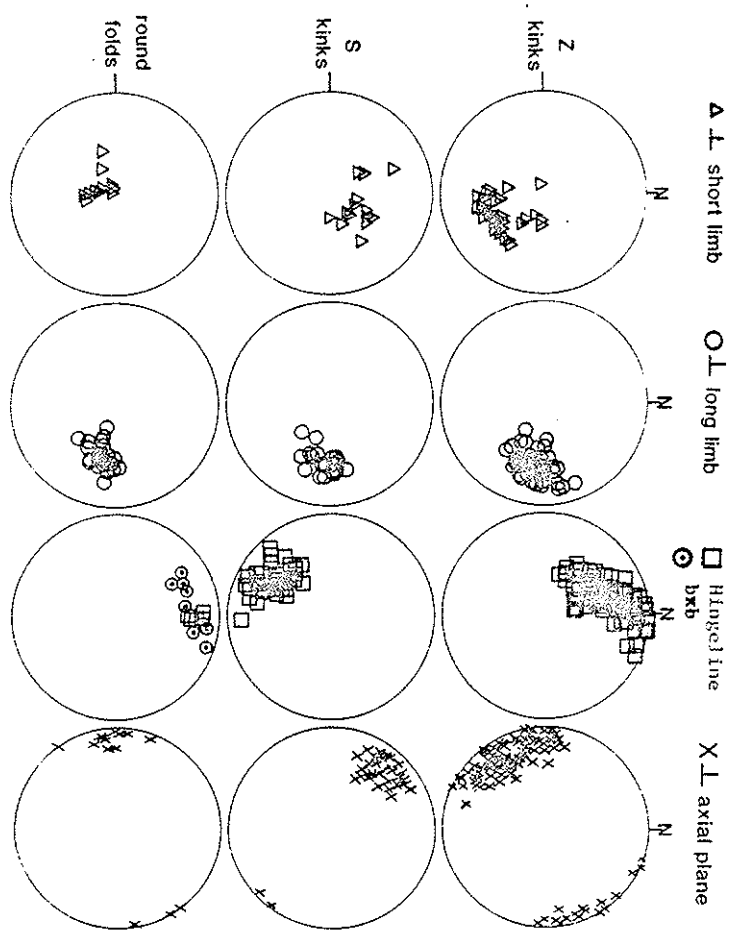


Figure 3-24. Orientation data of F3 folds in domain 7h5a.



Figure 3-25

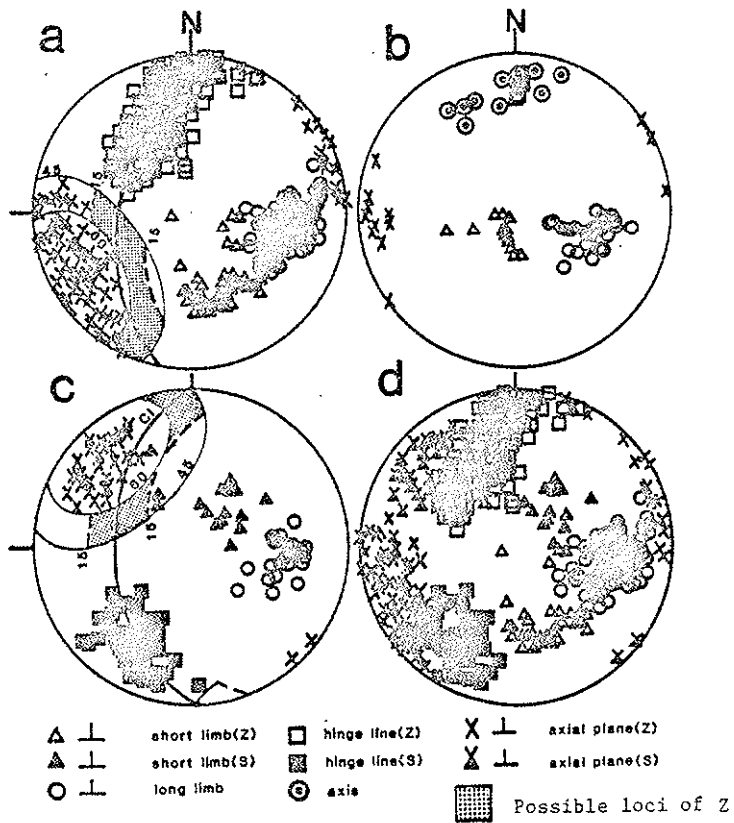
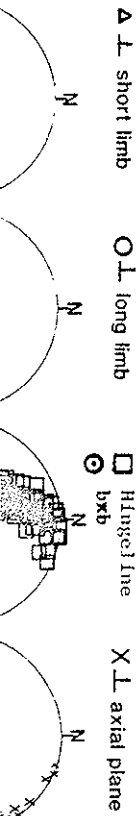


Figure 3-25. Summary fabric diagrams of (a) Z-kinks, (b) rounded folds, (c) S-kinks, and (d) all kinks in subdomain 7h5a.

between  $N25^{\circ}E$  and  $N75^{\circ}W$ . All sinusoidal folds in this domain have Z asymmetry and approximately the same orientation as Z kinks except for their short limbs. Hingelines of the S kinks define a SW trending, moderately plunging maximum on axial surfaces that generally strike NE and dip steeply SE. The long limbs are the only fabric element that are parallel among S and Z kinks.

NE and SE dipping kinks (Z and S kinks, respectively) do occur together in rare exposures as small as 1 square meter and are referred to as intersecting kinks (Figure 3-26b). Orientation data of six intersecting kinks in subdomain 7h5a is shown on Figure 3-26a. The average intersection of the S and Z kink planes is nearly perpendicular to the hingelines of both S and Z kinks. The fabric elements of the intersecting S and Z kinks are parallel to those of the S and Z kinks that occur individually (compare Figure 3-25d & 3-26a). The permissible range of the maximum principal compression (Z) responsible for the formation of the kinks can be approximated using the following procedure.

Maximum compression lies within  $5^{\circ}$  of the long limb cleavage for conjugate and between  $10^{\circ}$  and  $15^{\circ}$  for individual kinks, and  $45^{\circ}$  to  $65^{\circ}$  from the mean kink planes (Anderson, 1964; Patterson and Weiss, 1966; Donath, 1968; Ramsay, 1967; Kleist, 1972; Gay and Weiss, 1974). The loci of all lines  $45^{\circ}$  to  $60^{\circ}$  from the average kink planes define small circles centered at  $45^{\circ}$  to  $30^{\circ}$  about the poles to the kink planes. Similarly, the loci of lines that are  $0^{\circ}$  to  $15^{\circ}$  from the cleavage define small circles centered around the poles to these cleavages. These elements are plotted on Figures 3-25, 3-26, 3-28, and 3-32, and

domain have Z  
kinks except for  
SW trending,  
ally strike NE  
element that

ly) do occur  
d are referred  
of six inter-  
a. The average  
icular to the  
the intersect-  
kinks that occur  
sible range of  
formation of  
re.

cleavage for  
and 45° to 65°  
Weiss, 1966;  
s, 1974). The  
define small  
kink planes.  
the cleavage  
se cleavages.

d 3-32, and

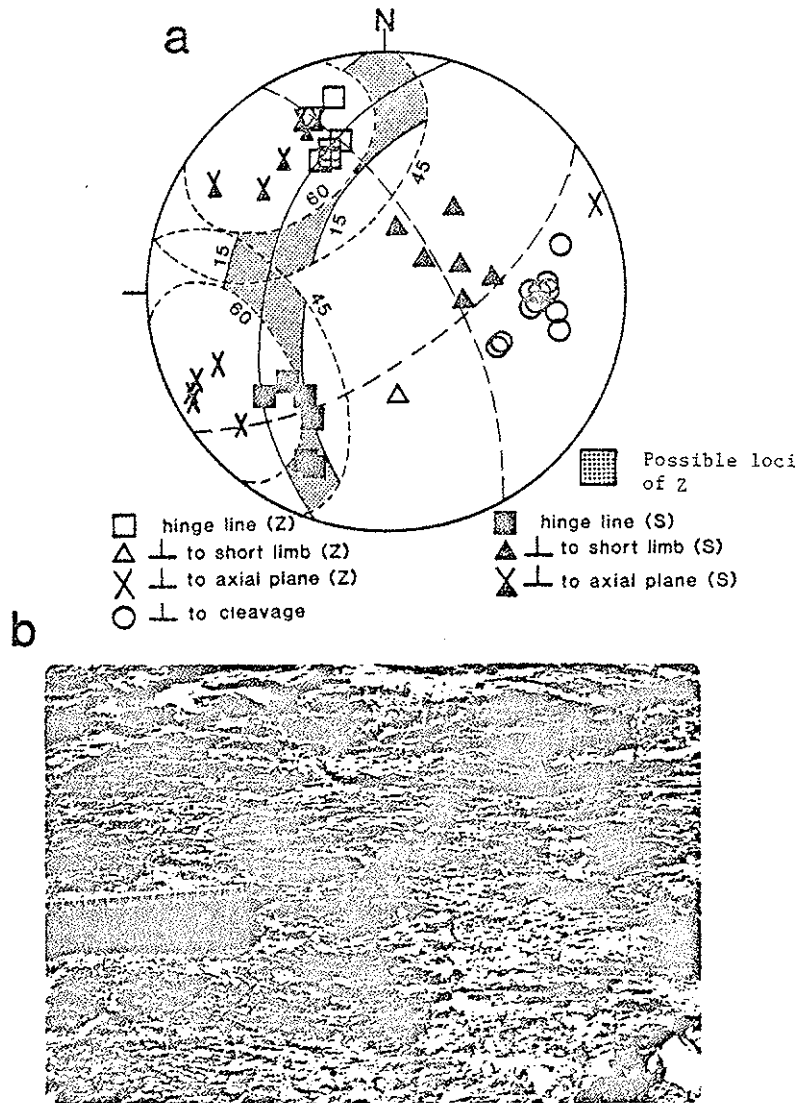


Figure 3 26 . Orientation and a picture of the intersecting kinks in domain 7b

the regions where both conditions are met are shaded to define possible positions of Z axis. In domain 7h5, the resolved Z axes plunge mostly SSW, W, and NNW for both the individual and intersecting kinks.

Figure 3-27 depicts the orientation of F3 folds in subdomains 7h5b1 and 7h5b2, on the east dipping limb of the F2a macroscopic fold in Ophir and Wisconsin Canyons (Figure 3-18). The orientation of an intersecting set and individual kinks and their corresponding fields of Z in subdomain 7h5b1, located at the hinge zone of the macrofold, are shown on Figure 3-28a. Here, the intersection of the S and Z kink planes of the intersecting set is close to cleavage and is subparallel to both the S and Z hingelines. Figure 3-28b plots the orientation data of S kinks in subdomain 7h5b2 where hingelines and axial planes of these kinks parallel those of the Z kinks in subdomain 7h5a (Figure 3-25a).

Kinks are differently oriented in the southern part of domain 7h5a compared to the rest of this domain (Figure 3-29). This distribution can be explained by deformation due to the latest motion along the Golconda thrust (see the Golconda thrust zone).

#### Domain 8

Kinks are oriented differently in this domain which is dominated by a well foliated sandstone and conglomerate (Figure 3-30). The southern part of this domain is close to the Golconda thrust (Figure 3-1), and includes F3 orientations with steep hingelines that may result from rotation as in the southern part of domain 7h5a. However, steep kink planes and cleavage are probably the reason for the steep plunge. This



to define possible  
axes plunge mostly  
ing kinks.

ds in subdomains  
a macroscopic fold  
orientation of an  
sponding fields of  
e macrofold, are  
f the S and Z kink  
d is subparallel  
ts the orientation  
d axial planes of  
n 7h5a (Figure 3-

rt of domain 7h5a  
This distribution  
on along the Gol-

ch is dominated  
3-30). The south-  
t (Figure 3-1),  
t may result from  
ver, steep kink  
teep plunge. This

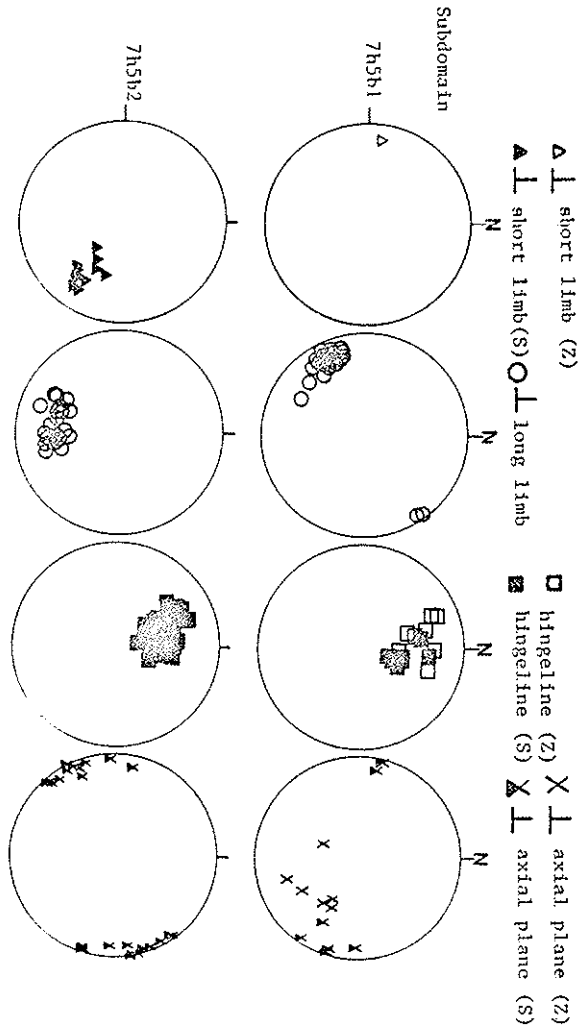


Figure 3-27. Orientation data of F3 folds in domain 7h5b.

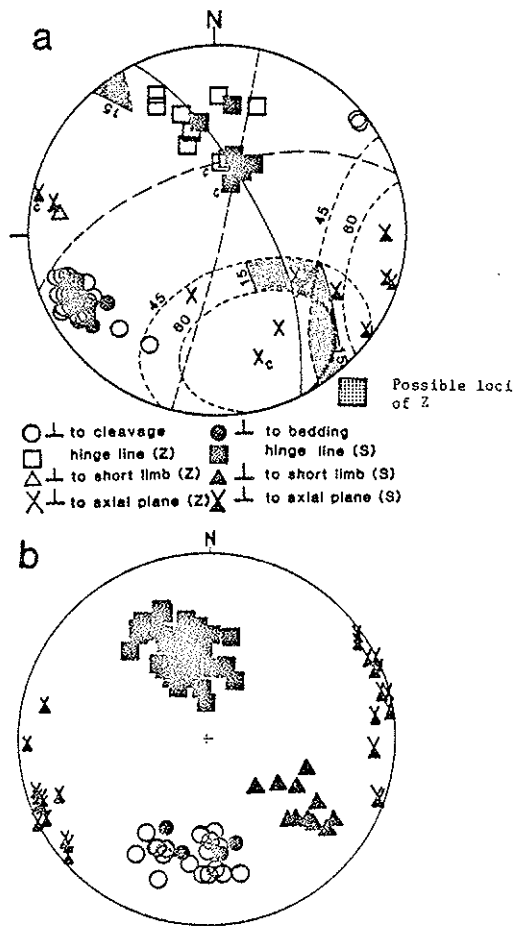


Figure 3-28. Summary fabric diagrams of F3 folds in  
 a) domain 7h5b1 and b) domain 7h5b2.

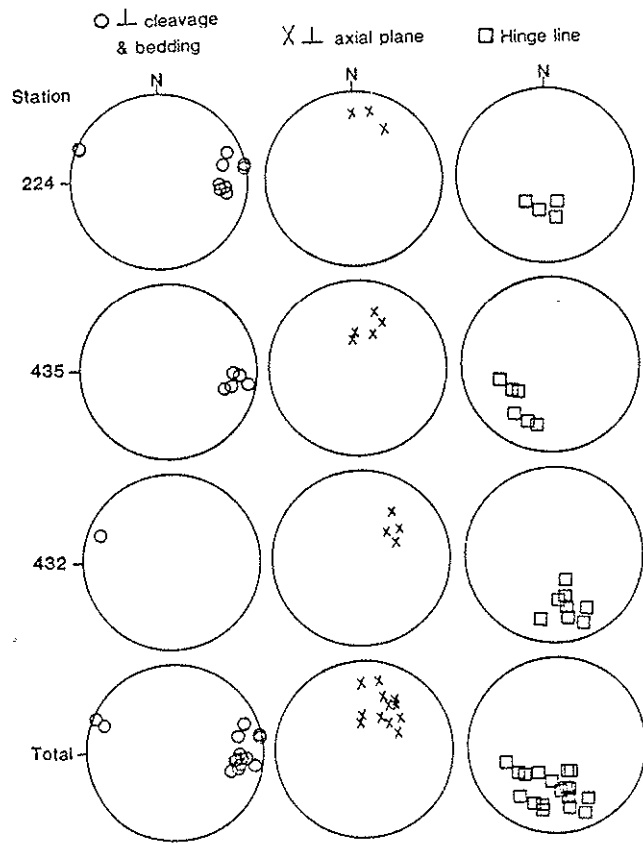


Figure 3-29. Orientation data of kinks in the southern part of domain 7h5a.

in

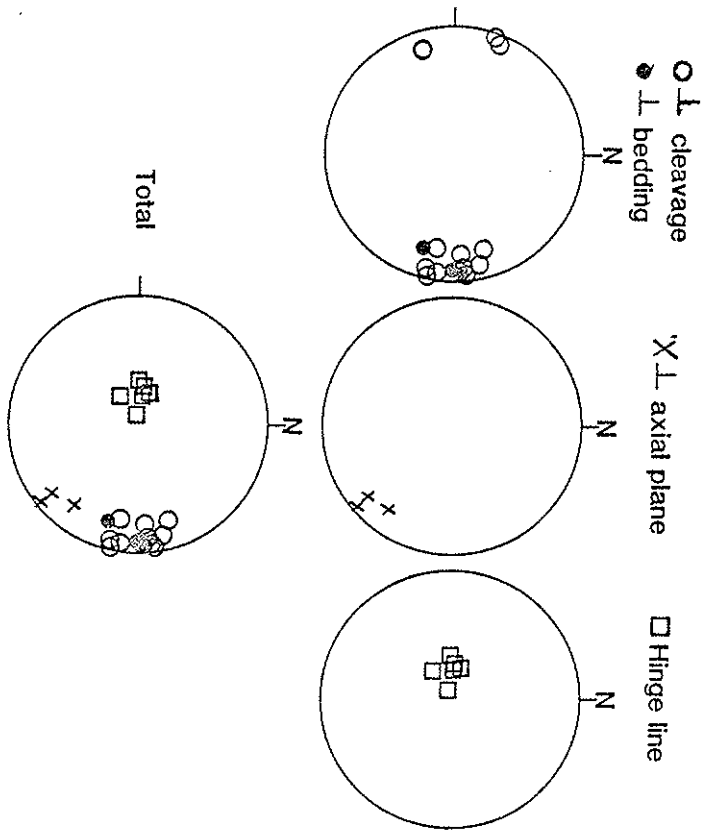


Figure 3-30. Orientation data of F3 folds in domain 8.

is a  
 orie  
 Doma  
 clea  
 sinu  
 not  
 S an  
 set  
 axes  
 axis  
 simi  
 symm  
 (Fig  
 fold  
 metr  
 nous  
 subd  
 have  
 SW (R  
 cleav  
 Discu

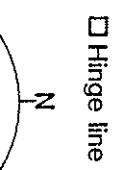
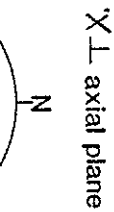
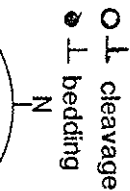
is supported by the fact that bedding and cleavage are not differently oriented close to the Golconda thrust from other parts of this domain.

#### Domain 12

The main structure of this domain is a NW striking vertical slaty cleavage that parallels bedding in chert (Figure 3-4). Kinks and minor sinusoidal folds in cleavage and bedding occur in this domain though not as commonly as in domain 7h5. Figure 3-31 shows the orientation of S and Z kinks and sinusoidal folds in domain 12. Figure 3-32a and 3-32b set out the orientation of intersecting kinks and their corresponding Z axes and of individual kinks at two locations in domain 12b. Here, Z axis is differently oriented compared to that in domain 7h5a but is similar to that in domain 7h5b1. The modal cleavage is approximately a symmetry plane with respect to all the fabric elements of S and Z kinks (Figure 3-32c). Comparing Figures 3-31 and 3-32, S and Z sinusoidal folds have identical orientation to the kinks with corresponding asymmetries, indicating, as in domain 7h5, that they were formed synchronously. The major difference compared to the intersecting kinks in subdomain 7h5a is that the intersecting S and Z kinks in domain 12b have parallel hingelines. S kinks in subdomain 12a plunge moderately SW (Figure 3-33) most probably because of different orientation of cleavage in this subdomain.

#### Discussion

Kinks have different attitudes in different domains. In domain 7h5, orientation of kinks is a function of their position relative to



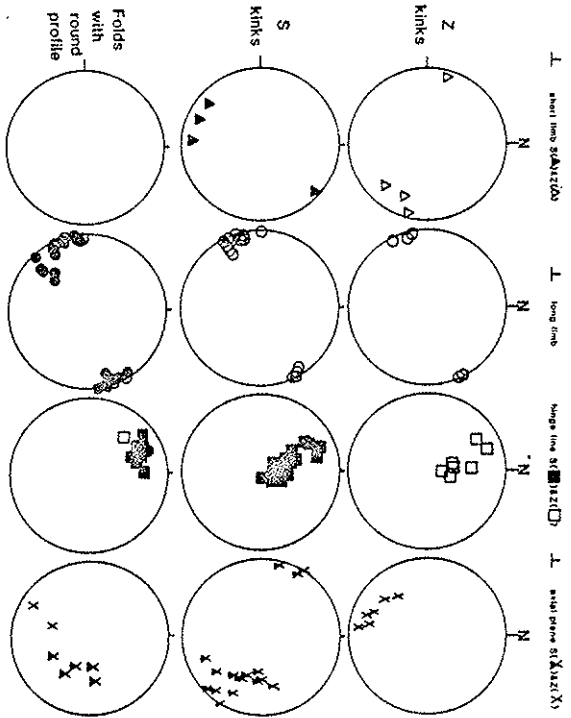


Figure 3-31. Orientation data of F3 folds in domain 12b.

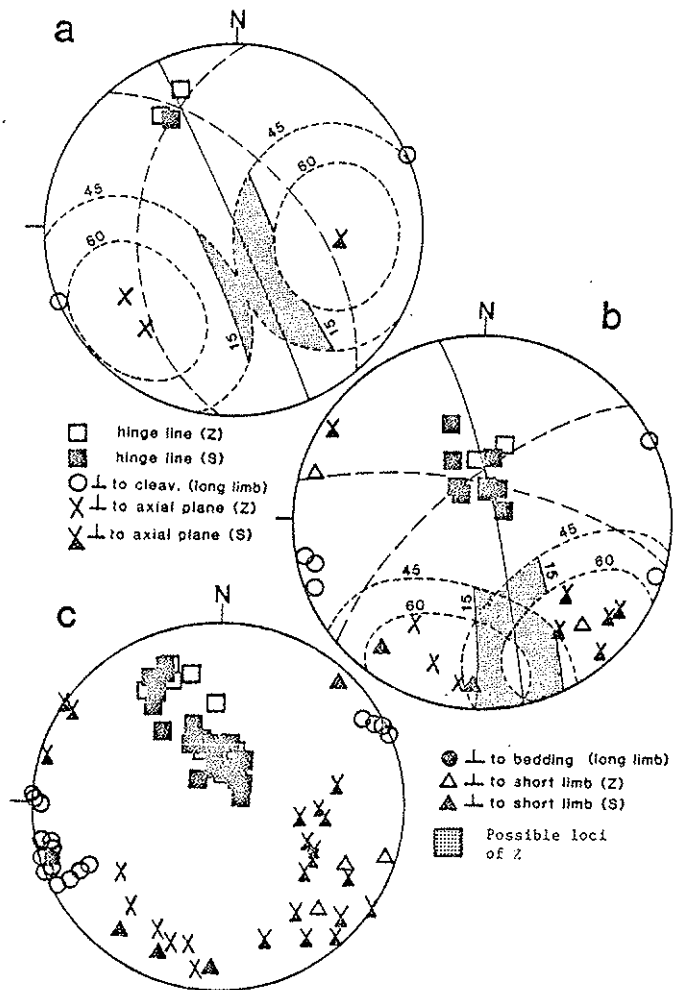


Figure 3-32. Orientation data of a) & b) intersecting kinks and c) all kinks in domain 12b.

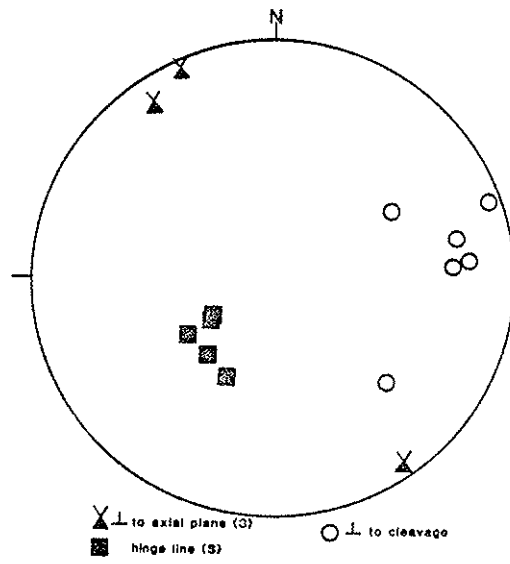


Figure 3-33. Orientation data of F3 folds in domain 12a.



106

the macroscopic F2a fold. In the lower limb of this fold, in domain 7h5a, orientation of the intersecting and individual kinks with corresponding asymmetries are identical, indicating that they are of the same generation. On the upper limb in subdomain 7h5b2, all the kinks are S-shaped and have nearly similar orientation as the Z-shaped kinks in domain 7h5a. The intersecting S and Z kinks in domain 7h5b1 have the same attitude as individual S and Z kinks. Here, S and Z hingelines are subparallel, and Z kink planes are differently oriented compared to those in domain 7h5a. The southern part of domain 7h5a is characterized by deformed kinks due to a latest motion along the Golconda thrust (see the Golconda thrust zone). Kinks in domains 12b and 7h5b1 have similar orientation in contrast to those in other domains of packet 12 and 7.

The following sequence of events becomes apparent from the analysis of shortening directions during kink folding in different domains. The parallelism of the shortening axes in the upper and lower limbs of the macrofold (domains 7h5b2 and 7h5a) indicates that kinks in these domains were formed simultaneously due to a westly plunging shortening after the macrofold was formed. This is supported by the incompatible sense of down-plunge asymmetry of kinks in both limbs if they are parasitic to the macrofold. During this phase of deformation, the orientation of cleavage in domain 7h5b1 and in packet 12 were at a high angle to shortening such that kinks could not be formed. A younger episode of N-S shortening generated kinks in the appropriately oriented cleavage in different domains. Southerly plunging shortening formed

107

conjugate kinks in domain 7h5b1 and packet 12 because it was at a low angle (less than  $15^{\circ}$ ) to cleavage in these domains. The northerly plunging shortening in this episode of kink folding resulted in cleavage-parallel slip in domain 7h5a as it was subparallel to the strike of the cleavage in this domain. This resulted in rotation of the axes and axial planes of the previously formed Z-kinks, probably by heterogeneous simple shear, as evidenced by the large dispersion of these fabric elements compared to the almost constantly oriented cleavage in this domain (Fig. 3-25a).

#### Geometric analysis of kinks

Two main models have been proposed for kink formation through experimental and theoretical work: Kink rotation (Donath, 1968; Clifford 1968; Rousell, 1980) and kink migration (Patterson and Weiss, 1966; Weiss, 1968; Gay and Weiss, 1974). In the following paragraphs these models are discussed, followed by analysis of the results of this study.

MIGRATION MODEL - According to this model (Figure 3-34a), kinks nucleate at a point or line and grow both parallel and normal to the kink plane. The orientation of kink plane relative to cleavage is fixed during growth, but their line of intersection migrates as kinks develop. Assuming no change of thickness of cleavage (flexural slip), angles  $\alpha$  and  $\beta$  remain equal and constant. Gliding on foliation in the kinked sector is the only mechanism of deformation. In terms of linear and angular parameters, this model requires  $\alpha = \beta$  and variable L for all the kinks.

was at a low  
s. The northerly  
ng resulted in  
parallel to the  
rotation of the  
ks, probably by  
dispersion of  
stantly oriented

mation through  
th, 1968; Clif-  
on and Weiss,  
wing paragraphs  
results of this

3-34a), kinks  
d normal to the  
o cleavage is  
grates as kinks  
lexural slip),  
oliation in the  
erms of linear  
variable L for

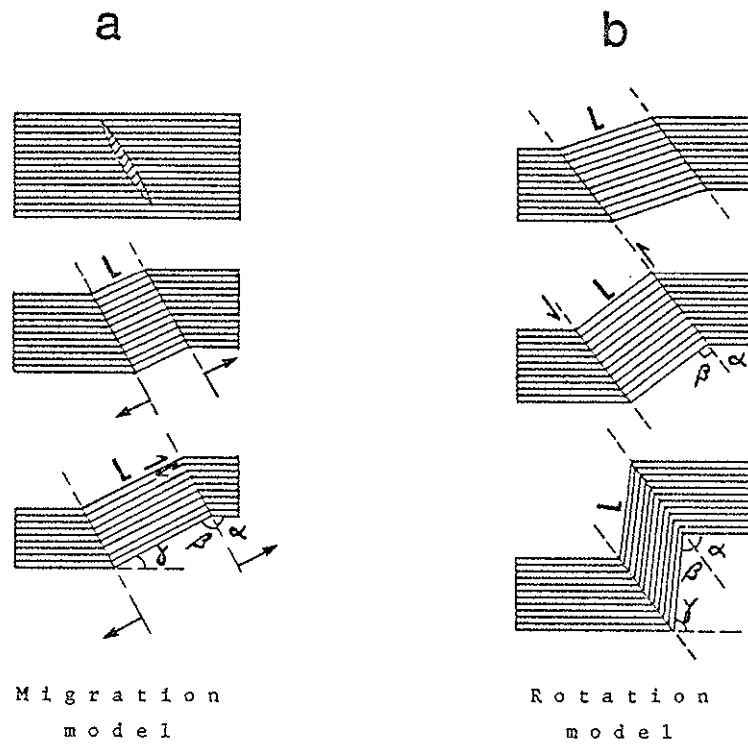
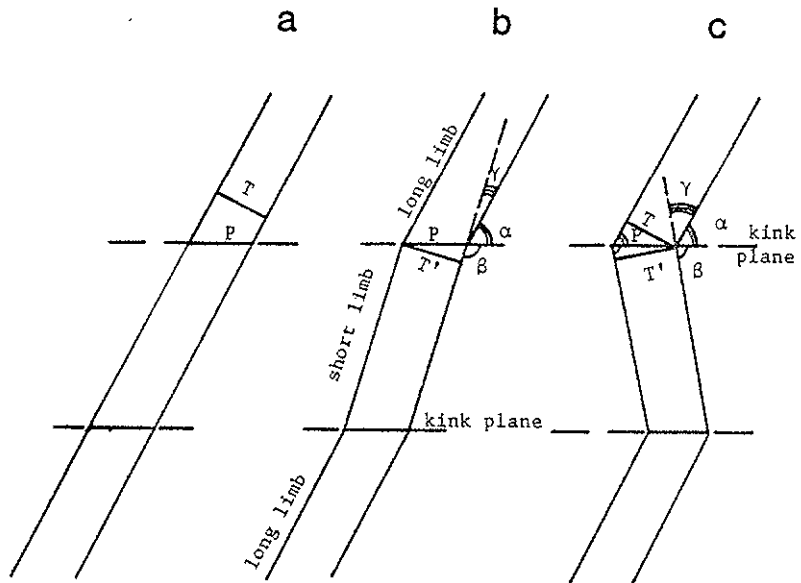


Figure 3-34 . Migration and rotation models for formation and growth of kinks



T = true thickness  
of cleavage on long  
limb.

P = thickness of  
cleavage parallel  
to kink planes.

$$\sin(\alpha + \gamma) = T'/P$$

$$T' = P \sin(\alpha + \gamma)$$

$\therefore T'$  is maximum  
when  $(\alpha + \gamma) = 90^\circ$ , that is  
when  $\beta = 90^\circ$ , where  
 $(\alpha + \beta + \gamma) = 180^\circ$

$$\sin \alpha = T/P$$

$$\sin \beta = T'/P$$

$$T/T' = \sin \alpha / \sin \beta$$

$\therefore T = T'$  only when  $\alpha = \beta$

(after Rousell, 1980)

Figure 3-35. Relationship between dilation ( $T'$ ) and angular parameters (a) and locking position (b) in a flexural slip model for a kink undergoing rotation. See text for explanation.

ROTATION MODEL - This model (Figure 3-34b, 3-35) assumes that the distance between kink band boundaries is fixed during deformation and that the short limb is hinged at the boundaries of kink bands and rotates. This leads to a decrease in  $\beta$  and an increase in  $\alpha$ . Several mechanisms such as gliding on cleavage, cataclasis, and dilation operate in the short limb. As long as the resolved shear stress along cleavage in the short limb is greater than frictional and cohesive resistance to gliding, rotation of the short limb continues. Cleavage in the short limb separates during rotation leading to dilation and dissolution of soluble minerals. Dilation, measured by increase of thickness in the short limb, is a sine function of angle  $\beta$  (Figure 3-35, Rousell, 1980), and thus is maximum when  $\beta$  has decreased to  $90^\circ$  (Figure 3-35b). Thereafter, thickness of the short limb decreases as  $\beta$  becomes less than  $90^\circ$  approaching the value of  $\alpha$  as rotation continues (Figure 3-35c). Assuming flexural slip, that is, slip between laminae in the short limb is the only deformation mechanism and the thickness of laminae in the long and short limbs remain equal, further rotation of kinks is not possible when  $\alpha = \beta$ , and the fold becomes locked (Figure 3-35c) (Verbeek, 1978; Rousell, 1980). Therefore constant  $L$ , variable  $\alpha$ , and  $\beta$ , and dilation in kinks characterize the rotation model.

#### Results

The distribution of all the parameters measured for kinks is shown on Figure 3-36 and 3-37. Among angles,  $\alpha$  has the lowest variation (Figure 3-36a),  $\gamma$  the highest (Figure 3-36c), and  $\beta$ , intermediate (Figure 3-36b).  $\alpha$  and  $\beta$  are equal for most of the folds since ( $\alpha = \beta$ )

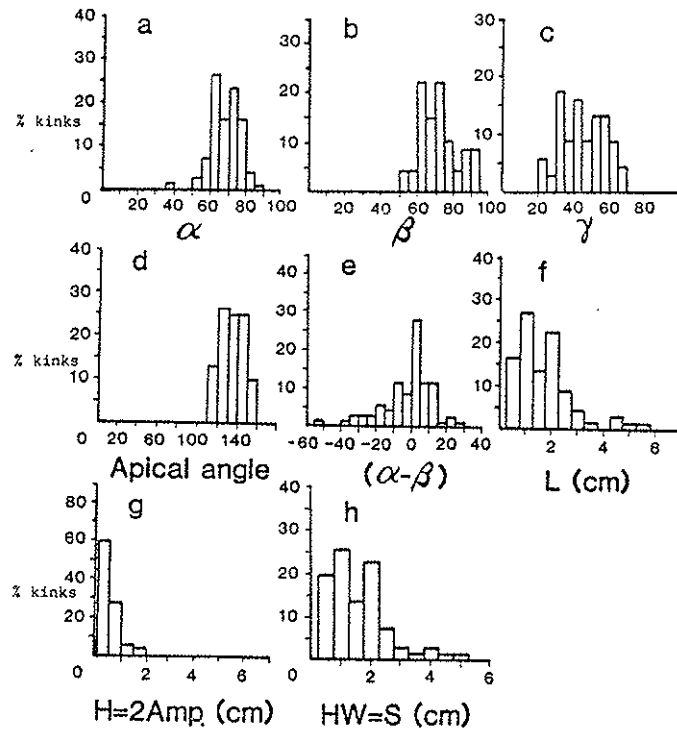
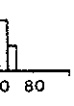


Figure 3-36. Distribution of linear and angular features of kinks in the study area.



n)

atures of

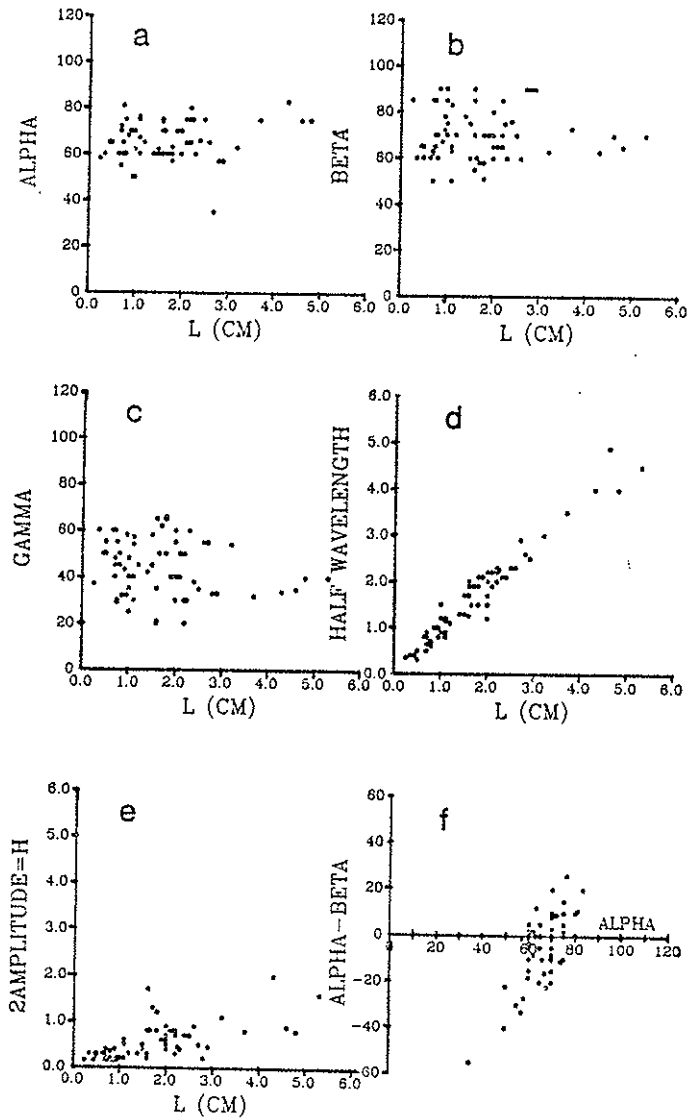


Figure 3-37. Relationships between geometric features of kinks,

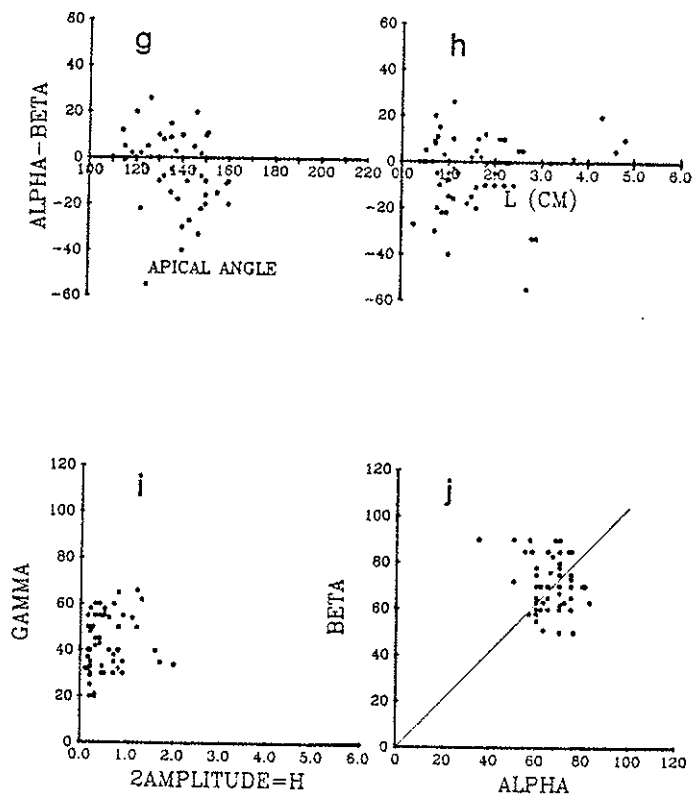


Figure 3-37 . cont'd



averages 0 (Figure 3-36e).  $\alpha$  is larger than  $\beta$  for kinks with L greater than 3 cm (Figure 3-37a, b), and they are about equal (i.e., kinks are symmetric) for kinks with L smaller than 3 cm (Figure 3-37a, b, h). As  $\beta$  decreases,  $\alpha$  increases until folds become symmetric. This pattern continues until folds become asymmetric with high  $\alpha$  and low  $\beta$  (Figure 3-37f, j).  $\gamma$  ( $180 - (\alpha + \beta)$ ) is very variable for kinks with L less than 3 cm and is less variable as L increases (for the given population) (Figure 3-37c).

L ranges between 0.25 and 5.75 cm (Figure 3-36f). Defining  $(\alpha - \beta)$  as a symmetry index for kinks, such that perfectly symmetric kinks have  $(\alpha - \beta) = 0$ , the kinks have high symmetry when  $\alpha$  is between  $60^\circ$  and  $80^\circ$  (Figure 3-36e and 3-37f). The symmetry is uncorrelated with the apical angle, suggesting that it can be achieved at any angle of  $\alpha$  and  $\beta$  (Figure 3-37g). The size of the kinks is shown on Fig. 3-36f, g, and h. All dimensions of kinks are less than 7 cm. Amplitude of kinks has a weak positive correlation with L (Figure 3-37e) and is constant for different values of  $\gamma$  (Figure 3-37i).

Joints parallel to kink planes cut discordantly across short limbs of kinks with  $\beta = 90^\circ$ . Very low amplitude small kinks also occur on the short limb of the kinks (Figure 3-38b).  $\alpha$  is variable for kinks with  $\beta = 90^\circ$  (Figure 3-37j). Kinks with  $\alpha = \beta$  have fine cracks on their long limbs close to the kink planes, possibly as incipient kink planes and indicating migration (Figure 3-34a) of kink boundaries by extending their short limb into the long limbs (Figure 3-34b). Thin sections made from small kink bands indicate high concentrations of iron oxides

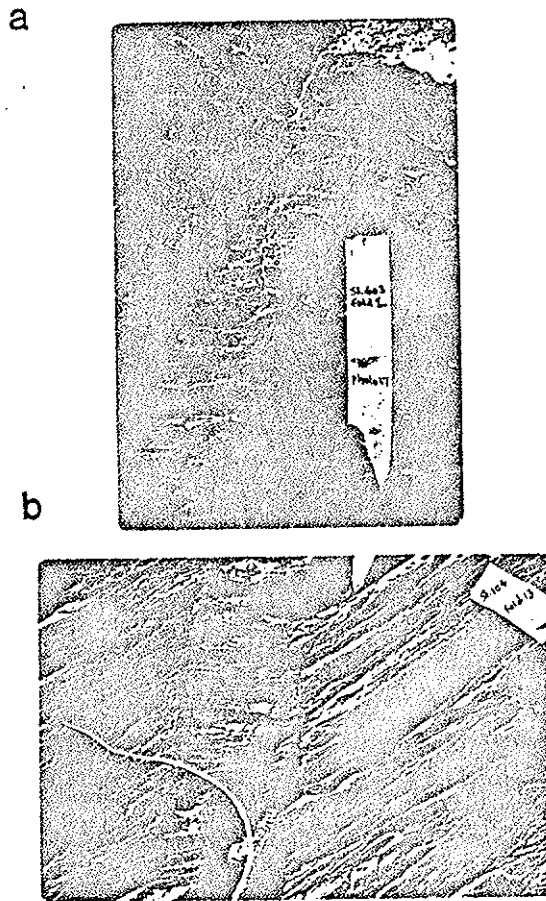


Figure 3-38. Photographs of kinks showing axial plane cracks and fractures, as well as small kinks in the short limb of kinks.

on the  
remov  
conve  
and a  
limbs  
tion  
model  
limbs  
the sl  
Incom  
area.  
two c  
differ  
Tector  
T  
immedi  
occur  
50 cm  
struct  
Figure  
three  
folds  
angles  
axial

on the short limbs, probably as residue after soluble minerals were removed due to dilation on this limb. Kink bands terminate both by convergence of kink boundaries and gradual decrease in amplitude.

Subequal  $\alpha$  and  $\beta$  for the majority of kinks of variable length ( $L$ ) and apparent lengthening of their short limb by extending into the long limbs (Figure 3-38a) probably support the migration model for nucleation and growth of the kink bands in the study area. However, this model can not explain the presence of the small kinks in the short limbs of the larger kinks when  $\beta=90^\circ$ , nor can it explain dilation in the short limbs. These can be better explained by the rotation model. Incomplete evidence of both models exists in the kinks of the study area. It is possible that different growth pattern described by these two or other models (see for example Verbeek, 1978), may operate at different times and conditions during progressive deformation.

#### Tectonic fabric at the Golconda thrust zone

This zone includes the basal part of packet 7 at Ophir Canyon, immediately above the Golconda thrust. Mesoscopic folds cut by faults occur at this area. The folds occur only adjacent (commonly less than 50 cm) to faults and are locally cut by them, suggesting that the two structures are either contemporaneous or that the fault is younger. Figure 3-39 shows the orientation of the folds and associated faults in three different locations in this zone. Although one is conjugate, folds have E and ENE vergence (Figure 3-39b). Axial planes are at low angles to the associated faults. The intersection of the faults and axial planes is subparallel to the hingelines at each location. Using



e cracks  
n the

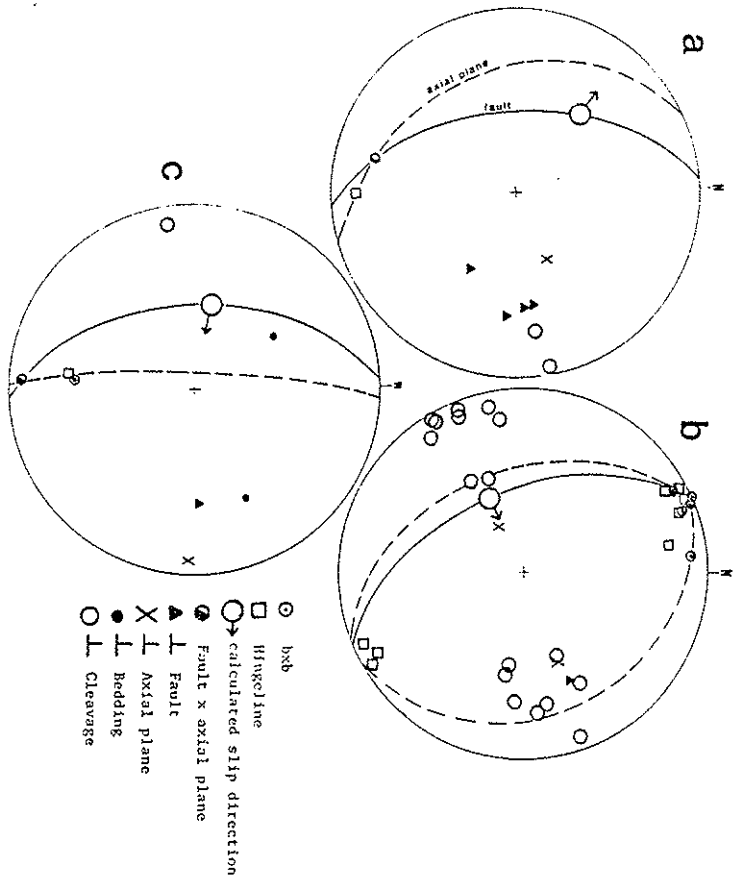


Figure 3-39. Orientation data of F4 folds and associated faults in the Golconda thrust zone.

the  
imat  
direc  
norma  
Golco  
tions  
moder  
block  
thrus  
rever  
these  
kinks  
Kinks  
howeve  
thetic  
the Go  
In th  
from t  
about  
cleavag  
gests t  
thrust.



the method of Figure 3-40, slip directions for these faults are approx-  
 118  
 imated assuming that the faults and folds are contemporaneous. The  
 directions trend westerly; two of these indicate thrust, and one is  
 normal. They are subparallel to some striations on the faults at the  
 Golconda thrust (Figure 3-41), supporting the validity of the assump-  
 tions of the model directions. Local faults at the Golconda thrust dip  
 moderately W. This and slip directions in them indicate that faulted  
 blocks moved both up and down relative to the west dipping Golconda  
 thrust in different parts of the thrust leading to both normal and  
 reverse faulting.

Kink folds occur in the Golconda thrust zone. The orientation of  
 these folds in the northern side of Ophir Canyon is about the same as  
 kinks in domain 7h5a farther from the thrust (Figure 3-24, 3-25, 3-42).  
 Kinks at the thrust zone in domain 8 and southern part of domain 7h5a,  
 however, have rotated attitudes (Figure 3-43a). Figure 3-43b is a syn-  
 thetic fabric diagram of a flexural slip model showing the effect of  
 the Golconda thrust on kinks at the thrust zone south of Ophir Canyon.  
 In this model, orientation of the S kinks in subdomain 7h5a, being far  
 from the thrust, is taken to be the initial attitude. These are rotated  
 about an axis parallel to the intersection of the axial planes and  
 cleavage in subdomain 7h5a and the Golconda thrust. The good fit sug-  
 gests that kinks are older than the latest reactivation of the Golconda  
 thrust.

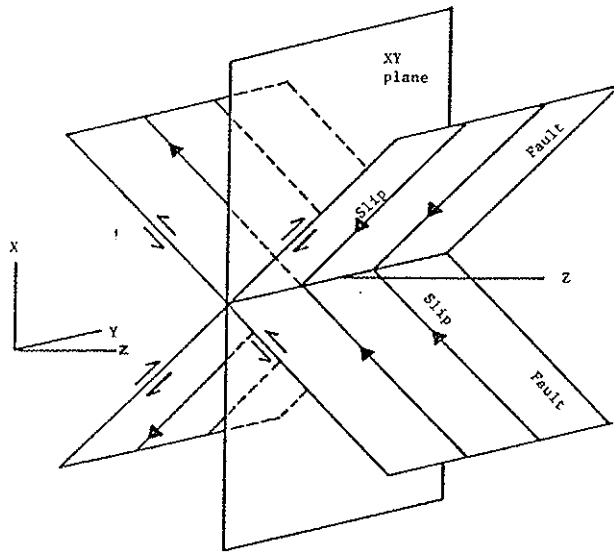


Figure 3-40. A method to determine slip direction using axial plane of a fold and associated fault.

Assumptions:

- 1) fold is formed during faulting
- 2) strain is plane such that both fault and axial plane are normal to the XZ plane.
- 3) the axial plane is normal to Z.

Procedure:

Slip parallels the intersection of the XZ plane and the fault.  
Slip direction is determined on the XZ plane assuming that the fault is formed at  $45^\circ$  to the Z axis.

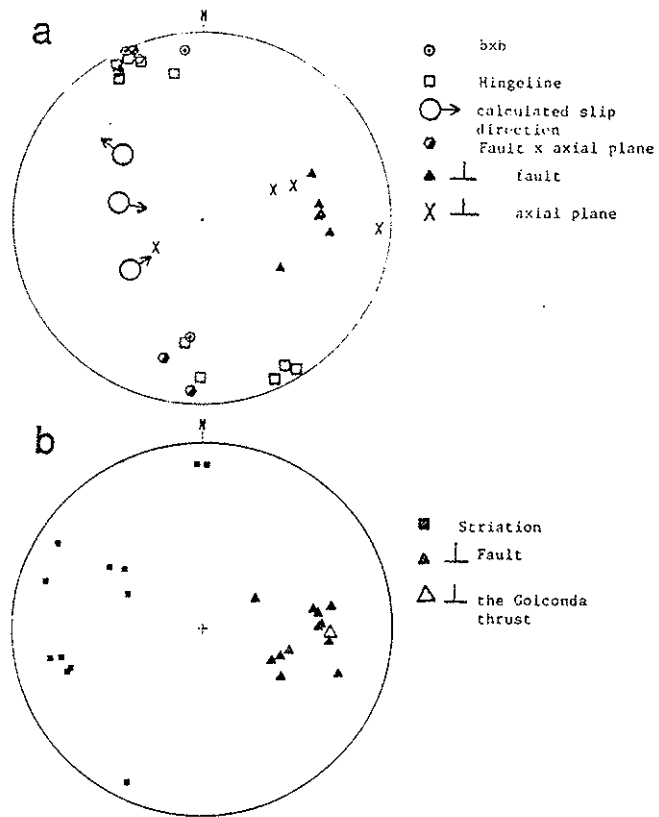


Figure 3-41. Orientation data of (a) folds and slip and (b) faults and striations in the Golconda thrust zone.

Assumptions:

1) fold is formed during faulting

2) strain is plane such that both

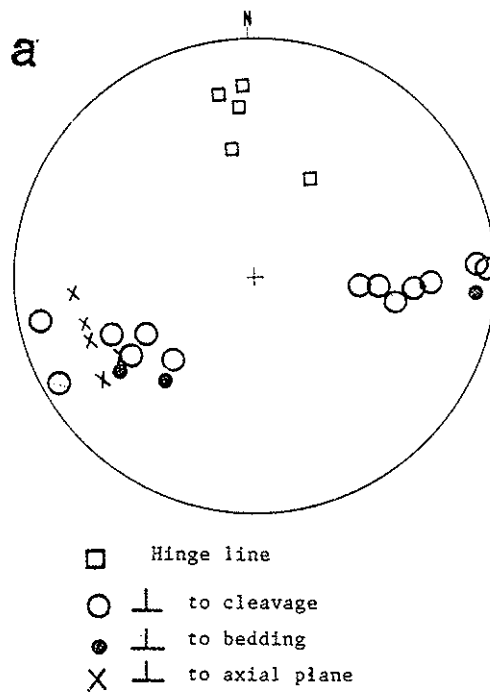


Figure 3-42. Orientation data of kinks in the Golconda thrust zone.



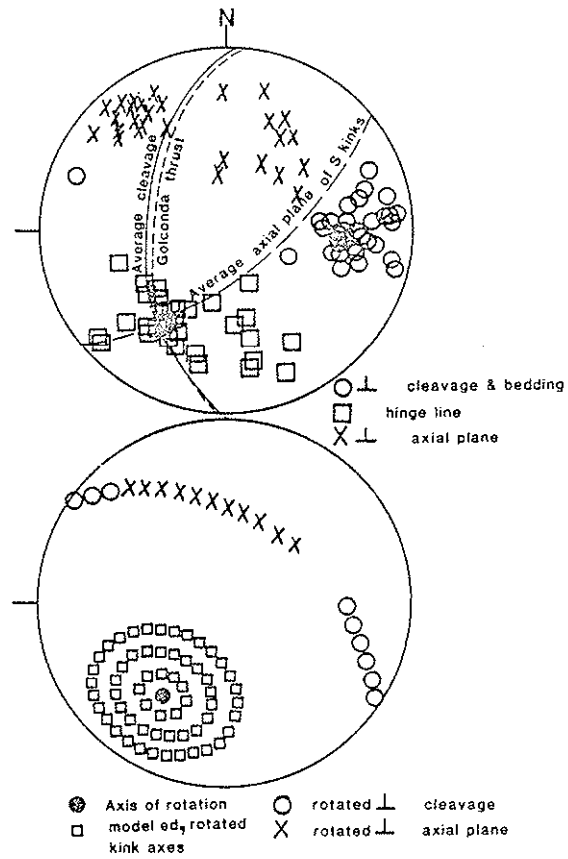


Figure 3-43. a) Orientation data of kinks south of Ophir canyon in the Golconda thrust zone, b) a model for their formation. See text for explanation.

Golconda

Tectonic fabric in packet 9

Packet 9 contains lower Paleozoic (?) rocks that are included in structural subdomain 9a, and upper Paleozoic (?) sedimentary breccia (t5) in subdomain 9b. The orientation of deformed tabular clasts in the sedimentary breccia in subdomain 9b is shown on Figure 3-44. These are oriented similar to bedding and cleavage in domain 9a in packet 9 and to those in upper Paleozoic packets of the Golconda allochthon. The lower Paleozoic (?) rocks in subdomain 9a contain tectonic fabrics which differ in part from those of subdomain 9b and other domains of the allochthon. Two generations of cleavage exist in domain 9a (Table 3-2, Figure 3-45, and 3-49): one (S1) is parallel to bedding and is penetrative, and the other is a sporadic and weakly developed spaced cleavage (S3) oblique to bedding and the first cleavage. The S1 cleavage is folded by chevron, conjugate, and other types of folds (F2a) and shows large variations in attitude. The folds have sharp to curved hinges, straight to curved limbs, and apical angles ranging between  $40^{\circ}$  and  $140^{\circ}$  (Figure 3-46a). The amplitudes and half-wavelengths of these folds range between 1 and 70 cm with a mode of less than 20 cm (Figure 3-46b,c).

Although there are not evident superposed folds, the variable orientation of the axes and axial planes of these folds indicates multiphase generation and (or) heterogeneous strain for the reason to be discussed. In areas of 20x20 meters, the orientation of all the fabric elements varies significantly. Two such exposures were studied in detail (stations 146 & 147) about 40 meters apart, and in each, piece-

DEFORMATION	FOLD	AXIAL PLANE	AXIS	FOLIATION	COMMENTS
D <sub>1</sub>	F <sub>1</sub>	Ap <sub>1</sub>	Ap <sub>1</sub> x S <sub>0</sub>	S <sub>1</sub>	isoclinal folds in bedding with axial plane slaty cleavage.
D <sub>2</sub>	F <sub>2a</sub>	Ap <sub>2a</sub>	Ap <sub>2a</sub> x S <sub>0</sub> Ap <sub>2a</sub> x S <sub>1</sub>		mesoscopic folds in bedding and cleavage (F <sub>2</sub> ).
	F <sub>2b</sub>	Ap <sub>2b</sub>	Ap <sub>2b</sub> x S <sub>0</sub> Ap <sub>2b</sub> x S <sub>1</sub>		homoaxial folding of F <sub>2a</sub> folds (F <sub>2b</sub> )
D <sub>3</sub>				S <sub>3</sub>	formation of spaced cleavage oblique to all other structures.

Table 3-2. Deformation events in the lower Paleozoic (?) packet 9 of the Golconda allochthon.

are included in  
 diminary breccia  
 lar clasts in the  
 e 3-44. These are  
 in packet 9 and  
 allochthon. The  
 tectonic fabrics  
 other domains of  
 domain 9a (Table  
 o bedding and is  
 developed spaced  
 cleavage. The S<sub>1</sub>  
 types of folds  
 ds have sharp to  
 angles ranging  
 half-wavelengths  
 less than 20 cm  
 , the variable  
 s indicates mul-  
 e reason to be  
 f all the fabric  
 ere studied in  
 in each, piece-

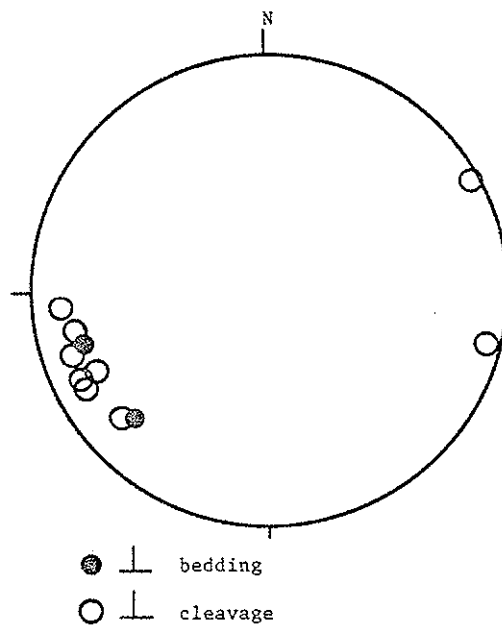


Figure 3-44. Orientation of tabular clasts and bedding in domain 9b.

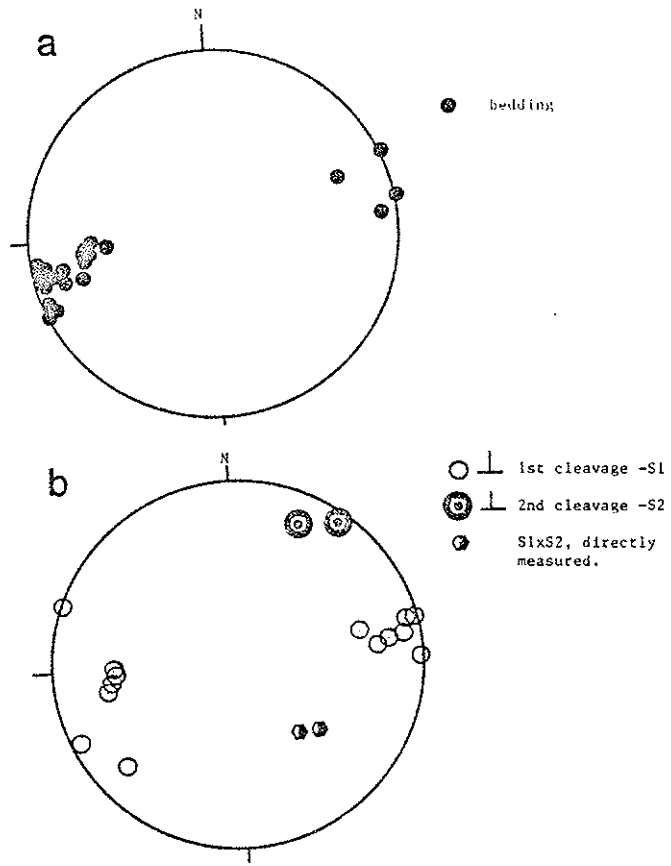


Figure 3-45. Orientation of (a) unfolded bedding and (b) unfolded  $S_1$  and  $S_3$  cleavages in domain 9a.

bedding

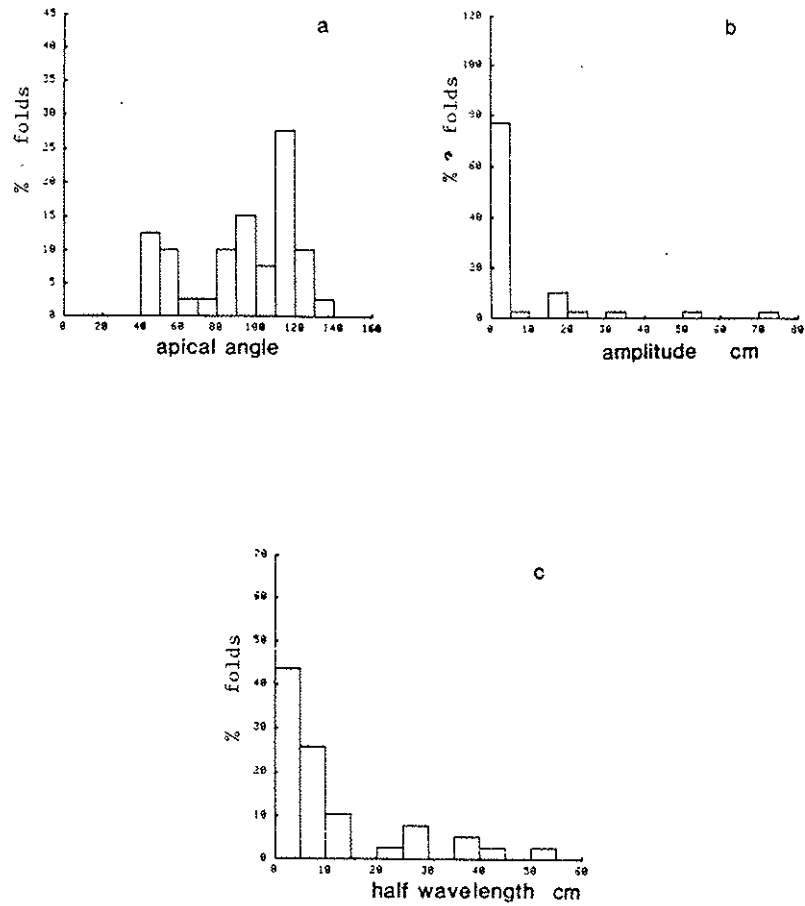


Figure 3-46. Distribution of (a) apical angle and size (b & c) of folds in domain 9a.

b

50 100 150 200  
tude cm

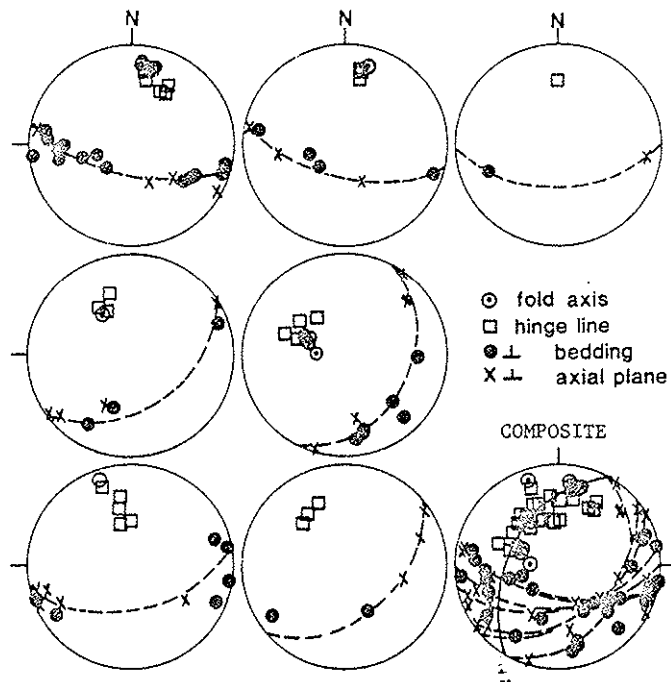


Figure 3-47 . Orientation of folds in station 146 of domain 9a.

and size

wise cylindrical folds were measured. Figure 3-47 shows the fold structures in different parts of station 146. In each position at this station, poles to bedding and axial planes lie on great circles with zonal axes parallel to the hingelines and axes of the folds. This suggests either nearly homoaxial refolding, fanning of the axial planes, conjugate geometry, or a combination of these. The continuous girdle of axial planes makes fanning and conjugate geometry unlikely. However, a perfect box was recorded at station 146, indicating that some folds may be conjugate. Folds with S and Z asymmetries occur with symmetric folds close to one another in distances of few meters at this station.

Orientation data of folds at station 147 are depicted on Figure 3-48. Here, the asymmetry of these folds varies in distances of 1 m. Hingelines plunge shallower and are oriented differently over a more continuous girdle compared to those at station 146. Axial planes, like 146, spread similar to bedding, though over different girdles.

At both stations, hingelines and fold axes of different asymmetries spread over their entire girdle. The composite diagrams (Figure 3-47 & 3-48) of all the folds at stations 146 and 147 show that the local bedding and axial plane girdles have nearly colinear intersection that parallel the normal to the girdle of the hingelines and axes in each station.

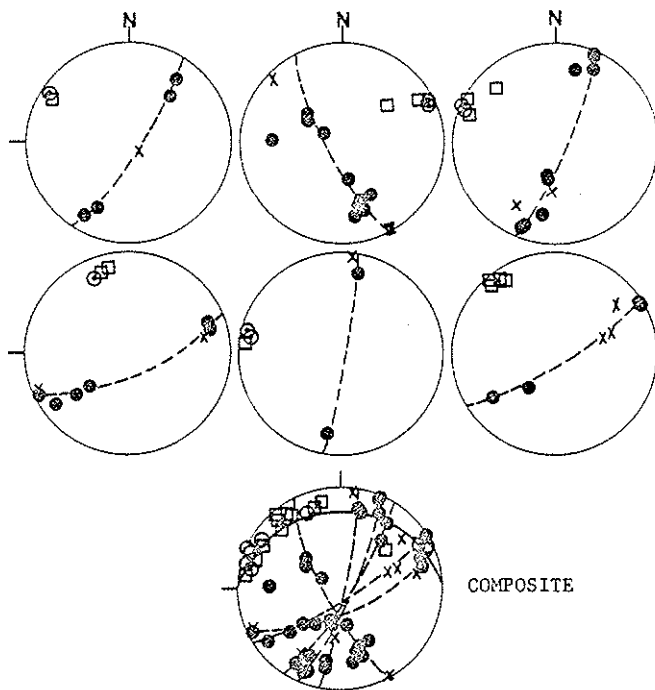
The tectonic fabric in packet 9 is different from those in upper Paleozoic packets because of 1) their deformed folds which except for the rotated F2b folds do not exist in the Golconda allochthon, and 2) their second generation spaced cleavage. The orientation of the S1



the fold struc-  
 tion at this sta-  
 tion at this sta-  
 circles with zonal  
 da. This suggest  
 planes, conju-  
 continuous girdle of  
 tely. However, a  
 at some folds may  
 with symmetric  
 at this station.  
 uted on Figure  
 distances of 1 m.  
 y over a more  
 ial planes, like  
 irdles.

different asym-  
 e diagrams (Fig-  
 47 show that the  
 ear intersection  
 s and axes in

those in upper  
 which except for  
 chthon, and 2)  
 tation of the Sl



- ⊙ fold axis
- hinge line
- ⊙ ⊥ bedding
- X ⊥ axial plane

Figure 3-48 . Orientation of folds in station 147 of domain 9a.

131

cleavage in packet 9 is similar to that of S1 cleavage in many upper Paleozoic packets. The spaced cleavage, S3, on the other hand, although subparallel to some S1 slaty cleavages in upper Paleozoic packets, is absent in these packets. It is quite likely that at least S1 cleavage in packet 9 is of pre-Golconda age, and formed by the deformation associated with the Antler orogeny, because it is parallel to isoclinal bedding in chert and limestone interbeds of probable early Paleozoic age.

The relationship of S1, S2, and S3 are schematically shown on Figure 3-49. S3 is about normal to both the hingeline girdles at stations 146 and 147 (Figure 3-45, 3-47, and 3-48), indicating that it was not formed with F2a fold and probably is the youngest structure in packet 9. Figure 3-49 explains: a) abrupt change in the asymmetry of the folds, b) curvilinear orientation of hingelines of the S and Z folds at different substations that when combined, display great circle distribution at both stations, and c) parallelism of bedding and S2 girdles.

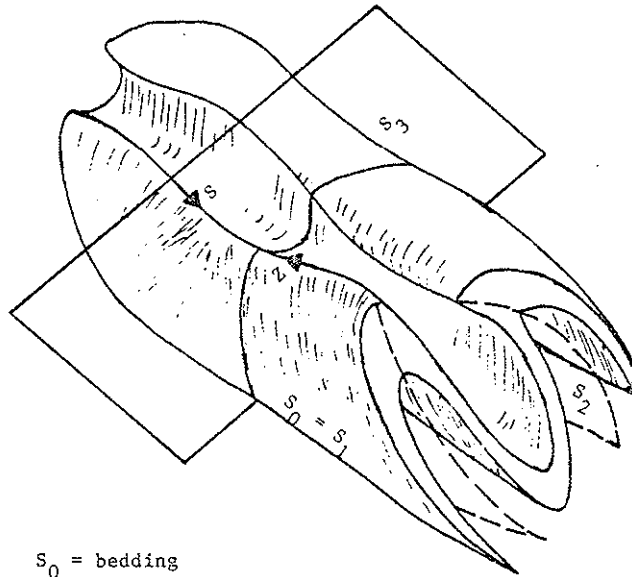
#### Tectonic fabric of the Diablo Formation (Pd)

The autochthonous Diablo Formation lies above deformed lower Paleozoic rocks and below the Golconda thrust in Last Chance, Ophir, and Wisconsin Canyons. The Golconda thrust above the Diablo is defined by the occurrence of carbonatized and fresh serpentinite and a sharp structural and lithological break. Unlike deformed beds immediately above the thrust, the Diablo Formation is homoclinal and is not affected by the microscopic F2a fold in Ophir Canyon (Figure 3-50). Foliation is the prevalent structure of Diablo and is defined by the

cleavage in many upper  
 other hand, although  
 Paleozoic packets, is  
 at least S1 cleavage  
 the deformation asso-  
 parallel to isoclinal  
 ble early Paleozoic

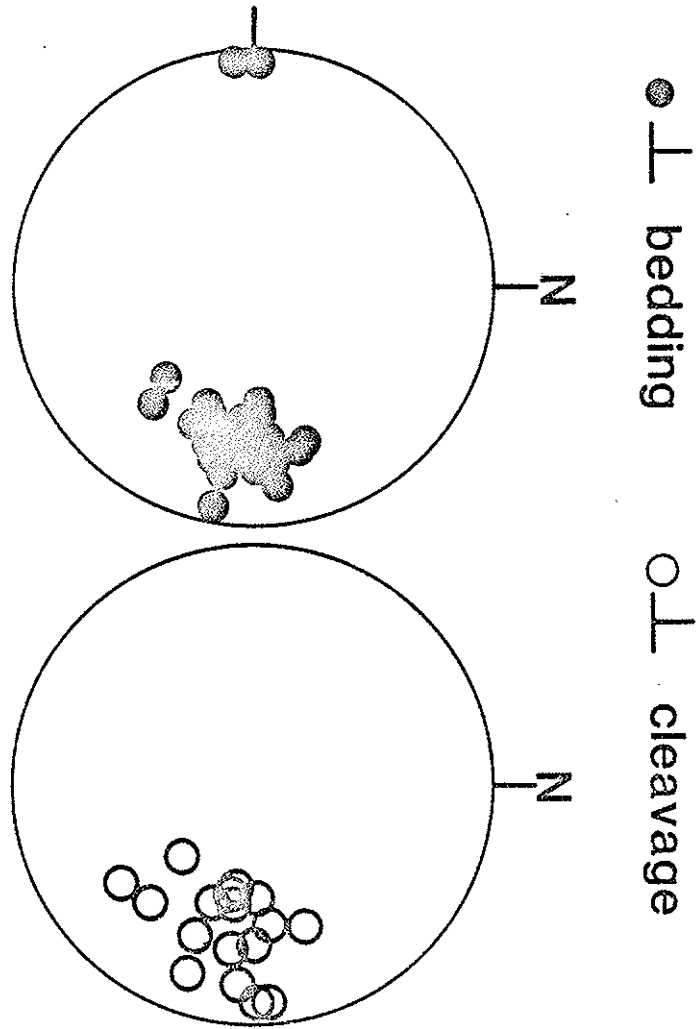
tically shown on Fig-  
 e girdles at stations  
 ing that it was not  
 t structure in packet  
 e asymmetry of the  
 the S and Z folds at  
 great circle distri-  
 ding and S2 girdles.

bove deformed lower  
 Last Chance, Ophir,  
 the Diablo is defined  
 entinite and a sharp  
 d beds immediately  
 moclinal and is not  
 yon (Figure 3-50).  
 nd is defined by the



- S<sub>0</sub> = bedding
- S<sub>1</sub> = slaty cleavage
- S<sub>2</sub> = axial plane of F<sub>2a</sub> folds
- S<sub>3</sub> = spaced cleavage
- S and Z are down plunge shape of folds

Figure 3-49. Schematic diagram showing the relationship between different structural elements in domain 9a.



134  
 preferred orientation of tabular clasts of chert that lie parallel and subparallel to bedding (Figure 3-50). The clast shape and orientation is tectonic because their tabularity parallels an anastomosing foliation in the matrix and because their aspect ratio is too great to be sedimentary. Bed are upright and dip W, the facing of which is recognized by graded and cross beds and erosional surfaces between chert conglomerate and calcarenite (Chapter 2).

Mesoscopic folds exist in the Diablo Formation. At the contact with pelites of packet 7 of the Golconda allochthon, a class 1B fold occurs in well-bedded fine-grained sandstones of the Diablo formation. Orientation data of this fold is given on Figure 3-51. The fold is isolated halfwave and exists only in the hanging wall and within 50 cm of a fault. Using the method described on Figure 3-40, slip direction on the fault is calculated. Because the resolved slip is perpendicular to the axial plane (Figure 3-51), the fold could not have formed during the faulting and rather is older as it is cut by the fault.

Disharmonic folds are common in the interbedded medium to coarse-grained calcarenite and fine to medium grained calcareous sandstones of the Diablo Formation on the southern side of Ophir Canyon. These folds are most probably soft sediment structures because they are single halfwaves which die out in less than a meter and are bounded by unfolded beds with depositional contact. Hingelines and axial planes of these folds are very much spread with no systematic distribution (Figure 3-52).

The strong foliation in the chert conglomerate of the Diablo For-

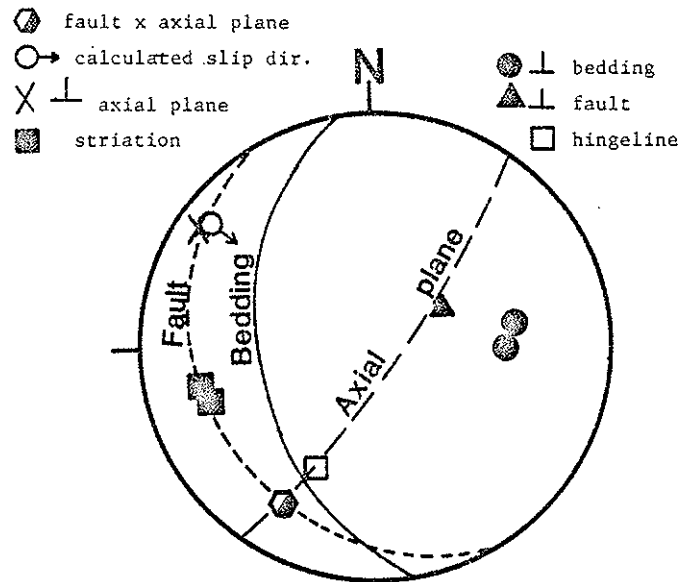


Figure 3-51. Orientation data of a fold and an associated fault in authochthonous Diablo Formation.

ding  
lt  
geline

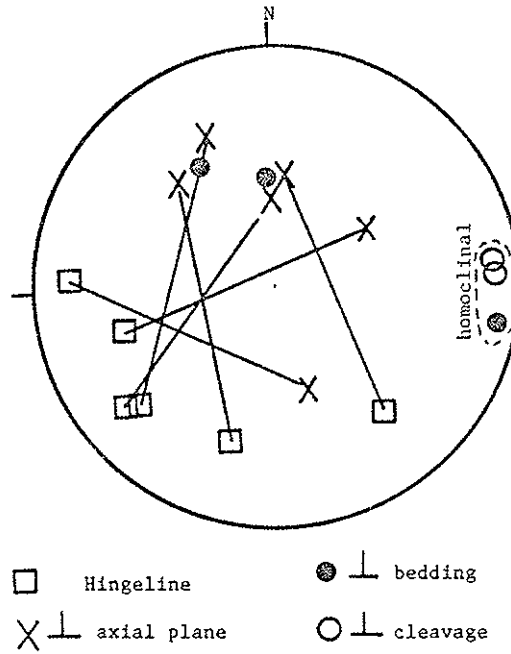


Figure 3-52. Orientation of disharmonic folds in Diablo Formation. Tie lines are between corresponding hingeline and axial plane of individual folds.

associated  
mation.

mation can be attributed to the emplacement of the Golconda allochthon or to intrusion of the Ophir pluton (Tgr). The rocks of the Diablo Formation are thermally metamorphosed as indicated by the presence of marbles. Although there is not an evident gradient in foliation development with respect to the Golconda thrust, the subparallelism of bedding, foliation, and the Golconda thrust and other faults (Figure 3-50 and 3-41b), favor the idea that foliation was formed after the allochthon was emplaced, most probably due to loading by the upper plate. An age younger than the Golconda thrust for the foliation is further suggested by its homoclinal attitude, in contrast to the intensely deformed allochthonous packets in the Golconda allochthon and underlying lower Paleozoic rocks. Although there is no clear increase in foliation development toward the pluton, younger intrusion of the Ophir pluton as the cause of formation of the foliation can not be ruled out.

#### Tectonic fabric of the autochthonous lower paleozoic rocks

Autochthonous lower Paleozoic rocks occur below the Golconda thrust and the Diablo Formation. They were at least deformed before deposition of the Diablo Formation. At Ophir and Wisconsin Canyons, tabular clasts in the lower Paleozoic sedimentary breccia form a foliation by their planar orientation. The foliation originated by flattening indicated by folds in quartz veins that have axial planes parallel to these clasts. Bedding and cleavage in these rocks are parallel and mostly dip shallowly to moderately W, SW, and NE, and strike between NE and NW (Figure 3-53). These planes have similar orientation to those in upper Paleozoic packets and in packet 9. Although only one bedding is



Golconda allochthon  
 of the Diablo For-  
 the presence of mar-  
 tian development  
 parallelism of bed-  
 dings (Figure 3-50  
 and after the allo-  
 chthonic upper plate.  
 This foliation is further  
 developed in the intensely  
 folded and underly-  
 ing increase in foli-  
 ation of the Ophir  
 cannot be ruled out.

rocks

show the Golconda  
 was deformed before  
 the Wisconsin Canyons,  
 which form a folia-  
 tionated by flatten-  
 ed planes parallel  
 to the bedding and  
 are parallel and  
 strike between NE  
 to those in  
 any one bedding is

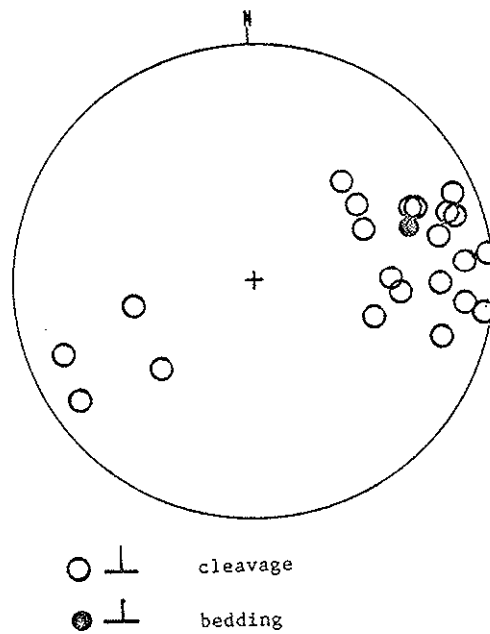


Figure 3-53. Orientation of bedding and cleavage in the  
 autochthonous lower Paleozoic rocks, east of  
 of the Golconda thrust

shown on Figure 3-53, bedding and cleavage are parallel in interbedded chert and pelite, and define probably isoclinal first folds. Bedding and cleavage are deformed by chevron folds in Summit Canyon. This, their early Paleozoic age, and the fact that they are unconformably overlain by homoclinal Diablo rocks, suggest a pre-Diablo age for these structures despite their similar orientation to the same fabric elements in the Golconda allochthon.

#### Introdu

Sl.  
 conda a  
 is defin  
 quartz a  
 parallel  
 cut by  
 chert g  
 have lar  
 tions is  
 grains  
 axial ra  
 foliatio

In  
 in parti  
 strain m

#### Theory o

Fin  
 deviator  
 orientat  
 is a c  
 ments, s  
 Ramsay,

el in interbedded  
 rst folds. Bedding  
 t Canyon. This,  
 are unconformably  
 ablo age for these  
 e same fabric ele-

### Introduction

Slates and thin sandstones of upper Paleozoic packets of the Golconda allochthon such as 7 and 12, include a penetrative foliation that is defined by planar orientation of micaceous minerals and flattened quartz and chert grains. The foliation is a D1 structure because it is parallel to the axial planes of F1 isoclinal folds and because it is cut by D2 thrusts and folded by F2 and F3 folds (Table 3-1). Quartz and chert grains are elliptical in sections perpendicular to foliation and have large axial ratio of up to 13. The average long axis in these sections is within 3° of the trace of the foliation. The alignment of the grains is interpreted to be at least partly tectonic because their axial ratios are too large on perpendicular sections and too low in foliation parallel sections to be sedimentary.

In this section, strain in general and strain of elliptical grains in particular are discussed, followed by a discussion of the results of strain measurement in the study area.

### Theory of strain of elliptical grains

Finite strain of a rock represents the sum of all incremental deviatoric strains, volumetric strains, and rotations that can vary in orientation and magnitude with each increment. Generally, deformation is a continuous process that includes a series of successive increments, superimposed non-coaxially in different stages (Flinn, 1962; Ramsay, 1967; Durney and Ramsay, 1973). In a grain-matrix system with

a well developed slaty cleavage, grains may have rigidly rotated and (or) changed shape during each increment of deformation.

All strain determinations in deformed rocks are based on using one or more of the following: 1) lines of known original length, 2) lines of known original relative length, and 3) initial angle made between intersecting lines (Ramsay, 1967). During deformation, both the length and angles between intersecting lines change. The change in length can be measured using extension (  $e$  ), defined by the ratio of the change in length and original length (Eqn. 3-1) (Ramsay, 1967, p. 52).

$$e = (l - l_0) / l_0 \quad (3-1)$$

where  $l$  is final length and  $l_0$  is the original length. Quadratic elongation (  $\lambda$  ), defined by Equation 3-2, is commonly used in strain studies for longitudinal strains.

$$\lambda = (l / l_0)^2 = (1 + e)^2 \quad (3-2)$$

Another measure of geological strain is logarithmic or natural strain which is defined by Equation 3-3.

$$\epsilon = \ln (1 + e) \quad (3-3)$$

A measure of change in angle is given by shear strain  $\gamma$ , defined by Equation 3-4,

$$\gamma = \tan \phi \quad (3-4)$$

where  $\phi$  is the deflection from perpendicular of two lines which were originally at  $90^\circ$  to one another.

To better visualize the geometric effects of strain, deformation of an original sphere with unit radius is considered in rocks. After strain, this sphere becomes an ellipsoid, the finite strain ellipsoid (Ramsay, 1967). The three principal axes of this ellipsoid define the principal longitudinal strains,  $(1+e_1) > (1+e_2) > (1+e_3)$ , with quadratic elongations  $\lambda_1 > \lambda_2 > \lambda_3$ .

In geological problems, unfortunately, the original length ( $l_0$ ) is unknown, and lines are generally not initially perpendicular, therefore, rather than actual extensions along the axis of the strain ellipsoid, their ratios are calculated. Volume change can not be computed also without actual extensions.

To calculate shape and orientation of the strain ellipsoid in deformed rocks, the common procedure is to calculate two dimensional sections of the ellipsoid (strain ellipse) on two or three sections of the rock and then combining them to find the three dimensional strain.

Among strain markers in rocks, the shape and orientations of deformed elliptical grains in slate, sandstone, and conglomerate have been used extensively to measure strain (Flinn, 1956; Hobbs and Talbot, 1966; Ramsay, 1967; Gay, 1968a,b, 1969; Hossack, 1968; Dunnet, 1969; Elliott, 1970; Dunnet and Siddans, 1971; Mukhopadhyay, 1973; Gay and Fripp, 1976; Mitra, 1976; Tobisch and others, 1977; Oertel, 1978; Chapman and others, 1979; Lisle, 1979). The question continuously arises as to whether the strain measured using these grains represent the bulk strain. The final grain shape after deformation depends on several factors: 1) initial grain shape, 2) initial grain orientation, 3) ductil-

ity contrast between grain and matrix, 4) orientation, amount, and axial ratio of deviatoric strain, 5) volumetric strain, and 6) incremental rotations. Methods designed for strain analysis are only capable to consider part of these factors and therefore involve some degree of uncertainty. The following is a brief analysis of these factors.

Initial shape - Sphere and ellipse are the two simplest shapes which are commonly assumed for grains in undeformed rocks. The only proof of initial shape is the existence of equivalent undeformed rocks and any assumption of original shape contributes an error. It is only for spherical grains, deformed homogeneously with their matrix, that the strain measured from the grains is the same as the bulk finite strain (Cloos, 1947, 1971; Ramsay, 1967; Elliott, 1970). However, strain markers are seldom originally spherical, and this is among the reasons why initial elliptical shapes are more frequently assumed and different techniques have been developed. Fortunately, there are some two dimensional methods, for example  $Rf/\phi$  and polar graph (Appendix I), that can estimate initial eccentricities of the grains. Others, such as method of Robin (Appendix I) work for grains of any shape. The error generated by ignoring original shape is large (Hossack 1968).

Initial grain orientation - The initial angle between the long axis of an elliptical grain and the finite deformation axes controls the eccentricity of the grains during deformation. In cases where the long axis of a grain is parallel or perpendicular to the long axis of the strain ellipse, the grain becomes longer or shorter, respectively, depending

amount, and  
and 6) incre-  
re only capa-  
ve some degree  
e factors.

shapes which  
only proof of  
ocks and any  
It is only for  
ix, that the  
finite strain  
strain mark-  
e reasons why  
and different  
me two dimen-  
I), that can  
uch as method  
error gen-

long axis of  
is the eccen-  
he long axis  
of the strain  
y, depending

on the axial ratio of the grain and strain ellipse (Ramsay, 1967; Elliott, 1970). On the other hand, if elliptical grains are at other angles to strain axes, they will deform both by rotation and change in shape (Gay, 1968a). Originally non-spherical grains can have either random or non-random orientations. Truly random orientations are rare in sedimentary rocks (Griffith, 1967; Elliott, 1970). Despite this, random orientation is assumed in many cases (e.g. Ramsay, 1967; Dunnet, 1969; Gay, 1969; Shimamoto-Ikeda, 1976; Robin, 1977). Original non-random orientations are more common and include linear (unimodal) and planar preferred orientations (Elliott, 1970; Dunnet and Siddans, 1971). Methods such as  $Rf/\phi$  and polar graph (Appendix I) have been designed to estimate the non-random distributions. The error contributed by ignoring initial orientation can be significant.

Ductility contrast between grains and matrix - Ductility is a measure of rheological condition of the deforming material and is approximately equivalent to the reciprocal of viscosity; more ductile materials are less viscous (Gay and Fripp, 1976). When the ductility of grains is less than that of the surrounding matrix, grains undergo a component of rigid body rotation during deformation of the grain-matrix system. This leads to superimposition of differently oriented incremental strains on grains that deform as they rotate (Ramsay, 1967; Gay, 1968a&b; Hossack 1968; Gay and Fripp, 1976). In this case, the bulk strain in the matrix may be irrotational and different from the strain in the grains. It is a common practice to assume that the ductility ratio of grains and matrix is 1, and therefore to take the grain ellipse as a

145

representative of the bulk strain ellipse. Gay (1968a&b) examined the behavior of non-rigid viscous elliptical grains during pure shear and circular grains during simple shear in a viscous matrix. He found that during pure shear, if the major axis of an elliptical particle and that of strain are not parallel, particles change shape and rotate toward the direction of extension (X), the rates of which decrease if viscosity ratio of particles and matrix (R) increased. Elliptical particles parallel to pure shear axes, only change their shape depending on the viscosity ratio (R); if  $R < 1$ , particle changes shape more rapidly than the pure shear strain ellipse; if  $R = 1$ , particle and strain ellipse are equivalent; if  $R > 1$ , particle changes shape more slowly than the strain ellipse. If circular grains are deformed by simple shear, they deform and rotate, simultaneously. Particles with low viscosity ratios need larger shear strain than the more viscous ones to become parallel to the X direction. More viscous particles rotate toward shearing direction quite rapidly.

Detrital rocks such as sandstone and conglomerate may contain one or more types of grains. Because different types of grains have different ductility with respect to the matrix, they will be strained and rotate differently. Incorporating shape and orientation of different grain types of one rock specimen during strain measurement can result in significant error if their ductility contrast is not taken into account (Gay, 1968a,b; Gay and Fripp, 1976). This problem is avoided by using grains of one type during measurement.

Volume change during strain - Rocks can undergo volume loss by



145  
examined the  
ure shear and  
He found that  
icle and that  
otate toward  
se if viscos-  
al particles  
ending on the  
rapidly than  
train ellipse  
ly than the  
e shear, they  
cosity ratios  
come parallel  
ard shearing  
  
contain one  
ins have dif-  
strained and  
of different  
can result  
ot taken into  
is avoided by  
  
ume loss by

146  
compaction, migration of solid and pore water, and densification, which  
can occur before or during deformation. Volume change is caused by the  
mean normal strain, that is, the non-deviatoric component of strain.  
Ramsay (1967), Ramsay and Wood (1973), and Wood (1974) have demon-  
strated that volume losses of up to 20% or more may be involved in the  
deformation of lithified and unlithified rocks, respectively. Deforma-  
tion plot is a two dimensional representation of the strain ellipsoid  
on an orthogonal coordinate system with  $\ln \left( \frac{1+e_2}{1+e_3} \right)$  as abscissa  
and  $\ln \left( \frac{1+e_1}{1+e_2} \right)$  as ordinate (e.g. Figure 3-67) (Flinn, 1962;  
Ramsay, 1967; Ramsay and Wood, 1973). Spheres plot at the origin and  
ellipsoids at the positive quadrant of the plot. If no volume change  
occurred during strain, the line of unit slope, passing through the  
origin of the plot, separates constrictional from flattening ellip-  
soids, or in other words, ellipsoids which have their intermediate axis  
contracted or expanded, respectively. However, if volume change did  
occur, this line no longer separates the two field, and rather divides  
fields of apparent flattening below from the field of apparent con-  
striction above it.

Comparing the densities of slate ( $2.7 - 2.85 \text{ gr/cm}^3$ ) and mudstone  
( $2.1 - 2.75 \text{ gr/cm}^3$ ) that slates derive from, Ramsay and Wood (1973) and  
Wood (1974) evaluated the significance of volume loss during formation  
of slaty cleavage. Wood (1974) places an upper limit of 10% for the  
volume loss during formation of slate and shows that only small errors  
are involved in ignoring volume change of this magnitude. However, he  
mentions that if volume changes exceed 20% they must be considered. In

rocks such as pelite and sandstone, matrix, being generally more compactable than grains, suffers a higher volume loss during deformation.

Orientation, amount, and axial ratios of deviatoric strain - The final axial ratio of elliptical grains in deformed rocks ( $R_f$ ) is a function of their initial axial ratio ( $R_i$ ), deviatoric strain axial ratio ( $R_s$ ) and orientation with respect to the long axis of the grains ( $\phi$ ) as indicated by Equation 3-5 (Dunnet, 1969, Eqn. 16).

$$\cos 2\phi = \frac{R_i (R_f^2 + 1)(R_s^2 + 1) \pm 2 (R_i^2 + 1) R_s R_f}{R_i (R_f^2 - 1)(R_s^2 - 1)} \quad (3-5)$$

Equation 3-5 is applied to calculate strain axial ratio in methods of two dimensional strain analysis such as  $R_f/\phi$  (Appendix I) using final axial ratios and orientations of elliptical grains for given initial grain ratios.

Incremental rotations - At any successive stage during progressive deformation, the principal axes of incremental and finite ellipsoids are generally non-parallel except when deformation is irrotational. This leads to superimposition of incremental distortion and rotation over the established finite strain at that increment (Ramsay, 1967, 1976; Ramsay and Graham, 1970; Durney and Ramsay, 1973). The final shape of grains embedded in a rock undergoing a progressive deformation is affected by the rotations and distortions at each increment. Grains elongated during previous increments may be contracted in later stages of strain depending on incremental rotation (Ramsay, 1967, p. 114).

erally more com-  
ng deformation.

ain - The final  
) is a function  
ial ratio ( $R_s$ )  
e grains ( $\phi$ ) as

$(R_s^2 - 1) (3-5)$

in methods of  
k I) using final  
given initial

ng progressive  
nite ellipsoids  
irrotational.  
on and rotation  
(Ramsay, 1967,  
973). The final  
ive deformation  
ement. Grains  
n later stages  
7, p. 114).

### Errors

Most of the strain methods are two dimensional and are used on thin sections, polished surfaces, photographs or natural surfaces in the field. For thin sections, the errors depend on: 1) the accuracy of reading the ocular scale and therefore determining length of the long and short axes of the grains; although it is their ratio which is used, the long and short axes, being independently measured, can involve certain error, 2) the accuracy of reading the angle between the long axis of the grains and a reference line (e.g. the trace of cleavage), 3) non-perfect ellipticity of the grains, leading to inaccuracy of reading their sizes, 4) grain population, as it might not be statistically enough to represent the whole rock, 5) the error involved in each of the two dimensional strain methods regarding the validity of their assumptions. In three dimensional methods, the major errors result from misorientation of the sectional planes and the errors involved in these methods because of the uncertainties concerning their basic assumptions.

### Strain measurement in the study area

Strain was measured from specimens in packet 7 and 12 of the allochthon because they contain slates and sandstones with elliptical strain markers and include identical rock types at different structural positions relative to the Golconda thrust (Figure 2-1, 3-1, 3-54). The objective was to detect a deformation gradient if one exists. Oriented samples were collected from locations shown on Figure 3-54 where kinks or other young structures are absent except for specimen OS10 where the

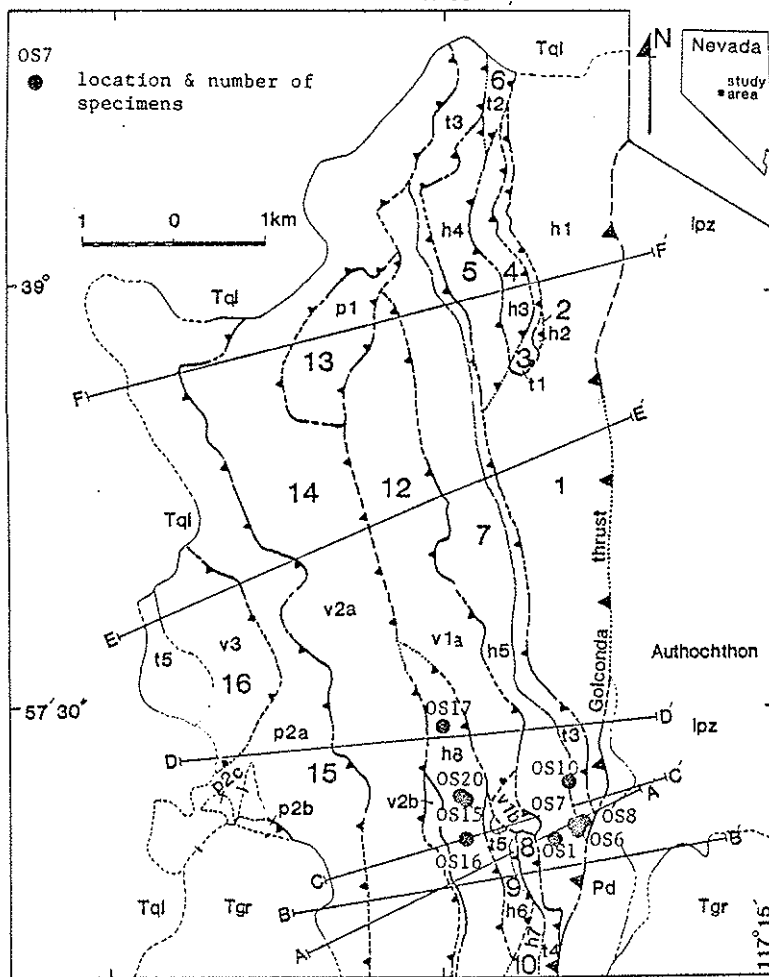


Figure 3-54. Map showing the location and number of oriented specimens for strain analysis.

effect  
 analysis  
 and hing  
 packets.  
 closures  
 Thi  
 detect  
 are almo  
 were the  
 and the  
 were pl  
 thin sec  
 cleavage  
 pendicul  
 the lon  
 between  
 ocular  
 grain as  
 of the  
 the grid  
 methods  
 number o  
 represen  
 ured on



oriented

effect of an F2a fold on D1 structures was the objective of the analysis. Other D1 structures besides the slaty cleavage are boudins and hingelines of F1 folds in the interbedded chert and pelite of these packets. The specimens were taken from the planar regions where F1 fold closures are absent.

Thin sections were first cut parallel to the cleavage in order to detect the existence of microscopic lineations. Because grain shapes are almost equant in these planes, three other oriented thin sections were then made perpendicular to the cleavage, two normal to one another and the third at about  $45^\circ$  to them. The orientations of the sections were plotted on a stereogram and the intersections of the cleavage and thin sections were determined (Figure 3-55 & 3-56). The trace of cleavage or an arbitrary line was taken as reference in sections perpendicular or parallel to the cleavage, respectively. The length of the long and short axes of individual elliptical grains and the angle between the long axis and the reference line ( $\phi$ ) were measured using an ocular micrometer and a mechanical stage. Rf was calculated for each grain as the ratio of its long and short axes. For systematic coverage of the whole thin section and avoiding repetition, the survey followed the grid of the mechanical stage. Because all the two dimensional methods used are statistical (Appendix I), they require a minimum number of grains to be measured for their shape and orientation to represent finite strain. In this study, the number of the grains measured on thin sections ranges between 70 and 108.

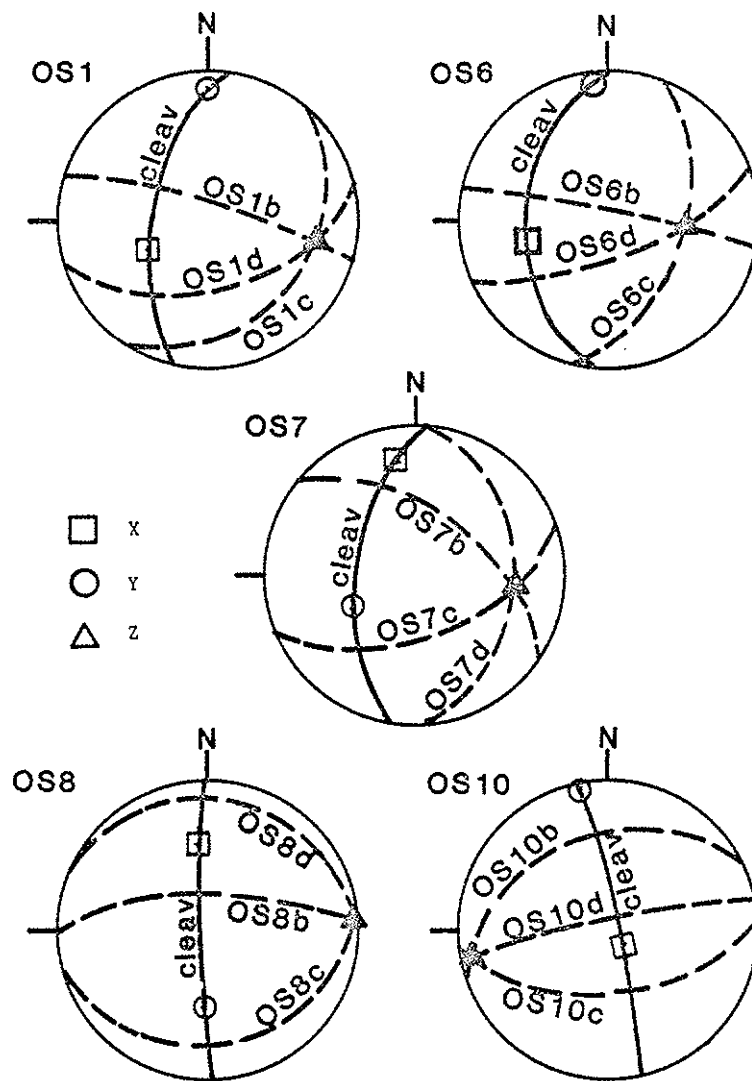


Figure 3-55 . Orientation of thin sections and calculated principal strains in the oriented samples in packet 7. Dash lines are thin sections.



culated  
mples  
tions.

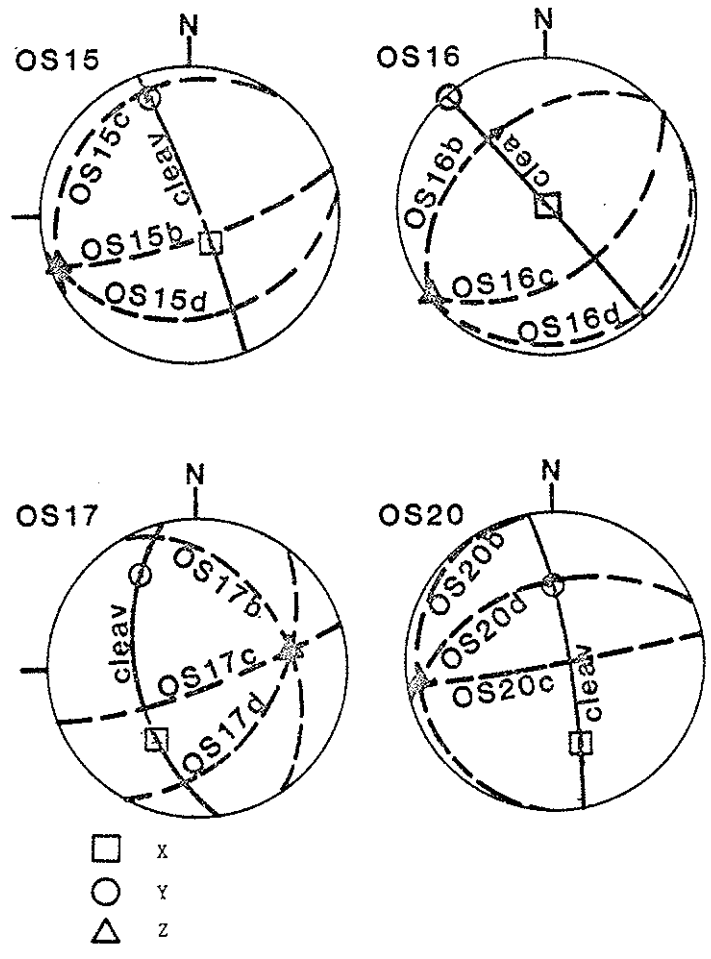


Figure 3-56. Orientation of thin sections and calculated principal strains in the oriented samples in packet 12. Dash lines are thin sections.

Several methods have been developed to calculate two dimensional rock strain ratio given dimensions and orientation of elliptical grains. The ones used for this study can be categorized into two groups: I and II. The methods of both groups are described in Appendix I, and for simplicity, they are referred to by letters A through H. Group I methods use arithmetic, geometric, and harmonic means of grain axial ratios and the slope of a best fit line on a long/short axis plot to estimate strain ratio. The methods of group I do not take into account the strain controlling factors mentioned in the previous section and assume that grains were initially spherical and therefore provide a less valid approximation to the actual rock strain than those of group II. They, nevertheless, are simpler and faster to measure compared to group II, and among them, the harmonic mean yields high quality results and therefore are used in this study. Group II methods, on the other hand, include more sophisticated algebraic, graphic, and statistical methods. Some of these are capable of evaluating the initial shape and orientation of the grains (Appendix I). Assuming that the results of group II methods are more accurate, the error in estimating the principal strains by methods of group I can be measured relative to the strain ratio determined by the methods of group II using Equation 3-6 (Lisle, 1977b).

$$\% \text{ Error} = (\text{slope or mean} - R_s) / R_s \times 100 \quad (3-6)$$

where mean or slope is the result of any of the group I methods, and  $R_s$



te two dimensional  
ation of elliptical  
egorized into two  
described in Appendix  
ers A through H.  
onic means of grain  
long/short axis plot  
p I do not take into  
the previous sec-  
and therefore pro-  
strain than those of  
ter to measure com-  
yields high qual-  
roup II methods, on  
, graphic, and sta-  
luating the initial  
Assuming that the  
error in estimating  
easured relative to  
p II using Equation

(3-6)

p I methods, and Rs

is the strain ratio determined by methods of group II. The % error is used to assess the quality of the results of group I and to find a relationship between methods of the two groups.

Because each method takes different assumptions and provides different results, all were used for each of the 34 thin sections that were made from 9 specimens in packets 7 and 12. The objective was to elucidate the effect of the assumptions involved in each method, evaluate the two dimensional strain by choosing the best results, find the errors of group I methods with respect to the more exact methods of group II, and approximate original shape and orientation of the grains.

### Results

Table 3-3 sets out the results of all the methods for the 34 thin sections. A typical long versus short axis plot provided by method A is shown on Figure 3-57. Because grains have finite size, a best fit line through the data points can not have an intercept and therefore is forced to pass through the origin as shown on this diagram. The slope of this line is used in method A to estimate strain axial ratio. In general, the short and long axes of quartz grains in slate specimens range between 0.003 and 0.112 mm, and 0.017 and 2.6 mm, respectively. The chert grains in sandstones have their short and long axes in the range between 0.028 and 1.2 mm, and 0.07 and 5.88 mm, respectively. For all the grains there is a good linear correlation between their long and short axes as is defined by  $r$ , the coefficient of goodness of linear correlation (Appendix I), indicating that the grains originally had almost constant initial axial ratio ( $R_i$ ) and orientation.  $r$  is

Arith. mean	Group I			Group II (Rs)				Rf/φ	r		θ
	Geo. mean	Harm. mean	Slope	Robin	Shim. Ikeda	Tobisch	Holst		Linear coeff.	Ri	
3.16	3.03	2.91	2.76	2.90	2.91	2.96	2.72	2.72	.96	1.45	7.63
3.21	3.06	2.94	2.73	2.78	2.79	2.92	2.69	2.79	.96	1.59	-2.20
3.34	3.16	2.98	2.76	2.74	2.74	2.91	2.68	2.72	.96	1.81	1.51
2.14	2.03	1.95	1.86	1.49	1.48	1.51	1.42	1.50	.96	1.89	.77
3.86	3.48	3.18	2.62	3.21	3.25	3.35	2.85	3.03	.93	1.73	.77
3.38	3.06	2.81	2.35	2.62	2.63	2.80	2.50	2.56	.93	1.90	-2.64
3.95	3.62	3.32	2.93	3.36	3.34	3.49	3.16	3.17	.93	1.71	7.19
2.15	2.08	2.00	1.90	1.50	1.50	1.43	1.47	1.60	.97	1.87	3.75
3.81	3.54	3.27	3.10	3.29	3.21	3.39	3.08	3.27	.93	1.72	-0.78
3.31	3.04	2.79	2.52	2.79	2.81	2.92	2.69	2.69	.91	1.67	8.17
3.80	3.48	3.17	3.03	3.15	3.14	3.31	3.01	3.07	.90	1.78	5.93
2.18	2.12	2.06	2.09	1.63	1.60	1.67	1.58	1.86	.98	1.81	-0.61
4.63	4.26	3.94	4.22	3.82	3.85	4.09	3.69	3.59	.88	1.78	-3.26
3.61	3.31	3.06	3.29	3.07	3.08	3.18	2.89	2.71	.88	1.70	1.91
4.49	4.27	4.04	3.90	3.88	3.87	4.12	3.71	4.04	.95	1.65	3.89
2.07	1.97	1.87	1.75	1.28	1.25	1.30	1.23	1.37	.95	1.97	1.86
3.23	3.28	3.11	2.98	2.85	2.85	2.96	2.72	2.83	.96	1.59	3.11
3.58	3.35	3.16	2.99	3.13	3.13	3.23	2.94	2.96	.94	1.58	.75
3.53	3.37	3.22	3.18	3.16	3.17	3.27	2.97	3.22	.95	1.51	.06
2.52	2.35	2.21	2.15	1.53	1.47	1.59	1.49	1.51	.94	2.23	-1.26
3.14	2.93	2.75	2.61	2.59	2.58	2.71	2.50	2.70	.94	1.74	8.66
3.72	3.43	3.16	2.85	3.03	3.00	3.21	2.92	3.01	.93	1.81	-10.43
3.48	3.23	3.02	2.71	2.81	2.77	2.97	2.23	2.72	.93	1.83	-7.16
2.65	2.48	2.34	2.19	1.62	1.55	1.69	1.58	1.59	.94	2.27	-1.04
3.25	3.02	2.83	2.64	2.66	2.63	2.79	2.54	2.58	.94	1.76	11.68
3.47	3.23	2.99	2.75	2.75	2.72	2.94	2.70	3.10	.93	1.92	-1.65
2.91	2.71	2.52	2.40	2.29	2.25	2.39	2.20	2.16	.93	1.87	2.11
2.58	2.48	2.38	2.24	2.08	2.06	2.17	2.01	2.08	.94	1.73	-5.04
3.52	3.25	3.02	3.01	2.71	2.69	2.94	2.70	2.87	.92	1.94	2.37
3.20	2.99	2.82	2.75	2.54	2.53	2.72	2.50	2.42	.94	1.80	-0.96
2.79	2.51	2.30	2.28	1.18	1.25	1.11	1.22	1.25	.93	2.70	-2.26
4.25	3.73	3.29	2.98	3.14	3.14	3.42	3.11	3.64	.87	2.13	2.74
3.89	3.45	3.08	2.72	3.15	3.17	3.31	3.01	3.28	.91	1.83	3.31
3.31	2.98	2.73	2.61	2.63	2.69	2.80	2.55	2.58	.89	1.78	1.29

Table 3-3. Results of two-dimensional strain analysis for 34 thin sections.



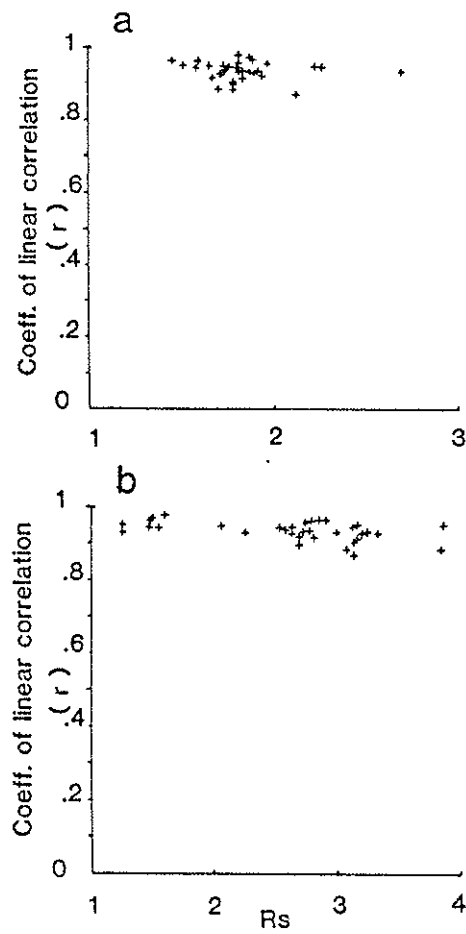


Figure 3-58. Relationship between  $r$ , the coefficient of linear correlation with  $\bar{R}_i$  and  $R_s$ .

ind  
gra  
3-3  
1.5  
(App  
59.  
(App  
indi  
an e  
not  
and  
3-60  
Corr  
great  
with  
betwe  
decre  
mean,  
deter  
avera  
deter  
it i  
diffe

independent of  $R_s$  and average  $R_i$  (Figure 3-58). The majority of the grains have mean initial axial ratio ( $R_i$ ) between 1.7 and 1.9 (Table 3-3). However, it is common for individual grains to have  $R_i$  less than 1.5 (e.g. Figure 3-60).

An example of the polar graphs in strained and "unstrained" states (Appendix I), plotted using polar graph method, is shown on Figure 3-59. The distribution on this graph can be described as heart shaped (Appendix I). Delta and heart shaped initial polar graph distributions indicative of initial unimodal grain distribution are common, whereas an elliptical distribution indicative of initial random distribution is not common in the thin sections studied. Typical graphs of  $R_f/\phi$ ,  $R_i/\theta$ , and Chi-Square plotted by the use of  $R_f/\phi$  method are shown on Figure 3-60.

#### Correlation between different methods

Strain ratios estimated by the arithmetic and geometric means are greater than those determined by methods of group II for all sections with low  $R_s$  values. However, in sections with larger  $R_s$ , the difference between the results of the two groups, indicated by the measured error, decreases but never becomes zero (Figure 3-61 and 3-62). The harmonic mean, on the other hand, approaches the value of the strain ratio determined by group II methods at moderate  $R_s$  values where its error averages zero as was also reported by Lisle (1977b). Although the error determined by the slope method decreases on sections with moderate  $R_s$ , it increases again at larger  $R_s$  values (Figure 3-61 and 3-62). The difference ( $\Delta$ error) between group I and II is larger for grains with

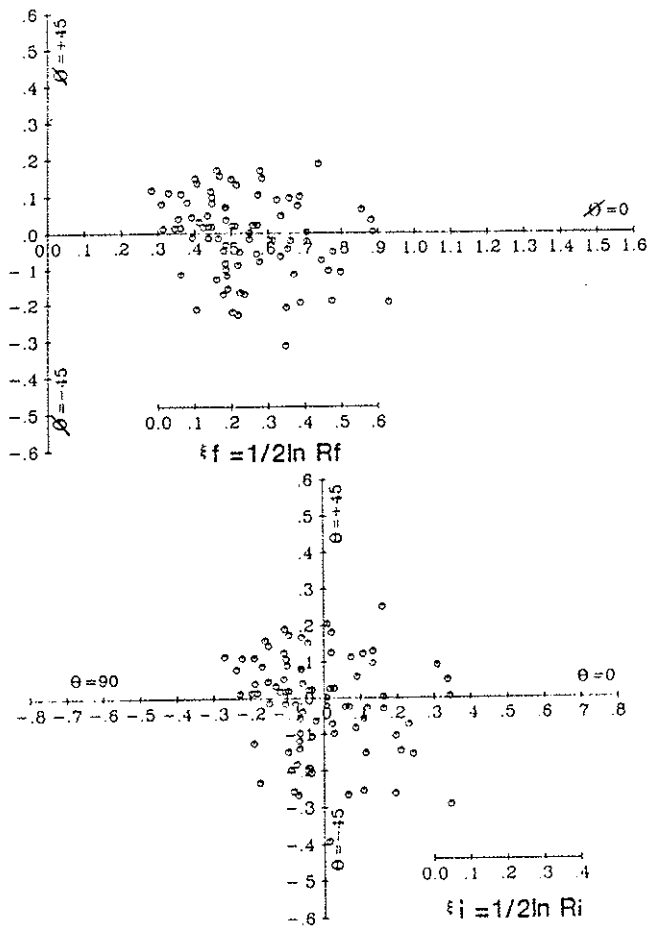


Figure 3-59. Polar graphs showing heart-shaped distribution in a) strained and b) unstrained slates.

$\bar{X}=0$   
1.4 1.5 1.6

$\bar{\theta}=0$   
6 7 8

3 4

In  $R_i$

ped distribution  
ed slates.

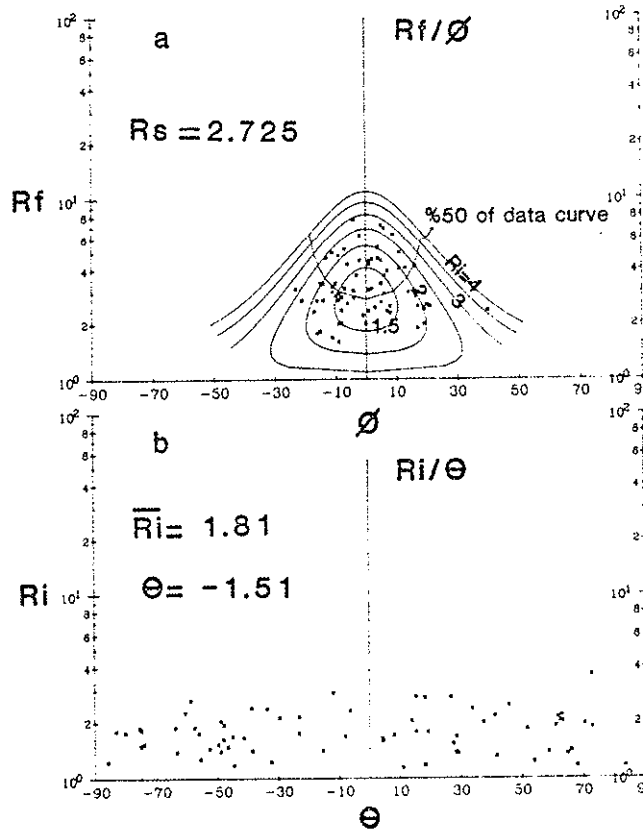


Figure 3-60. (a)  $Rf/\phi$  graph showing 50 % data curve, with its minimum at  $R_s$ . (b)  $Ri/\theta$  graph of same sample as (a), showing less common random initial distribution. (c) typical Chi-Square test graph (Chi-Square versus  $R_s$ ).

TOTAL NUMBER OF ELLIPTICAL MARKERS = 99  
 HARMONIC MEAN OF RF = 2.727 VECTOR MEAN OF PHI = .00  
 PRINCIPAL DIRECTION OF STRAIN = .0

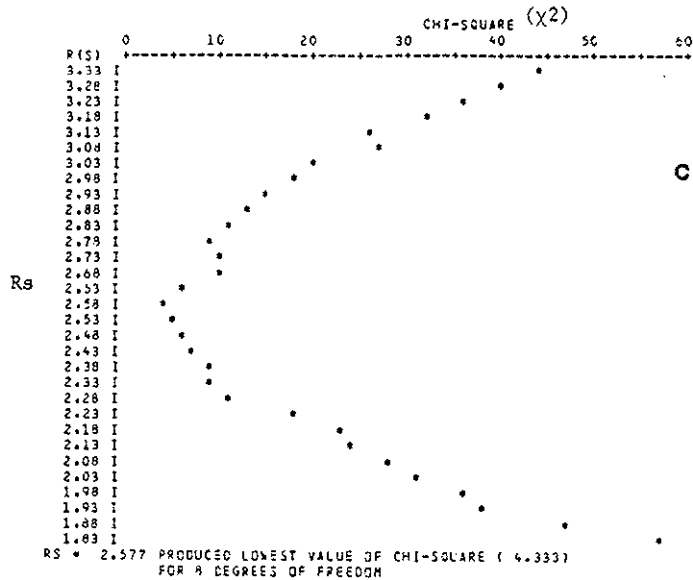


Figure 3-60 cont'd



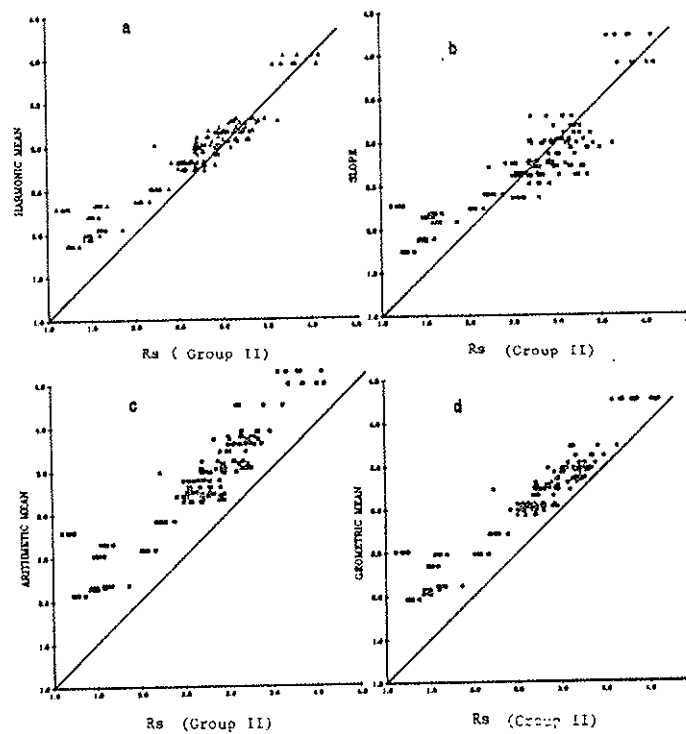


Figure 3-61. Relationship between the estimates of strain calculated by different methods of group I and all methods of group II.

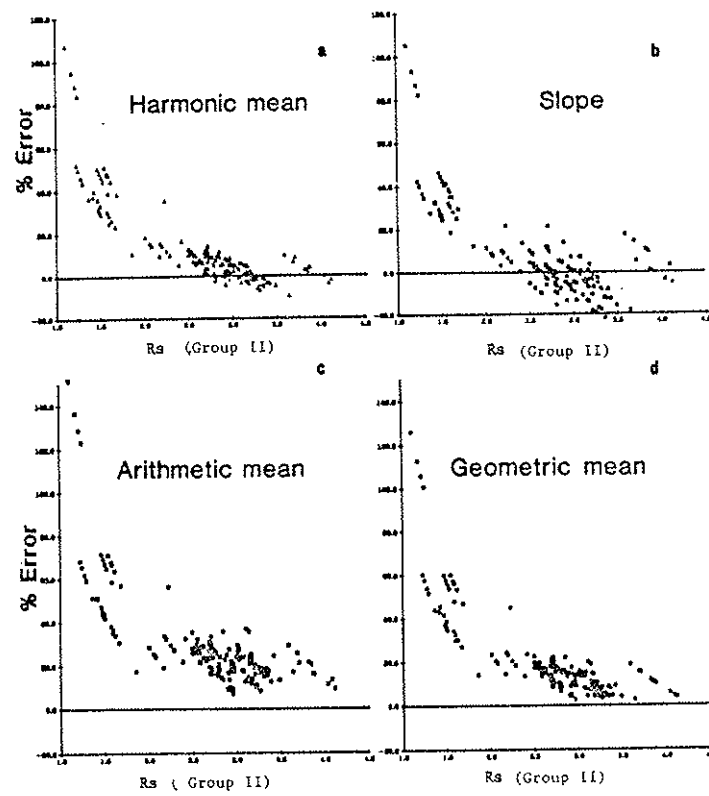


Figure 3-62. Relationship between % error of each method of group I and  $R_s$  of all group II methods.

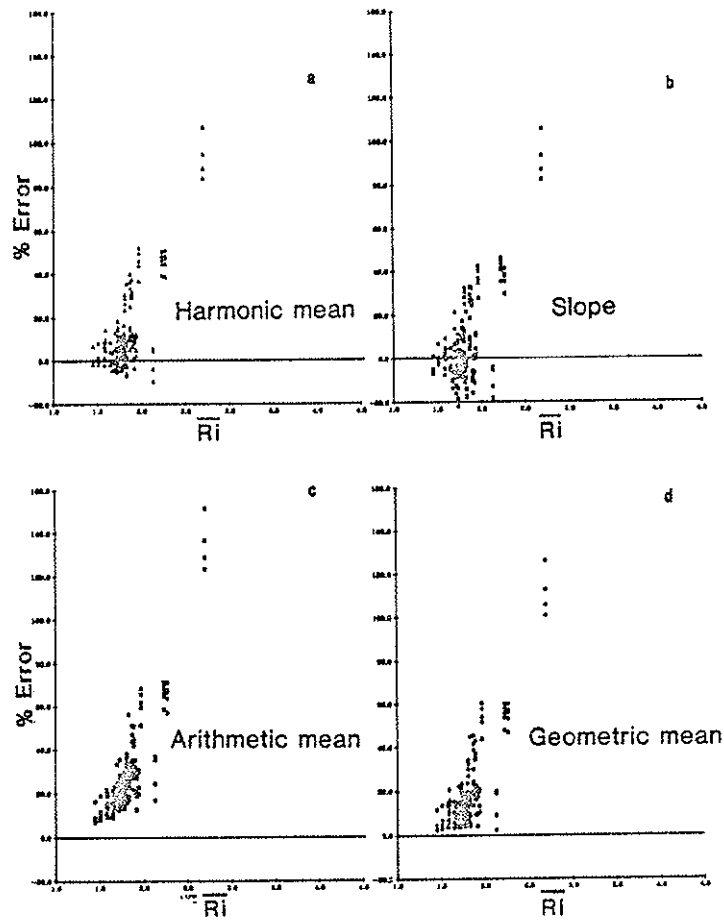
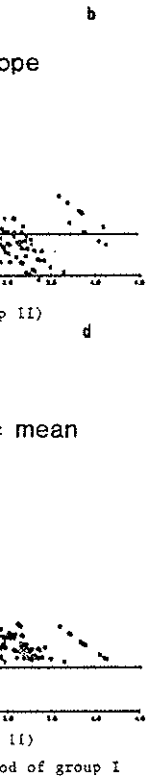


Figure 3-63 . Relationship between % error of each method of group I and  $\bar{R}_i$  (average initial axial ratio).

higher initial axial ratio (estimated by group II methods) (Figure 3-63) and is maximum for grains that initially had their long axes within  $5^\circ$  ( $\theta \leq 5^\circ$ ) of the major axis of the strain ellipse (Figure 3-64).

Figure 3-65 shows the relationship between  $R_s$  calculated by the method of Shimamoto-Ikeda (1976) and  $R_s$  found by other methods of group II. There is a good linear correlation between ratio of principal strains determined by methods of Shimamoto-Ikeda (1976) and Robin (1977).  $R_s$  measured by Holst method (Holst, 1982) is less well correlated with that of Shimamoto-Ikeda method. Except where it is low,  $R_s$  calculated by method of Tobisch and others (1977) is larger than that of Shimamoto-Ikeda as is expected (Appendix I). The results of  $R_f/\phi$  method are well correlated with almost all others at low  $R_s$  values and is less so at moderate  $R_s$ , where they are mainly less than the results of Shimamoto-Ikeda.

Implications

The harmonic mean is calculated more readily than  $R_s$  of group II methods and approximates the strain ratio better than any other method in group I. A graph incorporating the results of this study has been constructed using the harmonic mean values and  $R_s$  determined by methods of Shimamoto-Ikeda, Robin, and  $R_f/\phi$  (Figure 3-66). The best fit curve through data points on a plot of harmonic mean versus axial ratio has been found by the least square method and is shown with its equation in Figure 3-66. After having calculated the harmonic mean,  $R_s$  can be read directly from the graph.

Methods) (Figure 3-64).  
long axes within  
Figure 3-64).

calculated by the  
methods of group  
ratio of principal  
(1976) and Robin  
less well corre-  
where it is low, Rs  
larger than that  
the results of Rf/d  
low Rs values and  
than the results

Rs of group II  
any other method  
study has been  
determined by methods  
the best fit curve  
axial ratio has  
with its equation in  
an, Rs can be read

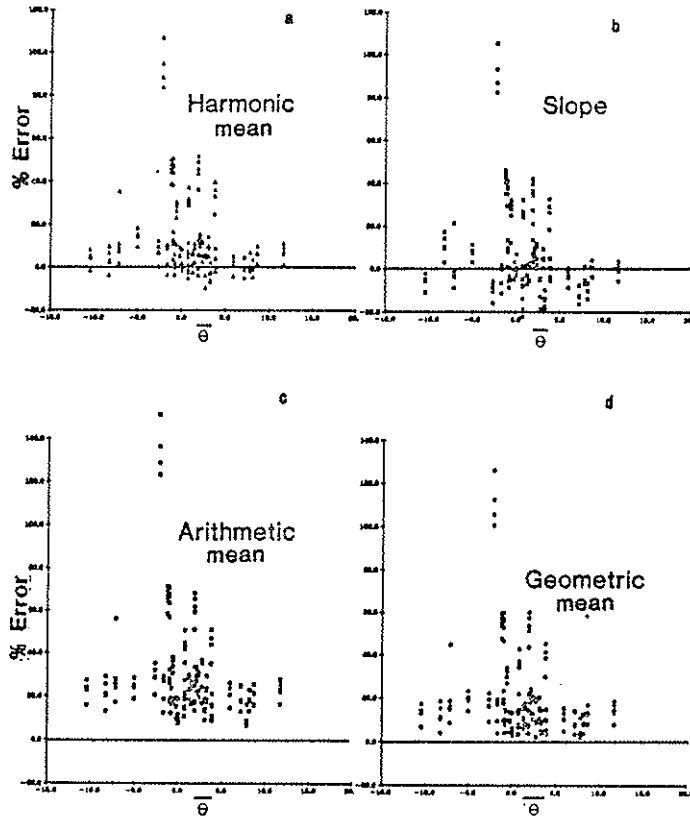


Figure 3-64. Relationship between % error and  $\bar{\theta}$  (average initial axial orientation).

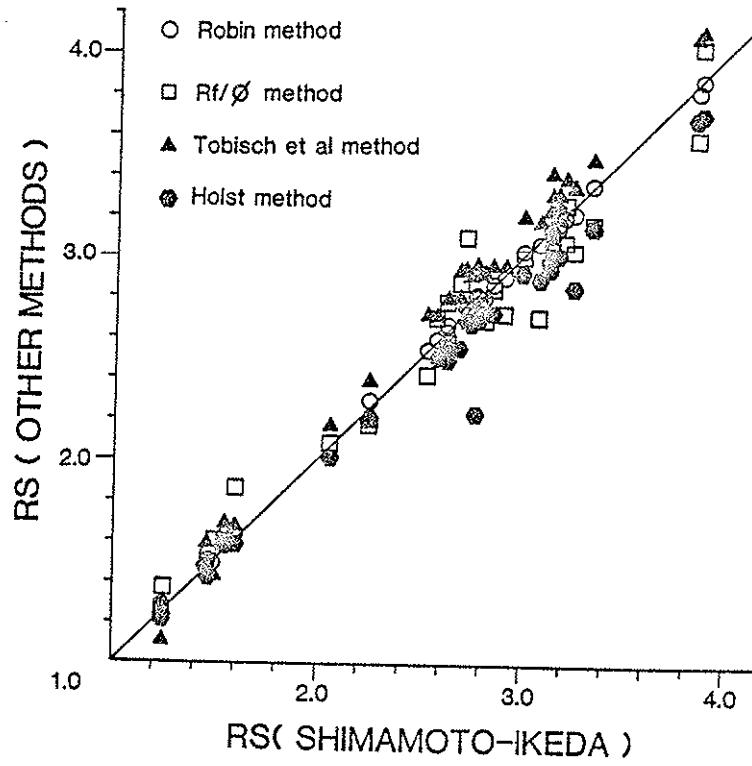
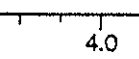
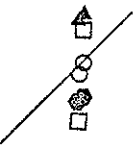


Figure 3-65 . Correlation between Rs found by the method of Shimamoto-Ikeda (method E) and other group II methods.



he method of  
her group II

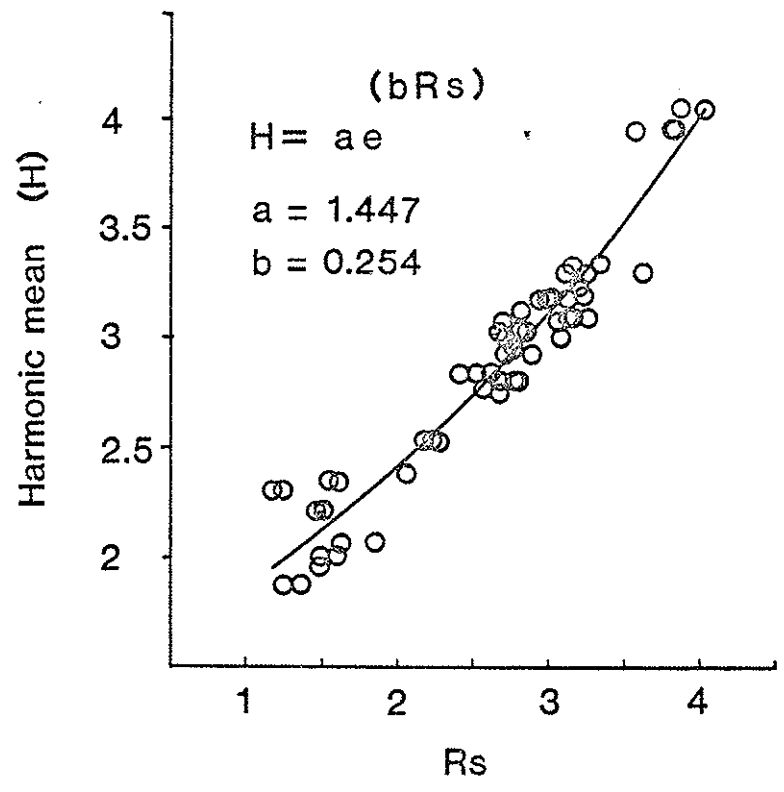


Figure 3-66. Relationship between the harmonic mean of group I methods and Rs of all methods of group II, showing also the curve and equation of the best fit line calculated by the method of least square.

It is recommended that the harmonic mean, corrected by the empirical curve above, be used as a fast, practical, and accurate estimate of  $R_s$  in cases where immediate application of other computerized methods is not feasible as was previously suggested by Lisle (1977b).

Three-dimensional strain analysis

The problem of whether cleavage is parallel to the XY principal plane of strain is a classic one and has been considered by many workers such as Ramsay (1967), Ramsay and Graham (1970), Cloos (1971), Siddans (1972), Wood (1974), and Williams (1976, 1977). It seems that cleavage, defined by flattened objects are parallel to the XY plane of finite strain probably because of high strain magnitudes in rocks with such structures. However, like all other planes, cleavage, if originally in other orientations, can rotate towards parallelism with the XY plane as strain increases (Williams, 1977). This probably explains why in places, a plane of shear might be seen parallel to cleavage. The mechanisms through which mica or planar grains attain their preferred orientation can include mechanical rotation and (or) dissolution and recrystallization (Tullis and Wood, 1975; Williams, 1977).

The method to calculate shape and orientation of strain ellipsoid from two dimensional data is as follows: the three thin sections that are cut normal to the cleavage for each specimen should have their common intersection parallel to the cleavage normal and to the minimum quadratic elongation ( $\lambda$ ) (see the section on theory of strain) if cleavage is parallel to the  $\lambda_1\lambda_2$  plane ( $\lambda_1 > \lambda_2 > \lambda_3$ ). On each thin section, the major and minor axes of the strain ellipse ( $\lambda_1^*$  and  $\lambda_3^*$ )



are within  $3^\circ$ , respectively, of the trace and pole of the cleavage, indicating that the pole to cleavage is parallel to the minimum principal elongation. The few degree discrepancy depends on 1) the error in orienting the thin sections, 2) the precision of aligning the long axes of grains parallel to the trace of cleavage, and 3) non-parallelism of the  $\lambda_3$  axis and the pole to cleavage. Because of the very low angles involved, it is reasonable to assume that  $\lambda_1^*$  and  $\lambda_3^*$  are parallel to the trace of cleavage on thin section and pole to cleavage, respectively, and therefore, that cleavage is parallel to the  $\lambda_1 \lambda_2$  plane.

$R_s = \sqrt{\lambda_1^* / \lambda_3^*}$  is known from the two dimensional measurement. Because  $\lambda_3^*$  is common in all the three sections, it is reduced to unity in order to determine  $\lambda_1^*$  using Equations 3-7 through 3-9,

$$R_s(b) = \sqrt{\lambda_1^* b / \lambda_3^* b} \quad R_s(c) = \sqrt{\lambda_1^* c / \lambda_3^* c} \quad R_s(d) = \sqrt{\lambda_1^* d / \lambda_3^* d} \quad (3-7)$$

where b, c, and d, refer to the three thin sections normal to cleavage.

Since

$$\lambda_3^* b = \lambda_3^* c = \lambda_3^* d = \lambda_3 \quad (3-8)$$

reducing  $\lambda_3$  to unity leads to:

$$\lambda_1^* b = (R_s(b))^2 \quad \lambda_1^* c = (R_s(c))^2 \quad \lambda_1^* d = (R_s(d))^2 \quad (3-9)$$

Now the problem is reduced to having the quadratic elongations along three lines at the intersection of cleavage and the three thin sec-

tions, and finding maximum and minimum quadratic elongations ( $\lambda_1$  and  $\lambda_2$ ) on cleavage. The procedure to obtain  $\lambda_1$  and  $\lambda_2$  is that of Ramsay (1967, p.80). Details of this method and an example are given in Appendix II. After the magnitude and orientation of  $\lambda_1$  and  $\lambda_2$  and X and Y are determined by this method, the radius of a sphere of equal volume to the ellipsoid is calculated and the deviatoric components of strain,  $X_d$ ,  $Y_d$ , and  $Z_d$ , and the simple elongations  $e_1$ ,  $e_2$ , and  $e_3$  are calculated using the relationships shown on Table 3-4.

### Results

Packet 7 - The five specimens studied in packet 7 were taken in different structural positions relative to the Golconda thrust (Figure 3-54). Specimen 1 and 10 are from the west and east dipping limbs of the F2a fold in Ophir Canyon, respectively. Specimens 6, 7, and 8 are taken closer to the Golconda thrust on the west dipping limb of the fold. Specimen 8 is sampled within few meters of the Golconda thrust. Specimens 8 and 10 are medium- to coarse-grained sandstone and specimens 1, 6, and 7 are slate.

Table 3-4 sets out the three dimensional results for the specimens in packet 7. The orientation of the principal strain axes and the deformation plot for each sample are shown on Figure 3-67. All the deformation ellipsoids plot in the apparent flattening field (Ramsay 1967, Ramsay and Wood 1973). Because volume change is unknown, these fields may not necessarily be of true flattening as discussed before. The deformation ellipsoids of slate and even sandstone plot in the

Specimen #	A <sub>1</sub>	A <sub>2</sub>	A <sub>3</sub>	X	Y	Z	r	Xd	Yd	Zd	e <sub>1</sub>	e <sub>2</sub>	e <sub>3</sub>	e <sub>1</sub>	e <sub>2</sub>	e <sub>3</sub>	Y/Z	X/Y	X/Z	a	b	k
OS1	8.66	7.43	1	2.94	2.73	1	2.00	1.47	1.36	0.50	0.47	0.36	-0.50	0.38	0.31	-0.69	2.73	1.01	2.94	0.078	1.09	0.072
OS6	12.66	6.23	1	1.56	2.50	1	2.07	1.72	1.21	0.68	0.72	0.21	-0.52	0.54	0.19	-0.73	2.50	1.62	3.56	0.130	0.92	0.44
OS7	10.53	7.75	1	3.24	2.78	1	2.08	1.56	1.34	0.68	0.56	0.34	-0.52	0.44	0.29	-0.73	2.78	1.16	3.24	0.150	1.02	0.150
OS8	18.50	8.33	1	4.30	2.89	1	2.32	1.05	1.24	0.43	0.85	0.24	-0.57	0.61	0.21	-0.84	2.88	1.49	4.30	0.400	1.05	0.90
OS10	11.17	6.60	1	3.34	2.52	1	2.05	1.63	1.25	0.49	0.63	0.25	-0.51	0.49	0.22	-0.71	2.52	1.30	3.34	0.260	0.94	0.250
OS15	9.05	6.62	1	3.00	2.57	1	1.97	1.52	1.30	0.51	0.52	0.30	-0.49	0.42	0.26	-0.67	2.57	1.17	3.00	0.160	0.93	0.170
OS16	10.20	5.02	1	3.19	2.24	1	1.93	1.66	1.16	0.57	0.66	0.16	-0.48	0.51	0.15	-0.65	2.24	1.42	3.19	0.360	0.80	0.450
OS17	7.94	4.05	1	2.82	2.01	1	1.78	1.58	1.13	0.56	0.56	0.13	-0.44	0.46	0.12	-0.58	2.01	1.40	2.82	0.330	0.70	0.480
OS20	16.26	7.19	1	4.03	2.68	1	2.21	1.82	1.21	0.45	0.82	0.21	-0.55	0.60	0.19	-0.79	2.68	1.50	4.03	0.410	0.99	0.410

Principal axes      Deformation plot axes      Elongations      Shear strains      Deformation plot coordinates

$X = \sqrt{\lambda_1}$        $Xd = Y/r$        $e_1 = Xd - 1$        $e_1 = \ln Xd$        $1 = \ln Xd/Yd$   
 $Y = \sqrt{\lambda_2}$        $Yd = Y/r$        $e_2 = Yd - 1$        $e_2 = \ln Yd$        $2 = \ln Xd/Yd$   
 $Z = \sqrt{\lambda_3}$        $Zd = Z/r$        $e_3 = Zd - 1$        $e_3 = \ln Zd$        $k = 2/3$

r = radius of sphere of equal volume =  $(XYZ)^{1/3}$

where,  $X > Y > Z$

Table 3-4. Results of three dimensional strain analysis for the 9 specimens in packets 7 and 12.

171  
 gations ( $\lambda_1$  and  
 is that of Ramsay  
 e are given in  
 $\lambda_1$  and  $\lambda_2$  and X  
 sphere of equal  
 ric components of  
 $e_2$ , and  $e_3$  are  
  
 taken in dif-  
 thrust (Figure 3-  
 ing limbs of the  
 s 6, 7, and 8 are  
 ng limb of the  
 Golconda thrust.  
 one and speci-  
  
 for the specimens  
 rain axes and the  
 3-67. All the  
 ing field (Ramsay  
 unknown, these  
 discussed before.  
 e plot in the

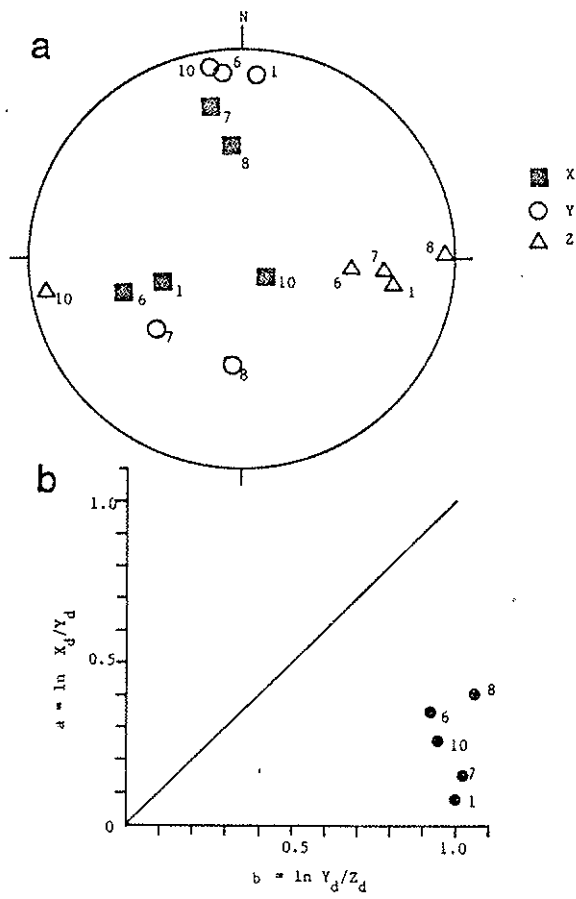


Figure 3-67. Principal directions (a) and deformation plot (b) for the specimens in packet 7.

$a = \ln X/Y$

1.0

Figure

■ X  
 ○ Y  
 △ Z

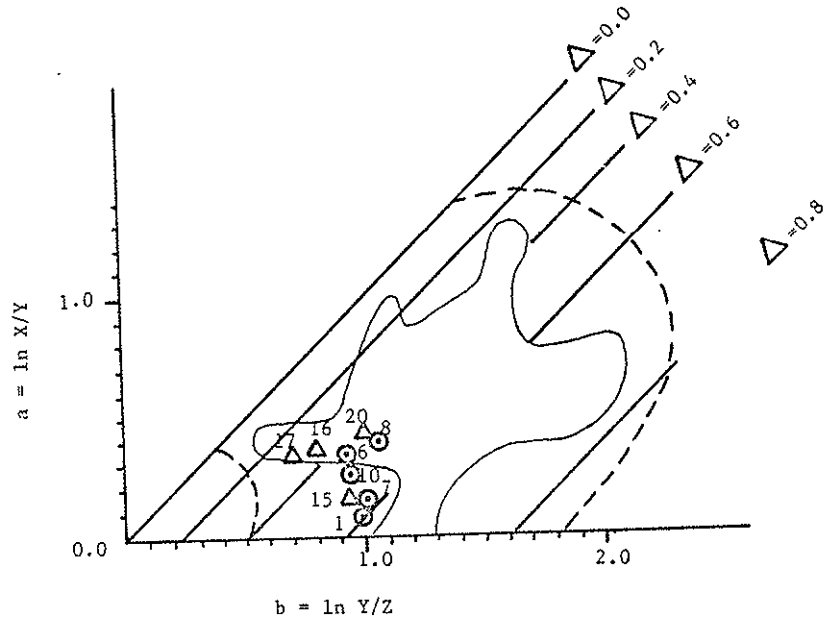


Figure 3-68. Ramsay and Wood's (1973) deformation plot for slates from the Caledonites of NW Europe and the eastern United States and the results of the present study.  $\Delta$  is total volume change per original unit volume.

lot (b)

deformation field of slates compiled by Ramsay and Wood (1973) (Figure 3-68). The principal extensions and axial ratios of strain ellipsoid are plotted for each specimen versus its structural position on Figure 3-69. Specimen 1 in the highest position has the lowest shortening and extension along the Z and X axis, respectively, and the highest extension along the Y axis. Specimen 8 followed by 6, both close to the Golconda thrust, have the highest extension along the X, shortening along the Z, and the lowest extension along the Y axis. Specimen 7 has an intermediate characteristics in terms of the principal extensions.\*

The structural position of specimen 10 is complicated by its position in the macroscopic F2a fold in Ophir Canyon and does not correlate with the pattern of the principal extensions as defined by the other specimens. The orientation of the principal axes in specimen 10 is most certainly influenced by the F2a fold. Comparing Figures 3-67 and 3-19, the orientation of the X and Z axes in this specimen can be explained by rotation about the axis of the F2a fold which is homoaxial with Y axes in samples 1 and 6 and with F1 fold axes. This and the fact that the magnitude of strain in specimen 10 is not much different from the others indicate that the recorded strain is older than the F2a folding and that the F2a fold has deformed the cleavage by flexural slip such that grain shapes have remained constant and the X and Z axes rotated about Y axis. Despite the nearly constant orientation of cleavage and Z axis in samples 1, 6, 7, and 8, the X and Y axes in specimens 7 and 8 are differently oriented from those of 1 and 6; these will be discussed later.

(1973) (Figure  
 rain ellipsoid  
 ition on Figure  
 shortening and  
 highest exten-  
 ose to the Gol-  
 hortening along  
 men 7 has an  
 xtensions.\*  
 ed by its posi-  
 s not correlate  
 by the other  
 imen 10 is most  
 3-67 and 3-19,  
 an be explained  
 coaxial with Y  
 d the fact that  
 rent from the  
 the F2a folding  
 ral slip such  
 Z axes rotated  
 cleavage and Z  
 ecimens 7 and 8  
 ll be discussed

Packet 12 - Except for specimen 17, which is a sandstone taken on the crest between Ophir and Wisconsin canyons, other specimens in this domain are slate (Figure 3-54). The orientation of cleavage in specimen 17 is different because of F2a folds compared to the almost homoclinal cleavage in other specimens. Specimens 15 and 20 are sampled in northern (subdomain 12b3) and specimen 16 in the southern (subdomain 12b2) sides of Ophir Canyon (Figure 3-54).

Table 3-4 shows the results of the 3D strain study in packet 12. The orientation and deformation field of the principal strain axes in this packet are shown on Figure 3-70. The Y axes plunge shallowly and moderately between N and NW. The X axes of specimens 15, 16, and 20 plunge moderately to steeply SSE on the vertical cleavage. The orientation of the principal axes in specimen 17 is different because of the younger F2a folds. No pattern is evident in the variation of the principal extensions and X/Y, Y/Z, and X/Z ratios as a function of structural position within this packet (Figure 3-69). The average shortening ( $e_3$ ) is less and the X/Y ratio is larger in this packet compared to those in packet 7. The deformation ellipsoids for these specimens plot closer to plane strain (assuming no volume change) in the apparent flattening field of the deformation plot than those in packet 7.

#### Discussion

Despite the existence of the apparent gradient in the magnitude of the principal extensions as a function of structural position relative to the Golconda thrust in packet 7, no such gradient exists in domain 12. This suggests that the strain related to the slaty cleavage is

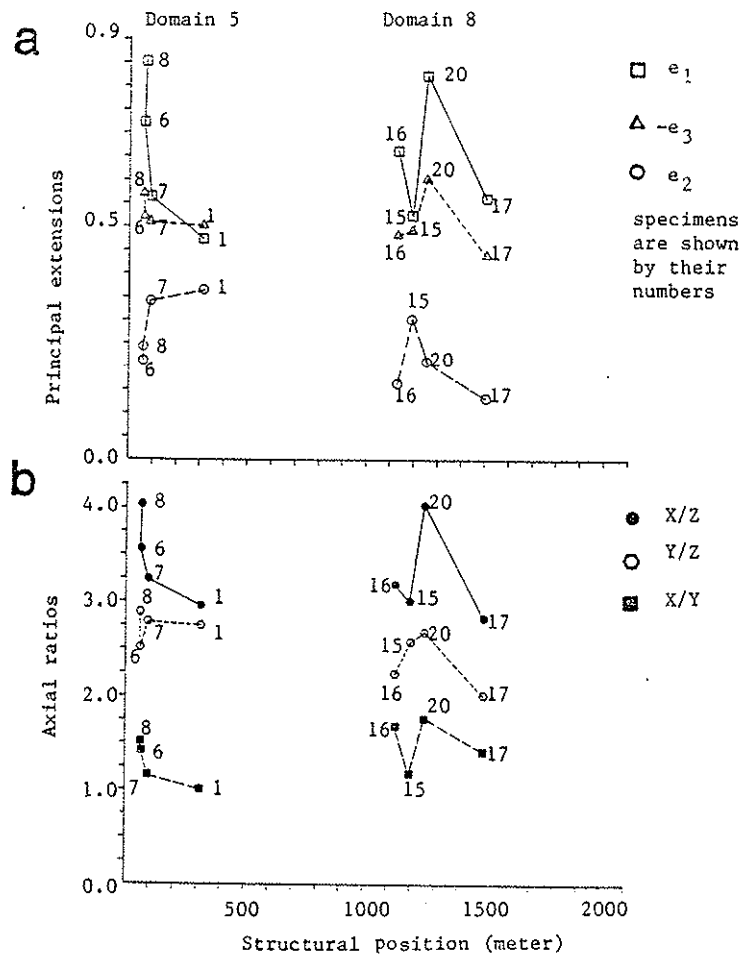


Figure 3-69. Relationship of the (a) principal extensions and (b) axial ratios with structural position of the specimens relative to the Golconda thrust in packet 7 and 12.



$\square$   $e_1$   
 $\triangle$   $-e_3$   
 $\circ$   $e_2$   
 specimens  
 are shown  
 by their  
 numbers

$\bullet$  X/Z  
 $\circ$  Y/Z  
 $\blacksquare$  X/Y

2000

extensions  
 position  
 conda

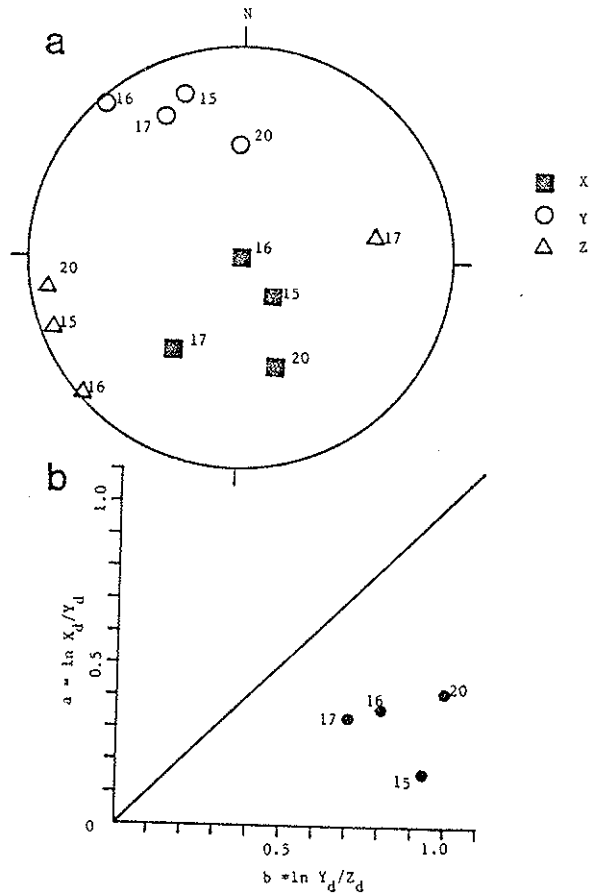


Figure 3-70. Principal directions (a) and deformation plot (b) for the specimens in packet 12.

older than the emplacement of the Golconda allochthon. If correct, the strain was applied in each packet during the D1 deformation phase as is also evidenced by the parallelism of cleavage, the XY plane, axial planes of F1 folds, as well as the Y axes of strain and fold and boudin axes. The sub-parallelism of the Y axis and the majority of the F1, F2a, and F3 fold axes suggests a consistent and continuous tectonic motion responsible for all these deformations. Assuming that the directions of the principal axes in the homoclinal part of packet 7, an area not affected by the F2a fold or other structure in this area, represent the tectonic motions, an east-west trend of shortening is apparent from the results of all specimens in this packet and from the orientation of F1 axial planes and cleavage. The maximum elongation occurred mainly subparallel to dip of the flattening plane except in specimens 7 and 8 where it was subhorizontal.

The difference in the orientation of X and Y of specimens 7 and 8 from those of 1 and 6 can be explained in four different ways:

1) The principal orientations in specimens 7 and 8 are because of superimposition of a later incremental strain with its major axis at a high angle to that of the established finite strain after D1 phase and due to the emplacement of the allochthon along the Golconda thrust.

2) The variation is contemporaneous with D1 and caused by variable displacements in the XY plane at the culminations and depressions of large F1 folds; this does not seem likely considering the parallelism in specimens 7 and 8 of X and F1 and F2a fold axes.

3) The difference in the orientation of X in specimens 7 and 8 is

If correct, the  
 tion phase as is  
 Y plane, axial  
 fold and boudin  
 ry of the F1,  
 tinuous tectonic  
 that the direc-  
 packet 7, an area  
 area, represent  
 s apparent from  
 e orientation of  
 occurred mainly  
 cimens 7 and 8  
 cimens 7 and 8  
 ways:  
 are because of  
 major axis at a  
 r D1 phase and  
 nda thrust.  
 sed by variable  
 depressions of  
 he parallelism  
 ens 7 and 8 is

due to rotation, for example as a result of reactivation along the Golconda thrust because of their low structural position; this is also unlikely because no such rotation is evidenced in the orientation of the cleavage and Z axis in these specimens.

4) The orientation of X in sandstone of specimen 8 is a result of heterogeneous flow parallel to F1 fold axes. The flow was formed because of rheological differences between pelite and sandstone, such that while the more compactable pelites of specimen 1 and 6 were being shortened, grains in sandstone of specimen 8 deformed and rotated. This is unlikely because: a) X in specimen 7, being a slate, is also subparallel to F1 fold axes and to X in sandstone specimen 8, b) specimen 10, a sandstone, attains X axis orientation subparallel to X in pelite specimens 1 and 6 after the removal of F2a folding, and c) shortening in specimen 10, a sandstone, is about equal in magnitude to shortening in pelitic specimens. Although shortening is maximum in sandstone specimen 8, it may be due to a younger superimposed strain when the allochthon was emplaced as discussed in the first hypothesis.

A comparison of the principal directions of specimen 1 and 6 and those of 15, 16, and 20, in the homoclinal parts of packets 7 and 12, respectively, suggests that the orientations of the principal axes in packet 12 are the result of rotation of directions such as those in packet 7 (Figure 3-67, 3-70) about an axis subparallel to the Y axis and F1 linear structures.

X and Y axes plunge moderately N and SW on an inclined plane parallel to the Golconda thrust in specimens 1 and 6 of packet 7 (Fig-

ure 3-67). This is probably because shortening during D1 phase of deformation was non-horizontal and that during D2 phase, when cleaved rocks were imbricated and thrust, the rigid body rotation if occurred, was homoaxial with the Y axis of D1 phase. Moreover, the contraction direction should have remained constant in order to emplace the allochthon over the Golconda thrust essentially subparallel to D1 cleavage.

The higher flattening in samples of packet 7 can partly be attributed to the emplacement of the Golconda allochthon, implying that the finite strain recorded in the rocks close to the Golconda thrust is a sum of D1 and a younger deformation that can be related to the thrust. It is also possible that an unidentified pre-D1 deformation such as gravitational compaction of the mudstones and sandstones contributed partly to the grain shapes which were measured in the slates and sandstones.

In  
present  
phy, t  
and to  
the stu  
with t  
tonic s  
Age of  
The  
divided  
lower P  
l can  
slice of  
into th  
The seco  
facies  
(Chapter  
the upp  
mian roc  
a maxim  
the base  
the fina

181  
g D1 phase of  
se, when cleaved  
dy rotation if  
reover, the con-  
er to emplace  
bparallel to D1  
rtly be attri-  
plying that the  
a thrust is a  
to the thrust.  
ation such as  
nes contributed  
ates and sand-

CHAPTER 4-- KINEMATICS OF SEQUENTIAL PROCESSES AND  
RECONSTRUCTION OF THE PALEOGEOGRAPHY

In this Chapter, the tectonostratigraphic and structural data presented in Chapter 2 and 3 are used to reconstruct the paleogeography, timing, and kinematics of emplacement of the Golconda allochthon and to analyze the source and tectonic significance of serpentinites in the study area. Data from other parts of the allochthon are compared with those in the study area to evaluate the regional extent and tectonic significance of the allochthon.

Age of emplacement of the Golconda allochthon in the study area

The rocks of the Golconda allochthon in the Toiyabe Range can be divided into three groups according to their age. The first includes lower Paleozoic rocks such as those in packet 1 and possibly 9. Packet 1 can be interpreted, for the reasons to be discussed, as a detached slice of the lower plate of the Golconda thrust which was incorporated into the allochthon probably after the deposition of Triassic rocks. The second group includes upper Paleozoic allochthonous rocks of varied facies that range in age between Late Mississippian and Permian (Chapter 2). The third includes Lower Triassic rocks below the rocks of the upper Paleozoic section. The main body of the allochthon has Permian rocks at various positions above the Golconda thrust that indicate a maximum age of Permian for the assemblage. Triassic rocks occur at the base of the allochthon and provide a maximum age of Triassic for the final emplacement of the allochthon.

The youngest rocks overthrust by the Golconda allochthon in the study area are those of the Diablo Formation with a Wolfcampian to Guadalupian (Early to Late Permian) age in Jett and Pablo Canyons (Speed and others, 1977) that indicate a maximum age of Permian for the thrust. A minimum age for the thrust is 42 and 54 my (K-Ar ages of the Ophir pluton). If the rocks of unit t6 (Chapter 2) prove to be Mesozoic and autochthonous, the minimum age can be increased to pre-t6.

The proto-Golconda thrust can be traced at the base of the structurally lowest packet of the upper Paleozoic section such as 7 and above the Triassic packet (Figure 4-6). This is the thrust above which the upper Paleozoic rocks were originally translated and emplaced over the continental slope or shelf or possibly subareal parts of the continental margin of North American plate. The present sole thrust of the Golconda allochthon above the Diablo Formation and at the base of packet 1 is a product of continued contraction and thrusting that spanned a time since the emplacement of the upper Paleozoic section over the continental margin through the deposition of Lower Triassic rocks and their tectonic juxtaposition under lower Paleozoic packets at the base of the allochthon.

#### Kinematics of sequential events

F1 folds and axial plane cleavage are the most pervasive structures that are detected in all the upper Paleozoic packets of the allochthon. These structures are cut by packet bounding faults. F1 and F2a folds and the thrust faults that occurred between these events provide evidence of transport direction and folding of the sediments before and

during t  
subparal  
subparal  
In  
chert bo  
location  
folding  
lowly and  
moderate  
faults in  
homocline  
between W  
on the  
hand, plu  
to F1 and  
ing horiz  
cleavage  
allochthon  
persisted

The u  
study are  
for the fo  
of coeval  
pelagic ro  
evidence o

allochthon in the  
 Permian to Gua-  
 Canyons (Speed  
 of Permian for the  
 K-Ar ages of the  
 prove to be Meso-  
 to pre-t6.  
 use of the struc-  
 tion such as 7 and  
 thrust above which  
 and emplaced over  
 parts of the con-  
 sole thrust of the  
 at the base of  
 and thrusting that  
 Paleozoic section  
 of Lower Triassic  
 Paleozoic packets at

pervasive struc-  
 tures of the allo-  
 chthon. F1 and F2a  
 events provide  
 evidence before and

during the attachment of each packet. The axes of F1 and F2a folds are subparallel in many packets, and plunge shallowly and moderately NNW subparallel to some F2b fold axes.

In parts of packet 12, the axes of F1 folds are subparallel to the chert boudin axes, bxc lineations, and the Y axes of strain in the same location (Figure 3-4, 3-5, 3-70) indicating that slaty cleavage and F1 folding are related. The minimum principal extension, Z, plunges shallowly and moderately E, and the maximum principal extension, X, plunges moderately WSW along the dip of the Golconda thrust and other local faults in the homoclinal part of packet 7 (Figure 3-41, 3-67). In the homoclinal part of packet 12, the Z strain axis plunges shallowly between W and SW, and the X axis plunges moderately to steeply S or SSE on the steep cleavage (Figure 3-4, 3-70). The Y axis, on the other hand, plunges shallowly and moderately between NNE and NW, subparallel to F1 and F2a fold axes in packet 7 and 12. These and the east trending horizontal projection of the pole to the axial planar slaty cleavage which is parallel to the Golconda and other thrusts in the allochthon, indicate a strong east-west component of contraction that persisted through most phases of deformation.

The upper Paleozoic section of the Golconda allochthon in the study area can best be described as an accretionary prism (Chapter 1) for the following reasons: 1) the tectonic juxtaposition among packets of coeval pelagic and arc related (?) volcanogenic rocks over hemipelagic rocks that in turn lie over slope-base rocks (Chapter 2), 2) evidence of shortening subnormal to the packet bounding thrusts and the





s indicated by  
tic relationship  
r attitude with  
pre-, syn-, and  
paragaphs, the  
ct the kinematic  
del described by  
for the Barba-

rust move near  
hly, and tighter  
ds with axial  
ts reach the toe  
ation of the Fl  
, is taken to be  
are not affected  
by west dipping  
ig and Sharman,  
eed, 1981; Speed  
ial planes and  
folds are formed  
ntraprism shor-  
, leading to the  
in most of the

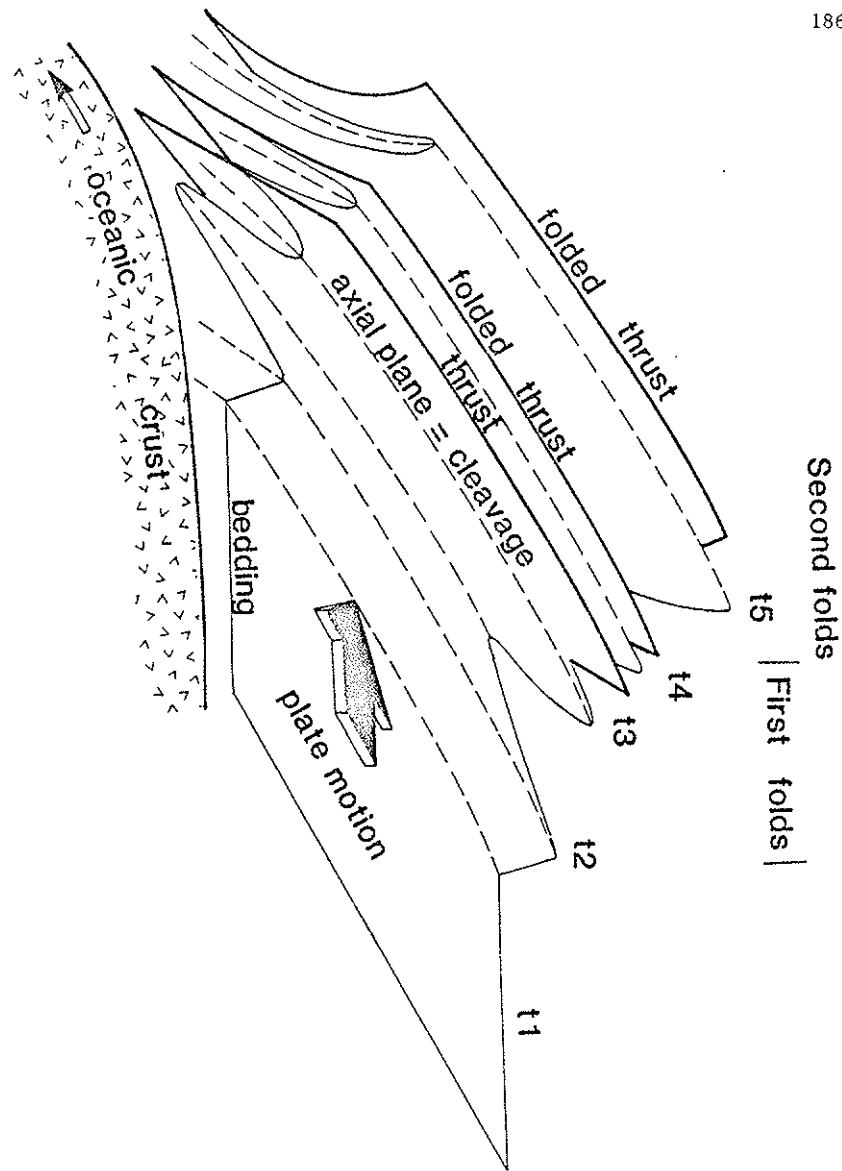


Figure 4-1. A schematic model for the formation of F1 and F2a folds in the Golconda allochthon.

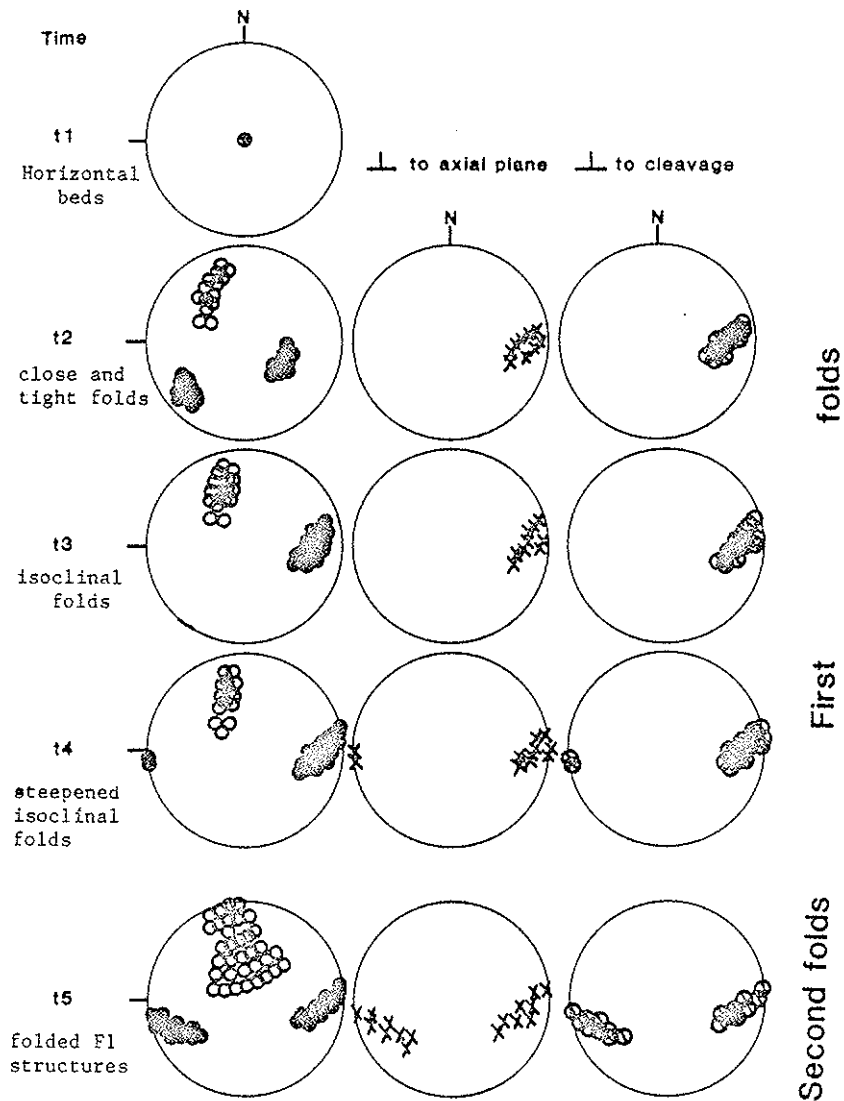


Figure 4-2. Synthetic fabric for the model F1 and F2a folding. see the text for the original orientation of fold axes and other structural elements.

betwe  
these  
folds  
to th  
moder  
local  
irreg  
were  
the th  
ular t  
NW tr  
which  
differ  
respec  
deform  
girdle  
rotate  
tial g  
planes  
gate f  
planes  
the up  
and no

eavage



folds

First

Second folds

a folding.  
a of fold

Local reactivation of packet bounding faults such as the one between packet 7 and 8, generated fault-contemporaneous F2b folds along these faults (Figure 3-22). Several local faults cut across the F2b folds at the fault contact, suggesting that they were formed according to the following model (Figure 4-3).

Bedding and cleavage at this contact, originally dipping moderately to the west as in the homoclinal part of domain 7h5a, were locally rotated due to faulting caused probably by the presence of irregularities such as bumps in the fault zone (Figure 4-3a). Folds were then formed in the rotated block due to the continued motion along the thrust. The axial planes in Figure 4-3b are taken to be perpendicular to a SW-NE trending shortening along the thrust, suggested by the NW trending axis of rotation of bedding and cleavage (Figure 4-3a), which also lies on the thrust. These folds could have had constant or differently oriented axial planes as depicted on Figures 4-3b and 4-3c, respectively. The other alternative is that these rocks were first deformed by F2b folds and later rotated so as to remove the bedding girdle from the pole to homoclinal bedding. The folds were then rotated homoaxially (Figure 4-3d-f) as suggested by the observed partial girdle and great circle distributions of their axes and axial planes, respectively (Figure 3-22). Other possibilities such as conjugate folding with initially differently oriented hingelines and axial planes, or rotation of axes by simple or pure constrictional shear in the upper plate are not accepted because F2b conjugate folds are absent and no evidence of high strain required for axial rotation exists.

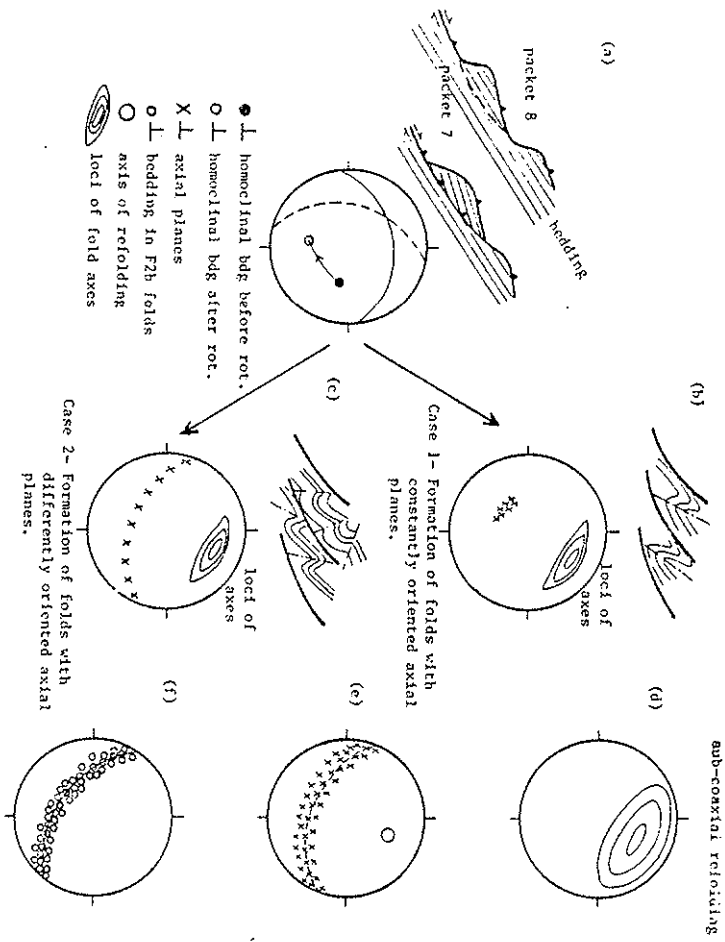


Figure 4-3. A forward flexural slip model for F2b folding. See the text for explanation.

folded  
kinks w  
individ  
macrosc  
the la  
tation  
the Go  
of kink  
conda  
contemp  
of the  
probabl  
conda t  
The  
zone, s  
lel to  
traction  
indicate  
within t  
The  
3-39 and  
autocth  
tion of  
this mo

The existence of non-deformed kinks within few meters of the folded F2b folds, at the contact of packets 7 and 8, indicates that kinks were formed after F2b folds. The form of the kinks, conjugate or individual, was most probably controlled by the limb attitudes of macroscopic F2a folds. F3 folding is either synchronous or older than the latest movement on the Golconda thrust, as indicated by the orientation of kinks in the southern part of domain 7h5a and other parts of the Golconda thrust zone (Figure 3-29, 3-43). The most plausible cause of kink folding is the final emplacement of the upper plate of the Golconda thrust that occurred after intraprisms thrusting and fault-contemporaneous folding, implying that kinks in different packets are of the same generation. Further motion along the Golconda thrust, probably by late reactivation, locally deformed the kinks at the Golconda thrust zone (Figure 3-43).

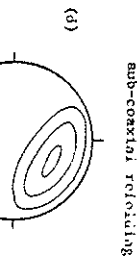
The parallelism of the striations on faults at the Golconda thrust zone, slip directions determined from faults associated with and parallel to the Golconda thrust (Figure 3-41), and the west plunging contractions (Z) resolved from intersecting F3 kinks (Figure 3-25, 3-26), indicate that the kinks are related to a succession of displacements within the Golconda allochthon.

The tectonic fabric at the Golconda thrust in Ophir Canyon (Figure 3-39 and 3-41) is consistent with an east to west underthrusting of the autochthon below the Golconda allochthon as indicated by the orientation of axial planes of F4 folds and slip on associated faults. During this motion which probably occurred after the allochthon was emplaced,

(c)



(d)



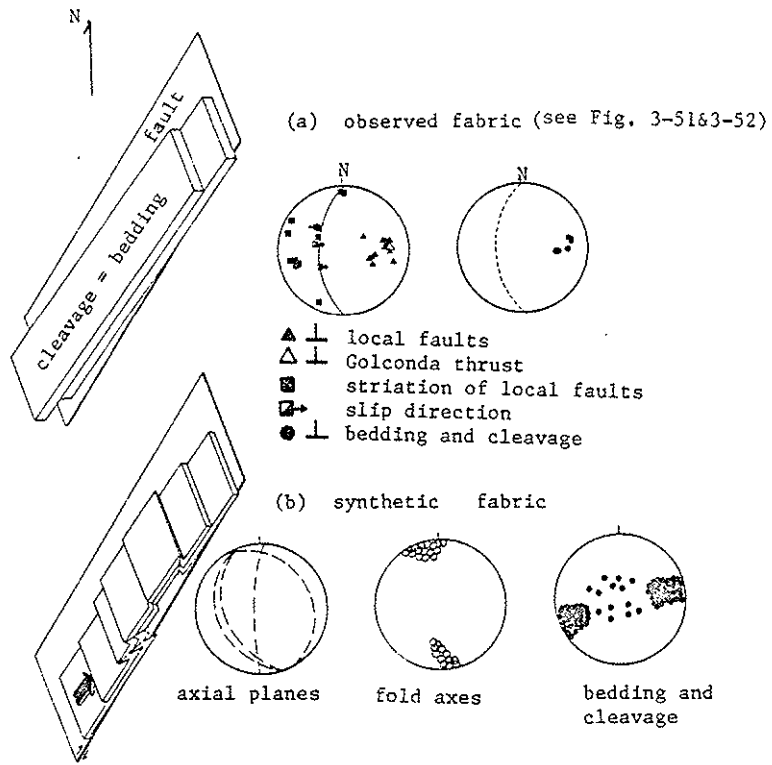


Figure 4-4. Observed fabric of the structures at the Golconda thrust zone (a) and a model for their formation. See text for explanation.

chert  
 faults  
 result  
 on Fig  
 and are  
 In  
 sequenc  
 sumptio  
 must be  
 litholo  
 the Gol  
 Paleoge  
 The  
 the Gol  
 phase fo  
 geny. T  
 Permian  
 (1982),  
 a migrat  
 western  
 Antler o  
 accretio  
 contract  
 zoic mag  
 oceanic b

chert beds in the upper plate, at low angles to the Golconda and local faults (Figure 4-4a), were folded by layer parallel compression, resulting in the formation of F4 conjugate folds as depicted on a model on Figure 4-4b. These folds are related to the D5 deformation phase and are restricted to the Golconda thrust zone (Table 3-1).

It should be noted that structural analysis only indicates the sequence and direction of displacements and styles of displacement consumption, not the transport distance of packets in the allochthon. This must be determined by paleomagnetism, paleobiofacies, or by some unique lithologic ties. None of these exists. It can not be stated whether the Golconda allochthon is wholly locally or partly distally derived.

#### Paleogeography and plate tectonics reconstruction

The lower Paleozoic rocks that are autochthonous with respect to the Golconda thrust have not been studied in detail. These show multi-phase folding and were deformed during the mid-Paleozoic Antler orogeny. They are in many places overlain by the autochthonous homoclinal Permian rocks of the Diablo Formation. According to Speed and Sleep (1982), deformed lower Paleozoic rocks formed an accretionary prism to a migrating island arc system. Collision between the arc and the western passive margin of the North American continent caused the Antler orogeny in the Mississippian. The island arc that propelled the accretionary prism (Roberts Mountains allochthon) sank due to thermal contraction (Speed and Sleep, 1982). The subsidence of the lower Paleozoic magmatic arc was probably accompanied by the formation of another oceanic basin and westward shift of the subduction zone (Speed, 1979).

Some rocks of the Golconda allochthon were then deposited on the outer shelf, slope, and floor of this oceanic basin that was situated between the Antler highlands and a convergent boundary to the west, the polarity of which has been a matter of debate (Chapter 1). Sedimentation in the oceanic basin continued from the Mississippian to Permian or possibly Early Triassic.

The purpose of this section is to discuss the sedimentologic and structural data that bear on interpretation of the polarity of the convergent boundary, and therefore, the nature of the continental margin of the western North American plate and the paleogeography in late Paleozoic and Early Triassic time.

Terrigenous and hemipelagic packets in the lower part of the allochthon (Chapter 2) lack the volcanogenic rocks that are characteristic of the age equivalent upper packets of the allochthon. Moreover, a volcanic terrane that could have supplied the clasts to the volcanogenic packets does not exist in the autochthon east of the Golconda thrust. Thus the source of volcanogenic material should have been to the west of the oceanic basin where the volcanogenic and other upper Paleozoic rocks were deposited in the present geographic coordinates assuming no rotation and translation of the allochthon after its emplacement. Sonomia, the magmatic arc of Speed (1979), or another intra-oceanic arc, west of the oceanic basin, is assumed to be the source of the volcanogenic material. Pelagic packets, in the highest structural position, containing mainly radiolarian cherts, pelite, minor volcanogenic rocks, and basalt slices, were probably deposited in an oceanic basin



d on the outer  
 tuated between  
 st, the polar-  
 imentation in  
 mian or possi-  
 entologic and  
 ty of the con-  
 nental margin  
 ography in late

rt of the allo-  
 characteristic  
 reover, a vol-  
 ne volcanogenic  
 lconda thrust.  
 een to the west  
 pper Paleozoic  
 tes assuming no  
 s emplacement.  
 r intra-oceanic  
 rce of the vol-  
 tructural posi-  
 r volcanogenic  
 n oceanic basin

with no access to terrigenous material. The terrigenous rocks contain clasts that correlate by their age and lithology to the rocks immediately under the Golconda thrust in the study area. These were deposited at the continental slope or its base (Chapter 2). The depositional settings of the four allochthonous upper Paleozoic facies which are given in Chapter 2 are used in the following paragraphs to reconstruct the prevailing paleogeography of the local western margin of the North American continent, assuming that the Golconda allochthon was emplaced at its present geographic location.

Figure 4-5 is an schematic illustration of the paleogeography and sequential tectonic and depositional processes between the Mississippian and Permian times based on the accretionary model discussed in the previous section. According to this model, the upper Paleozoic section of the Golconda allochthon evolved by progressive accretion of the pelagic, volcanogenic-basaltic, hemipelagic, and terrigenous rocks in that order. The Golconda accretionary prism was underthrust by the passive local continental margin, probably during Triassic, due to the convergence of the arc (Speed, 1979) and continental crust.

The existence of a packet of Early Triassic rocks, in the basal part of the Golconda allochthon above the allochthonous lower Paleozoic rocks, indicates that the sole thrust of the allochthon is younger than the Triassic rocks. The calcareous Triassic clastic rocks apparently do not possess the penetrative F1 foliation that exists in the upper Paleozoic rocks. Despite the sandy texture of the Triassic rocks which may have inhibited the development of a foliation without large strain,

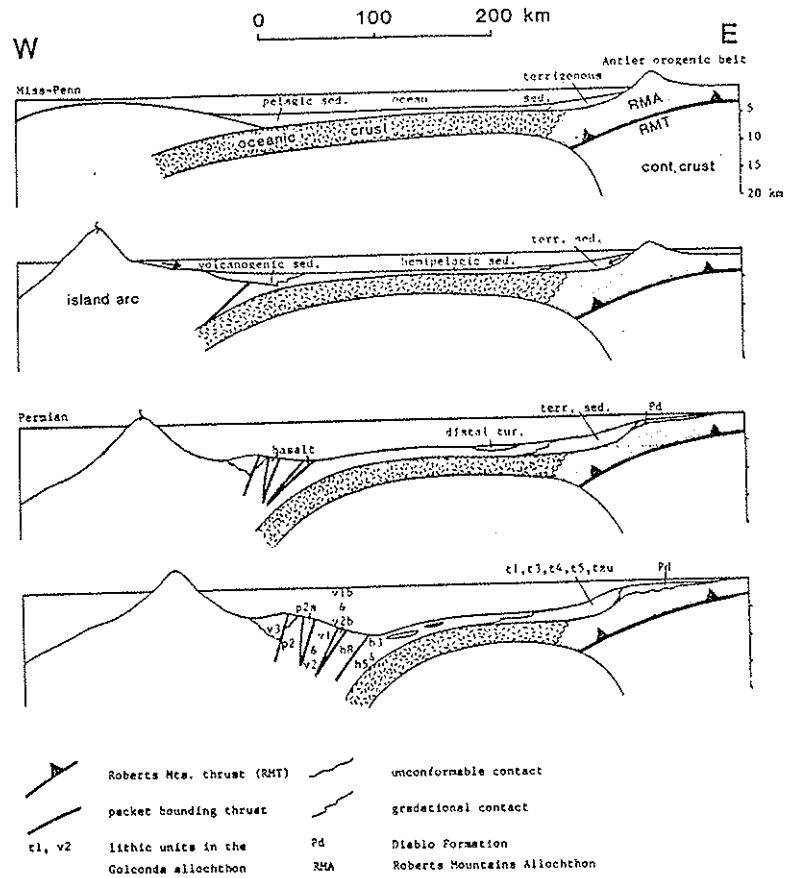
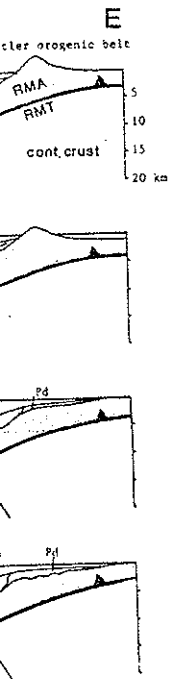


Figure 4-5. A model for the late Paleozoic tectonic and depositional processes before final emplacement of the Golconda allochthon based on the accretionary model of Speed (1979).

the well textured matrix that (Chap) sited packe between to the Trias the T and qu likely the Go first sphere formati Speed a probabl contin ary pri zoi ro gence



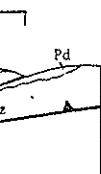
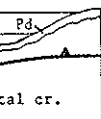
nic and  
emplace-  
d on the

the undeformed pelecypod shells in these sandstones, and the pervasive, well developed foliation in upper Paleozoic sandstones with similar texture, suggest that the Triassic rocks did not undergo the D1 deformation event that is typical of all the upper Paleozoic rocks. Assuming that D1 structures are related to the Pre-thrust accretionary processes (Chapter 3), the Triassic rocks can be interpreted to have been deposited after the upper Paleozoic rocks were deformed and assembled in packets. The deposition of the Triassic rocks can be further narrowed between the emplacement of the upper Paleozoic section and attachment to the allochthon of the lower Paleozoic packets that lie below the Triassic rocks.

The angular chert, quartz, and plagioclase rich volcanic clasts in the Triassic packet indicate a source terrane rich in volcanic, chert, and quartz bearing rocks. The upper Paleozoic section is the most likely candidate for such a source. During the Early Triassic, when the Golconda accretionary prism of mainly upper Paleozoic rocks was first emplaced on the continental margin, elastic loading of the lithosphere by the prism probably resulted in downwarping of the margin and formation of a foreland basin at the toe of the prism as described by Speed and Sleep (1982) and shown on Figure 4-6 and 4-7c. The basin probably received sediments shed east from the prism and west from the continent. The Triassic rocks were later overthrust by the accretionary prism and were partly incorporated into it, along with lower Paleozoic rocks, due to continued eastward motion of the prism as convergence persisted. This resulted in eastward tectonic progradation of



E



contact  
rocks

and

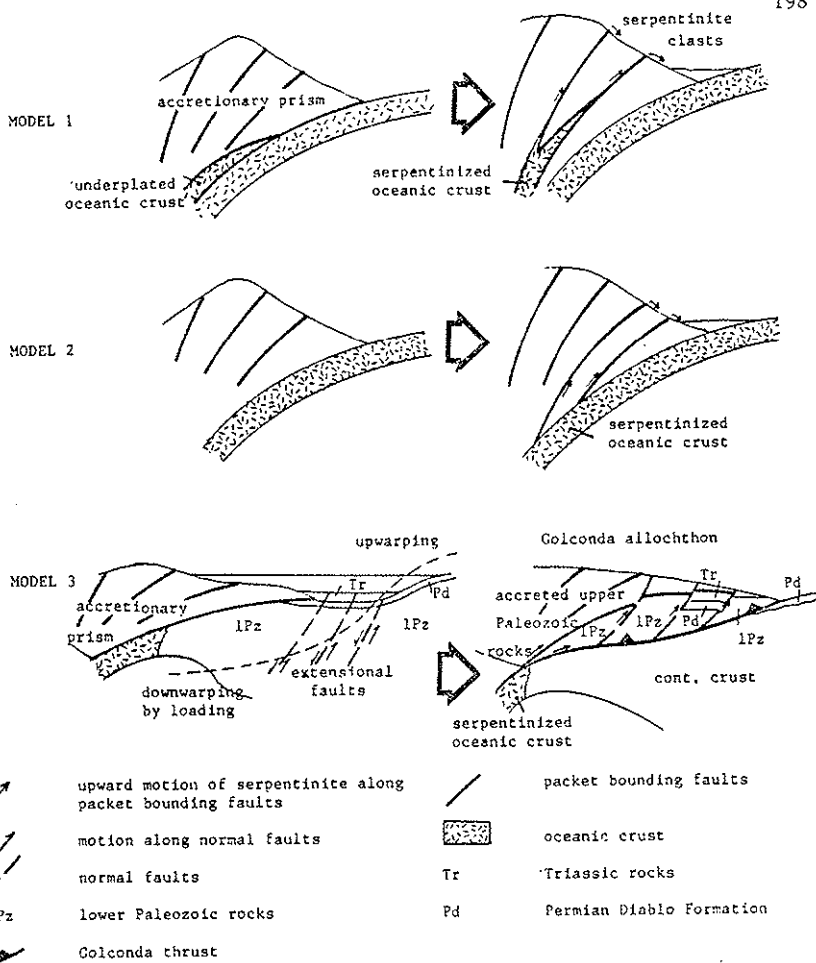


Figure 4-7. Three alternative tectonic models for the origin and mode of emplacement of serpentinites in the Golconda allochthon.

the allochthon by imbrication and incorporation of lower Paleozoic rocks of the lower plate in packets such as 1 and 9.

The rest of this section is an analysis of possible origins and modes of emplacement of serpentinite in the Golconda allochthon (Chapter 2).

#### Serpentinization

Serpentine can be formed by hydration of peridotite, harzburgite, and lherzolite (Coleman, 1971, 1977); type of rocks that are commonly found in oceanic crust. Serpentine minerals can be stable over different ranges of P-T conditions depending on activity of H<sub>2</sub>O, composition, and oxygen fugacity (Faust and Fahey, 1962; Yoder, 1967; Barnes and O'Neil, 1969; Iishi and Saito, 1973; Coleman, 1977). Experimental work shows that most of serpentinites can form from ophiolite peridotites in the temperature range of 100°-300° C (Wenner and Taylor, 1971).

The amount of water needed to form serpentine from a peridotite depends on the original content of olivine, pyroxene, and plagioclase in the ultramafic rock, and on the mobility of Mg, Si, or both (Coleman, 1977). Stable isotope studies of serpentinites dredged from ocean floors and those from ophiolite serpentinites indicate that the source of water for ocean serpentinite is ocean water, whereas many ophiolite serpentinites were formed by meteoric water, in a continental crustal environment, at temperatures between 0° and 300° C (Magaritz and Taylor, 1974; Wenner and Taylor, 1971; Coleman, 1977).

Du  
gr/cm<sup>3</sup>  
tectoni  
Mansfie  
believe  
low str  
their lo  
alternat  
allochth  
Model 1  
an ocean  
tionary  
to the  
Kay, 1981  
been faci  
a depth w  
vert the  
4-7a). Wa  
was supp  
consolida  
porting  
observed  
drilling  
with these  
Huene and

ible origins and  
lconda allochthon

ite, harzburgite,

s that are commonly

stable over dif-

ty of H<sub>2</sub>O, composi-

er, 1967; Barnes

(1977). Experimental

ophiolite perido-

(Wenner and Taylor,

from a peridotite

ne, and plagioclase

l, or both (Cole-

dredged from ocean

te that the source

reas many ophiolite

ontinental crustal

(Magaritz and Tay-

During serpentinization, density of peridotite decreases from 3.3 gr/cm<sup>3</sup> to 2.5 gr/cm<sup>3</sup> in serpentinite. If serpentinites become intensely tectonized, their shear strength may be reduced to 1 bar (Cowan and Mansfield, 1970; Coleman, 1977). In this context, it is reasonable to believe that sheared serpentinites can plastically flow upward under low stress, for example along weak zones such as faults, because of their low density and weak nature (Coleman, 1977). The following are alternative models for emplacement of the serpentinite in the Golconda allochthon based on the above discussion.

Model 1 - The fault-zone serpentinites (Chapter 2) are originated from an oceanic crust which lied under upper Paleozoic rocks. In an accretionary model, the ocean crust could have partly segmented and attached to the base of the prism in the upper plate by underplating (Karig and Kay, 1981; Moore and others, 1981), a tectonic process that could have been facilitated by serpentinization of the oceanic crust as it slid to a depth where temperature and activity of H<sub>2</sub>O were high enough to convert the ultramafic lower layer of the crust into serpentinite (Figure 4-7a). Water needed to form serpentinite from peridotite or harzburgite was supplied by dewatering of the subducted sediments as they became consolidated or by chemical reactions (Von Heuene and Lee, 1982). Supporting evidence for this hypothesis are the high fluid pressure observed in modern subduction zones, for example Barbados, from DSDP drilling (Moore and other, 1982) and by other observations associated with these high elevated pore pressures such as shale diapirs (Von Huene and Lee, 1982). Moreover, packets of massive and pillow basalts

201

are common in the Golconda allochthon (e.g. v1b, v2b, P2b units). Basalts of the Golconda allochthon, 20 km to the south of the study area, are related to ocean floor through chemical analysis by Speed (1977a). The presence of basaltic slices in the Golconda allochthon of the study area, assuming that they were part of an oceanic crust, suggests that the oceanic crust which went under the Golconda accretionary prism was partly accreted to the prism probably through underplating. Chemical and mineralogical studies of serpentinite slices in unspecified positions in Paleozoic rocks indicate that they are derived from olivine-rich rocks such as dunite and harzburgite (Poole, 1973). Poole (1973) interpreted these serpentinites as fragments of Paleozoic or older upper mantle that were incorporated in the Roberts Mountain and Golconda allochthon through unspecified tectonic processes during Paleozoic plate convergence.

Model 2 - Fault-zone serpentinites are originated from serpentinitized part of an oceanic crust after it moved under the accretionary prism through upward plastic diapiric movement that was facilitated by its buoyancy and low shear strength as discussed before (Figure 4-7b).

Model 3 - Fault-zone serpentinites are diapirically injected from beneath the Golconda accretionary prism, after or during its last stage of emplacement, along extensional faults (R. C. Speed, Pers. Comm., 1982) which were formed by flexing the underriding lithosphere because of the load of the accreted or accreting Golconda allochthon as modeled by Speed and Sleep (1982) (Figure 4-7c). The source of the serpentinite



2b, P2b units).

south of the study  
analysis by Speed  
Golconda allochthon of  
oceanic crust, sug-  
Golconda accretionary  
through underplating.  
slices in unspéci-  
are derived from  
Poole, 1973). Poole  
of Paleozoic or  
Roberts Mountain and  
processes during

from serpentinitized  
accretionary prism  
facilitated by its  
(Figure 4-7b).

ly injected from  
ing its last stage  
ed, Pers. Comm.,  
lithosphere because  
allochthon as modeled  
of the serpentinite

could be those discussed in models 1 and 2 or from the upper mantle.

The flexural model is appealing because it also explains the emplacement of the allochthonous lower Paleozoic packets and formation of a basin for the deposition of the now allochthonous Triassic rocks (Figure 4-6 and 4-7c).

Model 4 - Fault-zone serpentinites were deposited as large olistostromes which were carried with other clastic debris into the depositional site of the terrigenous rocks. The source of these olistostromes could have been in the older Roberts Mountain allochthon, or older serpentinites in structurally higher positions in the Golconda allochthon which themselves were formed by models 1, 2, and 3. Although there is a serpentinite slice in the lower Paleozoic autochthonous rocks in Wisconsin Canyon, this model is not favored because of the apparent lack of more of such serpentinites in the autochthon, and because not all the large serpentinite slices are associated with terrigenous clastic rocks. Moreover, this model does not explain the presence of fault-zone serpentinites along packet boundaries. The clastic serpentinites could have been supplied from the fault-zone serpentinites as they were exposed on the surface of the accretionary prism in models 1 and 2, and from the autochthon in model 3.

#### Correlation with other parts of the Golconda allochthon

Jett to Wall Canyons - The nearest place, where the allochthon has been studied in detail is between Jett and Wall Canyons, about 20 km to the south of the study area (R. C. Speed 1971-3 unpub. data; Speed, 1977a;

Speed and others, 1977). Here, the allochthon, identified by a succession of fault bounded packets of upper Paleozoic rocks, and the underlying Diablo Formation and lower Paleozoic rocks, are well correlated with rocks of the study area (Speed and others, 1977; Speed, 1977a). The major difference, however, is in the absence of the coarse-grained volcanogenic sedimentary rocks in this southern part of the allochthon. Here, the volcanic rocks are pillow basalts that are correlated chemically to oceanic tholeiite (Speed, 1977).

Speed (1977a) interpreted the allochthon in this area to comprise tectonic slices of oceanic pelagic and volcanic rocks that have since been dated as Mississippian-Permian (R. C. Speed, pers. comm.). The time of emplacement of these rocks on the continental margin is taken to be Late Permian or Mesozoic. The surface, separating the allochthon and the lower plate Diablo Formation is the folded Golconda thrust.

The tectonic fabric in the allochthon in this area is dominated by a slaty cleavage in pelite and axial planes of isoclinal folds of chert, both parallel to bedding except in hinges of folds (R. C. Speed 1977a, unpub. data). Here, chert beds are lenticular along the foliation. Such structures are well correlated with F1 structures in the study area.

The environment of deposition of upper Paleozoic allochthonous rocks is interpreted as the deep sea floor, either distal from a continental source or close to a continent but with a continental sediment bypass. (Speed, 1977a).

New Pass Range - Rocks of the New Pass Range assigned to the Golconda

tified by a succes-  
 ks, and the under-  
 are well correlated  
 7; Speed, 1977a).  
 the coarse-grained  
 of the allochthon.  
 e correlated chemi-  
 area to comprise  
 ks that have since  
 ers. comm.). The  
 al margin is taken  
 ng the allochthon  
 lconda thrust.  
 ea is dominated by  
 isoclinal folds of  
 olds (R. C. Speed  
 r along the folia-  
 structures in the  
 ic allochthonous  
 distal from a con-  
 tinentals sediment  
 to the Golconda

allochthon (MacMillan, 1972) can mostly be correlated with those in the  
 study area (Speed, 1977a). Here, the Golconda allochthon includes  
 highly deformed interbedded chert and pelite, homogeneous chert, vol-  
 canogenic sedimentary rocks, pillow basalts, pebbly mudstone, and  
 carbonate-quartz-chert sandstone (MacMillan, 1972; Speed, 1977a). The  
 allochthonous rocks of the New Pass Range are overlain by upper Lower  
 Triassic rocks with an angular unconformity. The allochthon is juxta-  
 posed by the Golconda thrust over autochthonous homoclinal upper Paleo-  
 zoic rocks, which correlate with the Antler Sequence (Chapter 1), and  
 highly deformed lower Paleozoic rocks of the Valmy Formation. Here,  
 the contact between the lower and upper Paleozoic rocks is an angular  
 unconformity.

MacMillan (1972) demonstrated that the emplacement of the Golconda  
 allochthon occurred before the deposition of the late Early Triassic  
 rocks, and further narrowed its age between post Guadalupian and pre-  
 Smithian (latest Late Permian to late Early Triassic).

The allochthonous upper Paleozoic rocks have undergone two major  
 folding events in the new Pass Range (MacMillan 1972). First folds are  
 isoclinal with W to WNW plunging axes. These are refolded homoaxially.  
 These folds do not exist in the upper Paleozoic terrigenous clastic and  
 shallow water autochthonous rocks below the Golconda thrust. The second  
 folding occurred when the upper Paleozoic rocks were moved over the  
 Golconda thrust. In this second event, folds were formed both in the  
 allochthonous rocks and locally in the upper thin layer of the auto-  
 chthon with coplanar axial planes dipping shallowly WNW. These folds

are overturned toward the east, indicating a significant west to east component of displacement over the Golconda thrust.

Northern Nevada - The rocks belonging to the Golconda allochthon in northern Nevada (The Havallah sequence) include chert-greenstone-jasperoid units that range in age from Mississippian to Permian, chert and argillite of Late Devonian to Permian age, siliciclastic, calcareous, and volcanoclastic turbidites, and massive sulfide and siliceous Fe and Mn deposits (Snyder and Brueckner, 1983). These authors interpret the rocks to have been deposited in an ocean basin with active spreading (during late Paleozoic) which were emplaced over the continental North America between latest Permian and late Early to Middle Triassic. Through diagenetic, lithologic, and structural analyses, these workers suggest that the allochthon was pre-packaged through accretionary processes during late Paleozoic, before its eastward emplacement along the Golconda thrust.

An evidence of an unconformable contact between upper Middle Triassic rocks, the Havallah Sequence, and the Golconda thrust is given by Nichols (1971), indicating that in this part of Nevada, the Golconda thrust is older than late Middle Triassic (Silberling, 1973).

Miller and others (1982), correlating the Schoonover complex in the Independence Mountains and the Havallah sequence, prefer a back arc thrusting model (Chapter 1) for the evolution and emplacement of the Golconda allochthon.

Lithology and structural fabric of the allochthonous and autochthonous rocks in the New Pass Range and probably other parts of

icant west to east

da allochthon in

chert-greenstone-

to Permian, chert

iclastic, calcare-

de and siliceous

ese authors inter-

asin with active

aced over the con-

e Early to Middle

ructural analyses,

-packaged through

fore its eastward

een upper Middle

da thrust is given

vada, the Golconda

, 1973).

nover complex in

prefer a back arc

placement of the

honous and auto-

bly other parts of

northern Nevada correlate well with those in the study area, indicating<sup>206</sup> that the allochthon is a coherent and continuous tectonic assemblage with regional extent and systematic depositional and tectonic history which can best be explained by plate interactions during late Paleozoic and early Mesozoic.

### References

- Anderson, T. B., 1964, Kink bands and related geological structures. Nature, v. 202, p. 272-274.
- Anderson, T. B., 1968, The geometry of a natural orthorhombic system of kink bands. Can. Geol. Surv. Pap., v. 52, p. 200-228.
- Anderson, T. B., 1974, The relationship between kink bands and shear fractures in the experimental deformation of slate. Jour. geol. Soc. Lon., v. 130, p. 367-382.
- Barnes, I. and O'Neil, J. R., 1969, The relationship between fluids in some fresh Alpine-type ultramafic rocks and possible modern serpentinization, western United States. GSA Bull., v. 80, p. 1947-1960.
- Bell, T. H., 1978, Progressive deformation and reorientation of fold axes in a ductile mylonite zone: The Woodruffe thrust. Tectonophysics, v. 44, p. 285-320.
- Berger, W. H., 1974, Deep-sea sedimentation. In: C. A. Burke and C. L. Drake eds. The geology of continental margins. p. 213-241, Springer-Verlag, New York.
- Borg, I. and Handin, J., 1966, Experimental deformation of crystalline rocks. Tectonophysics, v. 3, p. 249-367.
- Boulter, C. A., 1976, Sedimentary fabric and their relation to strain analysis methods. Geology, v. 4, p. 141-146.
- Bouma, A. H., 1962, Sedimentology of some flysch deposits: A graphic approach to facies interpretation. Elsevier, Amsterdam, 168p.
- Bouma, A. H. and Hollister, C.D., 1973, Deep ocean basin sedimentation. In: Turbidites and deep water sedimentation. SEPM, Pacific section, short course, Anaheim, p. 79-118.
- Burchfiel, B. C., and Davis, G. A., 1972, Structural framework and evolution of the southern part of the Cordilleran orogen, western United States: Amer. Jour. of Sci., v. 272, p. 97-118.
- Burke, D. B., 1973, Reinterpretation of the "Tobin" thrust: Pre-Tertiary geology of the southern Tobin Range, Pershing County, Nevada. PhD thesis, Stanford University, 82p.
- Chapman, T. J., Milton, N. J., & Williams, G. D., 1979, Shape fabric variations in deformed conglomerates at the base of the Lakesfjord Nappe, Norway. J. geol. Soc. Lon., v. 136, p. 683-691.

- Churkin, M. Jr., and Kay, M., 1967, Graptolite-bearing Ordovician siliceous and volcanic rocks, northern Independence Range, Nevada: GSA Bull., v. 78, p. 651-668.
- Churkin, M. Jr., 1974, Paleozoic marginal basin-volcanic arc systems in the Cordilleran foldbelts. SEPM Spec. Pub. 19, 174-192.
- Clifford, P. M., 1968, Kink band development in the Lake St. Joseph area, northwestern Ontario. Can. Geol. Surv. Pap., 68-52, p. 229-242.
- Cloos, E., 1947, Oolite deformation in the south Mountain fold, Maryland. GSA Bull., v. 58, p. 843-918.
- Cloos, E., 1971, Microtectonics along the western edge of the Blue Ridge Maryland and Virginia. The John Hopkins Press, Baltimore and London.
- Cogbill, A. H., 1979, Relationships of crustal structures and seismicity, western Great Basin. PhD thesis: Northwestern Univ. Evanston, Ill., 253p.
- Coleman, R. G., 1971, Petrologic and geophysical nature of serpentinites. GSA Bull., v. 82, p. 897-918.
- Coleman, R. G., 1977, Ophiolites, ancient oceanic lithosphere? Springer-Verlag Berlin, Heidelberg, New York, 229p.
- Cowan, D. S. and Mansfield, C. E., 1970, Serpentinite flows on Joaquin Ridge, southern coast Ranges, California. GSA Bull., v. 81, p. 2615-2628.
- Dewey, J. F. 1965, Nature and origin of kink bands. Tectonophysics, v. 1, p. 459-494.
- Dewey, J. F., 1969, The origin and development of kink bands in a foliated body. Geol. J., v. 6, p. 193-216.
- Dickinson, W. R., 1977, Paleozoic plate tectonics and the evolution of the Cordilleran continental margin. In Stewart, J. H., Stevens, C. H., and Fritsche, A. E., eds., Paleozoic paleogeography of the western United States: SEPM Pacific section, Pacific paleogeography sym. 1, p. 137-155.
- Donath, F. A., 1968, Experimental study of kink band development in Martinburg shale. Can. Geol. Surv. Pap., 68-52, p. 225-242.
- Dunnet, D., 1969, A technique for finite strain analysis using elliptical particles. Tectonophysics, v. 7, p. 117-136.

- Dunnet, D. & Siddans, A. W. B., 1971, Non-random sedimentary fabrics and their modification by strain. Tectonophysics, v. 12, p. 307-325.
- Durney, D. W. and Ramsay, J. R., 1973, Incremental strain measured by syntectonic crystal growth. In Dejong, K. A. and Scholton, R. eds., Gravity and tectonics. Wiley, New York, N. Y.
- Escher, A. and Watterson, J., 1974, Stretching fabrics, folds and crustal shortening. Tectonophysics, v. 22, p. 223-231.
- Elliott, D., 1970, Determination of finite strain and initial shape from deformed elliptical objects. GSA Bull., v. 81, p. 2221-2236.
- Fagan, J. J., 1962, Carboniferous chert, turbidites, and volcanic rocks in northern Independence Range, Nevada: GSA Bull., v. 73, p. 595-612.
- Ferguson, H. G., Muller, S. W., and Roberts, R. J., 1951, Geology of the Winnemucca Quadrangle, Nevada. U. S. Geol. Surv. GQ-11.
- Ferguson, H. G., Roberts, R. J., and Muller, S. W., 1952, Geologic map of the Golconda Quadrangle, Nevada. U.S. Geol. Surv. GQ-15.
- Ferguson, H. G., and Cathcart, S. H., 1954, Geologic map of the round Mountain Quadrangle, Nevada: U.S. Geol. Surv. Geol. Quad. Map GQ-40.
- Faust, G. T., and Fahey, J. J., 1962, The serpentine-group minerals. U.S. Geol. Surv. Prof. Pap., v. 384-A, p. 1-91.
- Flinn, D., 1956, On the deformation of the Funzie conglomerate, Fetlar, Shetland. Jour. Geology, v. 64, p. 480-505.
- Flinn, D., 1962, On folding during three dimensional progressive deformation. Q. J. geol. Soc., v. 118, p. 385-433.
- Fyson, W. H., 1968, Profile variation in a kink set. Can. Geol. Surv. Pap., 68-52, p. 243-254
- Gay, N. C., 1968a, Pure shear and simple shear deformation of inhomogeneous viscous fluids. 1. Theory. Tectonophysics, v. 5, p. 211-234.
- Gay, N. C., 1968b, Pure shear and simple shear deformation in inhomogeneous viscous fluids. 2. The determination of the total finite strain in a rock from objects such as deformed pebbles. Tectonophysics, v. 5, p. 295-302.
- Gay, N. C., 1969, The analysis of strain in the Barberton Mountain Land, Eastern Transvaal, using deformed pebbles. J. Geol. v. 77, p. 377-396.



imentary fabrics  
v. 12, p. 307-

n measured by  
olton, R. eds.,

folds and cru-

initial shape  
p. 2221-2236.

volcanic rocks  
73, p. 595-612.

1, Geology of  
GQ-11.

, Geologic map  
GQ-15.

of the round  
quad. Map GQ-40.

roup minerals.

merate, Fetlar,

gressive defor-

n. Geol. Surv.

on of inhom-  
v. 5, p. 211-

on in inhom-  
he total finite  
s. Tectonophy-

erton Mountain  
Geol. v. 77, p.

Gay, N. C. and Weiss, L. E., 1974, The relationship between principal stress directions and the geometry of kinks in foliated rocks. Tectonophysics, v. 21, p. 287-300.

Gay, N. C. & Fripp, R. E. P., 1976, The control of ductility on the deformation of pebbles and conglomerate. Phil. Trans. R. Soc. Lond. A., v. 283, p. 109-128.

Griffiths, J. C., 1967, Scientific method in analysis of sediments. New York, McGraw-Hill Book Co, 508 p.

Helms, D. G. & Siddans, A. W. B., 1971, Deformation of a slaty lapillar tuff in the English Lake Districts: Discussion. GSA Bull., v. 82, p. 523-531.

Hobbs, B. E. and Talbot, J. L., 1966, The analysis of strain in deformed rocks. Jour. of Geology, v. 74, p. 500-513.

Hobson, D. M., 1971, Deformed agglomerates near Tintagel, North Cornwall. Geol. Mag., v. 108, p. 383-391.

Hobson, D. M., 1973, The origin of kink bands near Tintagel, North Cornwall. Geol. Mag., v. 110, p. 133-144.

Holst, T. B., 1982, The role of initial fabric on strain determination from deformed elliptical objects. Tectonophysics, v. 82, p. 329-350.

Hossack, J. R., 1968, Pebble deformation and thrusting in the Bygdin area (S. Norway). Tectonophysics, v. 5, p. 315-339.

Iishi, K. and Saito, M., 1973, Synthesis of antigorite. Am. Mineralogist, v. 58, p. 915-919.

Karig, D. E. and Sharman, G. E., 1975, Subduction and accretion in trenches. GSA Bull., v. 86, p. 377-389.

Karig, D. E. and Kay, R. W., 1981, Fate of sediments on the descending plate at convergent margins. Phil. Trans. R. Soc. Lond. A-301, p. 233-251.

Kay, M., and Crawford, J. P., 1964, Paleozoic facies from the miogeosynclinal to the eugeosynclinal belt in thrust slices, central Nevada: GSA Bull., v. 75, p. 425-454.

Ketner, K., 1982, Jurassic or later age of Golconda thrust - evidence from Quinn River and Pinnon-Adobe range areas. Presented at the Sonoma Penrose Conference " Sonoma orogeny and Permian to Triassic tectonism in western North America. Winnemucca, Nevada.

- Kistler, R. W. and Peterman, W. E., 1973, Variations in Sr, Kd, K, Na, and initial  $^{87}\text{Sr}/^{86}\text{Sr}$  in Mesozoic granitic rocks and intruded wall rocks in central California. GSA Bull., v. 84, p.3489-3512.
- Kistler, R. W., 1974, Phanerozoic batholiths in western North America. Ann. Rev. Earth and Planet. Sci., v.2, p. 403-419.
- Kistler, R. W., and Peterman, Z. E., 1978, Reconstruction of crustal blocks of California on the basis of initial Sr isotopic compositions of Mesozoic plutons: U.S. Geol. Surv. prof. paper 1061, 27p.
- Kleinhampl, F. J., and Ziony, J. I., 1967, Preliminary geologic map of northern Nye county, Nevada: U.S. Geol. Surv. open file map, scale 1:250,000.
- Kleist, J. R., 1972, Kink bands along Denali fault, Alaska. GSA Bull., v. 83, p. 3487-3490.
- Krumbein, W. L. & Graybill, F. A., 1965, An introduction to statistical models in Geology. McGraw Hill, New York.
- Laine, M, 1977, The origin of the Toiyabe Quartz Latite. Ms thesis, Northwestern University, Evanston, Il.
- Laule, S. W., Snyder, W. S., and Ormiston, A. R., 1981, Willow Canyon Formation, Nevada, an extension of the Golconda allochthon: GSA Abs. with Prog. v. 13, p. 66.
- Lisle, R. J., 1977a, Clastic grain shape and orientation in relation to cleavage from the Aberyswyth grits, Wales. Tectonophysics, v. 39, p. 381-395.
- Lisle, R. J., 1977b, Estimation of the tectonic strain ratio from the mean shape of deformed elliptical markers. Geol. Mijnbouw, v. 56, p. 140-144.
- Lisle, R. J., 1979, Strain analysis using deformed pebbles: The influence of initial pebble shape. Tectonophysics, v. 60, p. 263-277.
- MacMillan, J. R., 1972, Late Paleozoic and Mesozoic tectonic events in west central Nevada. PhD thesis, Northwestern University, 146p.
- MacMillan, J. R., 1974, Re-examination of the Diablo Formation, Jett Canyon, Toiyabe Range, Nevada. GSA Abs with Prog., v. 6, p. 211.
- Magaritz, M. and Taylor, H. P., Jr., 1974, Oxygen and hydrogen isotope studies of serpentinization in the Troodos ophiolite complex, Cyprus. Earth Planet. Sci. Lett., v.23, p.8-14.
- Matti, J. C., and McKee, E. H., 1977, Silurian and lower Devonian

s in Sr, Kd, K, Na,  
ks and intruded wall  
p. 3489-3512.

tern North America.  
9.

struction of crustal  
Sr isotopic composi-  
paper 1061, 27p.

ary geologic map of  
open file map, scale

Alaska. GSA Bull.,

ction to statistical

atite. Ms thesis.

1981, Willow Canyon  
allochthon: GSA Abs.

ation in relation to  
ctonophysics, v. 39,

ain ratio from the  
bl. Mijnbouw, v. 56,

bbles: The influ-  
60, p. 263-277.

ectonic events in  
iversity, 146p.

o Formation, Jett  
k., v. 6, p. 211.

nd hydrogen isotope  
ophiolite complex,

nd lower Devonian

paleogeography of the outer continental shelf of the Cordilleran miogeoclinal, central Nevada. In Stewart, J. H., Stevens, C. H., and Fritsche, A. E., eds., Paleozoic paleogeography of the western United States: SEPM Pacific Section. Pacific Coast paleogeography Sym. 1, p. 39-65.

McKee, E. H., 1976a, Geologic map of the Austin Quadrangle, Lander County, Nevada: U.S. Geol. Surv. geol. Quad. Map GQ-1307, scale 1:62,500.

McKee, E. H., 1976b, Geology of the northern part of the Toquima Range, Lander, Eureka, and Nye counties, Nevada. U.S. Geol. Surv. Prof. paper 931, 49p.

Middleton, G. V. and Hampton, M. A., 1976, Subaqueous sediment transport and deposition by sediment gravity flows. In: Stanley, D. J., and Swift, D. J. P., eds. Marine sediment transport and environmental management. p. 197-218. New York, Wiley-Intersci. publ.

Miller, E. L., Bateson, J., Dinter, D., Dyer, J. R., Harbaugh D., and Jones, D. L., 1981, Thrust emplacement of the Schoonover sequence, northern Independence Mountains, Nevada: GSA Bull., v. 92, p. 730-737.

Miller, E. L., Kanter, L. R., Larue, D. K., Murchey, B., and Jones, D. L., 1982, Structural fabric of the Paleozoic Golconda allochthon, Antler Peak Quadrangle, Nevada: Progressive deformation of an oceanic sedimentary assemblage. Jour. Geophys. Res., v. 87, p. 3795-3804.

Mitra, S., 1976, A quantitative study of deformation mechanism and finite strain in quartzites. Contrib. Mineral. Petrol., v. 59, p. 203-226.

Moore, E. M., 1970, Ultramafics and orogeny, with models of the U. S. Cordillera and the Tethys. Nature, v. 228, p. 837-842.

Moore, J. C., Watkins, J. S., and Shipley, T. H., 1981, Summary of accretionary processes, Deep Sea Drilling Project Leg 66: offscraping, underplating and deformation of the slope apron. Initial Repts. of the DSDP, v. 66, p. 825-836.

Moore, J. C. and others, 1982, Offscraping and underthrusting of sediment at the deformation front of the Barbados Ridge: Deep Sea Drilling Project Leg 78A. GSA Bull. v. 93, p. 1065-1077.

Mukhopadhyay, D., 1973, Strain measurements from deformed quartz grains in the slaty rocks from Ardennes and the northern Eifel. Tectonophysics, v. 16, p. 279-296.

- Muller, S. W., Ferguson, H. G., and Roberts, R. J., 1951, Geology of the Mount Tobin Quadrangle. U. S. Geol. Surv. Geologic quadrangle Map GQ-7.
- Mutti, E. and Ricci-Lucchi, F., 1978, Turbidites of the northern Apennines: Introduction to facies analysis. International Geology Review, v. 20, p. 125-166.
- Naha, K. and Halburton, R. V. 1974, Late stress systems deduced from conjugate folds and kink bands in the "Main Railo syncline", Udaipur District, Rajasthan, India. GSA Bull., v. 85, p. 251-256.
- Nelson, C. H. and Kulm, L. D., 1973, Submarine fans and channels. In: Turbidites and deep water sedimentation. p. 39-78. SEPM Pacific Section, Short course, Anaheim, Calif.
- Nelson, C. H. and Nilson, T., 1974, Depositional trends of modern and ancient deep-sea fans. In: Dott, R. H. and Shaver, R. H., eds. Modern and ancient geosynclinal sedimentation. SEPM Spec. Pub. v. 19, p. 69-91.
- Nichols, K. m., 1971, Overlap of the Golconda thrust by Triassic strata, north-central Nevada. GSA Abs with Prog. v. 3, p. 171.
- Normark, W. R., 1970, Growth patterns of deep sea fans. AAPG Bull., v. 54, p. 2170-2195.
- Normark, W. R., 1974, Submarine canyons and fan valleys: factors affecting growth patterns of deep sea fans. In: Dott, R. H. and Shaver, R. H. eds. Modern and ancient geosynclinal sedimentation. SEPM Spec. Pub. no. 19, p. 56-68.
- Oertel, G., 1978, Strain determination from the measurement of pebble shapes. Tectonophysics, v. 50, p. T1-T7.
- Patterson, M. S. and Weiss, L. E., 1966, Experimental deformation and folding in phyllite. GSA Bull., v. 77, p. 343-374.
- Peach, C. J. & Lisle, R. J., 1979, A FORTRAN IV program for the analysis of tectonic strain using deformed elliptical markers. Computers & Geosciences, v. 5, p. 325-334.
- Pfiffner, O. A., 1980, Strain analysis in folds (Intrahelvetic Complex, Central Alps). Tectonophysics, v. 61, p. 337-362.
- Poole, F. G., 1973, Alpine-type serpentinites in Nevada and their tectonic significance. GSA Abs. with Prog. v. 5, p. 90.
- Poole, F. G., and Sandberg, C. A., 1977, Mississippian Paleogeography and tectonics of the western United States. In Stewart, J. H.,

Stev  
of  
pale

Prohdeh  
U.S.

Ramsay  
Mag.

Ramsay,  
Hill

Ramsay,  
Canac

Ramsay,  
chang  
263-2

Ramsay,  
defor

Rhodes,  
tures  
of th  
114.

Roberts,  
U.S.

Roberts,  
Paleoz  
2857.

Roberts,  
system  
v. 12,

Robin, P.  
orient  
T16.

Rousell,  
Basin,

Sanderson  
region

Scholl, D

Stevens, C. H., and Fritsche, A. E., eds. Paleozoic paleogeography of the western United States: SEPM Pacific section. Pacific Coast paleogeography sym. 1, p. 181-215.

Prohdehl, C., 1979, Crustal structure of the western United States: U.S. Geol. Surv. prof. paper 1034, 74p.

Ramsay, J. G., 1962, The geometry of conjugate fold systems. Geol. Mag., v. 99, p. 516-526.

Ramsay, J. G., 1967, Folding and fracturing of rocks. New York, McGraw Hill Book Co., 568p.

Ramsay, J. G. and Graham, R. H., 1970, Strain variation in shear belts. Canadian Jour. Earth Sci. v. 7, p. 786-813.

Ramsay, J. G. and Wood, D. S., 1973, The geometric effects of volume change during deformation processes. Tectonophysics, v. 16, p. 263-277.

Ramsay, D. M., 1979, Analysis of rotation of folds during progressive deformation. GSA Bull., v. 90, p. 732-738.

Rhodes, S. and Gayer, R. A., 1977, Noncylindrical folds, linear structures in the X-direction and mylonite developed during translation of the Caledonian Kalak Nappe Complex of Finmark. Geol. Mag., v. 114, p. 329-341.

Roberts, R. J., 1951, Geology of the Antler Peak Quadrangle, Nevada: U.S. Geol. Surv. Geol. Quad. Map GQ-10, scale 1:62,500.

Roberts, R. J., Hotz, P. E., Gilluly, J., and Ferguson, H. G., 1958, Paleozoic rocks of north-central Nevada: AAPG Bul., v. 42, p. 2813-2857.

Roberts, D., 1971, Stress regime and distribution of a conjugate fold system from the Trondhaim region, Central Norway. Tectonophysics, v. 12, p. 155-165.

Robin, P. Y. F., 1977, Determination of geologic strain using randomly oriented strain markers of any shape. Tectonophysics, v. 42, p. T7-T16.

Rousell, D. H., 1980, Kink bands in the Onaping Formation, Sudbury Basin, Ontario. Tectonophysics, v. 66, p. 83-97.

Sanderson, D. J., 1973, The development of fold axes oblique to the regional trend. Tectonophysics, v. 16, p. 55-70.

Scholl, D. W., Von Huene, R., Vallier, T. L., and Howell, D. G., 1980,

Sedimentary masses and concepts about tectonic processes at underthrust ocean margins. Geology, v. 8, p. 564-568.

Shimamoto, T. & Ikeda, Y. 1976. A simple algebraic method for strain estimation from deformed ellipsoidal objects. 1. Basic theory. Tectonophysics, v. 36, p. 315-337.

Siddans, A. W. B., 1972, Slaty cleavage - A review of research since 1815. Earth Sci. Rev., v. 8, p. 205-232.

Silberling, N. J., 1959, Pre-Tertiary stratigraphy and upper Triassic paleontology of the Union District, Shoshone Mountains, Nevada. U. S. Geol. Surv. Prof. Pap., v. 332, 59p.

Silberling, N. J., and Roberts, R. J., 1962, Pre-Tertiary stratigraphy and structure of northwestern Nevada: GSA Spec. Paper 72, 58p.

Silberling, N. J. 1973, Geologic events during Permian-Triassic time along the Pacific margin of the United States: Alberta Soc. of Petrol. Geol. Mem. 2, p. 345-362.

Silberling, N. J., 1975, Age relationships of the Golconda thrust fault, Sonoma Range, north-central Nevada: GSA spec. paper 163, 28p.

Snyder, W. S., and Brueckner, H. K., 1983, Tectonic evolution of the Golconda allochthon, Nevada: Problems and perspectives: in Stevens, C. H., Pre-Jurassic rocks in western North American suspect terranes: SEPM Pacific section

Speed, R. C., 1971a, Permo-Triassic continental margin tectonics in western Nevada: GSA Abs with Prog., v. 3, p. 199.

Speed, R. C., 1971b, Golconda thrust, western Nevada: regional extent: Geol. Soc. Am. Abs. with prog. v.3, p. 199.

Speed, R. C. and Armstrong, R. L., 1971, K-Ar ages of some minerals from igneous rocks of western Nevada. Isochron West, v. 71-1, p. 1-8.

Speed, R. C., 1974, Record of continental margin tectonics in the Candalaria Fm., Nevada. GSA Abs with Prog., v. 6, p. 259.

Speed, R. C. and McKee, E. H., 1976, Age and origin of the Darrough Felsite, southern Toiyabe Range, Nevada: U.S. Geol. Surv. Jour. Research, v. 4, p. 75-81.

Speed, R. C., 1977a, An appraisal of the Pablo Formation of presumed Paleozoic age, central Nevada. In Stewart, J. H., Stevens, C. H., and Fritsche, A. E., eds., Paleozoic paleogeography of the western United States: SEPM Pacific section. Pacific paleogeography Sym. 1,

P.  
Speed,  
lat  
Ste  
of  
pal  
Speed,  
197  
and  
C.  
west  
GEOL  
Speed,  
earl  
Howe  
of  
pale  
Speed,  
Stat  
Speed,  
ary  
logi  
Speed, R  
catic  
Speed, R  
basin  
Speed. R  
Prese  
mian  
Nevad  
Speed, R.  
wester  
Speed, R.  
I. Cha  
Stanley,  
turbid  
ment i  
lin,  
287-34

nic processes at  
568.

ethod for strain  
asic theory. Tec-

f research since

d upper Triassic  
tains, Nevada. U.

ary stratigraphy  
per 72, 58p.

ian-Triassic time  
s: Alberta Soc. of

Golconda thrust  
E. paper 163, 28p.

evolution of the  
tives: in Stevens,  
can suspect ter-

in tectonics in

regional extent:

of some minerals  
West, v. 71-1, p.

onics in the Can-  
259.

of the Darrough  
Geol. Surv. Jour.

ion of presumed  
, Stevens, C. H.,  
of the western  
geography Sym. 1.

Speed, R. C., 1977b, Island-arc and other paleogeographic terranes of late Paleozoic age in the western Great Basin. In Stewart, J. H., Stevens, C. H., and Fritsche, A. E., eds., Paleozoic paleogeography of the western United States: SEPM Pacific section, Pacific coast paleogeography sym. 1, p. 349-362.

Speed, R. C., MacMillan, J. R., Poole, F. G., and Kleinhampl, F. J., 1977, Diablo Formation, central western Nevada: composite of deep and shallow water upper Paleozoic rocks. In Stewart, J. H., Stevens, C. H., and Fritsche, A. E., eds., Paleozoic paleogeography of the western United States: SEPM Pacific section, Pacific coast paleogeography sym. 1, p. 301-314.

Speed, R. C. 1978, Paleogeographic and plate tectonic evolution of the early Mesozoic marine province of the western Great Basin. In Howell, D. G., and McDougall, K. A., eds., Mesozoic paleogeography of the western United States: SEPM Pacific section, Pacific coast paleogeography Sym. 2, p. 253-270.

Speed, R. C., 1979, Collided Paleozoic microplate in the western United States: Jour. of Geology, v. 87, p. 279-292.

Speed, R. C., 1981, Geology of Barbados: implications for an accretionary origin. Oceanologica Acta, 26th Congress International de Geologie, Paris., p. 259-265.

Speed, R. C., and Larue, D. K., 1982, Barbados: Architecture and implications for accretion. Jour. of Geophys. Res. v. 87, p. 3633-3643.

Speed, R. C., and Sleep, N. H., 1982, Antler orogeny and foreland basin: A model: GSA Bull., v. 93, p. 815-828.

Speed, R. C., 1982, Tectonic history of the Sonoma orogeny Nevada. Presented at the Sonoma Penrose Conference "Sonoma orogeny and Permian to Triassic tectonism in western North America" Winnemucca, Nevada.

Speed, R. C., 1982b, Evolution of the sialic margin in the central western United States: AAPG Memoir, Hedberg vol. 34, p. 457-468.

Speed, R. C., 1983b, Structure of the accretionary complex of Barbados, I. Chalky Mount. GSA Bull., v. 94, p. 92-116.

Stanley, D. L. and Unrug, R., 1972, Submarine channel deposits, fluxoturbidites and other indicators of slope and base-of-slope environment in modern and ancient marine basins. In: Rigby, W. K. and Hamblin, W. K. eds. Recognition of ancient sedimentary environment, p. 287-340. SEPM Spec. Pub. v. 16, Tulsa.

- Stewart, J. H., 1972, Initial deposits of the Cordilleran geosyncline: evidence of a late Precambrian (850 m.y.) continental separation: GSA Bull., v. 83, p. 1345-1360.
- Stewart, J. H., and Poole, F. G., 1974, Lower Paleozoic and uppermost Precambrian Cordilleran miogeocline, Great Basin, western United States. In Dickenon, W. R., ed., Tectonics and sedimentation: SEPM spec. pub. 22, p. 27-57.
- Stewart, J. H., MacMillan, J. R., Nichols, K. M., and Stevens, C. H., 1977, Deep-water upper Paleozoic rocks in north-central Nevada- A study of the type area of the Havallah Formation. In Stewart, J. H., Stevens, C. H., and Fritsche, A. E., eds., Paleozoic paleogeography of the western United States: SEPM Pacific section. Pacific coast paleogeography sym. 1, p. 337-347.
- Stewart, J. H., and Carlson, J. E., 1978, Geologic map of Nevada. U.S. Geol. Surv. and Nevada Bur. of Mines and Geol. Scale 1: 500,000.
- Tobisch, O. T. and Fiske, R. S., 1976, Significance of conjugate folds and crenulations in the central Sierra Nevada, California. GSA Bull., v. 87, p. 1411-1420.
- Tobisch, O. T., Fiske, R. S., Sacks, S. & Taniguchi, D., 1977, Strain in metamorphosed volcanoclastic rocks and its bearing on the evolution of orogenic belts. GSA Bull., v. 88, p. 23-40.
- Tullis, T. E., and Wood, D. S., 1975, Correlation of finite strain from both reduction bodies and preferred orientation of mica in slates from Wales. GSA Bull., v. 86, p. 632-638.
- Turner, F. J. and Weiss, L. E., 1963, Structural Analysis of Metamorphic Tectonites. New York, McGraw Hill, 545p.
- Verbeek, E. R., 1978, Kink bands in the Somport slates, west central Pyrenees, France and Spain. GSA Bull., v. 89, p. 814-824.
- Von Huene, R. and Lee, H. M., 1982, The possible significance of pore fluid pressures in subduction zones. In: Watkins, J. S. and Drake, C. L., eds. Studies in continental margin geology. AAPG Mem, v. 34, p. 781-791.
- Walker, R. G. and Mutti, E., 1973, Turbidite facies and facies associations. In: Turbidites ad deep water sedimentation, p- 119-157. SEPM Pacific Section, Short course, Anaheim.
- Walker, R. G., 1975, Generalized facies models for resedimented conglomerates of turbidite association. GSA Bull., v. 86, p. 737-748.

Weiss, L.  
Can. J.

Weiss, L.  
sics,

Wenner, D.  
zation  
coexis  
p. 165

Williams,  
strain

Williams,  
sics, y

Wood, D. S.  
Ann. Re

Yoder, H.  
Washing



ran geosyncline:  
ental separation:

c and uppermost  
n, western United  
imentation: SEPM

Stevens, C. H.,  
central Nevada- A  
n Stewart, J. H.,  
ic paleogeography  
Pacific coast

of Nevada. U.S.  
le 1: 500,000.

conjugate folds  
California. GSA

, 1977, Strain  
ing on the evolu-

inite strain from  
of mica in slates

al Analysis of  
P.

s, west central  
14-824.

ificance of pore  
J. S. and Drake,  
AAPG Mem, v.

d facies associa-  
tion, p- 119-157.

for resedimented  
, v. 86, p. 737-

Weiss, L. E., 1968, Flexural slip folding of foliated model materials. Can. Geol. Surv. Pap., 68-52, p. 294-359.

Weiss, L. E., 1980, Nucleation and growth of kink bands. Tectonophysics, v. 65, p. 1-38.

Wenner, D. B. and Taylor, H. P., Jr., 1971, Temperatures of serpentinization of ultramafic rocks based on  $O^{18}/O^{16}$  fractionation between coexisting serpentine and magnetite. Cont. Mineral. Petrol., v. 32, p. 165-185.

Williams, P. F., 1976, Relationships between axial plane foliations and strain. Tectonophysics, v. 30, p. 181-196.

Williams, P. F., 1977, Foliation: A review and discussion. Tectonophysics, v. 39, p. 305-328.

Wood, D. S., 1974, Current views of the development of slaty cleavage. Ann. Rev. Earth and Planetary Science, v. 2, p. 1-37.

Yoder, H. S., Jr., 1967, Spilites and serpentinites. Carnegie Inst. Washington Year Book, v. 65, p. 269-279.

## APPENDIX I - METHODS OF TWO-DIMENSIONAL STRAIN ANALYSIS

The two dimensional strain methods used in this study are divided into two groups: I and II. These methods are described briefly in the following paragraphs and are informally referred to by letters A through H.

### GROUP I

#### Method A - (Slope method)

This method (Cloos, 1947, 1971; Ramsay, 1967) assumes that strain markers were initially spherical and is extended for the case of non-spherical grains by Mukhopadhyay (1973). If grains have an original axial ratio of 1, their axial ratio after strain reflects finite strain assuming that their ductility is the same as the matrix and that the strain is homogeneous, that is, amount and direction of strain are the same at every point of the rock. To determine whether grains in a deformed rock come from the same population of initial axial ratio, Mukhopadhyay (1973) used linear correlation of the long and short axis of the grains and defined,  $r$ , the coefficient of goodness of linear correlation (Krumbein and Graybill, 1965) (Eqn. 1),

$$r = \frac{\sum X_i Y_i}{\sqrt{(\sum X_i^2)(\sum Y_i^2)}} \quad (1)$$

where  $X$  and  $Y$  are the short and long axes of the grains. For perfect linear correlation,  $r$  is 1. A population of circular and elliptical

grains with constant initial axial ratio ( $R_i$ ) and orientation will after deformation show high values of  $r$  but still less than 1 because strain is in general inhomogeneous and therefore grains are elongated differently. However, if grains were originally elliptical with different  $R_i$  and (or) had random initial orientation,  $r$  will be low, and will decrease as strain increases (Mukhopadhyay, 1973).

The slope of a best fit line passing through the origin and data points on a long versus short axis plot (e.g. Fig. 3-57) will estimate the axial ratio of strain ellipse only if grains were initially circular and deformed homogeneously. Because grains have finite dimensions and can not attain zero length, the best fit line can not have an intercept. Equation 2 (Krumbein and Graybill, 1965; Mukhopadhyay, 1973) was used to calculate the slope of the best fit line forced to pass through the origin, where  $X$  and  $Y$  are as defined before.

$$\text{slope} = \frac{\sum X_i Y_i}{\sum X_i^2} \quad (2)$$

Methods B, C, and D - (Method of means)

Method B (Cloos, 1947, 1971; Ramsay, 1967; Lisle, 1977b; Hos-sack, 1969) assumes that grains had an original circular section and measures the arithmetic mean according to Equation 3, where  $R_f$  is the final axial ratio of the long and short axes of grains. Because the initial axial ratio and orientation ( $R_i$  and  $\theta$ ) of the grains are not included in this calculation, the arithmetic mean is an imprecise estimate of strain axial ratio unless grains were originally

circular and deformed homogeneously. Its validity for such an estimation is challenged in cases where initial eccentricity of the grains is unknown (Ramsay, 1967, p. 214; Lisle, 1977b).

Methods C and D use geometric and harmonic means of the grain axial ratios according to Equation 4 and 5, respectively, to estimate Rs.

arithmetic mean = A = ΣRf / N (3)

geometric mean = G = N / Rf<sub>1</sub> x Rf<sub>2</sub> x ... x Rf<sub>N</sub> (4)

harmonic mean = H = Σ(1 / Rf<sub>1</sub>) (5)

(where N is population of the grains )

The harmonic mean (H) was introduced for strain analysis by Lisle (1977b). The value of H is less than that of geometric mean, and both are less than the arithmetic mean.

The three means were tested against Rs through mathematical models by Lisle (1977b). He concluded that no simple mean of final axial ratios will give the strain ellipse, particularly when initial grain axial ratios are high and strain ratio is low. However, he also showed that if grains with moderate initial axial ratios (between 1 and 4) and with no preferred orientation are intensely but homogeneously strained, good estimate of strain ratio can be obtained from the harmonic mean of their axial ratios. He indicated further that the arithmetic mean of Rf is of little value for estimation of strain axial ratio because it is strongly dependent on initial shapes of the grains.

for such an esti-  
 ntricity of the  
 7b).  
 ns of the grain  
 ctively, to esti-

(3)

.... x Rf<sub>N</sub> (4)

(5)

alysis by Lisle  
 eometric mean, and

ough mathematical  
 ample mean of final  
 larly when initial  
 s low. However, he  
 ial axial ratios  
 tion are intensely  
 in ratio can be  
 tios. He indicated  
 e value for esti-  
 ongly dependent on

The methods of this group use axial ratio (Rf = long/short) and the angle between the long axis of grains and a reference line ( $\phi$ ). The reference line is usually the trace of cleavage on the sections where strain is measured. They use algebraic, graphic, and statistical procedures and take into consideration the factors that control the final shape of the grains as discussed in Chapter 3 (theory of strain) and therefore provide a better estimate of shape and orientation of two dimensional strain ellipse. Brief description of each of these methods is as follows:

Method E - (Method of Shimamoto and Ikeda, 1976)

This method assumes that initially randomly oriented ellipsoidal grains deform homogeneously with their matrix and is designed both for two and three dimensional strain analyses of which only the two dimensional part is discussed here.

The matrix representation of the strain ellipse is shown in Equation 6.

$$(X \ Y) \begin{pmatrix} \bar{E} & \bar{h} \\ \bar{h} & \bar{E} \end{pmatrix} \begin{pmatrix} X \\ Y \end{pmatrix} = 1 \quad (6)$$

This is a symmetric matrix and is called average final shape matrix (Shimamoto and Ikeda, 1976). The two measurable parameters, Rf and  $\phi$ , are used to calculate the components of this matrix using Equations 7 through 12.

$$f_i = 1 / Rf_i \cos^2 \phi_i + Rf_i \sin^2 \phi_i \quad (7)$$

$$g_i = 1 / Rf_i \sin^2 \phi_i + Rf_i \cos^2 \phi_i \quad (8)$$

$$h_i = (1 / ((1/Rf_i) - Rf_i)) \sin \phi_i \cos \phi_i \quad (9)$$

$$\bar{f} = 1 / N \Sigma f_i \quad (10)$$

$$\bar{g} = 1 / N \Sigma g_i \quad (11)$$

$$\bar{h} = 1 / N \Sigma h_i \quad (12)$$

The principal axes of the strain ellipse are eigenvalues ( $\lambda$ ) of the average final shape factor matrix and should satisfy the characteristic equation 13.

$$\begin{vmatrix} \bar{f} - \lambda_1 & \bar{h} \\ \bar{h} & \bar{g} - \lambda_2 \end{vmatrix} = 0 \quad (13)$$

Equation 13 can be diagonalized and solved for its two solutions;  $\lambda_1$  and  $\lambda_2$ . The length of the principal axes of the strain ellipse are  $1/\sqrt{\lambda_1}$  and  $1/\sqrt{\lambda_2}$ . The principal direction  $\theta$  is found by Equation 14.

$$\tan 2\theta = \bar{f} - \bar{g} \quad (14)$$

#### Method F - (Polar graph method of Elliott, 1970)

This method does not assume an initial random distribution of the elliptical grains and makes it possible to establish initial distribution solely by examining the deformed distribution on a

polar graph without information on the axial ratio or orientation of the strain ellipse.

Size and orientation of each deformed grain is plotted on polar coordinates with radius vector as a natural logarithm of the axial ratio ( $\epsilon_f$ ) and polar angle as the double of the long axis orientation ( $2\phi$ ).  $N$ , the grain population, is chosen during measurement such that a pattern (elliptical, heart-shaped, delta-shaped, point maxima, etc.) emerges on the polar graph. The pattern is indicative of initial preferred orientation of the grains. For example, delta- and heart-shaped distributions indicate an original unimodal preferred orientation and an elliptical shape is a result of deforming an initial random distribution. Once the shape of the distribution is apparent, it is contoured preferably by the method of Mellis (Turner and Weiss, 1963). To determine the strain ellipse, we need to locate a point on the polar graph that was initially circular (ICP) (Elliott, 1970; Boulter, 1976; Tobisch and others, 1977). For delta pattern, ICP is at the intersection of the dissector and base of the pattern. ICP is located at the center of elliptical pattern. Uncertainties for locating the ICP are discussed by Boulter (1976). ICP represents the strain ellipse on the polar graph for which  $\epsilon_f = \epsilon_s$ . Orientation of the strain ellipse can be directly read from the reference line on the polar graph using half the polar angle.

Method F1 - (Tobisch and others, 1977)

This method adopts a statistical procedure to calculate the

center of the distribution on a polar graph (method F) of Elliott (1970) by first converting the polar coordinates of all the grains into Cartesian coordinates using Equations 15 through 17. In this method, it is not necessary to identify the pattern or determine the ICP. After plotting all the points on a polar graph by their X and Y Cartesian coordinates, the center of the distribution is calculated by averaging the X coordinates (Eqn. 18). The distance in e units from this point to the origin of the plot is equal to  $\epsilon_s$ , from which  $R_s$  can be determined using Equation 19.

$$\epsilon f_i = 0.5 \ln R f_i \quad (15)$$

$$X_i = \epsilon f_i \cos^2 \phi_i \quad (16)$$

$$Y_i = \epsilon f_i \sin^2 \phi_i \quad (17)$$

$$\epsilon_s = \sum X_i / N \quad (18)$$

$$R_s = e^{(2\epsilon_s)} \quad (19)$$

The statistical way of finding the center of the distribution discussed above leads to a consistent overestimation of strain ratio for the following reason. Holst (1982, p. 341) indicated that ICP on elliptical patterns of polar graphs, representing deformation of grains with initially different axial ratio and circular pattern on polar graph, lies to the left of the center of the elliptical distribution calculated by the method of Tobisch and other (1977). Therefore, the distance of the statistical center to the origin of the polar graph in e units is larger than the distance of actual ICP from the origin, leading to an overestimation of  $\epsilon_s$  and therefore strain axial ratio.



Method F) of Elliott  
 all the grains  
 ough 17. In this  
 or determine the  
 by their X and Y  
 on is calculated  
 stance in e units  
 to es, from which

(15)

(16)

(17)

(18)

(19)

the distribution  
 n of strain ratio  
 icated that ICP  
 ng deformation of  
 ular pattern on  
 e elliptical dis-  
 d other (1977).  
 to the origin of  
 nce of actual ICP  
 es and therefore

Method F2 - (Method of Holst, 1982)

This procedure is essentially that of Elliott (1970) and Tobisch and others (1977). Holst (1982) showed that the percent of the overestimation of strain axial ratio, using statistical methods discussed above, increases with increasing  $R_s$ , but at a decreasing rate. To compensate for the error caused by this effect, he provides an empirical factor,  $F$ , that ranges between 0.87 and 1.00.  $R_s$  calculated by method F1 can be multiplied by an appropriate value of  $F$ , that can directly be read from his Figure 7, to provide an accurate measure of two dimensional strain.

Method G - (Method of Robin, 1977)

This method employs strain markers of any shape and assumes that they were initially randomly oriented and strained homogeneously. Robin (1977) presented a technique to calculate strain ratio in a section that contains grains with various outlines. The procedure for this general case is not considered here because the grains used in this study are elliptical in shape. However, he provided Equations 20 and 21 below to calculate strain ratio ( $\sqrt{\lambda_1}/\sqrt{\lambda_3}$ ) using  $R_f$  and  $\phi$  of elliptical grains.

$$a_i/c_i = ( (\tan^2 \phi_i + R_f^2) / (R_f^2 \tan^2 \phi_i + 1) )^{0.5} \quad (20)$$

$$R_s = e^{( \sum \ln a_i/c_i ) / N} \quad (21)$$

This method is straightforward and more objective than the graphic or statistical methods, and yields unique results which, although

calculated in an independent way, are close to those of Shimamoto and Ikeda method.

Method H - (Method of Lisle, 1977b; Peach and Lisle, 1979)

The original  $Rf/\phi$  method, first described by Ramsay (1967) and developed by Dunnet (1969) and Dunnet and Siddans (1971), requires that  $Rf$  and  $\phi$  of all the grains be plotted on a semi-logarithmic graph. The plot is then compared to a set of theoretical curves (Eqn. 3-16 of Dunnet, 1969) (Equation 3-5) for different values of  $R_s$  and  $R_i$ . The best fit library curves of  $R_s$  and  $R_i$  are taken as the representative of the axial strain ratio and the initial axial ratios of the grains, respectively (e.g. Fig. 3-60). No restriction on the initial axial ratio ( $R_i$ ) of grains is present in this method. However, grains are assumed to be initially elliptical with random orientation that deformed homogeneously.

Lisle (1977b) and Peach and Lisle (1979) improved this method by plotting curves of equal initial axial orientation ( $\theta$ ) on the  $Rf/\phi$  graphs.  $R_s$  is determined by comparing the distribution of the grains on the  $Rf/\phi$  plot with theoretical curves as described above except that the best fit is selected by the Chi-Square test. This fit is more reliable and objective. To do the test, the harmonic mean is first calculated and an incremental coaxial reciprocal strain with its long axis perpendicular to the vector mean of  $\phi$  is applied using  $R_s$  values between  $H+0.6$  and  $H-2.0$  in increments of 0.05. The  $R_s$  which produces the most uniform distribution on the basis of the Chi-Square test is taken as the representative of

e, 1979)

Ramsay (1967) and  
s (1971), requires  
semi-logarithmic  
theoretical curves  
ferent values of  
i are taken as the  
ne initial axial  
)). No restriction  
t in this method.  
otical with random

ved this method  
tation ( $\theta$ ) on the  
tribution of the  
s described above  
uare test. This  
est, the harmonic  
axial reciprocal  
ctor mean of  $\phi$  is  
n increments of  
tribution on the  
epresentative of

strain in the section. This occurs at the minimum Chi-Square when it  
is plotted against  $R_s$  (e.g. Fig. 3-60c). This test also provides a  
check on the validity of assumptions undertaken by the method.

APPENDIX II - METHOD OF THREE-DIMENSIONAL STRAIN  
ANALYSIS (RAMSAY, 1967, P. 80)

This method is designed for three-dimensional strain analysis in cases where the quadratic elongations of three lines and the angles between them are known. For this study, the three lines are the intersections of the three thin sections with the cleavage. The quadratic elongations are determined from the two-dimensional strain analysis.

Details of this method are described in progressive steps in the following paragraphs. At the end, an example, using specimen # 16 is provided.

- 1- Define lines i, j, and k parallel to the three intersections of cleavage with thin section b, c, and d, respectively. These are parallel to  $\lambda_{1b}^*$ ,  $\lambda_{1c}^*$ , and  $\lambda_{1d}^*$ .
- 2- Measure angles  $\alpha$ ,  $\beta$ , and  $\gamma$  between these lines on the stereonet, where  $\alpha = i \angle j$ ,  $\beta = j \angle k$ , and  $\gamma = i \angle k$ .
- 3- Draw triangle  $\acute{A}\acute{B}\acute{C}$  (deformed state) of arbitrary size, sides of which are chosen parallel to i, j, and k with their correct angular relationship (Figure APP-1).
- 4- Calculate the original length of the sides of this triangle (i.e. AB, BC, and AC) using their corresponding quadratic elongations ( $\lambda_1^*$ ) and final lengths ( $\acute{A}\acute{B}$ ,  $\acute{B}\acute{C}$ , and  $\acute{A}\acute{C}$ ) using the following relation-

$$AB = \overset{\prime\prime}{AB} / \sqrt{-\lambda^* b} \quad , \quad BC = \overset{\prime\prime}{BC} / \sqrt{-\lambda^* c} \quad , \quad AC = \overset{\prime\prime}{AC} / \sqrt{-\lambda^* d}$$

5- Draw triangle ABC and plot perpendicular lines (EF, BF, and DF) to its sides at points E, F, and D. Use the proportionality of the two triangles (e.g.  $\overset{\prime\prime}{AD}/\overset{\prime\prime}{DB} = AD/DB$ ) and locate points  $\overset{\prime}{D}$ ,  $\overset{\prime}{E}$ , and  $\overset{\prime}{F}$  on triangle  $\overset{\prime\prime}{ABC}$  (Figure APP-1).

6- Draw perpendicular lines to the sides of triangle  $\overset{\prime\prime}{ABC}$  at points  $\overset{\prime}{D}$ ,  $\overset{\prime}{E}$ , and  $\overset{\prime}{F}$ . Find the angle  $\psi$  (angular shear) between each line and lines of  $\overset{\prime\prime}{DF}$ ,  $\overset{\prime\prime}{BF}$ , and  $\overset{\prime\prime}{EF}$ .  $\psi_i$ ,  $\psi_j$ , and  $\psi_k$  correspond to the angular shears of lines i, j, and k, respectively.  $\psi$  is positive if an arrow connecting the perpendicular line and each of the lines  $\overset{\prime\prime}{DF}$ ,  $\overset{\prime\prime}{BF}$ , and  $\overset{\prime\prime}{EF}$  is clockwise (Figure APP-1b)

7- Having the quadratic elongations and angular shears for i, j, and k, calculate  $\gamma$ ,  $\lambda'$ , and  $\gamma'$  for these lines using the following relationships:

$$\gamma = \tan \psi \quad , \quad \lambda' = 1/\lambda \quad , \quad \gamma' = \gamma/\lambda$$

8- On an orthogonal coordinate system of  $\lambda'$  and  $\gamma'$ , plot lines i, j, and k as points  $P_i$ ,  $P_j$ , and  $P_k$  with the following coordinates:

$$P_i (\lambda'_i, \gamma'_i) \quad , \quad P_j (\lambda'_j, \gamma'_j) \quad , \quad P_k (\lambda'_k, \gamma'_k)$$

9- Draw the Mohr Circle passing through the three points and find its

- 10- Check the angles  $P_i c P_j$ ,  $P_j c P_k$ , and  $P_i c P_k$ . These should be equal to  $2\alpha$ ,  $2\beta$ , and  $2\gamma$ , respectively.
- 11- Find the intersections of the circle and the  $\lambda$  axis. These are  $\lambda'_1$  and  $\lambda'_2$  ( $\lambda'_1 < \lambda'_2$ ), or values of the reciprocal quadratic elongations on cleavage.
- 12- Read the angles subtended between  $\lambda'_1$  and lines i, j, and k ( $2\theta_i$ ,  $2\theta_j$ , and  $2\theta_k$ ).  $\theta_i$  is the angle between the principal axis of the longitudinal strain and line i for example. Draw these angles on triangle  $\overset{\wedge}{\wedge}{ABC}$  as well as on the stereonet. These constrain the direction of X and therefore Y on the cleavage (Figure APP-1b and APP-2).
- 13- Calculate  $\lambda_1$  and  $\lambda_2$ , hence X and Y and their ratio X/Y on the cleavage using the following relationships:

$$\lambda_1 = 1/\lambda'_1, \quad \lambda_2 = 1/\lambda'_2, \quad X = \sqrt{\lambda_1}, \quad Y = \sqrt{\lambda_2}$$

The steps used in this example correspond to the ones in Appendix II.

Step 1: (from 2D strain analysis)

$$\lambda_i^* = \lambda_{1b}^* = 6.1504$$

$$\lambda_j^* = \lambda_{1c}^* = 7.3984 \quad \text{where, b, c, \& d refer to thin sections.}$$

$$\lambda_k^* = \lambda_{1d}^* = 5.0625$$

Step 2: (from Fig. 3-49, specimen OS16)

$$\alpha = 90^\circ$$

$$\beta = 46^\circ$$

$$\gamma = 44^\circ$$

Step 3: (see Fig. 1a)

Step 4:

$$AB = \frac{AB}{\sqrt{\lambda_i^*}} = \frac{10}{\sqrt{6.1504}} = 4.032$$

$$BC = \frac{BC}{\sqrt{\lambda_j^*}} = \frac{10.3}{\sqrt{7.3984}} = 3.79$$

$$AC = \frac{AC}{\sqrt{\lambda_k^*}} = \frac{14.4}{\sqrt{5.0625}} = 6.4$$

Step 5: (see Fig. 1b)

$\frac{AD}{DB} = \frac{AD}{DB} = \frac{2.78}{1.25}$ $\therefore AD = 2.224 DB$	$\Rightarrow$	$\left. \begin{aligned} 2.224 + 1 &= 3.224 \\ 10 \div 3.224 &= 3.1 \\ 3.1 \times 2.224 &= 6.9 = AD \\ 3.1 \times 1 &= 3.1 = DB \end{aligned} \right\}$
$\frac{BE}{EC} = \frac{BE}{EC} = \frac{1.39}{2.44}$ $\therefore BE = 0.5697 EC$	$\Rightarrow$	$\left. \begin{aligned} 0.5697 + 1 &= 1.569 \\ 10.3 \div 1.569 &= 6.56 \\ 6.56 \times 0.5697 &= 3.74 = BE \\ 6.56 \times 1 &= 6.56 = EC \end{aligned} \right\}$
$\frac{AF}{FC} = \frac{AF}{FC} = \frac{3.35}{3.05}$ $\therefore AF = 1.098 FC$	$\Rightarrow$	$\left. \begin{aligned} 1.098 + 1 &= 2.098 \\ 14.4 \div 2.098 &= 6.86 \\ 6.86 \times 1.098 &= 7.54 = AF \\ 6.86 \times 1 &= 6.86 = FC \end{aligned} \right\}$

Step 7:

$\psi_i = +17^\circ$	$\psi_j = -20^\circ$	$\psi_k = -4.7^\circ$
$\gamma_i = 0.305$	$\gamma_j = -0.36$	$\gamma_k = -0.82$
$\lambda_i^* = 6.1504$	$\lambda_j^* = 7.3984$	$\lambda_k^* = 5.0625$
$\lambda_i' = 0.162$	$\lambda_j' = 0.135$	$\lambda_k' = 0.197$
$\gamma_i' = 0.049$	$\gamma_j' = -0.049$	$\gamma_k' = -0.017$

Step 8: (see Fig. 2)

The coordinates of the points i, j, and k on the Mohr circle are:

$pi(0.162, 0.049)$   
 $pj(0.135, -0.049)$   
 $pk(0.197, -0.016)$

step 9: (see Fig. 2)

Step 10:

The angle picpj  $\approx 180 \approx 2\alpha$   
 The angle picpk  $\approx 92.5 \approx 2\beta$  (see step 2 for  $\alpha, \beta, \gamma$ )  
 The angle pjcpk  $\approx 87 \approx 2\gamma$

Step 11: (see Fig. 2)

$\lambda_1' = 0.098$   
 $\lambda_2' = 0.199$

Step 12:

$2\theta_i = 105^\circ \quad \therefore \quad \theta_i = 52.5^\circ$   
 $2\theta_j = -75^\circ \quad \therefore \quad \theta_j = -37.5^\circ$   
 $2\theta_k = -161 \quad \therefore \quad \theta_k = -80.5^\circ$

Step 13:

$\lambda_1 = 1/0.098 = 10.2 \quad \therefore \quad X = 3.19$   
 $\lambda_2 = 1/0.199 = 5.02 \quad \therefore \quad Y = 2.24$



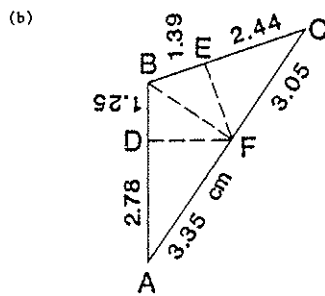
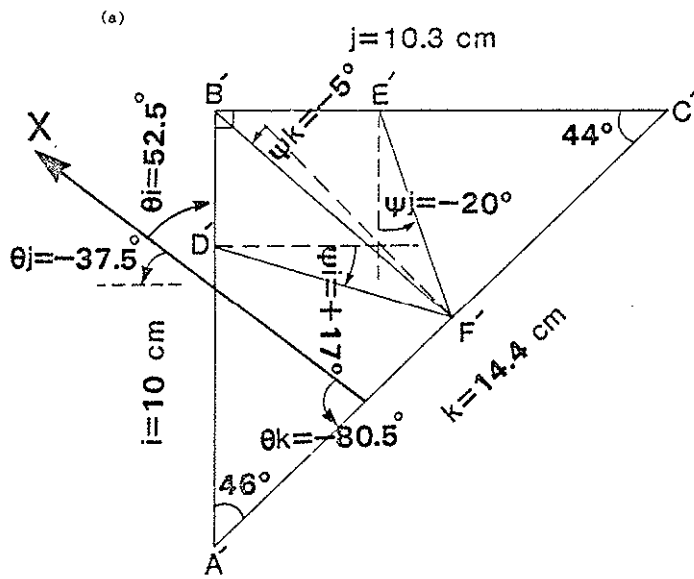


Figure APP-1. Triangle construction of three-dimensional method of strain analysis.

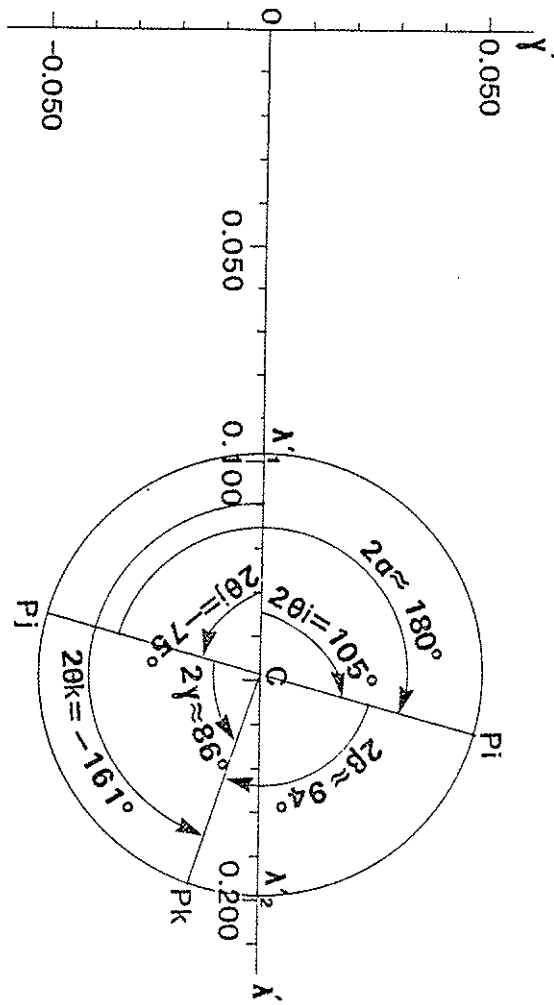


Figure APF-2. Mohr Circle construction of three-dimensional method of strain analysis.

Name: H  
 Place of  
 Date of  
 EDUCATIO  
 PhD, Aug  
 Ms, Jun  
 Bs, Jun  
 Publicat  
 Babaie, H  
 proble  
 Pub.  
 Babaie, H  
 yabe  
 Orogen  
 Winnem  
 -----, a  
 Golcom  
 15, p.  
 Babaie, H  
 folds  
 Submit  
 Babaie, H  
 using  
 Submit  
 Babaie, H  
 conda  
 graphi  
 -----, K  
 conda a

Name: Hassan Ali Babaie

Place of birth: Khorramshahr, Iran

Date of birth: June 22, 1951

EDUCATION

PhD, August, 1984, Northwestern University, Evanston Illinois.

Ms, June, 1980, Northwestern University, Evanston, Illinois.

Bs, June, 1973, Pahlavi University, Shiraz, Iran.

Publications

Babaie, H. A., 1973, The Ophiolite belt near Neyriz and the radiolarite problem. J. Earth and Space Physics, v. 2, p. 20-26, Tehran Univ. Pub.

Babaie, H. A., 1982, Tectonic fabric of the Golconda allochthon, Toiyabe Range, Nevada. Presented at the Penrose Conference "Sonoma Orogeny and Permian to Triassic tectonism in western North America", Winnemucca, Nevada.

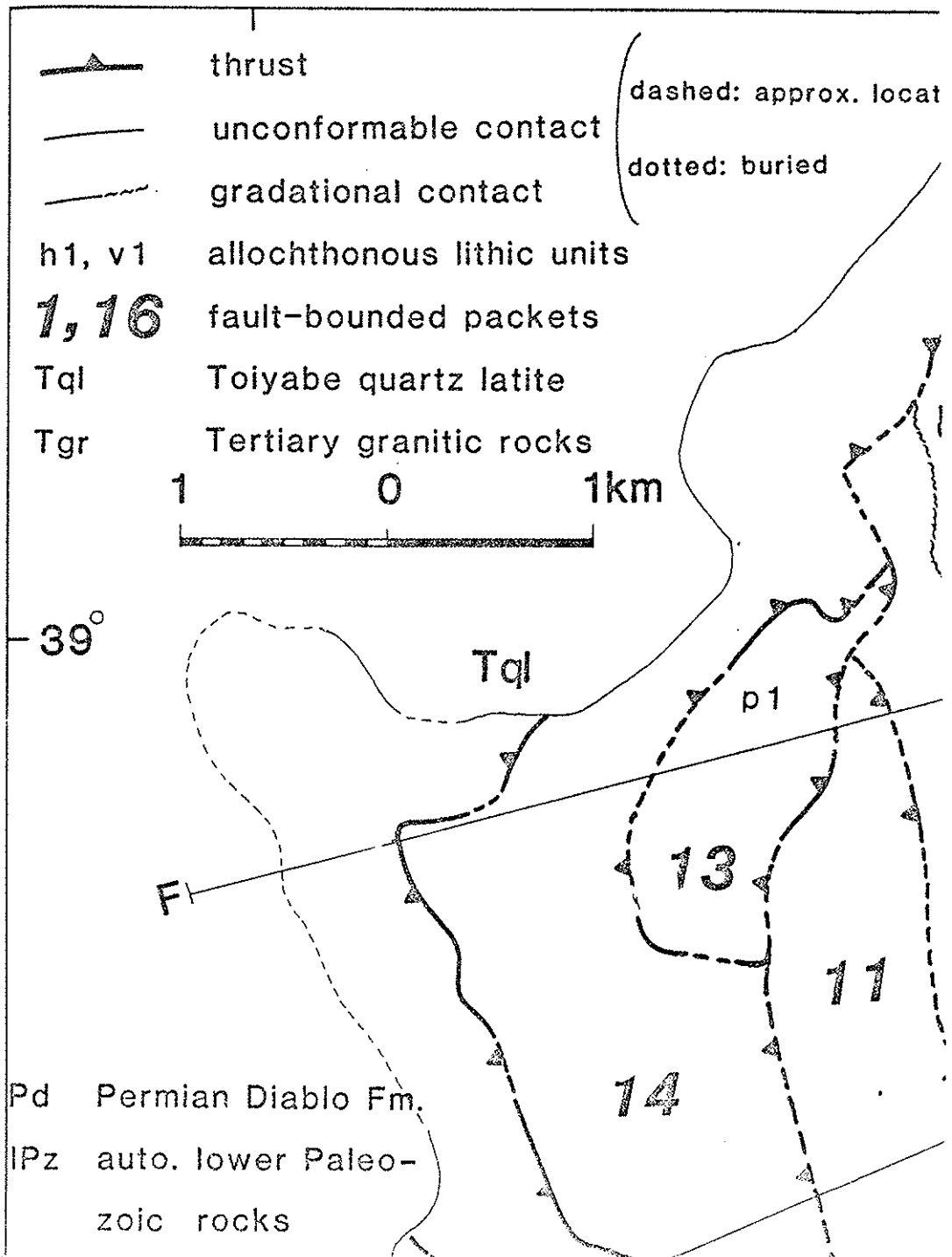
-----, and R. C. Speed, 1983, Significance of tectonic fabric of the Golconda allochthon in Toiyabe Range, Nevada. GSA Abs with Prog. v. 15, p. 382.

Babaie, H. A. and Speed, R. C., 1984, Tectonic significance of kink folds in the Golconda allochthon, southern Toiyabe Range, Nevada. Submitted to the GSA Bull.

Babaie, H. A., 1984, A comparison of two dimensional strain methods using elliptical quartz grains in slate and foliated sandstone. Submitted to Jour. of Struc. Geol.

Babaie, H. A. and Speed, R. C., 1984, Tectonostratigraphy of the Golconda allochthon in the southern Toiyabe Range, Nevada: Paleogeographic implications. Under review.

-----, Kinematic interpretation of the tectonic fabrics in the Golconda allochthon, southern Toiyabe Range, Nevada. Under review.



17' 30"

ashed: approx. located

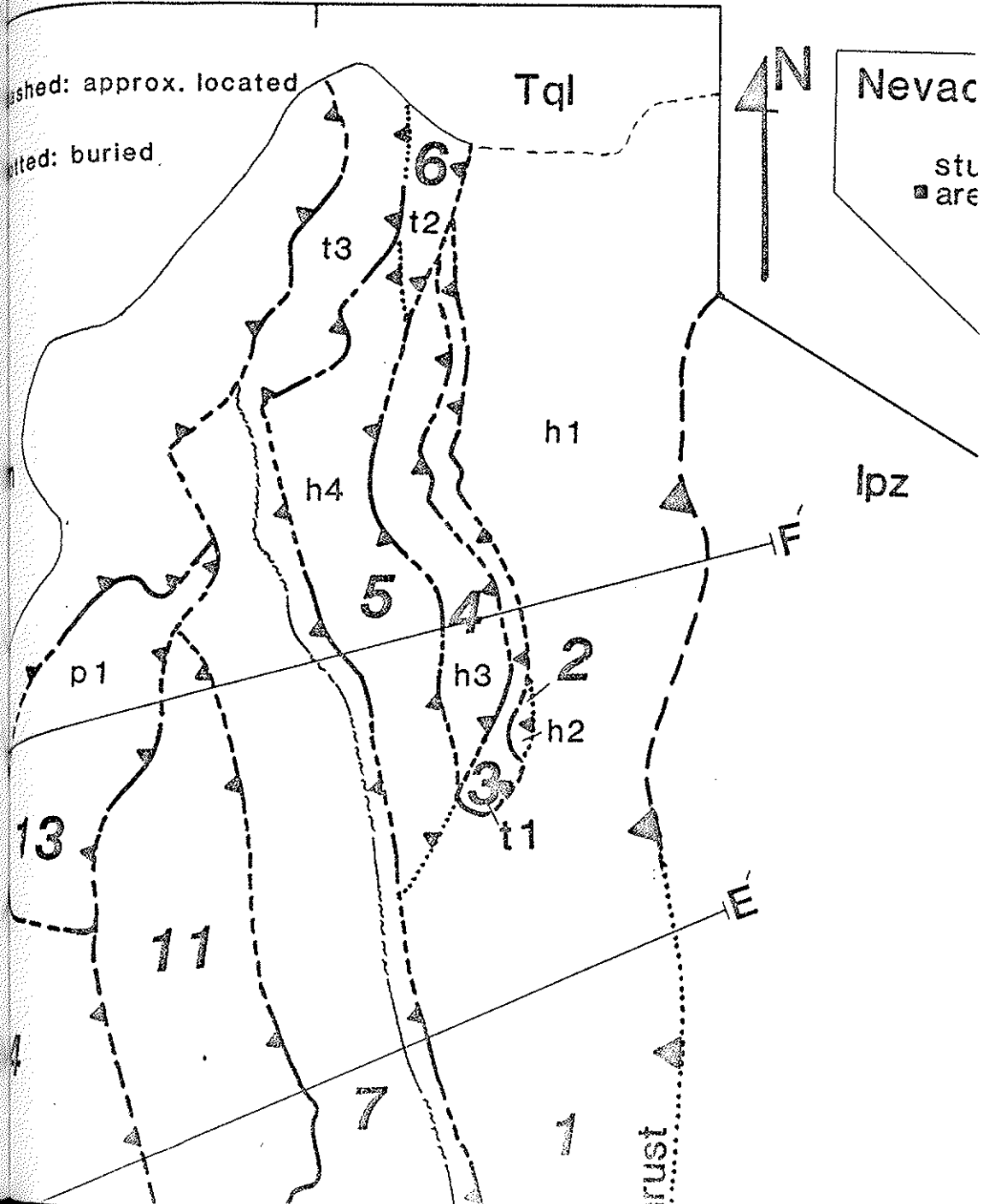
ited: buried

Tql

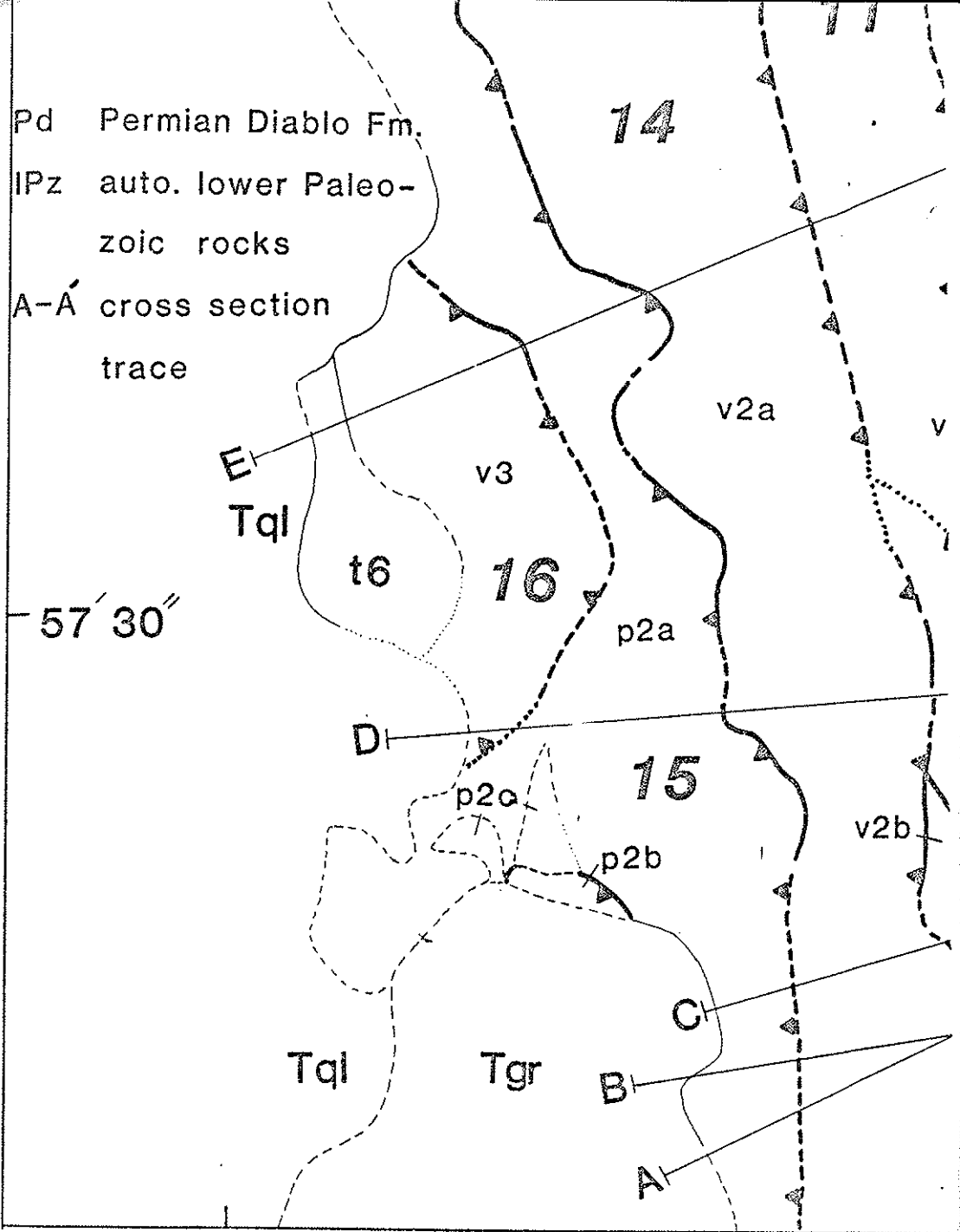


Nevac

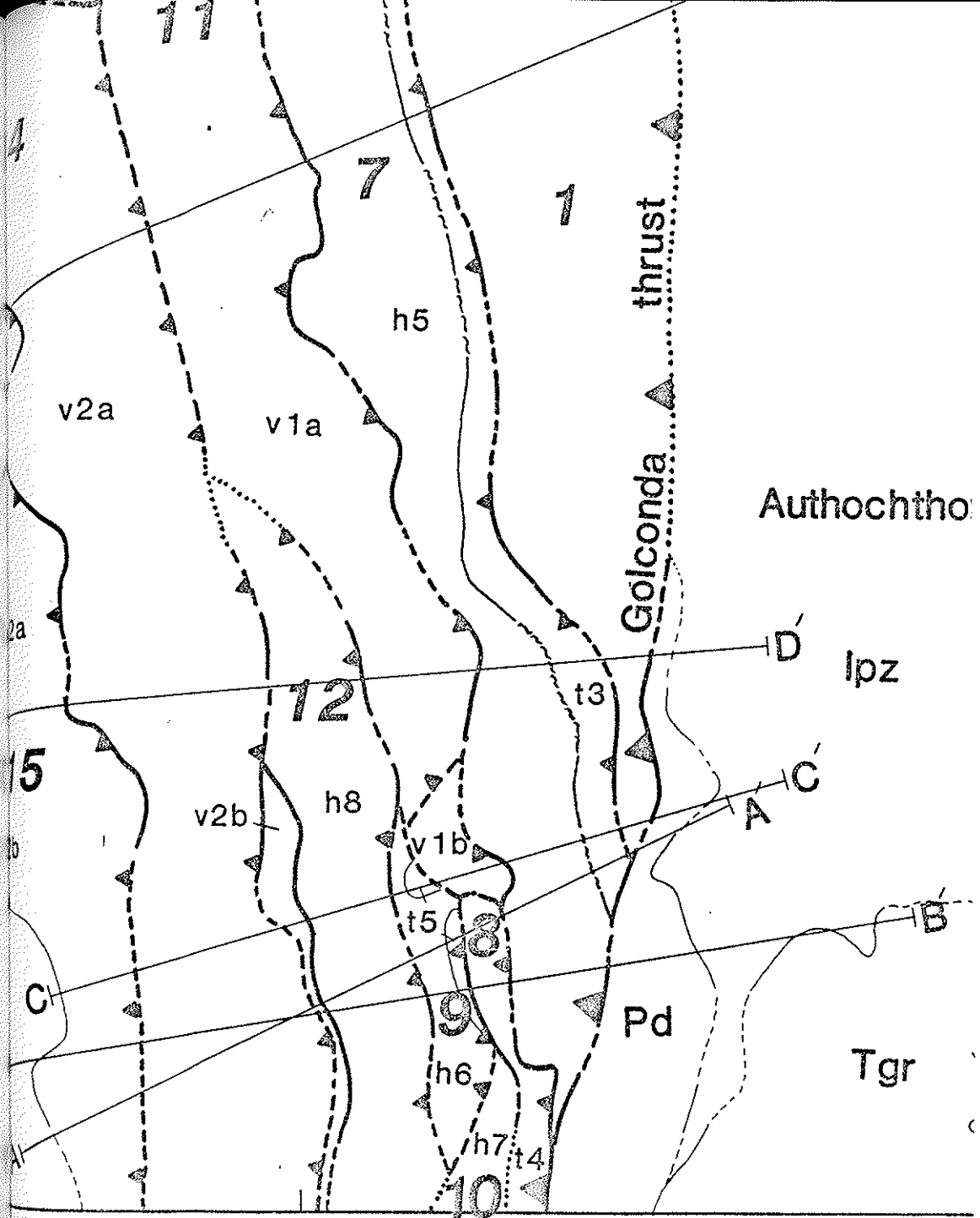
st  
are



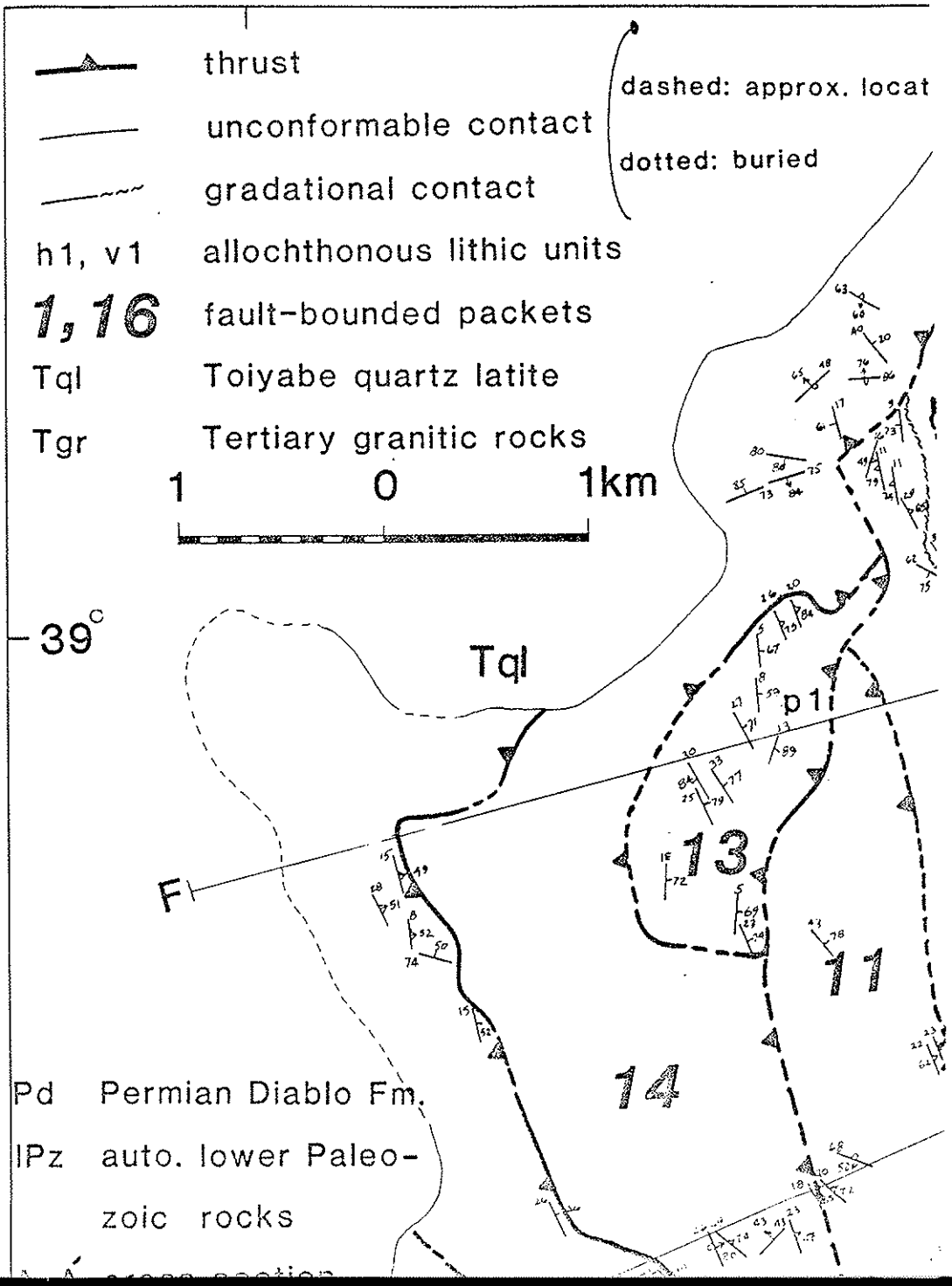
Pd Permian Diablo Fm.  
 IPz auto. lower Paleozoic rocks  
 A-Á cross section trace



GEOLOGICAL MAP OF THE GOL  
 SOUTHERN TOIYABE RANGE, NV



**THE GOLCONDA ALLOCHTHON II RANGE, NEVADA** H. A. Babaie Aug. 1977





17 30"

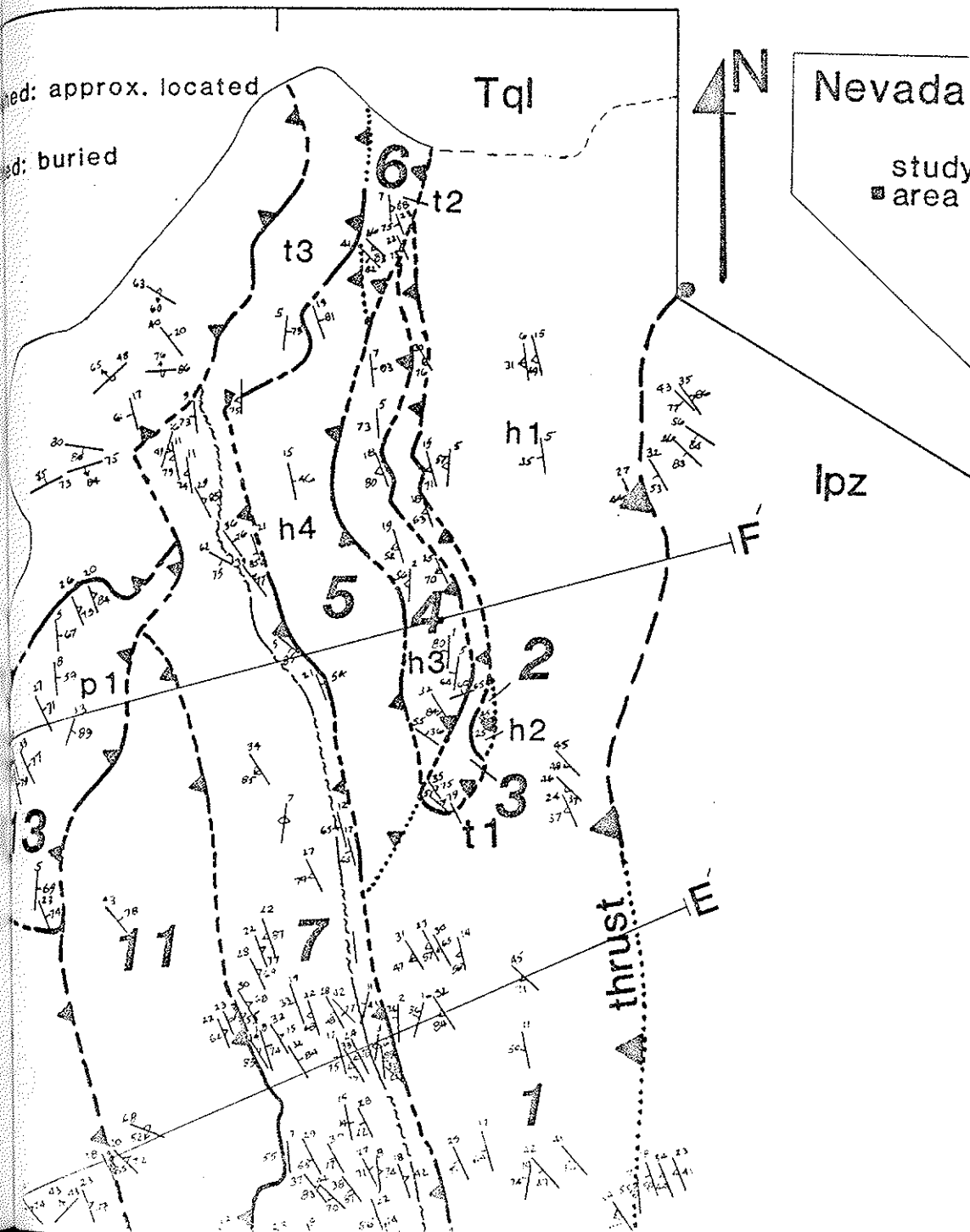
ed: approx. located

ed: buried

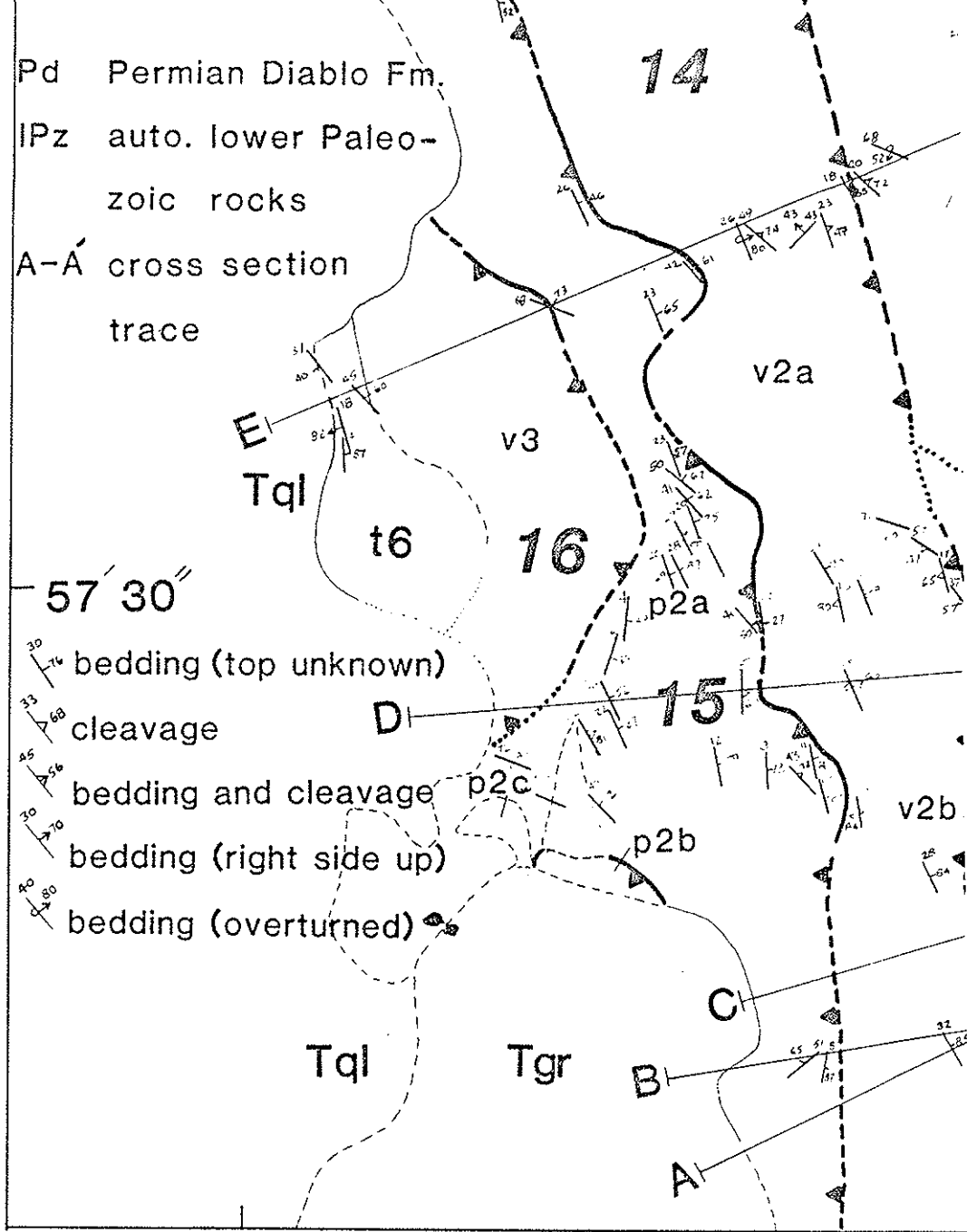
Tq1

Nevada

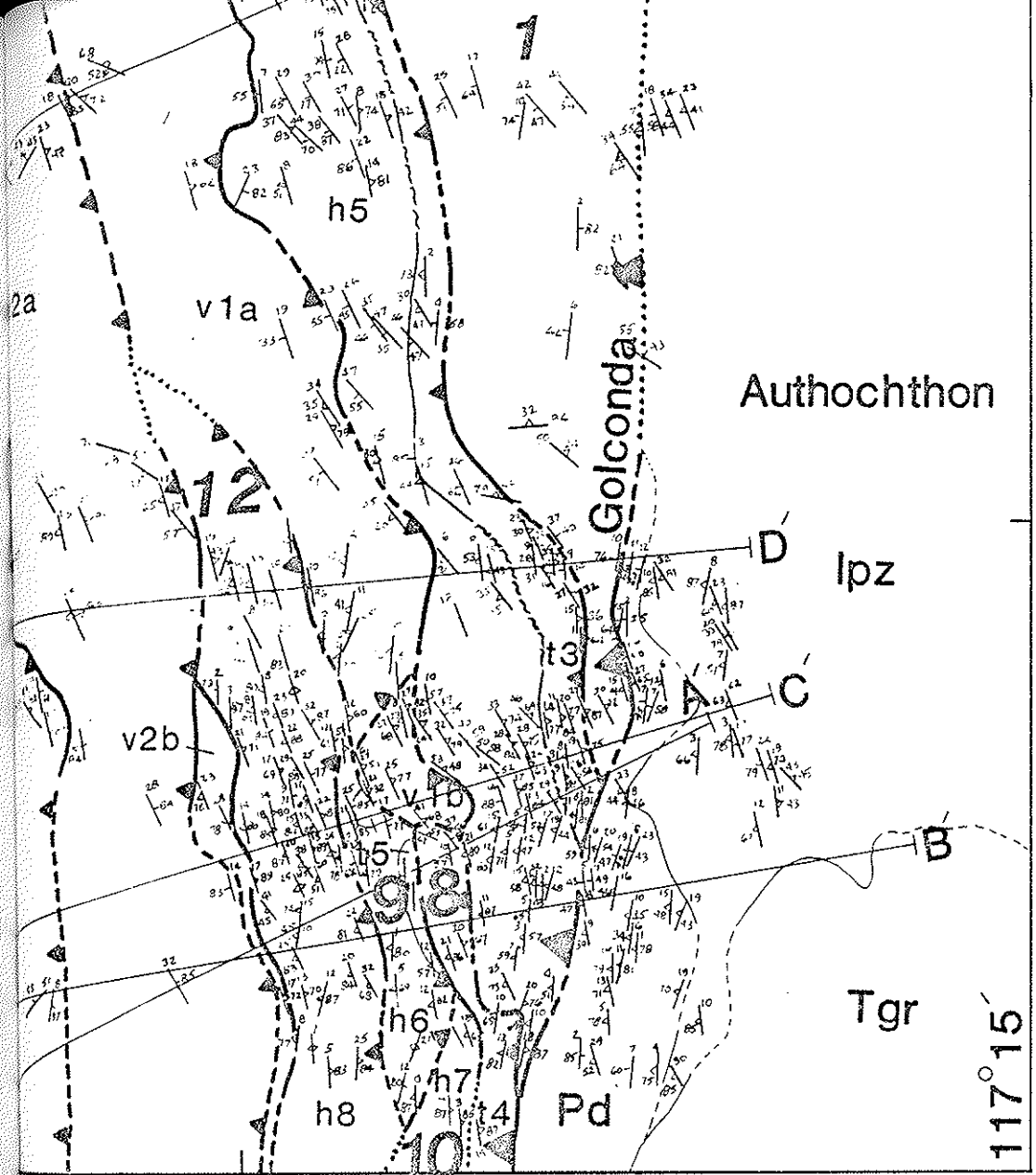
study area



Pd Permian Diablo Fm.  
 IPz auto. lower Paleozoic rocks  
 A-A' cross section trace



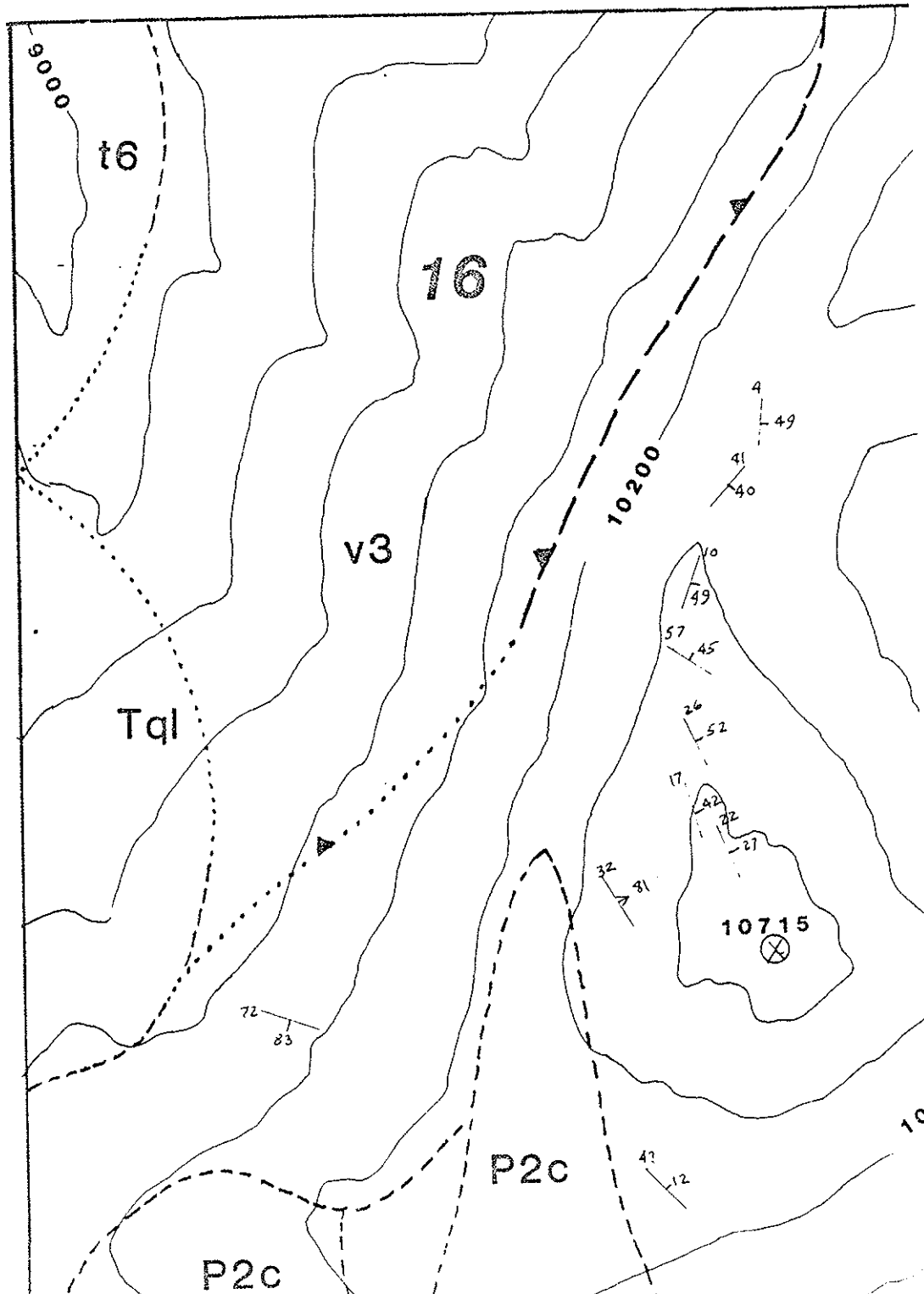
ORIENTATION OF BEDDING AND C  
 ALLOCHTHON, SOUTHERN TOIY

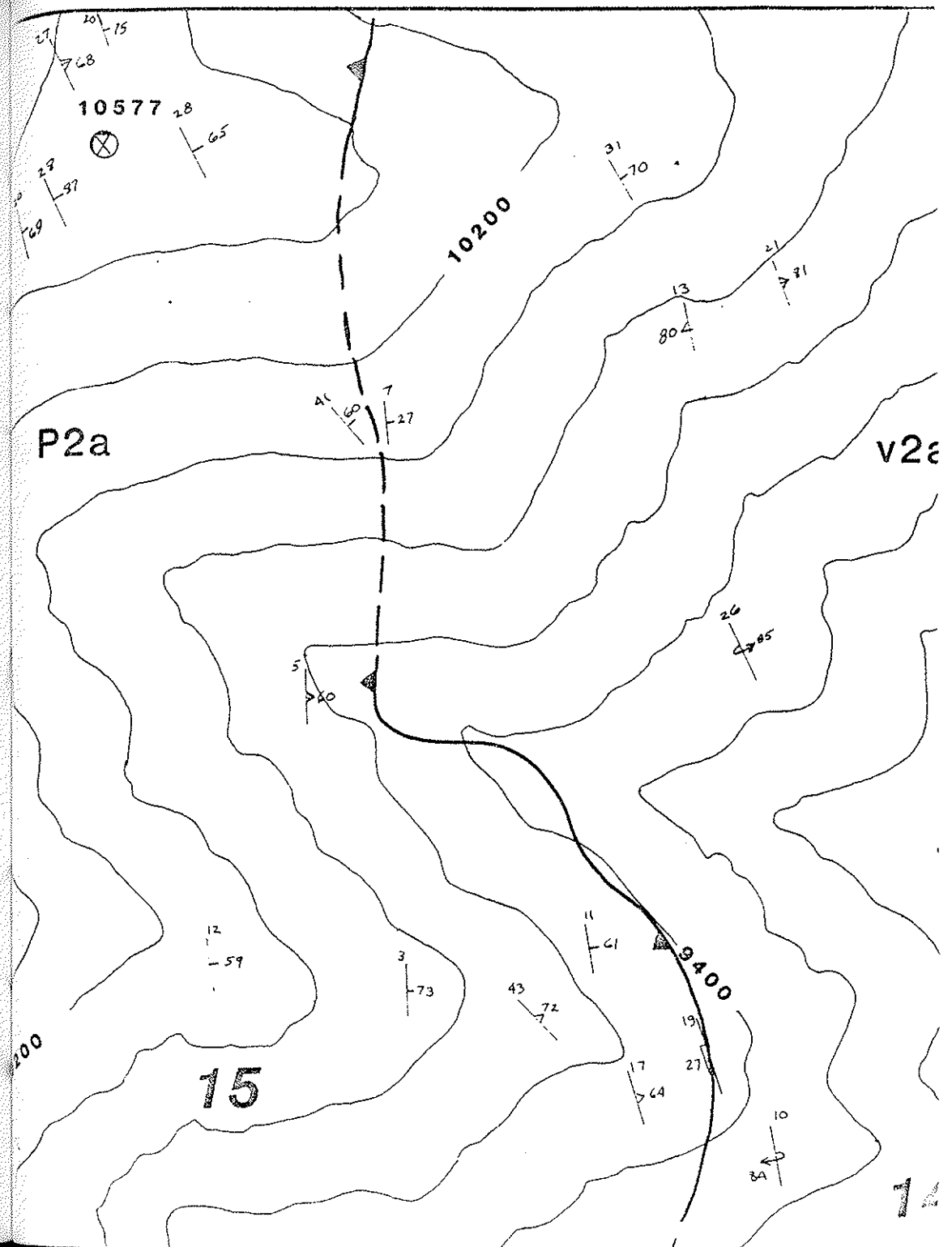


AND CLEAVAGE IN THE GOLCONDA,  
 IN TOIYABE RANGE NEVADA

H. A. Babaie Aug. 198

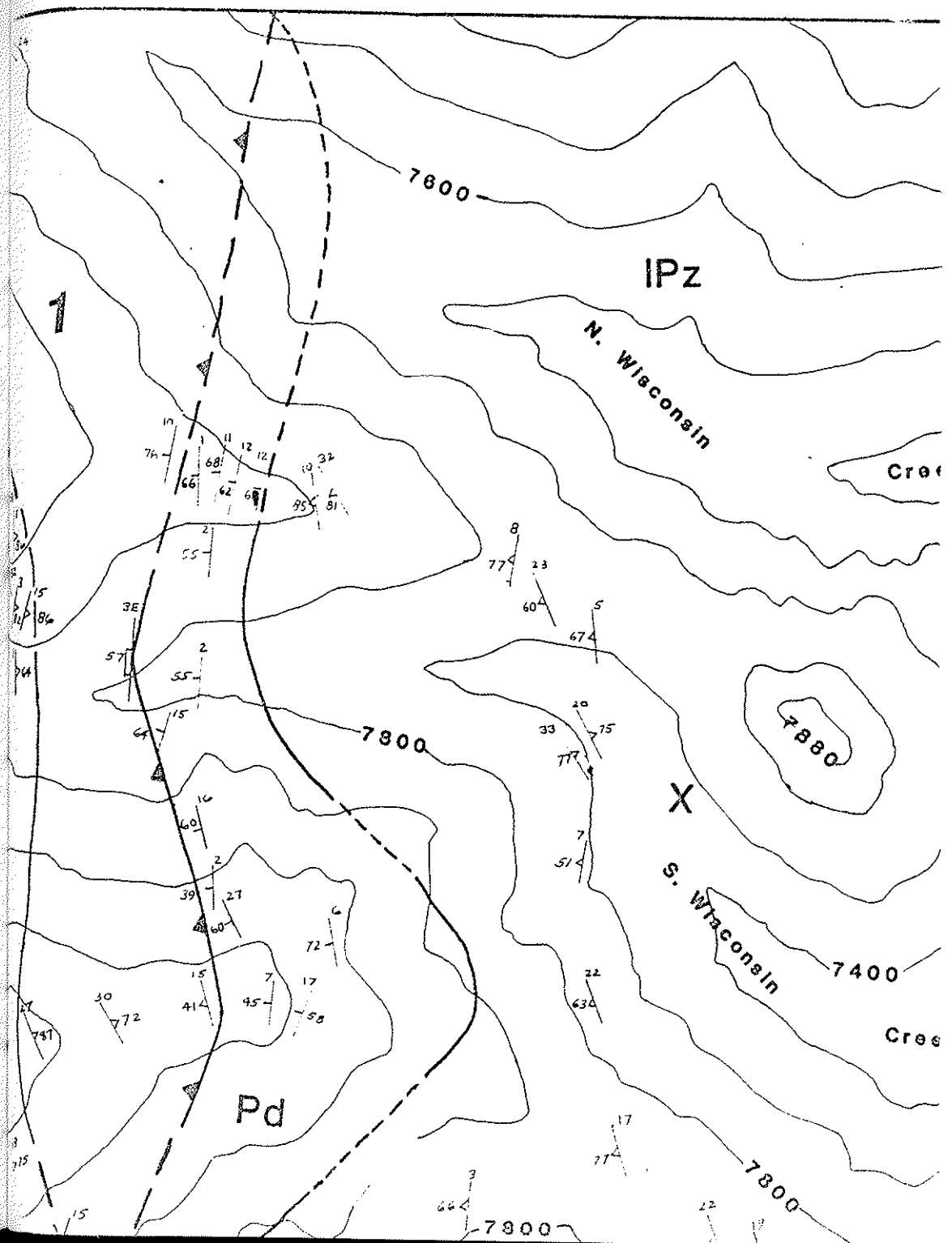
Plate 2



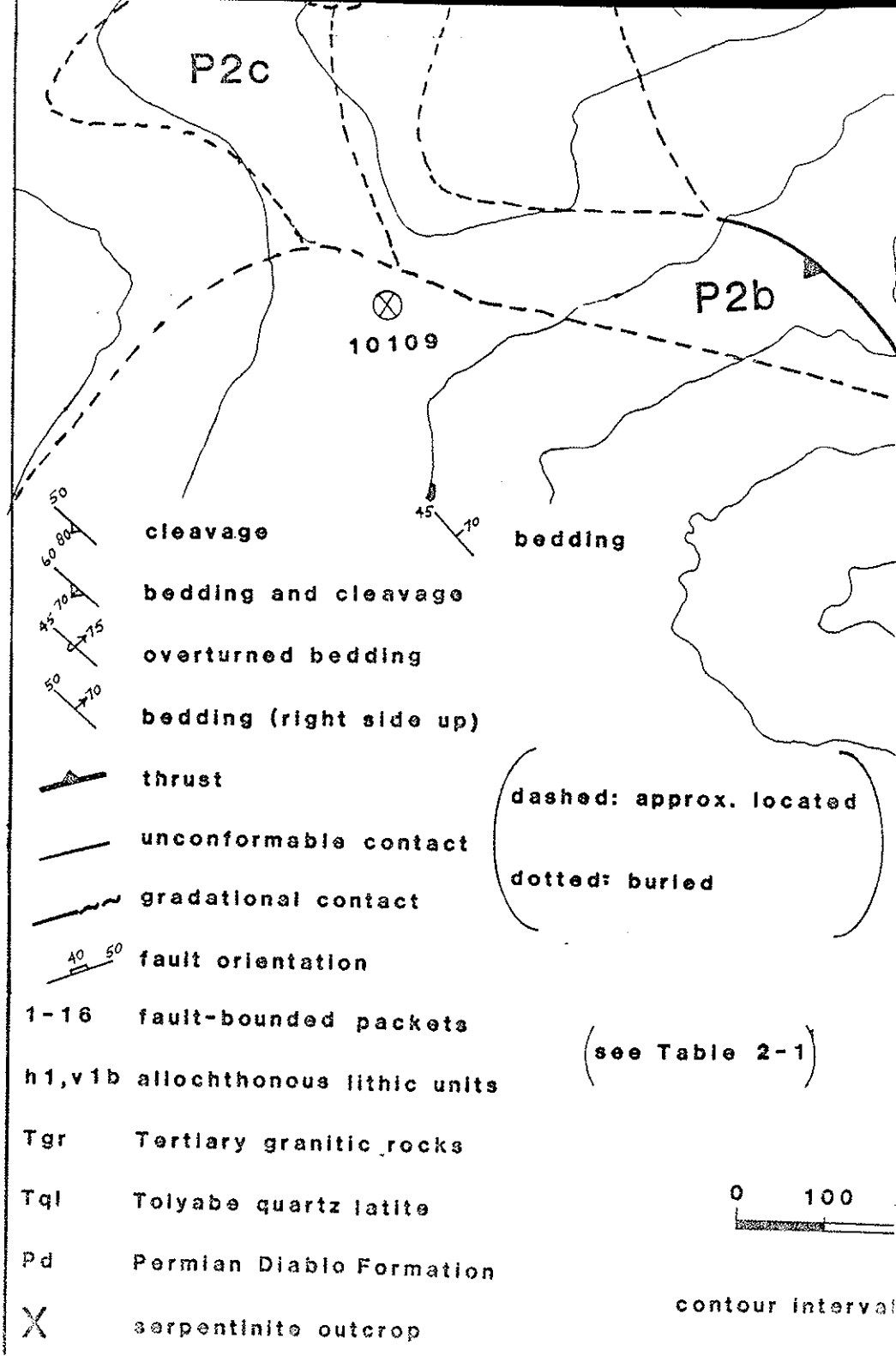


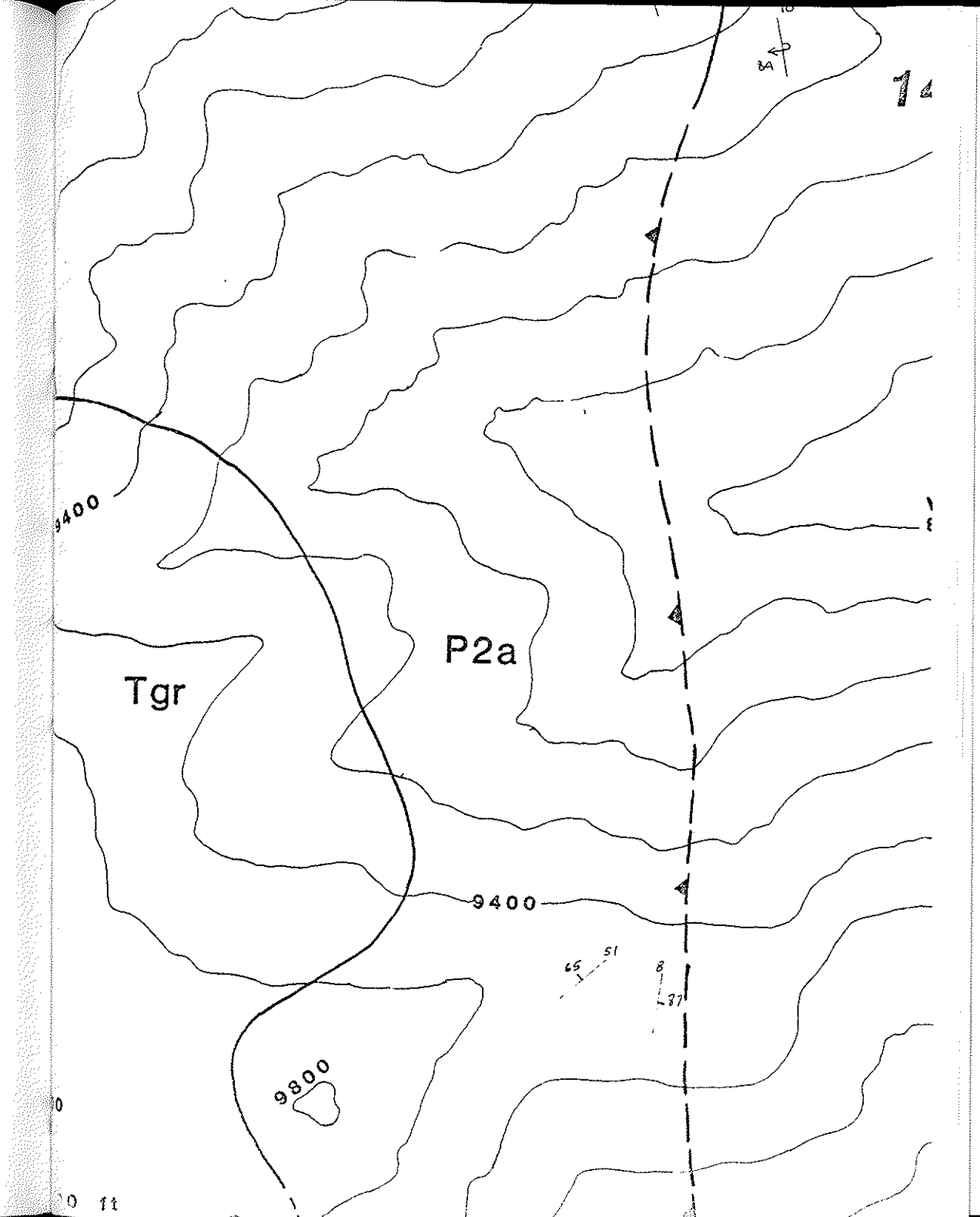




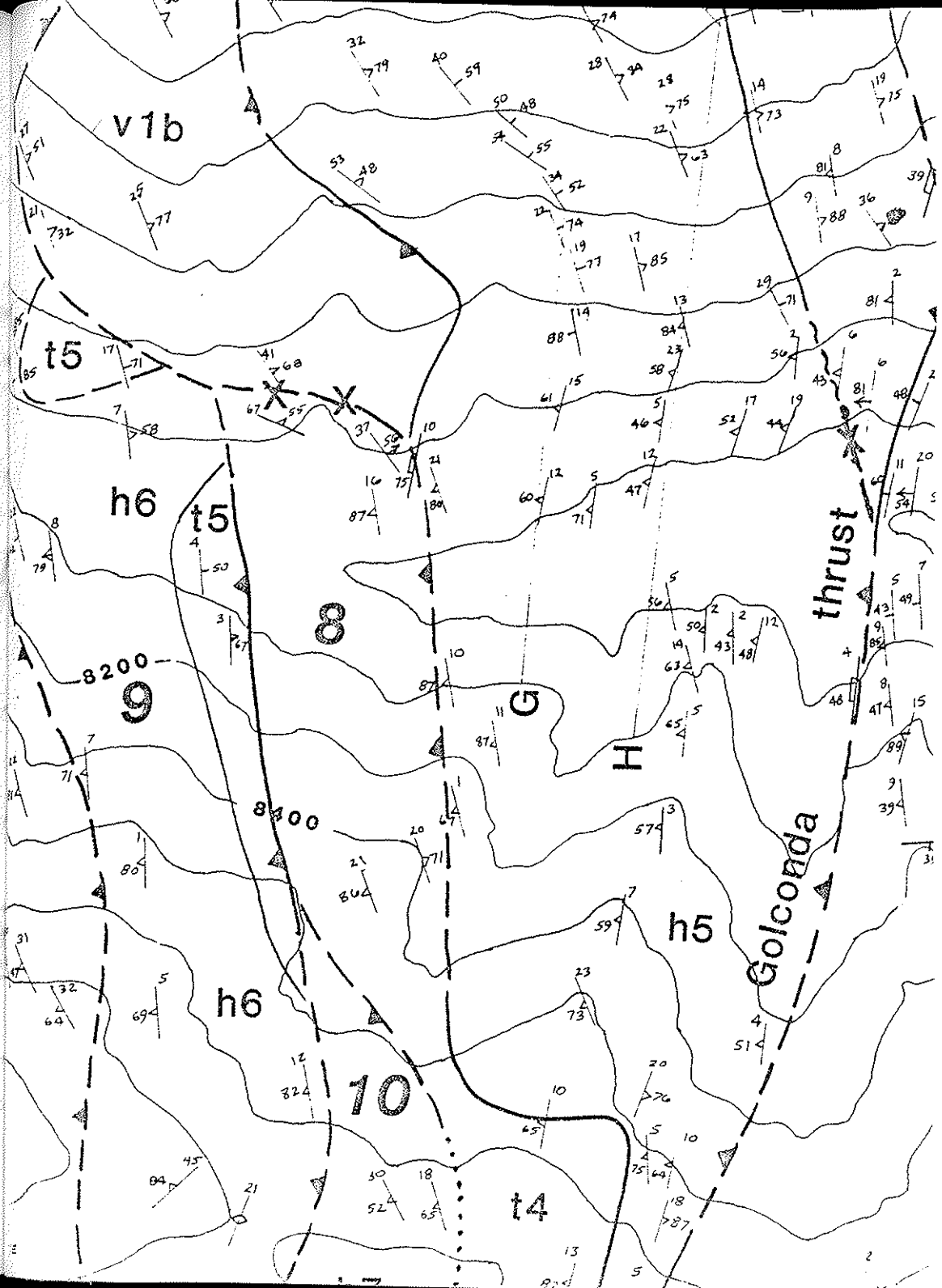


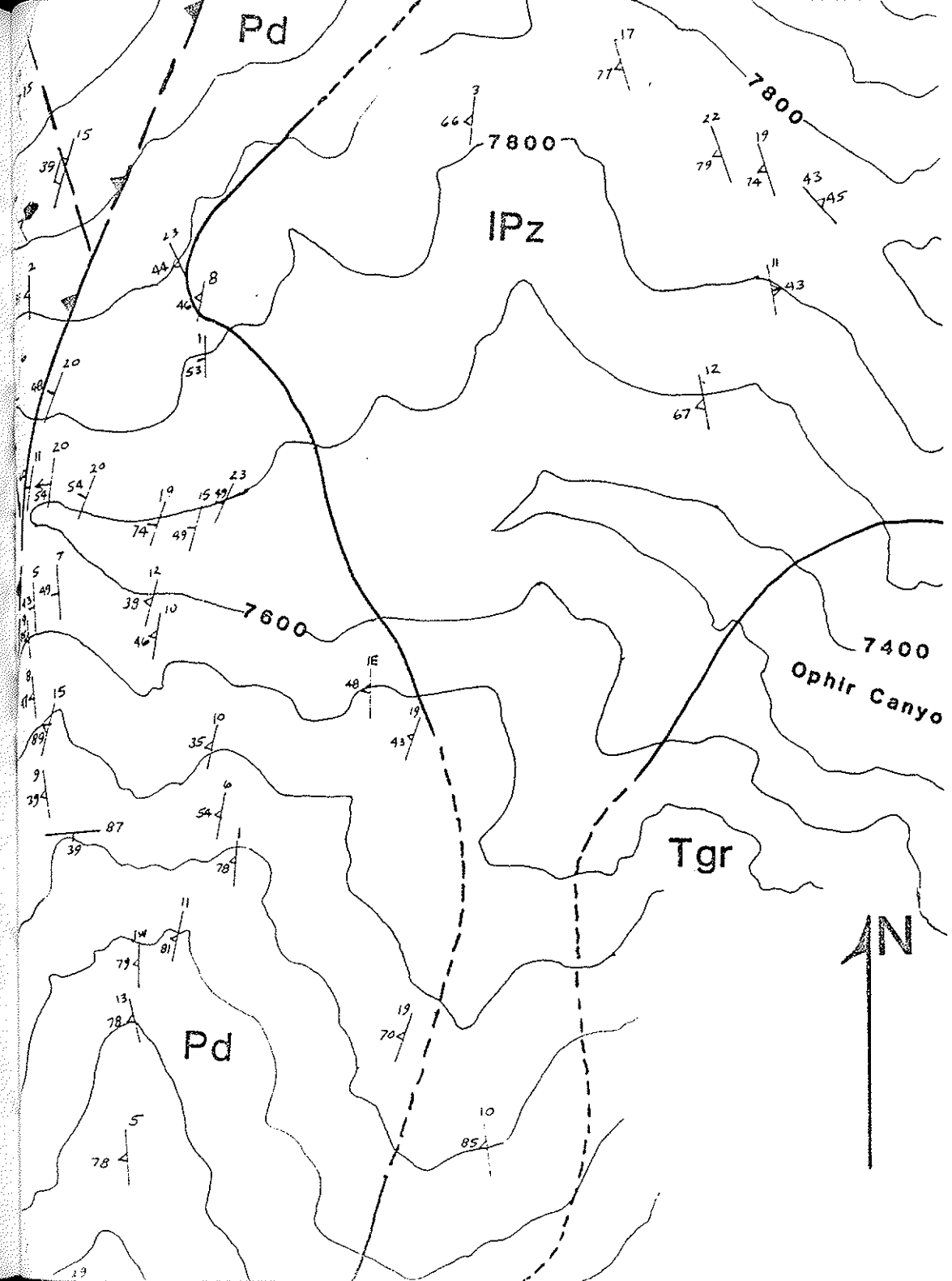


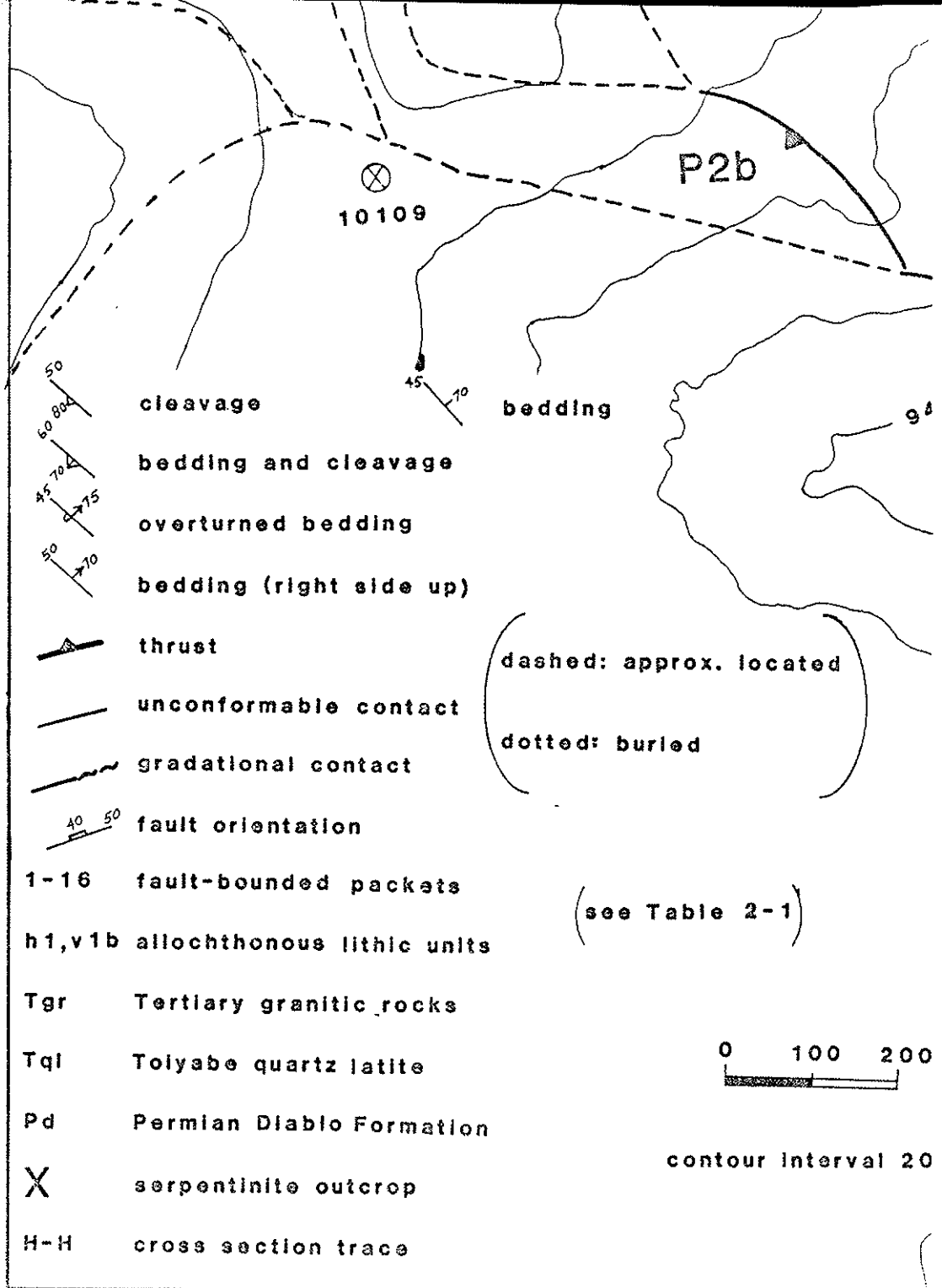




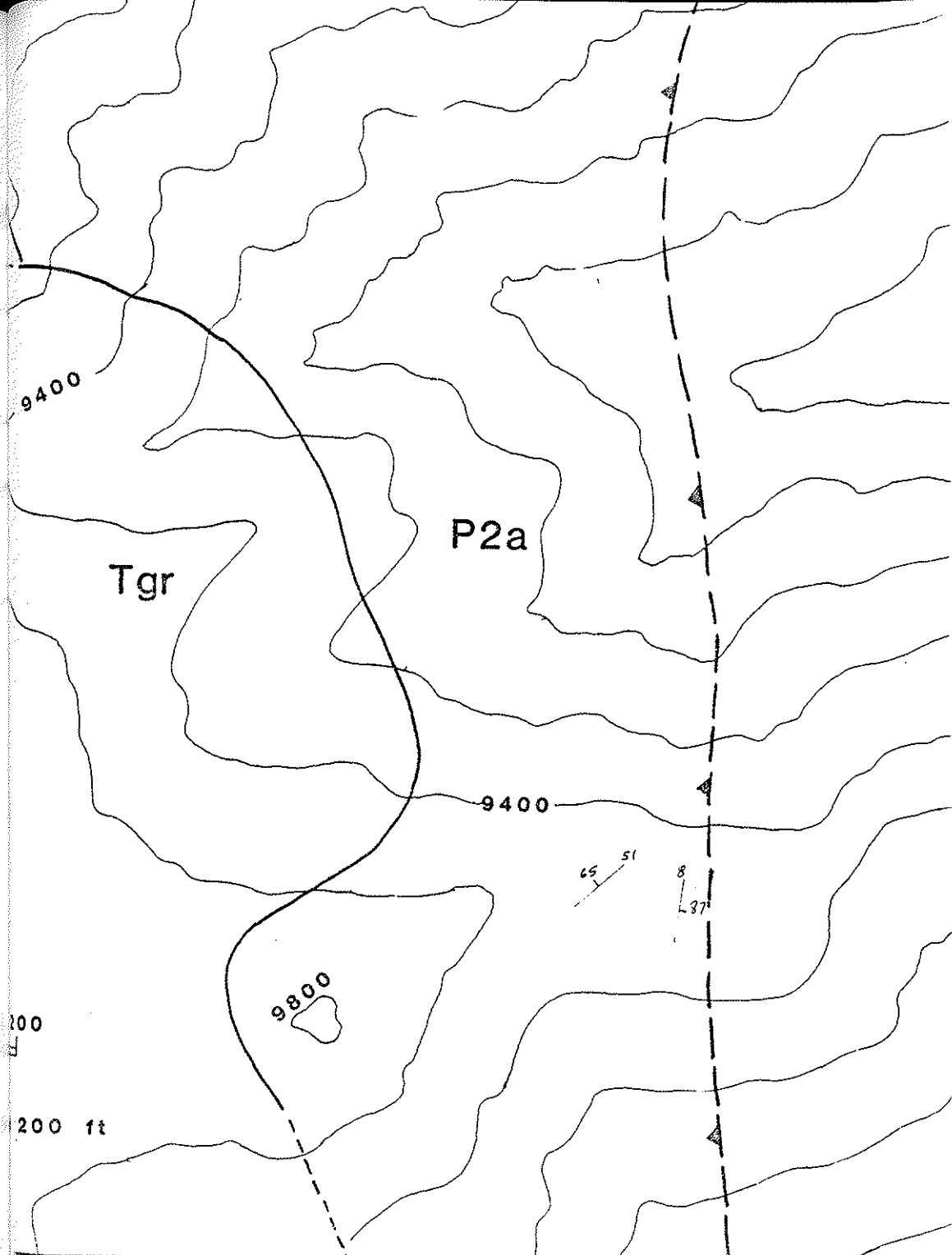




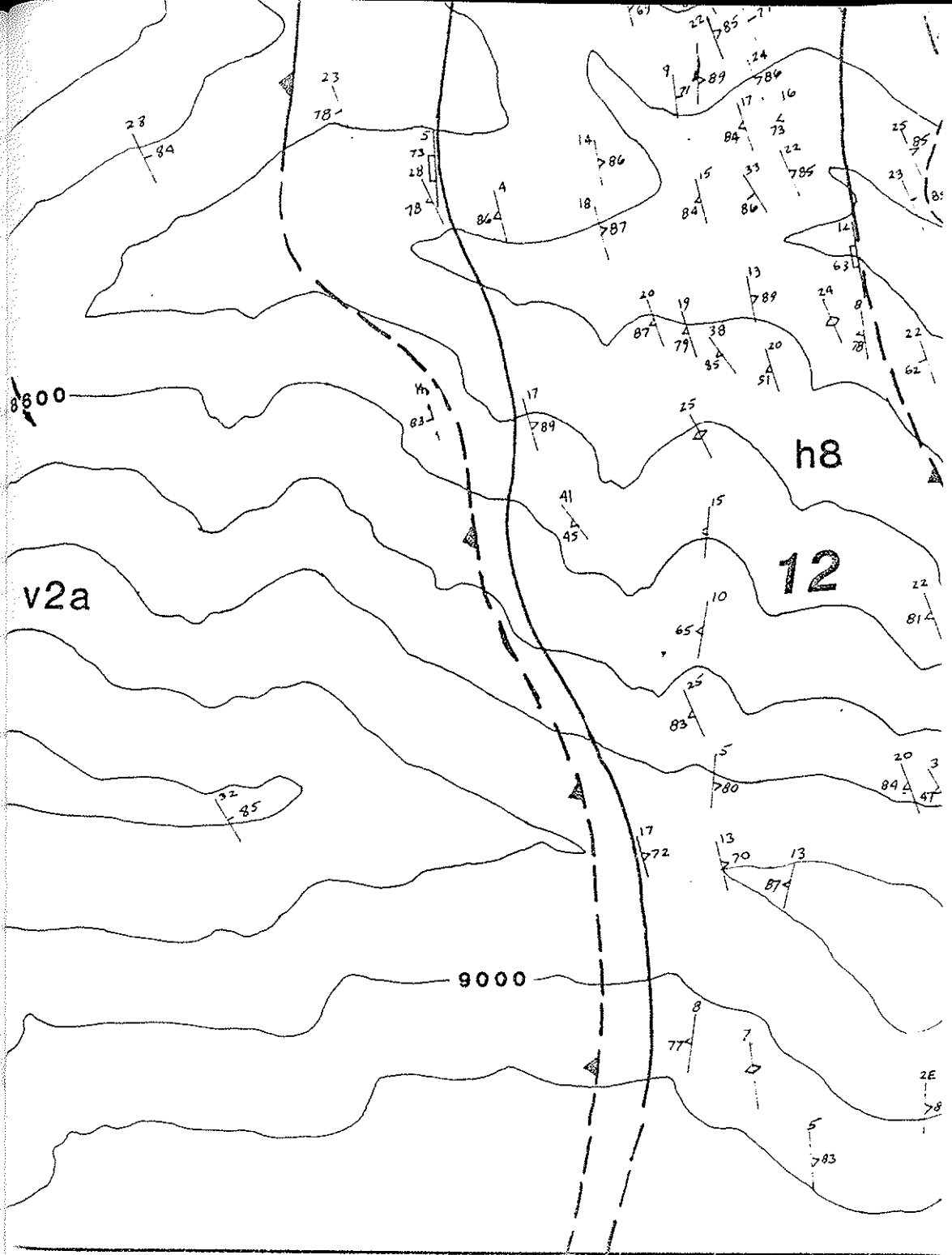




GEOLOGICAL MAP OF OPHIR



P AND WISCONSIN CANYONS 9



1. INTERNAL TOYARD RANGE NEVA



